



udp UNIVERSIDAD
DIEGO PORTALES

**TRACING THE FORMATION HISTORIES OF SPIRAL AND ELLIPTICAL
GALAXIES WITH INTEGRAL FIELD
SPECTROSCOPY**

A COMPREHENSIVE ANALYSIS OF GALACTIC EVOLUTION USING
SPECTRO-PHOTOMETRIC DECOMPOSITION OF GALAXY
COMPONENTS

A THESIS SUBMITTED BY

KEERTHANA JEGATHEESAN

TO THE

FACULTAD DE INGENIERÍA Y CIENCIAS
INSTITUTO DE ESTUDIOS ASTROFÍSICOS

IN PARTIAL FULFILLMENT OF THE REQUIREMENTS FOR THE
DEGREE OF DOCTOR IN ASTROPHYSICS

SUPERVISOR: **EVELYN JOHNSTON, PHD**

CO-SUPERVISOR: **BORIS HAEUSSLER, PHD**

UNIVERSIDAD DIEGO PORTALES
SANTIAGO, CHILE
DECEMBER 2024

© 2024, Keerthana Jegatheesan
All rights reserved

Acta de Deliberación
Defensa de Tesis Doctoral

En Santiago, el 13 de diciembre del 2024 el Tribunal de Defensa de Tesis Doctoral compuesto por la Dra. Evelyn Johnston (UDP), Dr. Roberto Assef (UDP), Dr. Boris Haeussler (ESO, Chile), Dra. Kshitija Kelkar (Vera C. Rubin Observatory, Chile) y Dra. Karen Masters (Haverford College, EEUU), sobre la base del texto del proyecto, la exposición del doctorando y sus respuestas a las intervenciones de los miembros del tribunal, ha resuelto aprobar la tesis doctoral “A comprehensive analysis of galactic evolution using spectro-photometric decomposition of Galaxy components” de la doctoranda Keerthana Jegatheesan.

Los miembros del Tribunal firman para constancia.



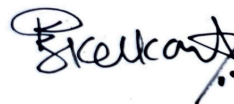
Evelyn Johnston
Supervisor, UDP



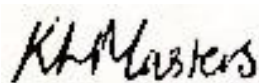
Roberto Assef
UDP



Boris Haeussler
ESO, Chile



Kshitija Kelkar
Rubin Observatory, Chile



Karen Masters
Haverford College, EEUU

To my lovely mum, Sangari Jegatheesan,
for her personal dedication to women's education.

என் அன்பான அம்மா சங்கரி ஜெகதீசனுக்கு,
பெண்களின் கல்விக்காக அவர் அளித்த தனிப்பட்ட அர்ப்பணிப்பும் ஆதரவுக்கும்.

And to all the wonderful souls who have
lifted me up along the way.

ACKNOWLEDGEMENTS

“It is often while travelling through the dark that you find the ones who shine brightest in your life. For they are the ones who remind you of your own beautiful light and show up, without a second thought, in your pain, as well as your glory.”

- Relief, Anna Taylor

I am often a sentimental writer when it comes to such matters of kinship and camaraderie, so I apologise if this gets quite maudlin at times, starting with the epigraph. The past four years have truly thrust me across a myriad of emotions and experiences, through the darkness and the light. And now that this chapter is finally over, and I take a step back to reflect, I am filled with a wave of immense gratitude for those who have stepped into the darkness and faced my demons with me, and just as steadfastly, walked into the light arm in arm with me. This journey has been the ultimate harvest of efforts that extend beyond just one individual, beyond simply me. And for that, if for nothing else, no amount of carefully chosen words and endless fountains of praise can ever fully capture my appreciation, but I shall try my best.

I would like to start by thanking my supervisors, Evelyn Johnston and Boris Häußler, for their guidance and unwavering support over the years. I have always been resolute in my belief that the true strength of a good teacher and mentor lies not in their ability to work with the gifted few, but in their capacity to uplift and nurture students of all calibres, regardless of their perceived potential. To that end, I consider myself fortunate to have had a team of supervisors who not only met this ideal but exemplified it — through their patience, their empathetic understanding, and their steady, gentle encouragement of my academic growth, in the face of overwhelming setbacks and occasional highs. It brings me no pleasure to think I may have ever inadvertently fallen short of your expectations and caused you disappointment, and I can only hope that, as this adventure closes, I have earned your pride. It has been a wonderful experience to learn from and alongside you both, to shape the projects of this thesis, and to bring it all to a joyful conclusion. The other person I would like to thank here is Paula Jofré, the director of the PhD programme, who has always kept a watchful and concerned eye on both my academic progress and my well-being. Your support, through personal conversations and the professional help you facilitated, has been invaluable in more ways than one. I am deeply grateful for the safe space you created for me to share my

darker moments with you and my supervisors, for all your flexibility in what could have been (and often is) a rigid system, in helping me navigate the challenges of particularly the past two years, and in reaching a successful and optimistic final defence. If I ever find myself in a position to mentor someone, I hope to uphold the values and qualities that each of you have imparted.

Next, for the crowning glory, I would like to extend my heartfelt thanks to every friend I have made here, from our start at the Núcleo to our evolution into the IEA. Knowing myself, I am fully aware that this section might turn inevitably into a love letter to all of you, but as someone who has always found comfort and solace in writing, what better way to express my gratitude than to etch it into the pages of my own work?

To Pedro, for his constant kindness and huge heart, always available for an impromptu “therapy” session to lift me up when I was caught in the throes of melancholy, and as equally, joined in with the eruptive laughter and joyful moments of the office. I could not have asked for a better first office mate, or a more whimsical partner in crime. Some of the best memories I have are with you and sweet Ana, whose gentle encouragement and dinosaur humour never failed to bring a smile to my face, even leading up to the days of the defence when I needed it most. The two of you will forever be my big brother and sister in my heart — and as clichéd as that may sound, no other words could capture it better, or barely even scratch the surface of how I blessed I feel to call myself your friend. To dearest Danielle, for her incredible sense of loyalty to her friends, never hesitating to go above and beyond to help them. I have learned so much from you, and alongside you, particularly in a personal sense, to better prioritise my own needs and boundaries in a world where our career dedication can make it all too easy to burn out. Our introverted hangouts, especially at “our” place - Café Piaf with Punto - have been the highlights over the time I have known you. That little spot will always remind me of safety, a feeling I have learned and come to cherish in your presence. To Trisha, for her empathy and her protectiveness over everyone at “the Office”. Being the only postdoc in the office at the time, you inadvertently became a mentor of sorts for the rest of us academic younglings. I would like to thank you from the bottom of my heart for being a shoulder to cry on when my anxious moments took over, and for your firm and persistent belief in my capabilities as a student. I may not have not believed it then, but your words of reassurance have had a lasting impact in building my self-esteem up from scratch over the past two years. I have watched you as a professional, as a mentor, and now as a mother, and it gives me pride to have been by your side through a part of your personal and professional journey. To the lovely Tatevik, whose unfailing faith in the goodness of others is a testament to her own kindness, warmth, and gentle heart. Your dedication to your friends, family, and your work has been inspiring, especially as I watch you balance it all, now including the beautiful new role of being a mother too. I am fairly certain that you were my missing puzzle piece in the office, and it was only after your arrival that I completely opened up

and joined in all the social gatherings of our little office family, ultimately strengthening and defining our relationships. As I am writing this, I am thrilled to report that as of now, time and distance have done nothing to diminish our bond, or that of anyone here who has had to leave Chile to start their next chapter. I have felt all of your support and love leading to the days of my defence, despite being continents apart. To Florence, for her boundless energy and enthusiasm, and her honesty. Your storytelling skills are truly a joy to behold, and I have no doubt that you will continue regaling people with every tale, big or small. You remind me to stay present in the simple moments, and I hope you keep sharing your vibrant spirit with everyone you meet - everyone needs a Flor in their lives. Thank you for the thoughtful defence poster, and for helping organise the celebration, a moment I never imagined would be etched into my memory as the best day of my life. Your company and encouragement in the past few weeks have directly played into my surviving the end of this journey, and for that, you have my warmest hugs. To Emilio, for his cool outward sarcasm, often hiding the deep care and thoughtfulness he carries within. Your unique way of balancing humour with genuine concern has often brought a sense of lightness to every situation, and I have come to appreciate your quiet and subtle strength. I am quite certain you will brush it off as you read this, but you know I am not wrong. I have felt your quiet concern, particularly during my difficult times, and you have always had an intuitive sense of when I am down, and knew when to check in. I hope you continue to carry that care for the people in your life, as much as you would like to convince us that you are on the Dark Side. To Prachi, for her cheer and her capacity for lending an ear without judgement. I would like to both thank you and apologise for “biting” said ear off with my rambling stories, to have talked through our experiences revolving around our shared culture - the good and bad. Your thoughtfulness was evident in your efforts at marking the end of my journey with the “necklace of love”, alongside Flor. To gentle Catalina, for her endless optimism, her exuberance, and more importantly, her good heart. My past has made me wary of trusting people right away, and I am happy to say you were the first to break through those walls. Thank you for waltzing into my life with your warm hugs and joyful words, and helping me believe in, and trust, the best in others, bringing with it a sense of positivity in my approach to life. I would also like to thank you for all your support regarding my health, and for constantly holding my hand through the hospital visits, brief as they were. Without you, I would have been quite disheartened to face it all alone. You truly are a blessing, not just to your friends, but to the IEA as well, and I wish you all the best in everything that lies ahead for you. To Pablo, for the steadfast care he offers to those fortunate enough to have earned his trust and friendship (I hope!). I would like to thank you for the time you put in for the other thoughtful defence poster. Moreover, I would like to appreciate you for being a walking Wikipedia in the office, entertaining us with facts we would otherwise never dream of looking up. For those interesting office discussions, for educating us on cultural points, for deeper and more personal reflections - you have my thanks. With the rest of the office currently scattered, I have been finding myself trying to hold on to the last piece, although it is

more likely that you would be one of the last ones standing. To Camilla, for her humour, and her continued commitment to our friendship, even after a year since our paths last crossed. I would first like to thank you for the time we shared as flatmates here, and during this brief stint, you have taught me to be more decisive, and more importantly, to prioritise my health while I struggled to find balance. You always offered your shoulder whenever I may have needed it at our home, bringing in pizza nights to cheer me up. I am fortunate enough to have met you at the verge of a difficult time two years ago, and to have built a strong, trusting relationship with you, one solid enough to share a home.

I may not know what the future holds, but wherever I may embark, I hope to carry all of this with me - your values, your words, our experiences, our memories, and the sense of community. As I continue writing, I truly understand for the first time when Winnie the Pooh said, "How lucky am I to have something that makes saying goodbye so hard". And on that note, I would like to quote a song lyric (probably to your chagrin) that has been bringing me to tears recently, as I think it describes this moment quite accurately:

*Long live the walls we crashed through
How the kingdom lights shined just for me and you
I was screaming, "Long live all the magic we made"
And bring on all the pretenders, I'm not afraid
Long live all the mountains we moved
I had the time of my life fighting dragons with you
I was screaming, "Long live that look on your face"
And bring on all the pretenders
One day we will be remembered
Hold on to spinning around
Confetti falls to the ground
May these memories break our fall
Will you take a moment?
Promise me this
That you'll stand by me forever
But if, God forbid, fate should step in
And force us into a goodbye
If you have children someday
When they point to the pictures
Please tell them my name
Tell them how the crowds went wild
Tell them how I hope they shine
Long live the walls we crashed through
I had the time of my life with you.*

- Long Live, Taylor Swift

And with that, I would like to thank all my fellow students, postdocs, and members of the faculty who have had an impact, big or small, through different epochs of my four

year journey. I would like to especially thank Chiara Mazzucchelli and Yasna Ordenes Briceño for all their help, and their kind words. I would also like to thank Lucas Cieza for his support, and for his efforts in discussing improvements in the PhD programme by asking for input from the students. Aside from the IEA, I would like to express my deepest gratitude to Payel Das and her family for their generosity in hosting me at their lovely home during my month in Surrey. Your care and the heartfelt conversations — whether about academia or life in general — have not gone unnoticed. I carry these moments with me and will continue to do so as I journey forward. To you and Robert Yates, for letting me pick your brains on multiple occasions during my time there, and for making me feel welcome amongst your group. For the boardgame nights and social gatherings at your home, I feel honoured and touched to have been part of it, if for only a brief moment.

I would be remiss if I did not acknowledge my first mentors during my master's at LAM, Olivier Ilbert and Iary Davidzon, at this stage. Thank you both for teaching me for the first time, the lasting positive impact supervisors can have on their students, when they share the ideal of “uplifting students irrespective of their perceived potential”. Olivier, it was under your training and guidance that I first set my sights on galaxy evolution research - none of this would have been possible without that single choice I made during my master's. There surely were struggles, but four years later, I am inclined to only revel in the brighter moments of that time, and I associate that to you.

At this point, I would like to take a moment to express my gratitude to every workshop and school I have had the privilege to participate in, and to the cohorts and fellow students I have had the fortune to learn from and alongside. To the LSST-DA Data Science Fellowship Program, in particular, Adam Miller and Bryan Scott for their unfaltering support for every student in each cohort, and for fostering a safe academic space with genuine inclusion in every way possible. For always being thoughtful and mindful of what each of us might be experiencing, and your dedication in imparting those values - through what I personally consider to be the best Code of Conduct ever - to what would be the new generation of astronomers (or individuals in any career), driven by empathy. To the DSFP fellows, I am grateful to have learned together with you, for the lunches and dinners, and for the enriching experience of being part of an international and diverse academic community. To the La Serena Data Science School, and to Amelia Bayo and Matthew Graham, for somehow managing to set up an interactive and engaging school in the midst of the pandemic. To the University of Tokyo Summer Internship Programme during my undergraduate days, where I first dipped my toes gently in the world of research and programming. I am also realising, in this moment, just how incredibly fortunate I have been to have had these enriching experiences early on in my life — experiences that have undoubtedly shaped many aspects of who I am today.

Stepping back a little in time, I would like to also thank my friends across the

continents, who have been through this journey virtually with me. To my dear friend Vanessa Serrano, whom I met a little over six years ago, when I first moved out to Marseille for my masters. I would like to thank you for your kindness and taking me under your wing, without whom the masters would have been quite a lonely journey. I marvel at the fact that six years later, nothing and everything has changed, and you still remain one of the first people I share any news with. You and your family have my earnest gratitude for genuinely cheering me on all of these years, for all my important moments. To the brilliant Shravya Shenoy, for all our video calls, if only to simply vent to each other, or to brainstorm and discuss our galaxy-related projects. Considering our paths only crossed once in person, it is quite remarkable how that seems to have had no effect on our friendship, so I would like to thank you for putting in the effort to make it work, for your support and encouragement have been invaluable over these years. To Deepti Hariharan, I would like to thank you for sharing the occasional bright moments of our undergrad days, and your constant virtual presence throughout the masters and PhD years. As a fellow expat navigating life in a new country for the first time with its cultural nuances, expectations, and academic and social challenges, our long conversations about our shared experiences in neighbouring countries were truly invaluable in helping me feel less alone. And finally, stepping back the furthest in time, I would like to thank Swetha Sriram, my oldest childhood friend, whom I have known for two decades, for being a familiar source of comfort through it all. Though our paths have diverged, the bond we share remains unshaken — a quiet yet steadfast reminder of the roots that keep us grounded no matter how far we grow.

I would also like to thank my therapist, Camila Molina, for her professional support during the past two years. While those who have known me well remark that they have witnessed my personal and professional growth over the last few years, there is no doubt that this sentiment is directly linked to the work we have done together. Having started with an adamant stance that personal and professional lives are entirely separate, my views and priorities are no longer the same - undeniably for the better - although some changes are seemingly harder to embrace than others. Through our work, I have learned to establish stronger boundaries, and be braver in speaking my mind, and one of the most significant shifts I have experienced is the quality time that I have been able to give my friends. From office dinners and birthday celebrations to escape rooms and baby showers, I am grateful to have been present for these moments without the lingering guilt I once felt. For this, and for your continual support until the day of the defence, you have my most sincere thanks.

And last, but by no means least, I want to express my deepest gratitude to my parents. To my father, Jegatheesan Periasamy, for every opportunity you have showered me with since my childhood. Growing up with stories of your own challenging past, I am filled with pride for your hard-working character, your early independence, and the perseverance that inevitably led to your well-earned happiness at present. To

my mother, Sangari Jegatheesan, to whom this thesis is dedicated to, I would like to thank you for your incredibly persistent devotion to your daughters, and for standing firm against everyone who brutally diminished the importance of education in the lives of young girls. Thank you for not following the herd, and for blazing a trail for us. I am forever grateful to have inherited the best of both of you, and I hope those qualities continue to guide me in whatever I pursue next, and I would like to state how proud I am to be your daughter. To my sister, Anjana Jegatheesan, for the memories we have shared and the bond we once had. Though time and circumstances have created distance between us, I want to express my hope that this joyful ending of a chapter brings us closer once again. You have held a special place in my heart, with your blind belief that I am doing something fancy with my choice of major despite my protests, and I look forward to the possibility of rebuilding the connection we once shared.

And with that, I shall sign off, leaving with a heart full of warmth, love, and appreciation. Until the next time.

ABSTRACT

Galaxies are born and shaped through their lifetimes mostly through gravitational interactions that drive the evolution of matter in the Universe through a range of physical processes across cosmic time. These interactions and processes have different impacts on the galaxies and influence the different components, whether they are distinctly termed as the “bulges” and “discs”, or more generically as the “inner component” and the “outer component”. The spectroscopic signatures left behind in the light of each component can reveal the processes that fuelled their evolution independently as well as a whole. Therefore, disentangling the light from various structural components of galaxies is crucial to extract their spectroscopic properties. On that note, this thesis addresses some of the key open questions in galaxy formation and evolution by examining the star formation histories of both spiral and elliptical galaxies and their components in the local Universe. While galaxy formation theories have been well explored over the past century, a complete and consistent framework that accounts for all observations is yet to emerge. By leveraging state-of-the-art integral field spectroscopy data and the novel structural decomposition software BUDDI, along with advanced spectral analysis techniques, this research contributes to a deeper understanding of the physical processes that shape the different galaxy types over cosmic time.

One of the lines of research in this thesis places a focus on disentangling the light from the bulges and discs of spiral galaxies, in order to investigate and compare their stellar mass assembly and in doing so, helping portray a picture of the formation mechanism involved in shaping the galaxies as a whole. Using data from SDSS-MaNGA survey in tandem with the spectro-photometric structural decomposition tool BUDDI, this work involved building the first statistical sample of cleanly extracted bulge and disc spectra of galaxies covering varied morphologies encompassing early to late type galaxies from ellipticals and lenticulars to the vastly diverse spirals. That being said, the analyses themselves centre on sub-sample of spiral galaxies, excavating the stellar populations in these components through the fossil-record method, tracing their evolution over the past ~ 14 billion years. In addition to the stellar population properties, the spectral synthesis allows one to reconstruct the mass-assembly histories, which together helps unveil the formation pathway of these galaxies. The analysis revealed broadly that while the bulges often show evidence of older stellar populations formed early in the Universe, the discs exhibit more prolonged star formation. This pattern supports inside-out growth models in the majority of cases, and is linked to the morphology of the spiral galaxy.

In parallel, the thesis explores the structural complexity of elliptical galaxies using MUSE observations, which present a more nuanced picture of galaxy formation under the two-phase scenario. BUDDI plays a significant role in this line of research, where it was rigorously tested several times for each of the three elliptical galaxies, to constrain with reasonable certainty (within the limits imposed by the instrument and observing conditions) the dual component nature which is seldom discerned in studies in comparison to the conventional single-component model. Through careful analysis of the surface brightness profiles and stellar populations of the inner and outer components, I constrain the physical significance of each component and its formation history. The inner regions typically show evidence of rapid, early star formation, while the outer regions often point towards accretion events and a more extended period of growth. This supports the two-phase formation model, where an early, intense burst of in-situ star formation is followed by the direct accretion of ex-situ stellar material from external galaxies through dry mergers.

Ultimately, this comprehensive analysis of two distinct morphologies contributes to the ongoing effort to understand the formation and evolution of galaxies observed at present-day. It serves to paint both a qualitative and a quantitative picture of structural complexity, star formation histories, and stellar populations. Therefore, it sheds light on the labyrinthine tapestry of interwoven processes that collectively drive the evolution of galaxies.

RESUMEN

Las galaxias nacen y se moldean a lo largo de sus vidas principalmente a través de interacciones gravitacionales que impulsan la evolución de la materia en el universo mediante una variedad de procesos físicos a lo largo del tiempo cósmico. Estas interacciones y procesos tienen impactos diferentes en las galaxias e influyen en los distintos componentes, ya sea que se les denomine específicamente como "bulbos" y "discos", o más genéricamente como "componente interior" y "componente exterior". Las firmas espectroscópicas que quedan en la luz de cada componente pueden revelar los procesos que alimentaron su evolución tanto de manera independiente como en conjunto. Por lo tanto, desentrañar la luz de los diversos componentes estructurales de las galaxias es crucial para extraer sus propiedades espectroscópicas. Esta tesis aborda algunas de las preguntas claves sin resolver sobre la formación y evolución de las galaxias mediante la examinación de las historias de formación estelar, tanto de galaxias espirales como elípticas y sus componentes en el universo local. Si bien las teorías de formación de galaxias han sido ampliamente exploradas en el último siglo, aún no ha surgido un marco completo y coherente que explique todas las observaciones. Al aprovechar los datos más avanzados de espectroscopía de campo integral, el novedoso software de descomposición estructural BUDDI y técnicas avanzadas de análisis espectral, esta investigación contribuye a una comprensión más profunda de los procesos físicos que han dado forma a los diferentes tipos de galaxias a lo largo del tiempo cósmico.

Una de las líneas de investigación de esta tesis se enfoca en desentrañar la luz de los bulbos y discos de galaxias espirales con el fin de investigar y comparar su ensamblaje de masa estelar, y a la misma vez con esta información ayudar a representar una imagen del mecanismo de formación involucrado en la configuración de las galaxias como un todo. Utilizando datos del sondeo SDSS-MaNGA en conjunto con la herramienta de descomposición estructural espectro-fotométrica BUDDI, este trabajo involucró la construcción de la primera muestra estadística de espectros de bulbos y discos extraídos de manera limpia y que cubren morfologías variadas que abarcan galaxias de tipo temprano y tardío, desde elípticas y lenticulares hasta las diversas galaxias espirales. Dicho esto, los análisis se centran en una sub-muestra de galaxias espirales donde se investigaron las poblaciones estelares en estos componentes a través del método de registro fósil, rastreando su evolución a lo largo de los últimos 14 mil millones de años. Además de las propiedades de las poblaciones estelares, la síntesis espectral permite reconstruir las historias de ensamblaje de masa, lo cual en conjunto ayuda a revelar la

vía de formación de estas galaxias. El análisis reveló que en términos generales mientras los bulbos muestran evidencia de poblaciones estelares más antiguas formadas en las primeras etapas del universo, los discos exhiben una formación estelar más prolongada lo que respalda los modelos de crecimiento de adentro hacia afuera en la mayoría de los casos.

Paralelamente la tesis explora la complejidad estructural de las galaxias elípticas utilizando observaciones de MUSE, que presentan una imagen más matizada de la formación de galaxias bajo el escenario de dos fases. BUDDI juega un papel importante en esta línea de investigación donde se probó rigurosamente varias veces para cada una de las tres galaxias elípticas, con el fin de restringir con razonable certeza (dentro de los límites impuestos por el instrumento y las condiciones de observación) la naturaleza de doble componente, la cual rara vez se discierne en los estudios en comparación con el modelo convencional de un solo componente. A través de un análisis cuidadoso de los perfiles de brillo superficial y de las poblaciones estelares de los componentes internos y externos, restrinjo la importancia física de cada componente y su historia de formación. Las regiones internas generalmente muestran evidencia de una rápida formación estelar temprana, mientras que las regiones externas a menudo apuntan a eventos de acreción y a un período de crecimiento más extendido. Esto respalda el modelo de formación de dos fases, en el que una explosión temprana e intensa de formación estelar in-situ es seguida por la acreción directa de material estelar ex-situ de galaxias externas a través de fusiones secas.

En última instancia, este análisis exhaustivo de dos morfologías distintas contribuye al esfuerzo continuo por comprender la formación y evolución de las galaxias observadas en la actualidad. Sirve para pintar una imagen tanto cualitativa como cuantitativa de la complejidad estructural, historias de formación estelar y poblaciones estelares. Por lo tanto, alumbra luz sobre el laberinto de procesos entrelazados que impulsan colectivamente la evolución de las galaxias.

CONTENTS

Contents	xvi
List of Figures	xxi
List of Tables	xxvii
1 Introduction	1
1.1 From nebulae to galaxies: a brief history of extragalactic discovery . . .	2
1.2 Cosmic architecture: Structure formation in the Universe	3
1.3 Galactic origins: Theoretical perspectives of galaxy formation and evolution	4
1.3.1 Formation of galactic discs	4
1.3.2 Formation of spheroids	5
1.3.3 Star formation and feedback in galaxies	6
1.4 A portrait of galactic structure: patterns and morphological diversity . .	8
1.4.1 The anatomy of a galaxy: dissecting the components	8
1.4.2 Morphological menagerie: the Hubble Sequence	10
1.4.3 Galaxy morphology as a tracer of evolution	15
1.5 An observational perspective: Optical spectroscopy of galaxies	16
1.5.1 Multi-object spectroscopy and the rise of Integral field spectroscopy	18
1.5.2 MaNGA: the middle ground between imaging surveys and re-	
solved spectroscopy	20
1.5.3 MUSE: deep individual observations for enhanced detail	21
1.6 The methodology: Decomposition of galaxy light profiles	23
1.6.1 Photometric decomposition: from GALFIT to GALFITM	23
1.6.2 Spectroscopic decomposition: the road ahead with BUDDI	27
1.7 Stellar population synthesis modelling: from spectra to quantifiable	
properties	29
1.7.1 Ingredients of SPS models	30
1.7.2 Full spectral fitting	31
1.8 Thesis outline	32

2	A dance of bulges and discs: decoding the stellar origins of spiral galaxies	34
2.1	Abstract	34
2.2	Introduction	35
2.3	Data and catalogues	39
2.3.1	SDSS	39
2.3.2	The MaNGA IFU survey	39
2.3.3	Galaxy Zoo: 3D	40
2.3.4	MaNGA PyMorph Value-Added Catalogue	40
2.3.5	MaNGA Visual Morphologies from SDSS and DESI images	41
2.3.6	The Nasa Sloan Atlas (NSA) catalogue	41
2.4	Galaxy decomposition in SDSS-MaNGA DR17	41
2.4.1	Input sample selection and data preparation	41
2.4.2	Bulge-disc decomposition with BUDDI	42
2.4.3	Selection of final sample	43
2.4.4	Caveats	44
2.5	Methods	45
2.5.1	Estimating bulge and disc stellar masses	45
2.5.2	Spectral fitting	51
2.6	Galaxy mass assembly histories	54
2.6.1	Individual and global trends: Component downsizing	54
2.6.2	Dependence on component stellar mass	59
2.6.3	Dependence on morphology	63
2.6.4	Effect of masking foreground stars	65
2.7	Stellar population properties of bulges and discs	67
2.7.1	Trends in mass-weighted stellar metallicity	68
2.7.2	Trends in mass-weighted stellar age	71
2.8	Discussion	72
2.8.1	Implications on galaxy stellar populations	73
2.8.2	Implications on galaxy assembly: downsizing and growth from the inside-out	76
2.9	Conclusions	80
3	The many faces of elliptical galaxies: unveiling the structural complexity and stellar histories	82
3.1	Abstract	82
3.2	Introduction	83
3.3	Data and observations	86
3.4	Methods	87
3.4.1	Galaxy decomposition with BUDDI	87
3.4.2	Spectral fitting for stellar population analysis	89
3.4.3	Voronoi binning for spatially resolved properties	90
3.5	Results	91

3.5.1	Component models and structural parameters	91
3.5.2	Mean stellar populations	95
3.5.3	Comparison with spatially resolved 2D stellar population maps	98
3.5.4	Temporal mass and luminosity contributions from inner and outer components	101
3.6	Discussion	107
3.6.1	Multiple structural components in ellipticals: implications from surface brightness profiles	107
3.6.2	Stellar population properties: inside-out formation and the two-phase scenario	109
3.6.3	Star formation histories: stellar assembly across time	111
3.7	Summary and conclusions	114
4	Summary and final remarks	116
4.1	Future perspectives	118
 Appendices		
A	SDSS photometry with BAGPIPES - Stellar mass dependence of e-folding time τ	149
B	Bulge Sérsic index as a function of galaxy stellar mass	152
C	Stellar population properties of bulges and discs	153
D	Half-mass formation timescales of bulges and discs	155
E	Reconciling stellar histories of ellipticals in BUDDI-MaNGA and MUSE	157

LIST OF FIGURES

1.1	The sketch of M51 (Whirlpool galaxy) by Lord Rosse.	2
1.2	Anatomy of the Milky Way showing its multiple components. Credits - Left: NASA/JPL-Caltech; right: ESA; layout: ESA/ATG medialab. . . .	9
1.3	The Hubble-de Vaucouleurs “tuning fork” diagram. Credit: Antonio Ciccolella/M. De Leo	11
1.4	A multi-wavelength view of Andromeda galaxy, with different features highlighted at each wavelength regime. Credit: Planck mission team/NASA/ESA.	15
1.5	The main instrument designs used in IFS to disperse the light at every spatial pixel. Credit: M. Westmoquette, adapted from Allington-Smith et al. 1998	19
1.6	Illustration of the hexagonal fibre bundles in MaNGA IFUs and its ability to obtain spatially resolved spectroscopy, shown in two different regions of the galaxy.	22
1.7	Illustration of the MUSE instrument layout and how the field is divided among the 24 IFUs, with each IFU further split into 48 slices.	23
1.8	Sérsic profiles as a function of radius from the galaxy centre, for different sérsic indices.	24
1.9	Example of a galaxy in SDSS DR7 modelled with different parametric forms and their combinations with GALFIT, taken from Zhang et al., 2024. From top to bottom - Exponential, Sérsic, Exponential + de Vaucouleurs, and Exponential + Sérsic.	26
1.10	Workflow of BUDDI for a bulge-disc decomposition scenario, where the disc is fixed with an exponential profile of $n = 1$. Adapted from Johnston et al., 2022a.	28

2.1	Histograms depicting the distributions of physical properties of different samples used in this study. Lower panels: Distributions of the galaxy stellar mass, morphological T-Type, and redshift in the successful fits in the new BUDDI-MaNGA DR17 sample, as defined in Sect 2.4.3 (darker shades), and for all the MaNGA galaxies observed with the 91 and 127 fibre IFUs (lighter shades). The dashed outlines depict the distributions of the galaxies that were successfully fit with PyMorph in the MPP-VAC-DR17, which determined the initial set of objects from which we built the BUDDI-MaNGA sample. The T-Types of the ellipticals and S0s from the VAC are reassigned indices of -2 and -1, respectively, for continuity in the distribution. Upper panels: Distributions of the fraction of successful BUDDI fits with respect to the PyMorph fits sample (lighter shades), and a fraction of successful BUDDI fits with respect to the MaNGA sample with the largest IFUs (darker shades).	40
2.2	Density plot of the disc masses estimated by BAGPIPES and the colour-mass relation in Barsanti et al. (2021). The black diagonal line shows the 1:1 correspondence, and the dashed lines mark the ± 0.3 dex offset from it. The inset shows the distribution of the difference between each BAGPIPES estimate and the CMR estimate, with the black dashed vertical line marking the median offset.	47
2.3	Similar to the density plot for Figure 2.2 but showing the bulge masses. .	47
2.4	Similar to the density plot for Figure 2.2 but showing the total galaxy stellar masses.	48
2.5	Bulge-to-total ratio of all galaxies in the r -band, as a function of morphology. The lower x-axis is labelled by the T-Type index, and the upper x-axis by the corresponding Hubble types. The inner parts of the violins contain a box and whisker plot. The white circles in the violin plots represent the median bulge-to-total ratios, while the thick black bar defines the interquartile (25th - 75th percentile) range of the distribution. The limits on the thin black bar extend to 1.5 times the interquartile range. The upper and lower ends of the violins mark the highest and lowest values of $(B/T)_r$ in each T-Type. The number of galaxies in each T-Type is denoted on top of its corresponding violin. The region shaded in red depicts the early-type galaxies (ETGs: E, S0, and S0a), that are not part of this analysis, which concentrates on the types with the white background. The ETGs will be discussed in a different publication. The region marked in grey with the late-type spiral galaxies (Sdm and Sm) are highlighted due to their very low numbers. Additionally, these are visually harder to separate as two distinct morphologies, and will be merged together in certain plots in the analysis.	50

- 2.6 **Individual and global trends of MAH in bulges and discs.** Left and centre columns: Individual MAHs of spirals separated by increasing T-Types (from top to bottom). In each panel, the mean-stacked MAH for high-mass components ($M > 10^{10} M_{\odot}$) are shown as thick black dot-dashed curves, and low-mass components ($M < 10^{10} M_{\odot}$) as thick black dashed curves. These are depicted as red dot-dashed and dashed curves respectively for the Sa type (row 1), which also serves as a reference for all following types for easier visual comparison. Right-most column: Bulge and disc masses in red and blue, respectively, with their median masses shown by dotted lines. 56
- 2.7 Formation time of the bulges and discs which marks the time it took to form 50 per cent of the stellar mass, colour-coded by the total stellar mass. The upper panels show the histogram of these formation times for the bulge and disc in red and blue respectively, with their median times in dashed lines. 57
- 2.8 **Dependence of MAH on component stellar mass.** Left-most column: Disc mass distributions in increasing steps of morphological type (top to bottom panels). Right-most column: Bulge mass distributions in increasing steps of morphological type. The vertical dashed line is the median component stellar mass for each type. Centre columns: disc and bulge MAH curves stacked in every corresponding mass bin shown in the histograms. Histogram bins and MAH curves have the same colour-coding, marked by the median mass of bulges or discs in each bin. Bins containing 3 objects or less are shown in white on the histograms, and their corresponding MAH curves have been excluded. 60
- 2.9 **Dependence of MAH on morphology:** Each panel is a stellar mass bin defined in the previous section, increasing vertically from top to bottom. The morphologies were binned and stacked to show median MAHs of types Sa (maroon), Sab/Sb (orange), Sbc/Sc (navy), and Scd/Sd (grey). The solid thick lines represent the bulges and the thin dot-dashed ones correspond to the discs. 64
- 2.10 Bulge-disc decomposition of galaxy 9509-9102 from the previous BUDDI run on DR15 (second row) and current DR17, which includes a foreground star mask (upper row). The final panel shows the MAH of the bulge (red) and disc (blue) resulting from both fits (solid curves for DR17 and dot-dashed curves for DR15), along with an SDSS *gri* image of the galaxy with the MaNGA field of view (91 fibre IFU) superimposed in purple. . . 65
- 2.11 Stellar population properties of bulges and discs along with their corresponding distributions. Left: Comparison of mean mass-weighted stellar metallicities of the bulges and discs, colour-coded by bulge stellar masses. Right: Same as the left panel, but for stellar ages. Joint histograms show the distributions in bulge and disc properties. 68

- 2.12 Comparison of bulge and disc metallicities and their dependence on morphology. Left panel: Bulge $[M/H]$ compared to disc $[M/H]$, colour-coded by the morphological type. The next two columns show split violin plots, with the upper half depicting the bulge metallicity distribution (red) and the lower half depicting the disc metallicity distribution (blue) in each type. The violin plots are marked with the median by the dashed black lines, and the quartiles are shown by the dotted lines. The grey shaded regions show the morphologies with very low-number statistics. 69
- 2.13 Comparison of bulge and disc stellar ages and their dependence on morphology. Left panel: Bulge $\log(\text{Age})$ compared to disc $\log(\text{Age})$, colour-coded by the morphological type. As in Figure 2.12 next two columns show split violin plots, with the upper half depicting the bulge age distribution (red) and the lower half depicting the disc age distribution (blue) in each type. The violin plots are marked with the median by the dashed black lines, and the quartiles are shown by the dotted lines. The grey shaded regions show the morphologies with very low-number statistics. 70
- 3.1 Fit to the median-stacked white-light image of the three ellipticals J020536, J205050, and J225546, from top to bottom. Left column: observed input image, the best-fit model, and the residual image. The images have all been scaled to the same flux for comparison. Upper right panel: 1D light profile of the galaxy at the central r -band wavelength along the major axis (black points), the Sérsic profiles of the inner (red line) and outer (blue line) components and the combined model (purple line). Lower right panel: residuals (in per cent) of the 1D data points and model as a function of distance along the major axis. 93
- 3.2 Left panel: Mass-weighted stellar populations showing the logarithmic stellar ages in years (lower x -axis) and their corresponding values in Gyr (upper x -axis), against stellar metallicities of the one-component and the two-component models. The three marker styles represent the three galaxies, while the colours represent the components - blue for the outer component of the double Sérsic model, red for the inner component, and purple for the single Sérsic component. The associated logarithmic error bars are also shown. Right panel: The same as the upper panel, but with light-weighted stellar populations instead. 98

3.3	Voronoi-binned stellar populations for galaxies J020536, J205050, and J225546 from left to right. From top to bottom, the rows indicate the logarithmic mass-weighted stellar ages, the light-weighted ages, the mass-weighted metallicities, and the light-weighted metallicities. The colour bars for the ages have been displayed in Gyr for better clarity, and the scale bars in each plot mark 1 kpc. The $1R_e$ and $2R_e$ contours from BUDDI of the inner component are marked as dashed black ellipses, and only the $1R_e$ contour of the outer component is shown as solid black ellipses, since the $2R_e$ contours are beyond the extent of the mapped regions of the galaxy. For object J225546, an additional contour is shown in grey, which marks the $1R_e$ ellipse of the adjacent galaxy modelled together with the target.	99
3.4	Stellar populations in metallicity-age grids and their subsequent assembly histories for galaxy J020536.	103
3.5	Stellar populations in metallicity-age grids and their subsequent assembly histories for galaxy J205050.	103
3.6	Stellar populations in metallicity-age grids and their star formation histories for galaxy J225546.	104
A.1	Dependence of e-folding time as a function of stellar mass. Upper panel: Variation of e-folding times of bulges τ_{bulge} (red) and discs τ_{disc} (blue) as a function of their corresponding component stellar masses. The stars represent the median value in each mass bin, and the error bars show the 16th-84th percentile range in the spread of values in each bin. Lower panel: Similar to above but with the total galaxy stellar mass along the x-axis. In both panels, the τ_{bulge} was shifted by 0.05 dex for clarity in visualisation.	150
B.1	Bulge Sérsic index as a function of the total galaxy stellar mass M_* . The red points show the individual galaxies, while the red stars show the binned median, with the error bars marking the 16th-84th percentile range. For statistically significant mass bins of $M_* > 10^{10} M_\odot$, the Sérsic index of the bulge increases with increasing galaxy mass, which arises from the bulge assembling from the discs. The timescale of assembly is expected to be shorter for the more massive galaxies, and longer for the less massive ones, which is consistent with our results on downsizing seen in low-redshift spiral galaxies.	152

- C.1 Stellar population properties of bulges and discs and their corresponding distributions. Upper panel: Comparison of mean mass-weighted stellar metallicities of the bulges and the discs (with their uncertainties), colour-coded by disc stellar masses. The distributions in bulge (disc) metallicities are shown in the right (upper) joint histograms. Each bin in the metallicity histogram of the bulges is colour-coded by the mean disc mass in that bin. Lower panel: Similar to the upper panel but for stellar ages. The black diagonal line marks the 1:1 correlation. 153
- D.1 Half-mass formation timescales of the bulges and discs, colour-coded by bulge mass. The upper panels show the histogram of these formation timescales for the bulge and disc in red and blue respectively, with their median times in dashed lines. 156
- E.1 Mass-assembly histories of two components (Sérsic+exponential) in elliptical galaxies in the BUDDI-MaNGA DR17 sample. The “exponential” component shows more delayed assembly histories possibly indicating accreted stellar mass in the later stages of evolution. In the Sérsic component, except for a few objects, the MAHs are clustered on the far right of the plot, where the entire stellar mass had been assembled in an extremely short timescale at the very initial stages of their formation. 157

LIST OF TABLES

1.1	The fibre configurations in each fibre bundle, the arcsec diameter of each IFU, and the number of fibres per plate.	21
3.1	The coordinates and properties of the three elliptical galaxies observed with MUSE.	86
3.2	Chebyshev polynomials introduced in the step fitting the narrow-band images of the datacube.	89
3.3	Structural parameters and the flux contribution of each component relative to the total flux for the single-component model (“single”) and for each component of the two-component model (“inner” and “outer”) at the r -band central wavelength 6166 Å.	92
3.4	Mean mass and light-weighted stellar populations properties listing the stellar metallicities, ages, formation times τ_{50} and τ_{90}	97
3.5	Mass fractions and light fractions estimated by pPXF. The fraction of contribution from the mass and luminosity of stellar populations that are old ($t > 8$ Gyr), of intermediate age ($4 < t < 8$ Gyr), and young ($t < 3$ Gyr).	102

I can never read all the books I want; I
can never be all the people I want and
live all the lives I want. I can never
train myself in all the skills I want.
And why do I want? I want to live and
feel all the shades, tones and
variations of mental and physical
experience possible in my life. And I
am horribly limited.

Sylvia Plath

INTRODUCTION

The formation and evolution of galaxies beyond our own Milky Way is a rich and active field of study in modern astrophysics, both from observational and theoretical standpoints. Most of these studies revolve around understanding gravitational interactions and their influence in driving the evolution of matter in the Universe through a variety of physical processes across cosmic time. Unravelling and decoding the formation and evolution of galaxies remains an important and open field of study, encompassing the wide diversity of galaxies, both near and far, their different morphologies, their kinematics and stellar populations, their chemical composition, and their environment. This is a crucial area of research because galaxies are often considered astrophysical laboratories, which are interconnected with the larger picture of cosmology and understanding how the Universe itself has been evolving and will continue to evolve in cosmic time.

In this thesis, I focus particularly on spiral and elliptical galaxies in the local Universe, both of which are generally described as visually opposing morphologies, with the spirals appearing the most complex and beautiful, and the ellipticals seeming simpler and less remarkable. The broad goal is to understand the formation and evolution mechanisms that have played a significant role in building the structure that we observe today and to explore the physical complexity or simplicity of these galaxies. I study this by retracing the assembly histories of the stars that reside in these galaxies and their individual components through a technique called the fossil-record¹ method. The central theme of the thesis is, in essence, deciphering the starlight from the components that make up nearby galaxies to reveal their origin stories.

Before diving into the research objectives, this introductory chapter establishes the groundwork and scientific context for the thesis. I discuss the relevant literature, setting the stage for the exploration into the fundamental processes that shape the evolution of galaxies. The following sections direct attention to the core ideas and themes that underpin the analyses in this work.

¹ the fossil in “fossil-record” refers to galaxies in the nearby Universe.



Figure 1.1: *The sketch of M51 (Whirlpool galaxy) by Lord Rosse.*

1.1 From nebulae to galaxies: a brief history of extragalactic discovery

A detailed study of galaxies and their evolution would be remiss without a brief overview of the historical discoveries that spearheaded the field of extragalactic astronomy. Our understanding of the nature of galaxies beyond our own had begun to take shape in the mid-seventeenth century. Christiaan Huygens pioneered the observations of distant objects that were called *nebulae* for their notably diffuse and nebulous appearance. In 1750, Thomas Wright, in his publication “An Original Theory or New Hypothesis of the Universe”, proposed that the structure of the Milky Way was made of a flattened disc of stars, and the Earth was located within this system. He also suggested that the diffuse nebulae that had been observed were objects that were distant but similar to the Milky Way. These ideas later influenced the philosopher Immanuel Kant to hypothesise in his 1755 publication “The Universal Natural History and Theories of the Heavens”, the existence of *island universes* that were in fact external galaxies whose light appeared diffuse due to their distance from our Galactic viewpoint. From 1771 to 1784, Charles Messier catalogued 110 astronomical objects in his “Catalogue des Nébuleuses et des Amas d’Étoiles”, some of these being the ambiguous “nebulae” described earlier.

The first record of the evidence of distinct spiral features in some of these “nebulae” was made in 1845 by Lord Rosse (Fig. 1.1), when he observed a Messier object M51 with his 75-inch reflector telescope, which was later nicknamed the Whirlpool Nebula. Such objects with a defined spiral structure were termed spiral nebulae. With technological advances in astronomical photography, the search for uncovering the nature of spiral nebulae led to what will be known as the Great Debate in 1920, when two astronomers,

Harlow Shapley and Heber Doust Curtis proposed contrasting theories to explain these objects. Shapley argued that spiral nebulae were simply gas clouds located within the Milky Way, which was meant to be the extent of the Universe at the epoch. Curtis contested this view, suggesting that spiral nebulae were “island universes” in their own right, independent of the Milky Way. The debate was finally put to rest in 1925, when Edwin Hubble measured the distance to M51 (known as the Andromeda Nebula) using Cepheid variable stars and discovered it to be larger than the size of the Milky Way, essentially confirming that it was an external galaxy and not a part of the Milky Way. This discovery was a crucial milestone in realising that the cosmos was much larger than initially believed, paving the way for extragalactic astronomy.

1.2 Cosmic architecture: Structure formation in the Universe

Unravelling the mysteries behind the formation of structures in the Universe fundamentally relies on a cosmological framework based on both theory and observation. The discoveries highlighted in Sect. 1.1 along with Hubble’s later ground-breaking discovery of the expansion of the Universe (Hubble, 1929) in the early-twentieth century have simultaneously all been leading to the development of Observational Cosmology. Employing technological instruments, this discipline investigates the origins, structure, content, and evolution of the cosmos, and uses observations to test cosmological models.

The structure of the Universe that we observe today, with the galaxies embedded within the cosmic web can be explained with the concordance model of cosmology: the cold dark matter (Λ CDM) model. In recent years, the Planck satellite has played a pivotal role in the field of observational cosmology, refining our understanding of the early universe and in establishing this current paradigm of cosmology. The high-precision measurements of the cosmic microwave background (CMB) by Planck have provided crucial insights into the cosmic framework. Planck observations have helped determine key cosmological parameters with unprecedented accuracy, such as the age of the universe, the rate of its expansion (Hubble constant), and the distribution of matter and energy (Planck Collaboration et al., 2016).

Hubble’s discovery of the expansion of the Universe (Hubble, 1926) led to the emergence of the Big Bang theory, which is the conventionally established framework for the formation of the Universe from a primordial singularity. This theory rests on two central pillars: the cosmological principle which posits that the universe is homogeneous and isotropic when viewed on a sufficiently large scale, and General Relativity which describes gravity as the curvature of spacetime.

The formation and evolution of the Universe under the Λ CDM cosmology follows a hierarchical growth through cosmic time. The primordial quantum fluctuations in the early homogeneous Universe and the consequent symmetry breaking triggered its inflation. These minuscule perturbations in the density of the Universe marked the first seeds of structure in the cosmos; they continued to grow due to gravitational instabilities in regions of high density, where gravity triumphs in the race against the

expansion of the Universe. The instabilities gradually amplified, causing the denser regions to draw in the surrounding matter, continuing to increase in density. In contrast, the low-density regions grew emptier, creating voids. The growth eventually resulted in achieving critical density in the clusters, after which matter collapsed under self-gravity to form dark matter halos, which are the cradles of galaxies. Under this cosmological framework of hierarchical growth, the dark matter halos themselves continue to grow by merging with other halos. Cosmological information is thus embedded in the structure and distribution of matter in the Universe, allowing galaxies to act as tracers of the underlying matter.

1.3 Galactic origins: Theoretical perspectives of galaxy formation and evolution

It is well established that the energy density of the Universe at present is dominated by the elusive dark components, with baryonic matter only contributing a small fraction. However, unlike dark matter which only interacts gravitationally, the baryonic matter composed mainly of gas, stars, and dust, is luminous and can be observed directly through the light that galaxies emit across a wide range of wavelengths in the electromagnetic spectrum. In the following sections, the formation of the major galactic structures, i.e., discs and spheroids, is elaborated in the context of the Λ CDM cosmology.

1.3.1 Formation of galactic discs

Under the hierarchical framework of the Λ CDM model, low-mass objects formed first in a bottom-up scenario. During the collapse, dark matter haloes formed from the primordial density fluctuations are believed to gain angular momentum via tidal interactions with neighbouring haloes (White, 1984) or through mergers with other haloes (Maller et al., 2002). These earliest generations of haloes, as they formed, would gravitationally accrete primordial gas, i.e., the baryonic material. At high redshifts and low mass haloes, the “cold-mode accretion” dominates through streams of cold, dense gas flowing along the cosmic filaments (Katz et al., 2003). However, at low redshifts, the gas accretion is primarily through the “hot-mode” (Silk, 1977; White et al., 1978; White et al., 1991), where the gas is shock-heated to the virial temperature of the dark matter halo as it falls in. Following this, the pristine primordial gas made of only hydrogen and helium, collapsed with a similar angular momentum to the surrounding dark matter in the halo. Over cosmic time, subsequent generations of massive haloes formed by merging with smaller haloes while simultaneously accreting gas and stellar material from satellite galaxies.

During the early stages of the evolution of the density fluctuations, the baryonic component is anticipated to follow the structure of the coalescing dark matter. However, after critical density was attained and the collapse of matter began, the dark matter component, being collisionless, continued to only evolve under the influence of gravita-

tional forces, and collapsed conserving its total energy. Conversely, the baryonic gas component was additionally governed by different dissipative dynamics, which allowed it to be shocked and heated due to their collisional nature (White et al., 1978). This leads to a crucial process in the formation of the galaxies: “dissipative collapse”. The gas, while collapsing, radiates away some of its energy through collisional processes while conserving its angular momentum, the result of which is a rotation-supported galactic disc at virial equilibrium at the centre of the dark matter halo (Fall et al., 1980; Peebles, 1969). This rotating gas disc would be the site of eventual star formation, feedback, and evolution that led to the stellar discs we observe today.

1.3.2 Formation of spheroids

Spheroidal galaxies are believed to have formed from distinct processes acting on different dynamical timescales compared to those involved in the formation of disc galaxies. Disc galaxies typically arise as a result of gradual gas accretion into the dark matter halo that eventually collapses and triggers star formation. This process leads to the formation of a “protogalaxy”, marking the initial phase of a galaxy when it first experienced star formation. In contrast, spheroidal galaxies form through a faster process driven by the strong gravitational potential of the dark matter halo. In the “rapid monolithic collapse” scenario (Larson, 1974), the potential causes a rapid infall of gas in a dynamical timescale much shorter than the gas accretion in disc galaxies. This is followed by an isothermal collapse of the gas and subsequent cooling through radiative processes. Ultimately, these processes trigger a rapid and intense burst of star formation across the entire protogalaxy.

An alternative model often invoked is the hierarchical merging scenario (Toomre et al., 1972; Cole et al., 2000; Hopkins, 2009; Avila-Reese et al., 2014), where gas-rich disc galaxies of comparable masses merge and result in the formation of a spheroidal galaxy. Mergers are expected to destroy the discs of the progenitor galaxies and transform them into a spheroidal galaxy with randomised stellar orbits throughout. This dissipative process is termed a “wet merger”, during which the gas from both galaxies is rapidly consumed in a voracious burst of star formation, occurring more prominently at high redshifts. Non-dissipative mergers can also occur at lower redshifts, between already-formed spheroidal galaxies. For instance, Khochfar et al., 2003 find that such “dry mergers” preserve the spheroidal shape of the galaxies involved, leading to the formation of massive spheroidal galaxies observed at present-day. The current model predicts the interplay between both major formation scenarios to explain the properties of spheroidal galaxies observed in the present day. In particular, the hybrid “two-phase” scenario (Oser et al., 2010; Johansson et al., 2012) posits that spheroidal galaxies observed in the present day are formed in two stages: the first dissipative phase of monolithic collapse or wet mergers at high redshifts, which forms a compact and dense spheroid through in-situ star formation; the second non-dissipative phase dominates at low redshifts, where dry mergers accrete stellar material through ex-situ

star formation. The contribution of each phase differs for the wide range of spheroidal galaxies observed in the Universe, and is investigated in detail in one of the projects of the thesis, in Chapter 3.

1.3.3 Star formation and feedback in galaxies

The formation of stars in galaxies is a crucial element of decoding galaxy evolution. This is an immensely complex process, the physics of which is still not entirely understood due to the different dynamics and interactions amongst a vast range of physical processes and environments involved. At its core, the necessary ingredient required for star formation boils down to cold gas, which was pristine and uncontaminated by metals in the first low-mass haloes.

Formation of stellar populations. This gas undergoes cooling mainly through neutral hydrogen gas molecules and atomic hydrogen, allowing it to reach the critical density required for forming molecular clouds that later fragment and form the first generation of stars. The star formation process does not wait for the disc to fully form within the halo, such that when it is settled, it typically consists of both gas and newly formed stars. In the case of spheroids, even though the gas collapse in the dark matter halo is considered relatively rapid, it still occurs with dynamical timescales of several hundred Myr. This duration is sufficient for the first stars to form, evolve, and ultimately reach the end of their lifecycles. In the early low-mass haloes, these were the now theoretical Population III stars (Bromm et al., 2002; Karlsson et al., 2013; Katz et al., 2023), which contain no heavy metals and would have been exceptionally massive and bright with short lifetimes. With masses likely over $100M_{\odot}$, these stars are expected to have ended their lives in supernovae explosions or black holes. The heavier elements that were subsequently synthesised within the cores of the Population III stars were ejected into the surrounding interstellar medium (ISM) as a result of stellar evolutionary processes. The ISM, now being enriched with metals, would act as the source for the formation of the next generation of stars in the massive haloes that emerged later by halo mergers. These are termed Population II stars (Fang et al., 2004; Maio et al., 2010), which are still relatively metal-poor, and Population I stars, which are the most recently formed with a higher abundance of heavier metals. The ISM thereby gets further enriched by every passing generation in a perpetual cycle of stellar formation and destruction. That being said, star formation in galaxies is not a continuously replenishing process and is rather regulated and slowed by stellar evolution and active galactic nuclei (AGN). Through negative feedback processes, they tend to efficiently remove baryonic material from galaxies, or make the environment inconducive for star formation to continue.

Stellar feedback. Stars significantly shape the interstellar medium (ISM) through a multitude of processes leading to *stellar feedback*. This feedback occurs through radiation, stellar winds, and supernovae, each impacting the interstellar medium (ISM). For

instance, massive stars emit significantly in the UV regime of the spectrum, and the stellar radiation pressure ionises the ISM, and can disperse the surrounding gas and dust. They also drive winds and outflows from star-forming regions, thereby suppressing further star formation.

When a massive star reaches the end of its life, it undergoes a sudden gravitational collapse, culminating in a supernova explosion that releases an immense amount of energy, reaching approximately 10^{51} ergs (Thielemann et al., 2004). This event has profound effects on the surrounding ISM and star formation processes. The intense heat generated by the supernova can prevent molecular hydrogen gas clouds from cooling, which is a necessary prerequisite for star formation. For smaller molecular clouds, a single supernova explosion can provide sufficient energy to completely unbind the system. Moreover, supernovae can trigger galactic winds, which are powerful outflows of gas that can escape the gravitational potential wells of galaxies. These winds serve a dual purpose in regulating star formation: they not only slow down ongoing star formation and introduce stochasticity in galactic evolution, but also reduce its efficiency by heating the ISM. This feedback mechanism is particularly impactful in low-mass galaxies with shallow potentials, where supernova feedback plays a dominant role in limiting star formation rates.

AGN feedback. An AGN is a highly luminous region at the centre of certain massive galaxies that can often dominate over the stellar continuum. It is established that AGN are powered by supermassive black holes that accrete gas and dust from their immediate environment. As the material falls inward, it forms an accretion disc around the black hole, where it gets heated to extremely high temperatures due to the combined effects of gravitational forces and friction. This process results in the galaxy emitting vast amounts of radiation, especially in the X-ray and radio frequencies. The energy output usually released by AGN exceeds the binding energy of the host galaxies and can photoionise the surrounding gas in the halo. These energetic processes effectively heat the ISM and prevent it from cooling down, or can push the gas out of the intergalactic medium (IGM) through jets, limiting the availability of cold gas to continue star formation. While supernovae feedback operates at energetic scales that tend to suppress and slow down star formation, AGN feedback downright stops it and quenches the galaxy. Both these processes operate at different mass regimes and are equally critical in regulating star formation, offering an explanation for the observed star formation histories of present-day galaxies.

The formation mechanisms and star formation processes described in this Section are merely a condensed and general overview of the multifaceted field of galaxy evolution. As such, only the core concepts of the subject that are immediately relevant to this thesis are addressed, and therefore a deeper dive into the theoretical and observational perspectives on the vast range of interwoven phenomena involved in shaping galaxies would be beyond the scope of this work.

1.4 A portrait of galactic structure: patterns and morphological diversity

The galaxies that are observed in the present day have been through aeons of evolutionary mechanisms throughout their lifetimes. Hidden in the patterns and morphologies today are echoes of the physical processes that have been driving the formation and evolution of galaxies throughout their history.

The study of galaxy morphologies is a vast field on its own, encompassing different methods ranging from human identification to machine learning, and schemes to classify galaxies based on their visual appearance in images or through diagnostic properties characteristic of different types of galaxies. In the context of this thesis, the *Hubble sequence* (see Sect. 1.4.2) is used for morphological classification. However, before delving into the complexities of this domain, an overview of the simplest components of a galaxy is required, for they will make a relevant appearance in visual galaxy classification and the Hubble sequence.

1.4.1 The anatomy of a galaxy: dissecting the components

With the wealth of imaging data of galaxies across the electromagnetic spectrum and subsequent studies over the last century with photometry and spectroscopy, there are a few distinct components of galaxies that emerge from them. These components display varying structures, properties, kinematics, and stellar populations, suggesting that the various parts of a galaxy develop and evolve along different pathways. Not all galaxies comprise all the components mentioned below, but these serve as an indicator of the vast diversity in galaxy morphology. It is important to isolate the different structural components of galaxies to get a well-rounded picture of the evolutionary processes through cosmic time that have led to the patterns and morphologies observed today. The following sections summarise the main properties of the principal components found in galaxies.

Bulge: a central, compact, and dense spheroidal component found in spiral and S0 galaxies (see Sect. 1.4.2). They are typically described by a Sérsic profile, where the surface brightness decreases steeply with radius from the centre. Bulges are often classified as either a “classical bulge” or a “pseudo-bulge”, with the boundary of distinction based on the Sérsic index n (see Sect. 1.6 for the parametric form of the Sérsic function). A classical bulge in principle has a higher central concentration of stars, and therefore a higher n , and is pressure-supported due to the randomised stellar orbits. This is indicative of formation scenarios linked to violent processes such as major mergers, or rapid dissipative collapse (see Sect. 1.3.2) in the early Universe. In contrast, pseudo-bulges have a comparatively extended surface brightness profile with lower n , resembling discs. This implies that pseudo-bulges have a flattened structure similar to

discs, instead of the spheroidal concentration observed in classical bulges. This structure suggests that these bulges were formed from gradual secular processes like internal disc instabilities and gas accretion. While classical bulges are red and typically host old and metal-rich stellar populations, the pseudo bulges are blue and host younger stellar populations that are reminiscent of their ancestral discs. The ambiguity around the definition of a classical bulge and a pseudo-bulge has been debated over the years, with new studies suggesting that it is not feasible to classify bulges into two distinct categories. For instance, [Breda et al., 2020b](#) advocate for a model where bulges exist on a spectrum of varying Sérsic indices and host a range of various stellar populations.

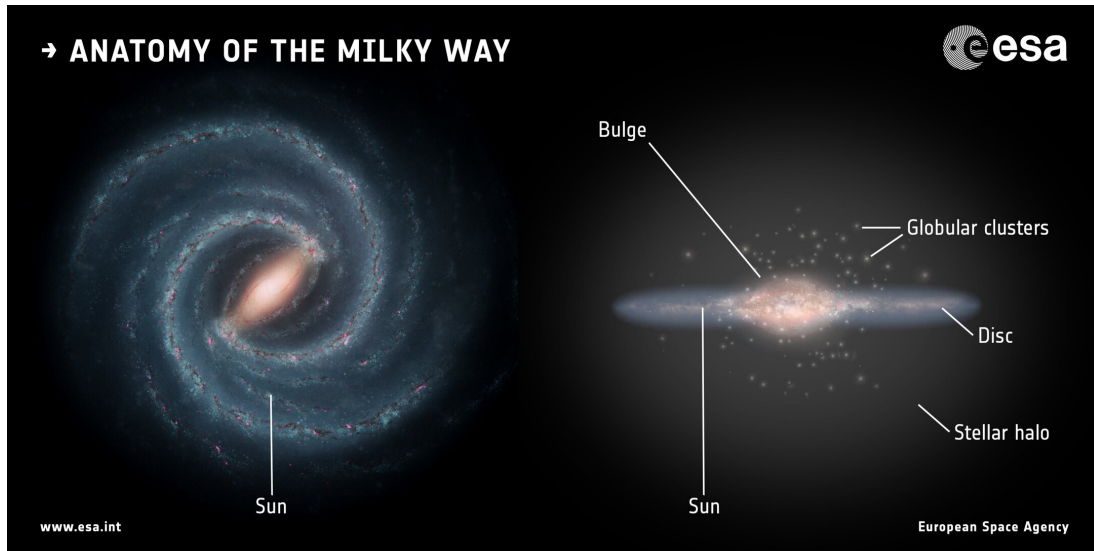


Figure 1.2: *Anatomy of the Milky Way showing its multiple components. Credits - Left: NASA/JPL-Caltech; right: ESA; layout: ESA/ATG medialab.*

Disc: a flat and extended structural component usually surrounding the bulge in spiral and elliptical galaxies. The disc is a rotationally supported structure with ordered stellar rotation, consisting primarily of stars, gas, and dust. The surface brightness profile of discs is often well described by an exponential function, with a gradual decrease in stellar density with radius. As stated earlier in Section 1.3.1, discs are believed to be formed from gradual gas accretion, leading to a dissipative collapse; although, minor dry mergers can add to the stellar content and mass at the outskirts of the discs. Furthermore, discs host additional sub-structures in the form of galactic bars and spiral arms, which are the most prominent sites of active star formation, often associated with the presence of blue and young stellar populations. However, this is contradicted by certain galactic discs (especially in S0 galaxies; see Sect. 1.4.2) that have evolved and rather contain red and old stars with a range of metallicities. During mergers and interactions, the disc is often the most affected component where stellar activity occurs, and therefore captures the effects of physical and dynamical processes, and chemical enrichment of galaxies over time.

Stellar halo: a diffuse, spheroidal component extending beyond the main body of the galaxy, reaching further than the disc. Accounting for about 1% of the stellar mass of the galaxy, this component typically hosts some of the oldest and most metal-poor stars, as well as globular clusters. The stellar orbits in the halo are quite eccentric, spanning a wide range of velocities, resulting in a dispersion-supported structure. The stellar halo is generally described by a power-law profile, with a shallow decline in luminosity with radius from the centre. The very low surface brightness exhibited by the stellar halo has proven challenging to study with standard photometric or spectroscopic surveys, and requires deep observations targeted toward high galactocentric radii. This low surface brightness, coupled with the high velocity dispersion of the stars, reflects a history influenced by the accretion and disruption of smaller satellite galaxies. While the stellar populations are still observable despite their low luminosities, the stellar halo also contains a significant amount of dark matter, which can extend to much larger physical scales.

The components described above are depicted in Figure 1.2 for the Milky Way. While these are the most basic components, additional features and sub-structures like spiral arms, bars, and nuclear discs have also been observed in galaxies both at low and high redshift. These components and structures are closely linked to galaxy morphologies and their evolution and transformations, and are key to determining whether a galaxy has always maintained its current morphology or if it has evolved from a different morphology over time.

1.4.2 Morphological menagerie: the Hubble Sequence

The classification of galaxies based on their morphology continues to be a subject of extensive research. The morphology of a galaxy is observed on the sky plane as a projection of its 3D structure and orientation with respect to the line of sight. Over the years, various classification systems have been proposed, with the Hubble classification (Sandage, 1961) being the most widely accepted. This system, often known as the Hubble tuning fork diagram (Fig. 1.3) due to its evident branched appearance, was initially devised to illustrate the evolutionary progression of galaxies from early-type galaxies on the left to late-type galaxies on the right. However, current observations contradict this interpretation with evidences of galaxies evolving in the opposite direction, yet the terminology remains in use.

The Hubble sequence in the low-redshift Universe begins with the “early-type” galaxies (ETG) on the left spanning both Ellipticals (E), Lenticulars (S0), and the “late-type” galaxies (LTG) spanning Spirals (S) and Irregulars (Irr) forming the right-most prongs of the tuning fork. Often, the ETGs are associated with quiescent and passive galaxies, while the LTGs are linked more to star-forming galaxies. However, these modes of classification are not directly interchangeable, since ellipticals and S0s have been discovered to host recent episodes of star formation (see Sect. 1.4.2.1), and must not be generalised as a quiescent population.

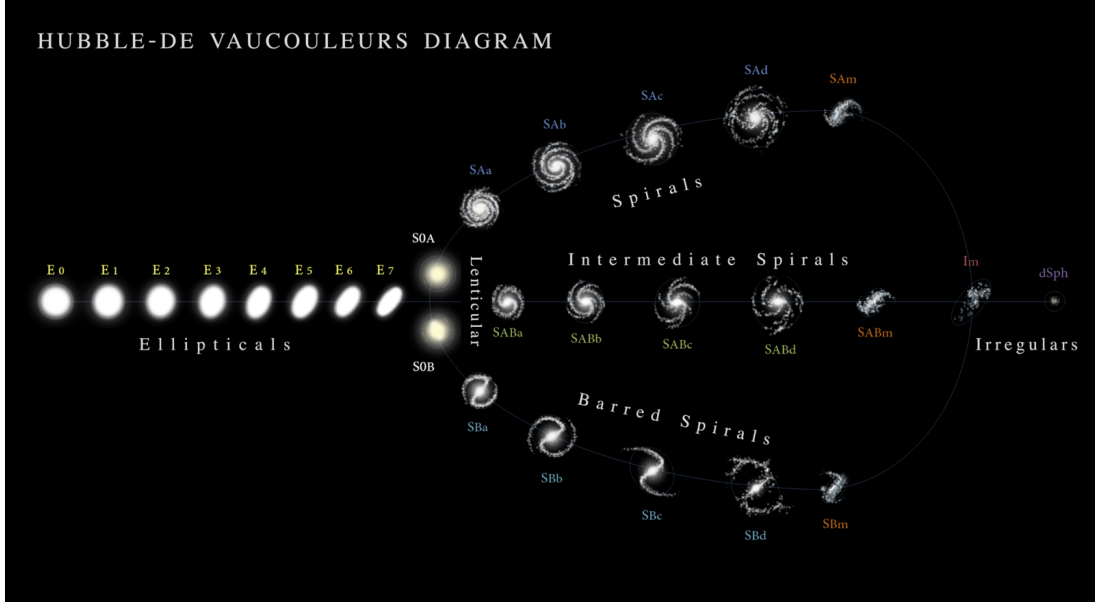


Figure 1.3: The Hubble-de Vaucouleurs “tuning fork” diagram. Credit: Antonio Ciccolella/M. De Leo

1.4.2.1 Elliptical galaxies (E)

Elliptical galaxies are typically characterised by their smooth, featureless visual appearance, lacking the spiral arms, dust lanes, or other complex structures seen in other types of galaxies. They tend to have a more homogeneous distribution of primarily old and red stars, and are often described as spheroidal in shape, with little evidence of ongoing star formation. In the Hubble classification scheme, elliptical galaxies are assigned numbers between 0 and 7 (Fig. 1.3), which corresponds to the degree of ellipticity as projected on the sky. E0 galaxies appear nearly spherical, while E7 galaxies appear as the most elongated ellipticals. While elliptical galaxies may have been traditionally dismissed as simple objects, decades of study have now conceded that these objects encompass a wide range of photometric and spectroscopic properties across several orders of sizes and stellar masses. The most massive galaxies in the local Universe tend to be elliptical galaxies, like the supergiant M87 in the Virgo cluster with a stellar mass of $2.5 \times 10^{12} M_{\odot}$. On the contrary, numerous compact and dwarf ellipticals with stellar masses of the order of $10^7 - 10^8 M_{\odot}$ have been discovered.

The classical massive “red and dead” galaxies in the nearby Universe that are traditionally associated with ellipticals can often be traced back to a combination of violent processes such as early monolithic dissipational collapse (Larson, 1974; Chiosi et al., 2002) or major mergers (Toomre, 1977; Hopkins et al., 2008) and hierarchical clustering (Toomre et al., 1972; Cole et al., 2000; Hopkins, 2009; Avila-Reese et al., 2014) over several Gyr. Mergers trigger a rapid burst of star formation, during which the available gas is voraciously consumed. Coupled with AGN feedback, which heats the surrounding ISM or dispersing the residual gas and preventing further star formation, this process ultimately results in a passive, quiescent galaxy. For the majority of massive galaxies, these red and dead classical ellipticals (CLE) are a reasonably accurate

representation. However, with newer instruments and deeper surveys, other classes of ellipticals which deviate from the classical picture have emerged, including recently-quenched ellipticals (RQE), and blue star-forming ellipticals (BSF). RQEs have been defined as ellipticals with younger ages and traces of tidal features but with no observed emission lines from star formation (McIntosh et al., 2014), suggesting a first-generation elliptical galaxy formed recently through a gas-rich merger or prominent interactions. On the other hand, BSF ellipticals show signs of ongoing star formation and even younger ages (Lacerna et al., 2016; Lacerna et al., 2020). These discoveries enforce the idea that the diversity of elliptical galaxies presents a rich opportunity to explore the processes of galaxy formation and evolution.

1.4.2.2 Spiral galaxies (S)

With a visually striking appearance, spiral galaxies are some of the most common types of galaxies in the local Universe. These are characterised by a centrally concentrated bulge, which is surrounded by a flat, rotating disc structure, and luminous spiral arms winding outwards from the bulge. In barred spiral galaxies, an additional bar structure stretches from the central bulge to the spiral arms. Due to the presence of complex and intricate sub-structures, spirals exhibit a varied distribution of stellar populations, ranging from old red stars in the bulge representing a retired quiescent component, to younger blue stars in the disc and spiral arms where active ongoing star formation primarily occurs. In highly inclined galaxies that are continuously forming new stars, dust lanes are sometimes visible as dark bands obscuring the disc light, composed of cold interstellar dust and gas. The diversity demonstrated by spiral galaxies in terms of their physical characteristics and properties similarly imply a range of stellar masses from $10^9 - 10^{12} M_{\odot}$ and luminosities from $10^8 - 10^{11} L_{\odot}$. Their structure and star formation activities make them key objects of study in understanding galaxy evolution and dynamics.

In the upper prong of the Hubble tuning fork (Fig. 1.3), these galaxies are further sub-classified progressively into Sa, Sb, Sc, Sd, and Sm based on the tightness of the winding spiral arms and the prominence of the bulge relative to the disc. The Sa-type galaxies have their spiral arms wound tightly around a pronounced central red bulge. The arms tend to have less star formation and are smoother, with fewer regions of gas and dust. This usually implies a bulge with old evolved stars that formed before the disc with newer and younger stars. At the other end, the Sd-type galaxies have very loosely wound or even fragmented spiral arms and a minimal, bluer central bulge. These bulges are often considered to be young pseudobulges, which form after the disc (see Chapter 2 for a detailed study on the stellar properties of different spiral morphologies). These galaxies are more irregular in appearance in comparison to the structured early-type spirals, with numerous star-forming regions scattered throughout the arms. The Sm galaxies refer to the Magellanic spirals, named for their resemblance to the Magellanic clouds, especially the Small Magellanic Cloud (SMC). Sm galaxies

are characterised by very loosely wound or disorganised and clumpy spiral arms that host active star formation, and they typically lack a well-defined central bulge. Between these major sub-classifications, intermediate types have also been introduced that bridge the characteristics of the main classes, such as Sab, Sbc, and Scd, forming a continuous sequence of spiral galaxies. A parallel sequence of barred spirals forms the lower prong of the tuning fork (Fig. 1.3), which share the characteristics of the spiral arms and bulges, with the addition of a central bar. However, it must be noted that visual morphology classifications are often crude and depend on the depth of the instrument and the wavelength used in the observations, and there is always a substantial chance of overlap.

While spiral galaxies are often portrayed as either having an old red bulge, or a younger blue bulge and a star forming disc, in reality, their properties and structures are far more complex. Both bulges and discs can exhibit a rather heterogeneous distribution of stellar populations, influenced by various internal and external factors such as the environment, stellar mass, and the unique formation pathways that have shaped each spiral galaxy into its present-day form. The multifaceted characteristics exhibited by spiral galaxies can often be traced back to an early primordial collapse of gas clouds (Larson, 1974; Chiosi et al., 2002), mergers that enhance star formation in the galaxies (Toomre, 1977; Hopkins et al., 2008) and accretion events building up the stellar mass, and long-term secular evolution driven by internal processes and sub-structures. Aside from this, anaemic spirals have been discovered and studied (van den Bergh, 1976; Elmegreen et al., 2002; Pak et al., 2019), revealing that they are passive galaxies with negligible ongoing star formation, most likely on the path to becoming S0 galaxies after being starved of cold gas. These spirals appear red due to the presence of old and evolved stars such as red giants, which dominate the luminosity output, not unlike elliptical galaxies (see Sect. 1.4.2.1). Considering their ubiquitous presence in the local Universe, accounting for $\sim 60 - 70\%$, studying spiral galaxies is essential for unlocking the complexities of galaxy formation and evolution, providing a detailed view of the processes that shape galaxies over cosmic time.

1.4.2.3 Lenticular galaxies (S0)

In between ellipticals and spirals on the Hubble sequence lies a population known as lenticular or S0 galaxies. These galaxies are considered a transitional type due to their structural similarities to both spirals and ellipticals. S0 galaxies often feature a bulge and a disc, similar to spirals, and may also contain a bar (Fig. 1.3). However, they host smooth discs lacking spiral arms and exhibit little to no active star formation. Their gas reservoirs are typically depleted, and they contain minimal dust, unlike spiral galaxies. Different observations over the years have not led to a consensus regarding formation scenarios, with S0 galaxies found to be hosting a myriad of stellar populations in their bulges and discs that are reminiscent of either spiral or elliptical galaxies. Due to these intermediate properties, they are believed to represent an evolutionary benchmark in galaxy transformations.

Drawing from the morphology-density relation (Dressler, 1980; Whitmore et al., 1991; Pfeffer et al., 2023) which ascertains the prominence of S0 galaxies in highly dense clusters, an environmental formation mechanism can be invoked to explain the origins of these galaxies. When a blue star-forming spiral galaxy falls into a high-density group or cluster, the gas from the outskirts of the galaxy disc is partially expelled by the diffuse intracluster medium through ram-pressure stripping (Gunn et al., 1972), or the gas is directly stripped from the halo, starving the galaxy of the fuel needed for further star formation (Larson et al., 1980). The remainder of the available gas in the galaxy migrates to the central regions of the galaxy, where new star formation can be ignited (Icke, 1985; Kronberger et al., 2008), leading to a bulge with younger stellar populations than the surrounding disc (Fisher et al., 1996; Sil'Chenko, 2006; Johnston et al., 2014). Without the gaseous fuel, the galaxy continues to evolve passively with its existing stellar populations, and over time develops into the S0 galaxy observed at present-day. Alternatively, in a lower density environment, a minor merger between a star-forming spiral and a smaller galaxy in a group can effectively be consumed in starbursts that exhaust the available gas (Mihos et al., 1994). Moreover, the turbulence induced by these interactions, while small, can affect the gas in the spiral galaxy, triggering its final episode of star formation and marking the start of its transformation into an S0 galaxy. Other processes reported in literature include recent bulge rejuvenation that reignites star formation leading to a young bulge, or inside-out quenching leading to an older bulge (Fraser-McKelvie et al., 2018), varying depending on the stellar mass and environment of the galaxy. Studying S0 galaxies and reaching a global consensus on their formation pathways not only deepens our understanding of this unique morphology but also sheds light on the nature of their ancestral spiral galaxies.

1.4.2.4 Irregular galaxies (Irr)

At the very end of the Hubble sequence are the irregular galaxies, with stellar masses ranging from $10^8 - 10^{10} M_{\odot}$ and luminosities from $10^7 - 10^9 L_{\odot}$, fainter than the star-forming spiral galaxies in the local Universe. The irregular galaxies do not show any resemblance in structure or characteristics to spirals, ellipticals, or lenticulars, and do not fit neatly into any of these classifications. They have no defined central bulge or spiral arms or bars, and instead have a rather chaotic shape with no symmetric structural features. However, they often contain knots of active star formation, scattered clusters of stars, and varying densities of gas and dust peppered throughout the galaxies. Some of these irregular galaxies may even be experiencing their first major phase of star formation (Mas-Hesse et al., 1999). The continuous active star formation in these galaxies produces a hot, young stellar population that appears blue. Galaxies that show a disturbed morphology on account of being in the process of merging, with the signatures of tidal tails appearing are also categorised as irregular galaxies. These are believed to be weakly evolved systems. The best-known irregular galaxies in the Galactic neighbourhood are the Large and Small Magellanic Clouds. Just as each distinct

morphology reveals unique insights into galaxy formation and evolution, irregular galaxies play a crucial role in understanding the diversity of this field, shedding light on the stellar content and star formation processes occurring in galaxies (Gallagher et al., 1984).

1.4.3 Galaxy morphology as a tracer of evolution

From the extent of complex diversity observed in galaxies, there is the inevitable implication of galaxy morphology as a fundamental tracer of evolution across cosmic time. The morphological classifications of galaxies as spirals, ellipticals, lenticulars, and irregulars reflect the various physical processes, both major and minor, that have shaped their structure. The most dramatic morphological transformations and star formation occur during major mergers, where progenitor spiral galaxies find their ultimate end as a single elliptical or lenticular galaxy. The emphasis on the significance of mergers throughout the introductory chapter would later prove evident in setting the stage for the lines of research explored in this thesis. Galaxies captured in the midst of a merger exhibit irregular tidal features resulting from the interaction, sometimes extending well beyond their individual physical sizes. Equally, galaxies falling into a cluster environment produce a visually striking display of “tentacles” created by the ram-pressure stripping of the disc, during the interaction between the ISM and the IGM, creating the aptly-named “jellyfish galaxies”. It is clear that the environment is one of the interconnected factors which plays a crucial role in influencing galaxy morphologies, with the morphology-density relation (Dressler, 1980) predicting the prominence of early-type galaxies in highly dense cluster environments.

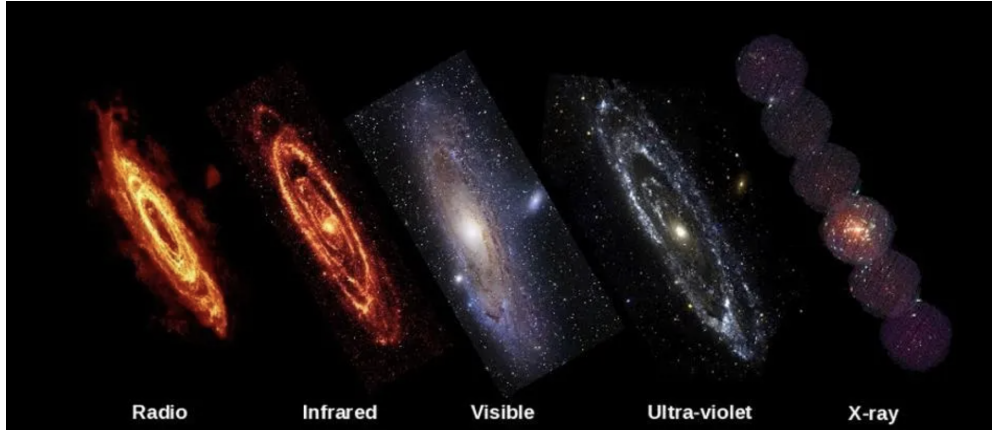


Figure 1.4: A multi-wavelength view of Andromeda galaxy, with different features highlighted at each wavelength regime. Credit: Planck mission team/NASA/ESA.

Contrary to the vividly intense external processes, in the absence of a crowded environment, the secular evolution of galaxies emerges as another mechanism, driving milder morphological changes over long timescales, relying on gentler internal processes (Kormendy et al., 2004). For example, a bar can develop in a pure-disc galaxy due to gravitational instabilities, which can then help in redistributing angular momentum

and gas in the disc. This often leads to the bar funnelling gas inwards to the centre of the galaxy, fuelling star formation there. With this mechanism, a bulge begins to form and grow through secular evolution, turning the galaxy morphology initially from a pure-disc to one with a small central concentration. The concentration then continues to grow under internal processes, until it transforms to a bulge-dominated galaxy. Secular evolution is typically invoked as the formation pathway of pseudo-bulges that appear to mimic the properties of discs. Overall, secular evolution offers a complementary framework for understanding how galaxies evolve morphologically in relatively isolated environments, highlighting the importance of both internal dynamics and external influences in shaping the diverse structures observed in galaxies today.

At this point, I must note that the work in this thesis is entirely based on optical wavelengths, and hence the descriptions of morphology and its role as an evolutionary tracer are limited to this visible range. This is vital since morphology is a wavelength-dependent property (see Fig. 1.4), and the optical observations and derived properties highlight the stellar content in spiral arms, discs, and bulges of galaxies. For example, the bluer wavelengths in this regime reveal newer episodes of star formation, while the redder wavelengths emphasise older and evolved stars throughout the galaxies. However, there exists a myriad of hidden features that can be unveiled in other wavelengths, and calls for a brief overview. For instance, infrared observations penetrate the dust clouds in star-forming galaxies, revealing a different morphology with star-forming regions that are obscured in the optical observations. Radio wavelengths, on the other hand, are crucial for studying AGN jets, and specifically the neutral hydrogen gas (HI), which is abundant in the ISM. The 21 cm HI observations often resemble the optical observations, but as a gas tracer, extend far beyond the physical scales of the optical regime. They help map the distribution and kinematics of this gas, and shed light on the galactic structure and dynamics. Although these non-optical wavelengths are not directly relevant to the conclusions of this thesis, they contribute to the global picture of galaxy evolution in the context of different morphologies, and the processes and structures they help trace through time.

1.5 An observational perspective: Optical spectroscopy of galaxies

Any progress in uncovering the depths of galaxy evolution in the nearby Universe relies primarily on the technological advances in instrumentation and the observational capabilities that improve with them. Imaging data from photometric surveys have become increasingly popular over the past decades, covering expansive swathes of the sky observed through a multitude of broad-band and narrow-band filters (see Sect. 1.6.1 for a list of such surveys). This indeed provides a comprehensive view of galaxy evolution trends through the analysis of their morphologies, their broad-band stellar population properties, and cosmic star formation histories in a large-scale statistical

manner.

However, the broad-band features lack the detail present at the wavelength resolution of spectroscopic data. For instance, the spectral features captured at the resolution of spectroscopic instruments allow for more precise redshift estimations, and therefore cosmological distances. One of the disadvantages of estimating photometric stellar populations from broad-band SEDs arises from the dust-age-metallicity degeneracy, which is challenging to disentangle at the resolution provided by broad-band or even narrow-band photometry. Moving into the realm of spectroscopy, spectral features at finer resolution help mitigate this effect and allow the estimation of stellar populations more accurately. Dust attenuation is established to be stronger at shorter wavelengths, and hence absorbs more of the light at bluer wavelengths, making the spectrum appear redder than it truly is. As a spectroscopic solution, the Balmer absorption lines at the red and blue ranges of the spectrum - $H\alpha$ at 6563 Å and $H\beta$ at 4861 Å for instance - are strong in the young stellar populations, and the influence of dust attenuation can in principle be disentangled by using the Balmer decrement ($H\alpha/H\beta = 2.86$, fixed by the principles of atomic theory; Calzetti, 2001). Other spectral features are used as stellar population diagnostics, based on their sensitivity to stellar age and metallicity independently: $H\beta$ is the most sensitive age indicator, with the galaxies dominated by young stars showing the strongest absorption line, which eventually becomes shallower as the galaxy ages. Similarly, the metal-sensitive absorption lines like Fe (5270 Å and 5335 Å), the Mg_2 index (5175 Å), and the CaII triplet (8498 Å, 8542 Å, and 8662 Å) are stronger in metal-rich galaxies. Furthermore, since $H\alpha$ is a tracer of recent star formation, the line strength of this emission line can be directly translated to a measure of the star formation rate (Kennicutt Jr, 1998).

The ability to analyse individual emission lines also allows us to probe ionisation processes and star-forming regions, as well as the influence of AGN, through diagnostics like the BPT diagram (Baldwin et al., 1981; Kewley et al., 2006). This distinction is essential for understanding feedback processes in galaxies, which play a significant role in regulating star formation and galaxy growth (see Sect. 1.3.3). Furthermore, galaxy kinematics, such as rotational velocity and velocity dispersion, offer insights into the mass distribution of galaxies, the presence of dark matter, and contain the dynamical traces of mergers and interactions. Since the 20th century, kinematics measurements have been pivotal in understanding the structural evolution of galaxies and most importantly, the presence of dark matter. Kinematic distortions or misalignment between the stellar and gas kinematics can indicate a recent interaction, which can provide further information on the history of the galaxy. These advantages open up a whole new window for galaxy evolution studies, widening the parameter space that can be explored with present-day instrumental capabilities.

While the advantages of spectroscopy are evident, that is not to say it has no limitations. Spectroscopic observations have increasingly high demands in terms of time and cost, and this limits the scope of such observations to smaller, carefully selected samples. This loses the wide sky coverage provided by photometric surveys, thereby

reducing the scale of statistical analyses significantly. Additionally, while spectroscopy helps mitigate the age-metallicity degeneracy better than photometry, it does not entirely remove this effect from stellar population analyses. Bearing in mind the strengths and weaknesses of both photometry and spectroscopy, it might be prudent to view them as complementary tools in galaxy evolution studies, combining the statistical benefits of the former and the fine details of the latter.

1.5.1 Multi-object spectroscopy and the rise of Integral field spectroscopy

The concept of Multi-object Spectroscopy (MOS) was introduced in the late 20th century, when astronomers realised the tedious impracticality of obtaining spectra of objects using the traditional single-object approach, especially with the rapidly increasing demand for data collection with imaging capabilities. In order to observe and gather spectra of several objects simultaneously, several efficient methods to integrate MOS were explored, including multi-slit and fibre-fed spectrographs.

Multi-slit spectrographs were built on the concept of single long-slit spectrographs, with slit masks placed at the focal plane, aligning with the galaxy (often along the major axis). Each slit is aligned with a different target object, allowing the telescope to capture light from multiple positions in multiple objects in one exposure. This technique served as an improvement over the traditional dispersion element in an imaging camera, which disperses the light from the entire image without properly accounting for the sky background contribution, leading to the spectra from different regions of the galaxy and the sky from overlapping. In the multi-slit approach, by masking the unwanted sky and only allowing light from the objects of interest to pass through the slits, this technique improved the quality of the data, making it easier to subtract the sky background accurately. However, this technique came with the downside of limited slit positions, and the inflexibility in choosing the scientifically relevant position along the galaxy. While this would not have a strong impact for galaxies whose 2D projection appeared axisymmetric, it can lead to a potential loss of significant features in non-axisymmetric galaxies, such as regions of star forming activity or morphological disturbances.

The field was then revolutionised with the introduction of fibre optics into astronomical spectroscopy (Vanderriest, 1980), which are positioned in the focal plane either manually or with automated robotic installations. The use of fibre optics based spectroscopy has now become one of the standards in MOS, transforming different fields of astronomy, including the study of galaxies. One of the statistical cases of fibre-based spectroscopy in extragalactic astronomy was with SDSS, where one spectrum was obtained per galaxy, using a single-fibre spectrograph. The flexibility that comes with the positioning of the fibres makes it a more feasible option compared to the multi-slit technique, allowing a slit-like configuration of the fibres at the entrance of the spectrograph. However, just as one limitation was overcome, the fibre-fed spectrographs introduced another in the form of fixed aperture sizes. This meant for galaxies with large angular sizes, the fibres only captured a small fraction of the galaxy light, often

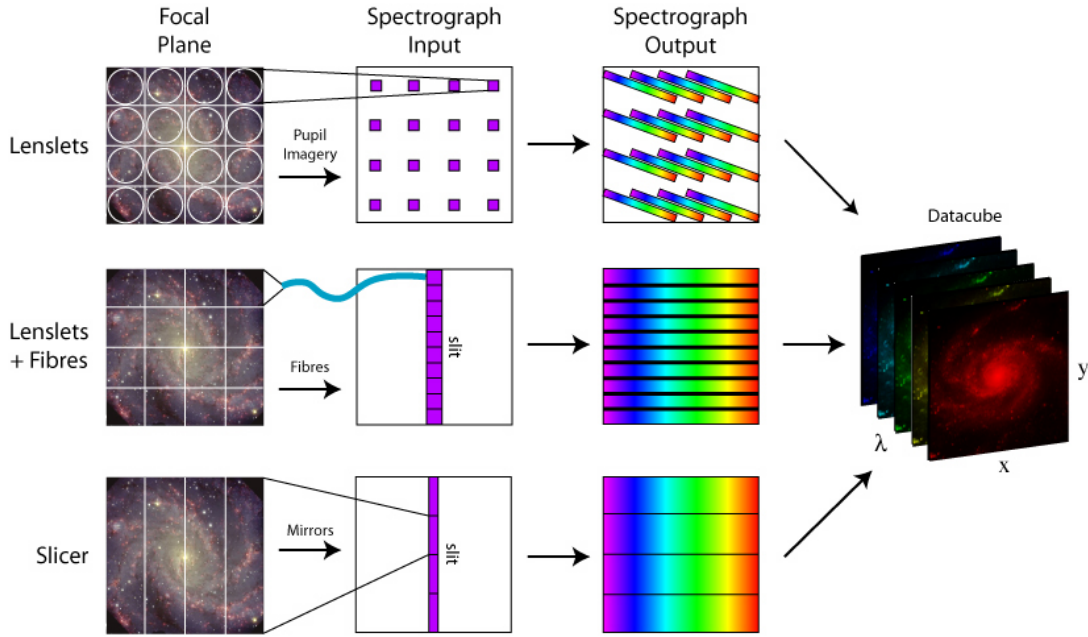


Figure 1.5: The main instrument designs used in IFS to disperse the light at every spatial pixel. Credit: M. Westmoquette, adapted from Allington-Smith et al. 1998

referred to as the well-known “aperture effect” in spectroscopic studies. This inevitably leads to inaccurate measurements of stellar populations and galaxy properties in the local Universe.

Integral Field Spectroscopy. Around the same time that MOS was conceived, integral field spectroscopy (IFS) evolved from those ideas. The central principle of IFS is its use of integral field units (IFU) to capture the spectra of different spatial regions of an object, providing a 3D datacube with two spatial axes (x, y) and a wavelength axis (λ). Unlike traditional spectroscopic methods like single and multi-object slit or aperture spectroscopy, which only collect light from a slit or point respectively, IFS captures spectra across the entire 2D FoV of the galaxy, allowing us to delve into both the spatial and spectral properties. IFS instruments now employ various methods of dispersing the light from each pixel of the object, or a galaxy in this context, including fibres, lenslets, and image slicers (Fig. 1.5). With this state-of-the-art tool, one can performed detailed analyses on stellar populations and kinematics, gas dynamics, chemical abundances, and star formation activity across the entire galaxy in the FoV, or even in different structural components of the galaxy as will be the core objective of Chapters 2 and 3.

While the concept of IFS had been proposed in the 1980s, its observational capability and sophisticated instrumentation have been picking up steam roughly over the last two decades, with instruments like SINFONI, GMOS (Hook et al., 2004), ATLAS^{3D} (Cappellari et al., 2011), CALIFA (Sánchez et al., 2012), SAMI (Bryant et al., 2015), MUSE (Bacon et al., 2010a), MaNGA (Bundy et al., 2015), and more recently, WEAVE covering the optical wavelength regime. The operations include both individual observations as well as multi-object surveys, with MaNGA forming the largest such IFS survey to date

with $\sim 10,000$ galaxies in the nearby Universe. The advent of MUSE, installed at the Very Large Telescope (VLT) in Chile, has further pushed the boundaries of IFS. MUSE is particularly well-suited for deep-field observations, revealing the faintest structures in both nearby and distant galaxies, mapping out galaxy evolution across cosmic time. However, alongside all these advantages, like all instruments and methods, IFS has its own biases. Surveys such as MaNGA and CALIFA have limited fields of view (FoV), which can result in the outer regions of galaxies with large angular sizes not being entirely captured. This plays a role in inevitably introducing a selection bias in studies that require the spectra of the galaxy outskirts, thereby forming an under-represented sample, as will be explored in the following chapter. In this work, I use both MaNGA and MUSE data to address the research objectives described in the abstract, from a fairly statistical outlook (Chap. 2) to deep individual objects (Chap. 3).

1.5.2 MaNGA: the middle ground between imaging surveys and resolved spectroscopy

MaNGA (Mapping Nearby Galaxies at Apache Point Observatory) is a major survey, which is one of the core programmes of SDSS-IV, designed to map the internal structures of thousands of nearby galaxies using IFS, enabling the study of spatially resolved galaxy properties in detail, effectively using both the imaging and spectral information. MaNGA disperses the light from galaxies using the BOSS spectrographs, which operate at a spectral resolution of $R \sim 2000$ and cover the wavelength range from 3600 to 10,300 Å. In the context of this thesis, this wavelength range is relevant for studying stellar populations, as it spans key diagnostic absorption and emission lines described in Section 1.5 (although this is not the only primary objective of the survey). This Section briefly summarises the IFU design used in the MaNGA survey, and serves as an introductory outline for Section 2.3.2.

The IFUs in MaNGA are made of small optical fibres bundled together in a hexagonal close-packed design, known as a fibre bundle (Drory et al., 2015). This IFS survey was one of the last to employ the manual plug-plate methodology used in the multi-object spectroscopy design of SDSS, maximising the survey efficiency. The plug-plate is an aluminium plate with precisely drilled holes corresponding to the positions of target objects in the sky. The plate is installed at the focal plane of the 2.5 m Sloan foundation telescope (Gunn et al., 2006). The optical fibres of the IFUs are manually plugged into these holes. The fibre bundles are then fed into the BOSS spectrographs (Smeed et al., 2013), and each fibre of the IFU produces a spectrum for a spatial position of the target galaxy.

The MaNGA survey utilises a set of 17 IFUs for simultaneous observation of multiple galaxies. These IFUs vary in size, containing between 19 and 127 individual fibres each. The configuration of the fibres and their corresponding angular diameters are listed in Table 1.1. The various sizes of the IFUs are designed to be able to effectively cover up to $1.5R_e$ or $2.5R_e$ of the targets at different distances. The more distant galaxies with

Table 1.1: *The fibre configurations in each fibre bundle, the arcsec diameter of each IFU, and the number of fibres per plate.*

Fibres per IFU	IFU FoV	Fibre-plate configuration
19	12''	2
37	17''	4
61	22''	4
91	27''	2
127	32''	5

smaller angular sizes would therefore be observed with the smaller IFUs, while the closer objects would be better observed with the larger bundles.

The optical fibres have a live-core fill factor of 54%, which would potentially induce dead spaces between the fibres during observations. In order to be able to fully sample the target galaxy spatially, a dither pattern is introduced in three 15 minute exposures along an equilateral triangle. The observations are then repeated until the S/N reaches 5 \AA^{-1} in each fibre in the r -band continuum. This setup and strategy has allowed MaNGA to efficiently collect the spectra of 17 galaxies simultaneously during a single observing session, ultimately leading to $\sim 10,000$ observed galaxies over its operation between 2015 and 2021, balancing the need for clear spatial coverage and multi-object spectroscopy.

1.5.3 MUSE: deep individual observations for enhanced detail

MUSE (Multi Unit Spectroscopic Explorer), installed on the ESO Very Large Telescope (VLT) at Paranal in Chile, is a powerful second-generation IFS instrument designed for deep and spatially resolved observations. This instrument has revolutionised IFS by bridging high-resolution imaging capabilities with detailed spectroscopy. MUSE can operate in wide-field mode (WFM) or the narrow-field mode (NFM), and can be chosen depending on the science case. The WFM provides a FoV of $1' \times 1'$ with a spatial sampling of $0.2''$ per spaxel, and the nominal wavelength coverage from 4650 to 9300 \AA , spanning from the optical to the near-infrared. The spectral resolution varies from $R \sim 1770$ at 4800 \AA to $R \sim 3590$ at 9300 \AA . This mode is the most often used, whose large field of view captures extended objects and even for deep surveys. On the other hand, the NFM, which is used in the adaptive optics (AO) mode since 2017, provides a much narrower FoV of $7.5'' \times 7.5''$, spatially sampled at $0.0125''$ per spaxel, making these observations comparable to space-based observations. These observations are more suited for more compact objects that require a high spatial resolution over a small region. The AO system is used to compensate for the image distortion induced by atmospheric turbulence. While the WFM can now be coupled with AO, this functionality was not offered during the observations used in this thesis, and will not be discussed hereafter. Moreover, the MUSE instrument has achieved strides in improved sensitivity, and was

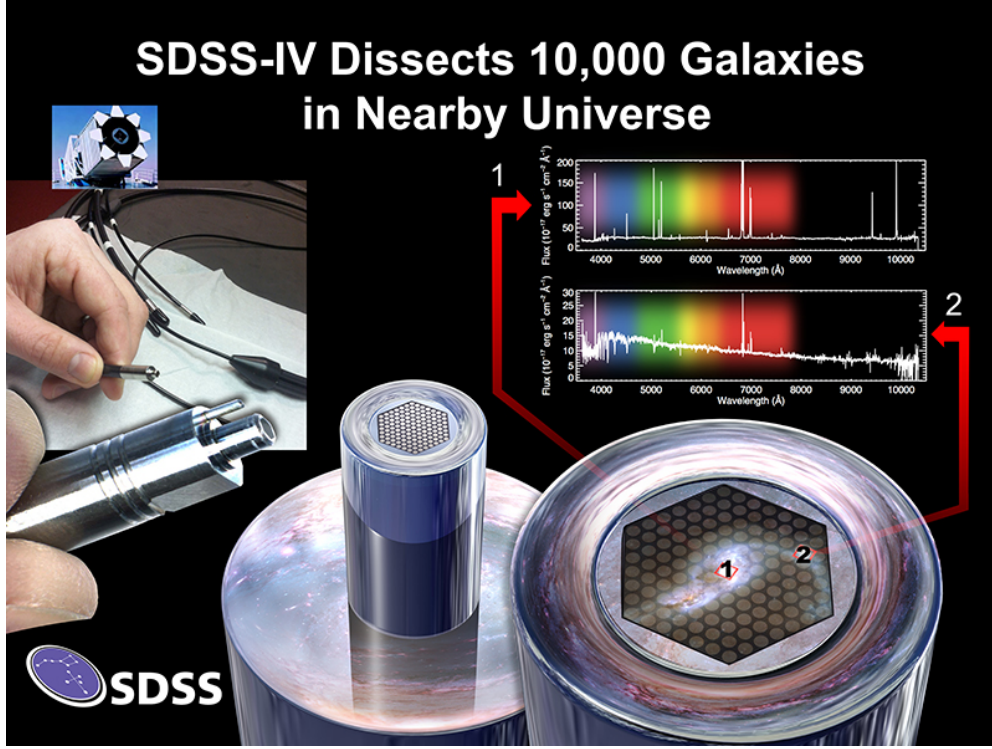


Figure 1.6: Illustration of the hexagonal fibre bundles in MaNGA IFUs and its ability to obtain spatially resolved spectroscopy, shown in two different regions of the galaxy.

designed to observe and study large samples of galaxies at intermediate and higher redshifts.

MUSE employs image slicers as the IFU component instead of the fibre bundles (see Fig. 1.5 for the difference between both designs) used by MaNGA, which helps achieve the large FoV, along with the use of field-splitters. The FoV of the instrument is first divided into 24 smaller sub-fields through an array of mirror slicers at the telescope focal plane, each of which is directed to a separate IFU. Each of the 24 sub-fields is further split into 48 slices, following a pre-defined pattern of 12 slices in 4 stacks. The 48 slices are then fed into a spectrograph, which disperses the light vertically across a CCD detector, resulting in 24 output images. The light from each slice is therefore converted into a 2D spectrum. The process is depicted in Figure 1.7. However, this raw output from the CCD images is not directly usable for scientific analysis. This is processed through a reduction pipeline (EsoRex; the elements of data reduction are highlighted in Section 3.3), which transforms the raw images into a datacube, combining spatial and spectral information for each pixel across the large FoV. The WFM observations were chosen for our study of elliptical galaxies in Chapter 3, which needed to capture the entire object sufficiently to analyse its surface brightness profile.

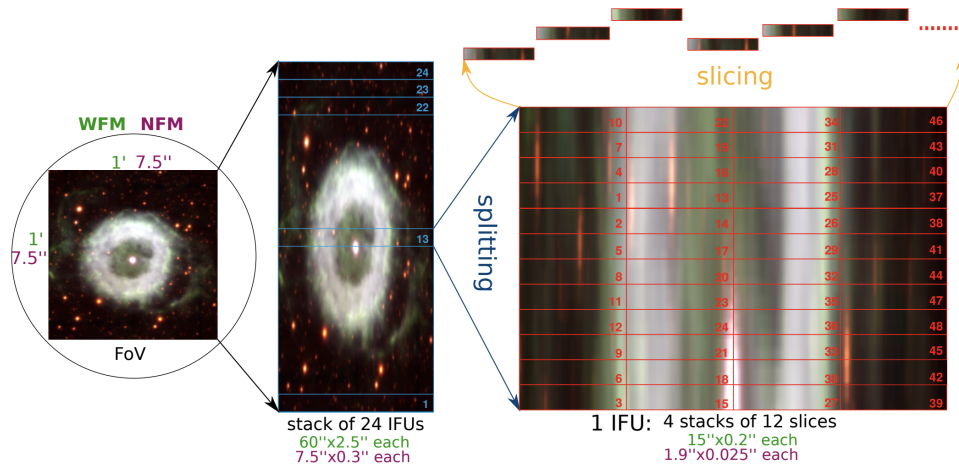


Figure 1.7: Illustration of the MUSE instrument layout and how the field is divided among the 24 IFUs, with each IFU further split into 48 slices.

1.6 The methodology: Decomposition of galaxy light profiles

The most direct observable from galaxy observations is the light, which encodes all possible quantifiable information regarding its formation and evolution, and any property derived therein would be from a careful and precise analysis of this light. On that note, surface brightness modelling is a fundamental tool that serves this purpose, providing insights into the structural properties of galaxies and their stellar components. By analysing how the surface brightness of a galaxy varies with distance from its centre, one can disentangle different structural components such as bulges, discs, and stellar halos. This technique yields structural parameters such as bulge-to-disc ratios, effective radii, and Sérsic indices, in addition to the flux. In effect, these parameters serve as powerful probes to understand the evolutionary history of a galaxy through a study of their component stellar populations and star formation histories.

1.6.1 Photometric decomposition: from GALFIT to GALFITM

The extensive volume of large photometric surveys conducted over the last decades has made it possible to perform statistical studies of galaxy properties through modelling their 2D surface brightness profiles. These include surveys such as COSMOS (Scoville et al., 2007a), SDSS (York et al., 2000), GAMA (Driver et al., 2011a; Liske et al., 2015a; Baldry et al., 2018a), GOODS (Dickinson et al., 2003a; Giavalisco et al., 2004a), CANDELS (Grogin et al., 2011; Koekemoer et al., 2011), J-PAS (Benitez et al., 2014), to name a few. Some of these offer high-quality spectral energy distributions (SED), including COSMOS covering over 30 photometric bands encompassing the wavelength range from UV to infrared, and J-PAS set to use a system of 56 filters to study stellar populations. Such multiband photometric surveys offer an excellent cost-effective way of analysing large datasets, with the notable trade-off of poorer spectral resolution. Fitting the light

profiles of galaxies allows one to derive the stellar masses, star formation histories, and stellar populations, in addition to performing detailed structural analyses.

Alongside the improvements in instrumentation came the development of sophisticated software to analyse the vast collection of astronomical data. The tools to perform two-dimensional light profile fitting incorporating the point spread function (PSF) of a given galaxy observed with a given instrument have effectively redefined the study of galaxy parameters and in deriving relevant physical properties. One of the software commonly leveraged for this purpose is GALFIT (Peng et al., 2002; Peng et al., 2011), which is also at the heart of this thesis. Other galaxy profile fitting tools like GIM2D (Simard et al., 2002), IMFIT (Erwin et al., 2015), ProFit (Robotham et al., 2017), and more recently even employing machine learning techniques like GalNets (Li et al., 2022; Qiu et al., 2023) have also been investigated in literature revolving around structural and photometric studies. GALFIT allows the analysis of galaxy images by fitting a parametric form to their surface brightness distributions in order to estimate vital galaxy parameters. The primary advantage of this method is the ability to not only fit the galaxy profile itself, but also to decompose the light profiles of different components within the galaxy, which are crucial ingredients that illuminate the origins of these objects in the Universe.

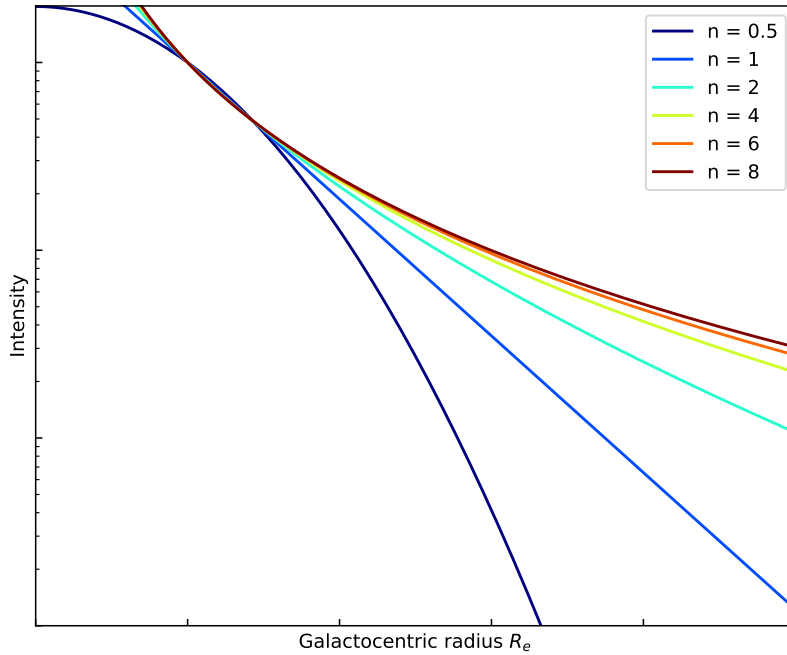


Figure 1.8: Sérsic profiles as a function of radius from the galaxy centre, for different sérsic indices.

The standard parametric function that has been proven to hold true to a good approximation for galaxies specifically in the nearby Universe, is the Sérsic function (Fig. 1.8), defined by:

$$I(r) = I_e \exp \left[-b \left(\left(\frac{r}{r_e} \right)^{1/n} - 1 \right) \right], \quad (1.1)$$

where n is the measure of the light concentration called the Sérsic index, r_e is the effective radius, and b is a constant depending on n . The value of n is traditionally constrained by the user to range between 0.1 and 8. In the specific case of $n = 4$, the Sérsic function reverts to the de Vaucouleurs profile (de Vaucouleurs, 1948), which is often used to describe the light profile of an elliptical galaxy or a classical bulge, which has a strong central concentration. However, being conscious of the existence of bulges on a continuous sequence, it is more prudent to use the flexible Sérsic profile to model these components, so as to eliminate a forced commonality assumed for the description of bulges, which are hosted by a wide diversity of galaxy types. The discs of spiral and S0 galaxies are typically described by an exponential function, which can again be easily generalised by the Sérsic function, where $n = 1$. The versatility and power of GALFIT lies in its ability to model these components and more simultaneously, along with any neighbouring objects in the field of view of the target galaxy (Häussler et al., 2007) that can potentially alter its surface brightness distribution. Where necessary, it also allows for masking out objects that can influence the fit to the galaxy. Figure 1.9 depicts several examples of using different parametric forms to model the galaxy light profile, including two variants of bulge-disc decomposition.

GALFIT and the other light profile fitting tools mentioned earlier have their benefits in deriving galaxy structural parameters, but they also have a limitation in being able to fit only a single-band image at a time. Studies have attempted to cross this bridge by first fitting the galaxy in a deep band, and then fixing the resulting parameters in the other bands to determine their magnitudes (Simard et al., 2011; Mendel et al., 2014), or by fitting the galaxy band-by-band, which can become tedious with the rapidly increasing filter systems in surveys. While the former approach alleviates the issue with single-band fitting, it does operate under the bold assumption that the galaxy parameters remain constant across the entire wavelength regime in question, which is well-established to be inaccurate (see Sect. 1.4.3). This effect is particularly relevant in bulge-disc decompositions of galaxies, where the bulge light dominates in the redder wavelengths, and becomes less significant in the bluer bands. Similarly, the opposite is true for discs which shine brighter in the bluer wavelengths, particularly in spiral galaxies. Constraining the structural parameters of a single-band image erases the wavelength dependence of structural components, thereby introducing systematic biases in the magnitudes, fluxes, and stellar masses derived from this approach. Depending on the choice of the “fixed” band, these effects can result in significant differences in different analyses in literature, making it harder to arrive at a consistent picture.

With that goal, the MegaMorph² (Measuring Galaxy Morphology) project saw the development of GALFITM and GALAPAGOS-2 as extensions of GALFIT and GALAPAGOS (Barden et al., 2012) respectively, to efficiently address multi-wavelength light profile fitting without sacrificing the vast amounts of information offered by observations in different wavebands. GALFITM enables the simultaneous modelling of the light profile

² <https://www.nottingham.ac.uk/astronomy/megamorph/>

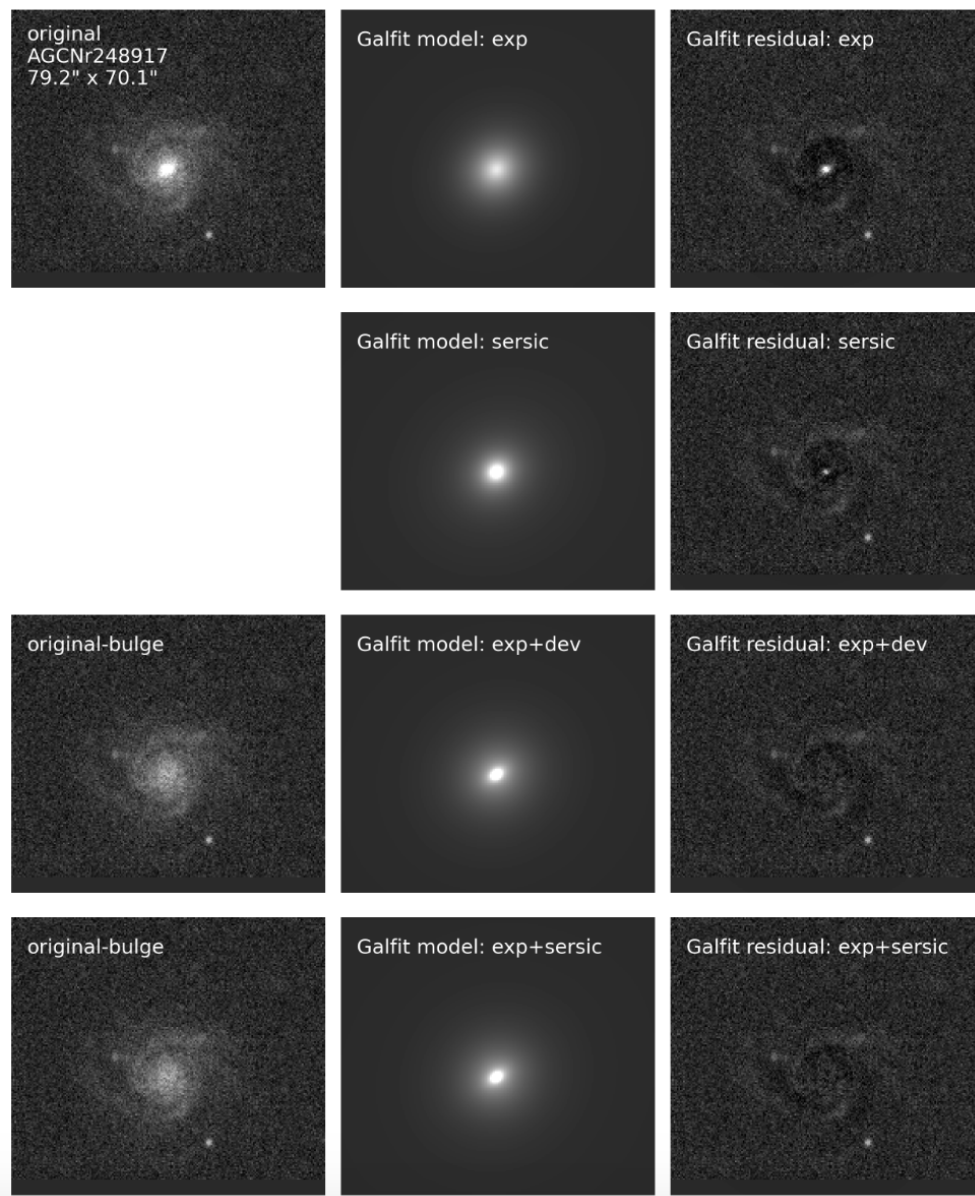


Figure 1.9: Example of a galaxy in SDSS DR7 modelled with different parametric forms and their combinations with GALFIT, taken from [Zhang et al., 2024](#). From top to bottom - Exponential, Sérsic, Exponential + de Vaucouleurs, and Exponential + Sérsic.

of the galaxy and its individual components across multiple photometric bands, thereby improving the signal-to-noise ratio (S/N) by utilising the additional data. The software allows for a smooth variation of the structural parameters across the bands through Chebyshev polynomials. This is prudent in cases where the image in a particular band has a low S/N, and leads to a physically implausible fit in a single-band image; therefore, forcing a smooth variation of the structural parameters remedies this effect in GALFITM, providing a more robust fit to each galaxy image (Häußler et al., 2013; Vulcani et al., 2014; Nedkova et al., 2021; Häußler et al., 2022). Furthermore, as stated earlier, the photometric colours in the multi-waveband images encode information about the prominence of bulges and discs across wavelengths (for instance, redder bands trace the light from classical bulges, while the bluer bands trace discs). The advantage of using GALFITM in this regard is that it simultaneously weights the images across all bands, allowing access to this colour information that helps decompose galaxies into their constituent components more accurately (Vulcani et al., 2014). In summary, the transition from GALFIT to GALFITM marks a significant advancement in galaxy surface brightness modelling and multi-component decomposition, particularly in the era of multi-wavelength surveys.

1.6.2 Spectroscopic decomposition: the road ahead with BUDDI

The importance of multi-wavelength photometric analyses cannot be understated, owing to their cost-effectiveness and speed, offering a broad wavelength coverage in some surveys extending from the ultraviolet to the infrared (COSMOS, CANDELS, LSST to name a few). However, while photometry can infer the presence of different stellar populations or regions of star formation, it lacks the precision needed to dissect the detailed properties of those populations and are often plagued by the age-dust-metallicity degeneracy described earlier in Sect. 1.5. This is where the usefulness of spectroscopic techniques becomes evident, with the spectrum of a galaxy containing a wealth of information that is otherwise lost in imaging and photometric data. With that in mind, this thesis essentially revolves around IFS (see Sect. 1.5.1), which integrates the best of both worlds, making use of imaging and spectroscopic capabilities simultaneously.

The next natural progression in galaxy modelling therefore extends to IFU datacubes. Leveraging the strength of GALFITM in modelling multi-wavelength images, enters BUDDI (BULge Disc Decomposition of IFU datacubes; Johnston et al., 2017) as a novel advancement in modelling the galaxy light profile in each image slice of IFU datacubes (which can be as high as ~ 4000 slices). This is an IDL routine that serves as a wrapper around GALFITM, designed to handle the large number of input image slices and the substantial output generated during the fitting process. The multi-component decomposition with BUDDI allows the clean extraction of the spectrum of each component, with minimal light contamination between them. The resulting component spectra open the door to more accurate stellar population analyses and reconstruction of galaxy star formation histories across cosmic time. The exact detailed workflow of BUDDI can be

found in Johnston et al., 2017, and is described in the context of the projects in this thesis in Chapters 2 and 3. The flowchart illustrating the steps in the method is depicted in Figure 1.10.

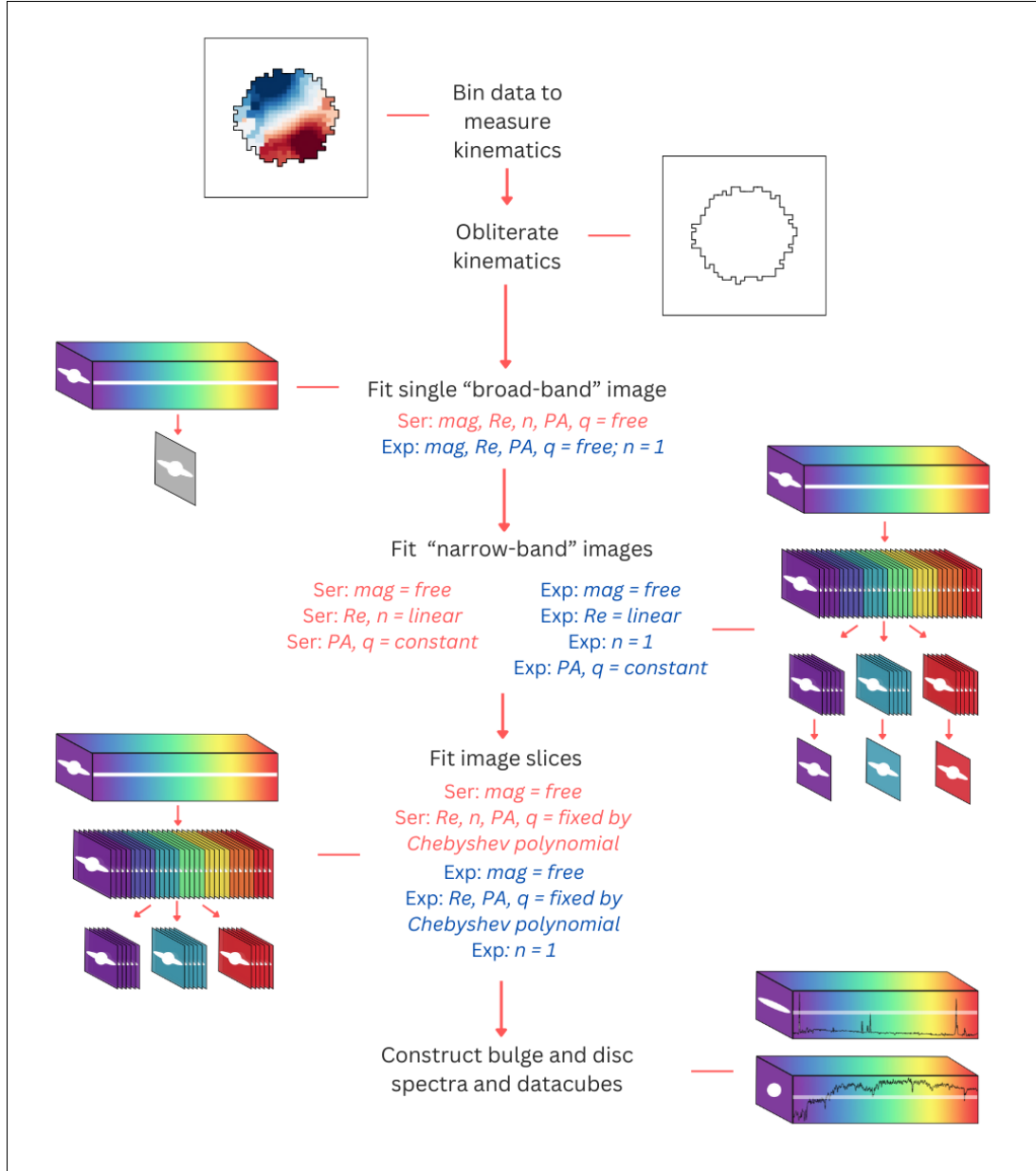


Figure 1.10: Workflow of BUDDI for a bulge-disc decomposition scenario, where the disc is fixed with an exponential profile of $n = 1$. Adapted from Johnston et al., 2022a.

The data preparation for BUDDI requires an extra step from GALFIT and GALFITM due to different input data formats. The IFU datacube is first binned following the Voronoi tessellation method of (Cappellari et al., 2003) to measure the galaxy kinematics, which are then obliterated by performing kinematics corrections (see Chapters 2 and 3). Similar to GALFIT and GALFITM, a PSF datacube and sigma datacube are also required. The fitting process in BUDDI begins by using GALFITM to first model the galaxy and/or its components in a single broad-band image produced by collapsing the datacube along

the wavelength axis. In the next step, datacube is binned into ~ 10 narrow-band images, which are then modelled using the broad-band image parameters as initial values. This is also the step where the wavelength dependence of the structural parameters using Chebyshev polynomials is introduced (Fig. 1.10), which is usually chosen to be fixed, constant, linear, or completely free (polynomial orders of 0, 1, 2, or n_{dof} respectively). In the next step where the individual image slices are modelled, the structural parameters are all fixed to the narrow-band fit parameters with only the magnitudes free. From this, the spectra of the galaxy and its components can be cleanly extracted. To avoid redundancy, this Section only provides a quick and brief overview of the method, and the details including the choice of polynomials depending on the science case are described in Chapters 2 and 3.

1.7 Stellar population synthesis modelling: from spectra to quantifiable properties

The most important stellar population properties - the age and metallicity - are crucial tracers of star formation activity, especially in nearby galaxies. These properties thereby contain clues to the star formation history and chemical evolution of these local galaxies, and reveal their role in shaping the cosmic stellar history of the Universe. While the stars in the closest galaxies, like the Andromeda galaxy, can be resolved, those in more distant but still low-redshift galaxies remain unresolved. For such galaxies, the average properties of the stellar populations must be derived from only their integrated light and spectra. In the context of this thesis, this extends to also investigating the stellar populations in various structural components of the galaxy, rather than focussing solely on the object as a whole. Stellar population synthesis (SPS) models are at the core of this “archaeological” approach to excavating stellar properties (Morgan, 1956; Tinsley, 1968; Faber, 1972; Spinrad, 1972) and tracing star formation histories from the past to the present.

SPS models can be leveraged in spectral analysis by fitting them to the integrated spectra of galaxies, through the “full spectral fitting” technique. The underlying foundation of this method is that the integrated spectrum is a linear combination of the spectra of different simple stellar populations (SSPs). An SSP refers to a group of stars that were born at the same time from a gas cloud, with the same chemical abundance and an initial mass distribution. From an observational standpoint, open and globular clusters serve as the best examples of SSPs. Estimating galaxy properties through this fossil-record method is at the precipice of both extragalactic astronomy and stellar physics, often referred to as “galactic archaeology” or “galactic palaeontology” depending on the literature. In the following Section, I outline the core ingredients of SPS models.

1.7.1 Ingredients of SPS models

Evolutionary tracks and isochrones. One of the three major ingredients in SPS models, stellar evolutionary tracks trace the temporal paths of individual stars of a given age and chemical composition (metallicity) on the Hertzsprung-Russell (HR) diagram, as they evolve over time since their birth as an SSP. Using the evolutionary tracks, stellar isochrones can then be built, which connect all the stars with the same age and chemical composition, but have different masses on the HR diagram. These lines represent the positions of stars at a given stage in their lifetime. In order to estimate stellar population properties with reduced biases, the stellar isochrones should effectively sample stars across a range of ages, metallicities, and masses, and represent the major evolutionary stages of different types of stars. Some of the oft-used theoretical isochrones in literature include the Padova model (Bertelli et al., 1994; Girardi et al., 2000; Marigo et al., 2008; Bertelli et al., 2008), the Bag of Stellar Tracks and Isochrones (BaSTI) model (Pietrinferni et al., 2004; Pietrinferni et al., 2006; Pietrinferni et al., 2013), and the Geneva model (Lejeune et al., 2001). The choice of model in stellar population synthesis varies by user, and these models often differ in their assumptions and incorporation of different aspects of stellar evolution theory. It is therefore important to be conscious of the limitations posed by each model when interpreting scientific results.

Stellar libraries. Stellar libraries provide the spectra of stars as a function of effective temperature, metallicity, and surface gravity. These are used to translate from observed spectra to measurable stellar population properties. Also called stellar atmosphere models, these have been built from both theoretical (Kurucz, 1992; Martins et al., 2005; Lançon et al., 2007; Coelho et al., 2007) and empirical approaches, for example, ELODIE (Prugniel et al., 2001), STELIB (Le Borgne et al., 2003), Indo-US (Valdes et al., 2004), MILES (Sánchez-Blázquez et al., 2006), and the X-Shooter library (Chen et al., 2011). Theoretical stellar libraries can be constructed by sampling large parameter spaces (Coelho, 2014), but they are limited by the assumptions made regarding stellar convection models, as well as the presence of atomic and molecular lines in the spectra. On the other hand, empirical libraries, built from observed stars, tend to be more realistic as they are not subject to theoretical model assumptions. However, since these stars are primarily from the Milky Way, the spectra may be biased towards the stellar population properties of our Galaxy. Furthermore, the observational constraints limit the sampling in the parameter space, leading to a less complete library compared to the theoretical ones. Similar to the isochrones, one must be aware of potential biases induced by the choice of stellar libraries in the stellar population synthesis of extragalactic objects.

Initial Mass Function. The final ingredient in stellar population modelling is the Initial Mass Function (IMF), which describes the distribution of masses of stars at the time of their birth in a single star forming event from a gas cloud. This temporal snapshot is referred to as the zero-age main sequence, which represents the stage in the lifetime

of a star, when it is newly formed and begins hydrogen fusion in its core, entering the main sequence phase of its life. The Salpeter IMF (Salpeter, 1955) is one of the earliest, and still commonly used parametrisation of the initial mass function. This IMF assumes a power-law form as $\xi(m) \propto m^{-2.35}$, where m is the mass of the stars. While this distribution well represents the high-mass stars, it tends to overestimate the number of low-mass stars when compared to observations. A more refined parametrisation arrived as the Kroupa IMF (Kroupa, 2001a; Kroupa et al., 2002). This assumes a broken power-law form, the slope of which changes for three different mass intervals ($0.01 < m/M_{\odot} < 0.08$, $0.08 < m/M_{\odot} < 0.5$, $0.5 < m/M_{\odot} < 100$). The Kroupa IMF effectively accounts for the distribution of low-mass stars. An even more sophisticated parametrisation was introduced in Chabrier, 2003, where the IMF assumes the form of a log-normal distribution for low-mass stars of $m < 1M_{\odot}$, and a power law for high-mass stars over $1M_{\odot}$. Each IMF impacts the inferred star formation rate, stellar mass function, and chemical evolution in galaxies.

Over the years, stellar population models have undergone substantial advancements, driven by incorporating more detailed stellar evolution physics and refined computational techniques. Additionally, the improved quality of voluminous observational data has provided stronger constraints, further improving the accuracy of these models. However, that is not to say that current SPS models perfectly capture all aspects of stellar physics, and future advancements in the field can potentially warrant further adjustments or modifications.

1.7.2 Full spectral fitting

The SPS models form the backbone of techniques that derive relevant properties of stellar populations, and building on this foundation, I highlight the “full spectral fitting” method used for this purpose. This has become a powerful tool in extragalactic spectroscopy, for it exploits not just specific spectral diagnostics (as in line strength or index measurements) but also the information from the entire stellar continuum, such as subtle changes in the continuum due to effects induced by dust or flux calibration, which helps to further mitigate age-metallicity degeneracy. This approach fits in well with the techniques used in this thesis, where we leverage the availability of “more” data to better constrain galaxy properties. Full spectrum fitting additionally allows for the estimation of stellar masses and, in the case of IFS, galaxy kinematics. Depending on the software used, it can also yield non-parametric star formation histories, providing a comprehensive approach to analysing stellar populations.

In very generic and non-exhaustive terms, the full spectral fitting software models the galaxy spectrum $F_{obs}(\lambda)$ as:

$$F_{obs}(\lambda) = \left[\sum_{i=1}^N w_i F_{SSP,i}(\lambda) \right] \otimes \mathcal{L}(v) + A(\lambda) \quad (1.2)$$

where, $F_{SSP,i}(\lambda)$ refers to each SSP model template included in the fitting process, and w_i is the weight assigned to each SSP template, denoting its fractional contribution to the galaxy stellar mass. These terms are convolved with the line-of-sight velocity distribution $\mathcal{L}(v)$, and any additive corrections for dust attenuation or instrument calibrations are included in $A(\lambda)$. As noted before, this is a non-exhaustive list of terms that can be used to model the observed galaxy spectrum. Different tools choose various approaches to account for correction effects, either incorporating additive or multiplicative terms through the use of polynomials. The ultimate goal of spectral fitting is to minimise the residuals between the observed and modelled spectrum, by adjusting the free parameters to recover the stellar population properties and star formation histories.

Some of the commonly used modern full spectral fitting codes include pPXF (Cappellari et al., 2004; Cappellari, 2017; Cappellari, 2023), STARLIGHT (Cid Fernandes et al., 2005a), STECKMAP (Ocvirk et al., 2006), Pipe3D (Sánchez et al., 2016), FIREFLY (Wilkinson et al., 2017), and FADO (Gomes et al., 2017). More recently, the use of Deep Learning has been explored in the context of spectral analysis with STARNET (Fabbro et al., 2018), which is a non-public code that employs convolutional neural networks (CNNs) to estimate and predict stellar parameters like effective temperature, surface gravity, and metallicity. The reader is referred to Ge et al., 2018 and Woo et al., 2024 for a detailed comparison of full spectral fitting codes and choices of stellar libraries. In this thesis, I have consistently chosen to use pPXF for analysing the IFS data, primarily due to its ability to resolve degeneracies during the optimisation by incorporating a "regularisation" term. This not only avoids discrete solutions but also produces more physically consistent, non-parametric star formation histories.

The work in galaxy evolution that this thesis lays out and the questions attempted to be answered during this work employs the elements described in this chapter. With that being said, this Section marks the end of the introductory part of the thesis.

1.8 Thesis outline

Now that the stage has been set with the scientific and technical background which will prove relevant in the coming chapters, it is time to turn our attention to the research that has been carried out for the duration of this thesis. With ever improving technological advancements increasing the level of detail and volume of accessible data, it is always prudent to constantly debate the re-evaluate the validity of previous research conducted with older observations and techniques. This includes developing new codes and software to extract physically relevant information from diverse astronomical datasets. Galaxy formation and evolution remains an unresolved field, lacking a universal theory that explains the breadth of observations collected over time. This thesis aims to contribute towards resolving some of the open questions within the field by focussing on the following objectives:

- To reconstruct the star-formation histories of the components in different galaxy morphologies especially spirals (bulge and disc) and ellipticals (inner and outer component), and study their stellar populations independently to understand the mechanisms and physical processes that drive their formation and evolution.
- To constrain the multiple components of elliptical galaxies and their underlying stellar populations for the intent of attributing physical significance to each component.
- To investigate the order of star formation and stellar mass assembly in galaxies, and the preference of inside-out and outside-in growth in different galaxy types.
- To explore the role and relative importance of stellar mass and morphology on their star-formation histories and transformations.

With these objectives at hand, the thesis is organised as follows: in Chapter 2, I address the physical processes shaping the formation of spiral galaxies in the nearby Universe, by examining their major structural components - the bulge and the disc - and tracing their stellar mass assembly over the last ~ 14 Gyr. For this line of research, I leverage a semi-statistical sample from the publicly available SDSS-MaNGA survey. The BUDDI-MaNGA project forms the first of its kind, providing the cleanly extracted bulge and disc spectra, which is central to this analysis. I also derive their masses and stellar populations, which combined together, provide detailed insights on the impact of these components in the formation and evolution of the spiral galaxies we observe today. In Chapter 3, I take a more individual approach to unravelling the structural components of three local elliptical galaxies observed with MUSE. This pilot study uses BUDDI for constraining the elliptical galaxy components, in order to better understand their surface brightness profiles and explore their multi-component formation under the two-phase scenario. Finally in Chapter 4, I present the summary and conclusions of the lines of research outlined in this thesis.

A DANCE OF BULGES AND DISCS: DECODING THE STELLAR ORIGINS OF SPIRAL GALAXIES

This Chapter is based on the paper published in the *Astronomy & Astrophysics* journal, titled “BUDDI-MaNGA III: The mass-assembly histories of bulges and discs of spiral galaxies”.

2.1 Abstract

The many unique properties of galaxies are shaped by physical processes that affect different components of the galaxy – such as their bulges and discs – in different ways, and they leave characteristic imprints on the light and spectra of these components. Disentangling these spectra reveals vital clues that can be traced back in time to understand how galaxies, and their components, form and evolve throughout their lifetimes. With BUDDI, we have decomposed the integral field unit (IFU) datacubes in SDSS-MaNGA DR17 into Sérsic bulge and exponential disc components and extracted clean bulge and disc spectra. BUDDI-MaNGA is the first large statistical sample of such decomposed spectra of 1452 galaxies covering morphologies from ellipticals to late-type spirals. We derive stellar masses of the individual components with spectral energy distribution (SED) fitting using BAGPIPES and estimate their mean mass-weighted stellar metallicities and stellar ages using pPXF. With this information, we reconstruct the mass assembly histories of the bulges and discs of 968 spiral galaxies (Sa-Sm types). Our results show a clear downsizing effect especially for the bulges, with more massive components assembling earlier and faster than the less massive ones. Additionally, we compare the stellar populations of the bulges and discs in these galaxies, and find that a majority of the bulges host more metal-rich and older stars than their disc counterparts. Nevertheless, we also find a non-negligible fraction of the spiral galaxy population in our sample contains bulges that are younger and more metal-enhanced than their discs. We interpret these results, taking into account how their formation histories and current stellar populations depend on stellar mass and morphology.

2.2 Introduction

The morphological classification scheme proposed in [Hubble \(1926\)](#) has brought about a search for the formation and evolution of the diverse galaxy types at various redshifts. Since then, it has become clear that each galaxy type is complex and diverse, built of elaborate components and sub-structures. The simplest picture and also the most standard one in the literature is that most galaxies have two structural and stellar components – the bulge and the disc. Disc galaxies may also contain bars and spiral arms that potentially drive evolution along a particular pathway. The primary disc component is often structurally observed as an extended component with an exponential surface brightness profile (for example, [Freeman, 1970](#); [Kormendy, 1977](#)), and it is typically a region of active star formation where new stars are born from clouds of gas and dust. The bulge on the other hand is believed to be a central compact component embedded in the midst of the disc that follows a de Vaucouleurs profile ([de Vaucouleurs, 1948](#)), or more generally a Sérsic profile ([Sersic, 1968](#)). Traditionally, this component has been linked to old quiescent stars with high metallicities, mirroring those in elliptical galaxies, but this simple picture has been contested over the last few decades.

Amongst these disc galaxies in the local Universe, the spiral galaxies form the predominant population, possessing a wide range of complexity in their structures. Despite their substantial contribution, the mechanisms that have shaped their components and sub-structures and the drivers of their evolution remain somewhat unresolved. Over the years, several theories have been proposed to explain their observed properties. Studying the structural and spatially resolved spectroscopic properties of these galaxies and their individual components, and tracing their star formation histories (SFH) across cosmic time, allows us to better constrain the processes involved in the formation and evolution of the components of spiral galaxies.

The classical picture follows within the hierarchical mass assembly scenario, wherein the stellar disc of a spiral forms by the collapse of gas in a rotating dark matter halo through angular momentum conservation ([Fall et al., 1980](#)). Bulges, on the other hand, tell a different story in terms of their formation pathway. Classical bulges are thought to have formed as a result of violent processes: the dissipative collapse of protogalaxies ([Larson, 1976](#)), major merger events or a series of minor mergers that rapidly exhaust the gas in star formation ([Hopkins, 2009](#)), or by coalescence of giant gas clumps found in high redshift discs ([Elmegreen et al., 2008](#); [Kormendy, 2016](#)). While these were the standard pictures for bulge formation for a long time, it has been challenged due to observations revealing a discrepancy in the form of disc-like bulges, where ‘bulges’ simply refer to a more central and concentrated component embedded within disc galaxies. These have been traced back to gentler secular processes, incited through bar and spiral arm instabilities ([Fisher et al., 2008](#); [Kormendy, 2016](#)).

There have been two major pathways of building galaxies described in the literature: the inside-out formation mode, whereby galaxies build up their centres first, and the outside-in formation mode, where the outermost regions form earlier and faster

compared to the central parts. The information encoded in the observations of stellar spectra in a galaxy can be used to excavate physical properties of their stellar populations and ionised gas and kinematics, and this enables the study of their origins by tracing back their star formation histories. The ‘fossil-record’ method recovers the SFH of a galaxy by realising the best combination of evolved single stellar populations (SSPs) that are constructed from observed stellar spectra, which fit the observed galaxy spectrum. This method has been adopted in recent integral-field spectroscopic (IFS) studies such as the one carried out by [Ibarra-Medel et al. \(2016\)](#). They find an average stellar mass formation time that decreases with radius, with the central regions having built up their masses earlier than the outskirts, which supports the inside-out formation history of galaxies. This is further validated by their finding of a negative mean stellar age gradient with older stellar populations in the centre, and younger stellar populations in the outer regions, consistent with the picture of inside-out formation. Similar negative age gradients have also been found in [Sánchez-Blázquez et al. \(2014\)](#), [Li et al. \(2015\)](#), [Goddard et al. \(2017\)](#), [Domínguez Sánchez et al. \(2020\)](#), and [Breda et al. \(2020b\)](#). More recently, [Lah et al. \(2023\)](#) confirmed that bulge-dominated regions of galaxies are older and more metal-rich than disc-dominated regions, again supporting an inside-out formation mode.

The evolution of a galaxy across its components is expected to follow one of two main scenarios: the inside-out and outside-in quenching modes. The inside-out mechanism suggests that a quenching phase begins in the central regions of the galaxy, which then spreads outwards slowly, leading to the quenching of the disc. Furthermore, the flow of gas towards the bulge can not only fuel central star formation, but also an active galactic nucleus (AGN). Massive bulges in spiral galaxies have shown signatures of negative AGN feedback that prevents gas cooling and suppresses star formation in the centre, while the disc remains actively star forming. The disc eventually quenches due to internal secular processes unless a constant supply of gas keeps up on-going star formation. An outside-in mechanism however has also been suggested in recent studies, where the disc of the galaxy begins to halt its star formation first, while the bulge is still forming stars. Environmental effects have been determined to be the major instigators for this phenomenon: events such as ram-pressure stripping ([Gunn et al., 1972](#)) and harassment ([Moore et al., 1996](#)) tend to remove the gas in the outer regions of the galaxy, where they are less strongly gravitationally bound, as they fall into a cluster or a group, quenching the outer discs first and ultimately quenching inwards to the centre.

The extensive photometric surveys such as the Cosmic Evolution Survey (COSMOS; [Scoville et al., 2007b](#)), the Sloan Digital Sky Survey (SDSS; [York et al., 2000](#)), Galaxy and Mass Assembly (GAMA; [Driver et al., 2011b](#); [Liske et al., 2015b](#); [Baldry et al., 2018b](#)), the Great Observatories Origins Deep Survey (GOODS; [Dickinson et al., 2003b](#); [Giavalisco et al., 2004b](#)), and the Cosmic Assembly Near-infrared Deep Extragalactic Legacy Survey (CANDELS; [Grogin et al., 2011](#); [Koekemoer et al., 2011](#)) have allowed independent studies of major galaxy components through their decomposition into bulges and discs. With the multiple wavebands in photometric surveys, this method can be extended to

fit the galaxy bulge and disc in each band, and extract their magnitudes and structural parameters. One of the tools that can do this is `GalfitM` (Häußler et al., 2013; Vika et al., 2014a; Häußler et al., 2022). `GalfitM` is a modified version of `Galfit` (Peng et al., 2002; Peng et al., 2011), which allows simultaneous multi-band fitting of galaxy light profiles, thereby making use of all available information at all observed wavelengths pertaining to a galaxy to fit every image. It does this by using Chebyshev polynomials of different orders to model the variation of the structural parameters with wavelength, thus ensuring a smooth and physically sensible transition across wavelength, rather than fitting each band individually. The resulting magnitudes and consequently their photometric colours can then be used to obtain the photometric stellar populations in each component by successive spectral energy distribution (SED) fitting (readers can refer to the review by Conroy, 2013). However, it has been shown that such SED fitting can suffer from an age-dust-metallicity degeneracy (Worthey, 1999; Conroy, 2013): the stellar ages and metallicities coming from photometric colours are highly degenerate, with the added issue of dust reddening. Where spectroscopic confirmation cannot be ensured, statistical photometric studies of large samples have the advantage of being less sensitive to catastrophic failures and misinterpretations that can happen when examining individual objects.

To break this degeneracy, the first step would be to introduce spectroscopic information, and several approaches have been developed over the last decade to isolate the bulge and disc light from long-slit spectra. Johnston et al. (2012) modelled the 1D galaxy light profile of the bulges and discs of S0 galaxies in the Fornax and Virgo clusters at every wavelength of the long-slit spectra aligned along the major axis of the galaxy. A more complex approach was taken in Sil'chenko et al. (2012), for a study of S0 galaxies with long-slit spectroscopy using SCORPIO (Afanasiev et al., 2005), on the 6-m Special Astrophysical Observatory telescope, where the radius of the disc-dominated region was determined using isophotal fitting; this was followed by building a 2D model image of the disc first by masking out the inner regions, and then subtracting this from the full galaxy image to obtain the bulge parameters. Consequently these final bulge and disc parameters from this multi-step decomposition were used to extract the bulge and disc spectra from the long-slit spectrum of each galaxy. Alternatively, Coccato et al. (2011) and Johnston et al. (2013) adopted a kinematic decomposition of the bulge and disc, where the bulge was assumed to be dispersion supported and the disc to be rotationally supported. The drawback of long-slit spectroscopy is that the spatial distribution is not well resolved, and the bulge-disc decomposition can only occur along the major axis of the galaxy, and it would therefore lose information on non-axisymmetric features where there might be regions of renewed star formation. Therefore, any results about the stellar populations in these components are not necessarily representative of the galaxy properties as a whole. The best way to resolve this is to bring in both spatial and spectroscopic information simultaneously. With the advent of wide-field IFS such as the Multi-Unit Spectroscopic Explorer (MUSE; Bacon et al., 2010b) and surveys such as the Mapping Nearby Galaxies at APO (MANGA; Bundy et al., 2015),

the Calar Alto Legacy Integral Field Area Survey (CALIFA; [Sánchez et al., 2012](#)), and the Sydney-Australian-Astronomical-Observatory Multi-object Integral-Field Spectrograph Galaxy Survey (SAMI; [Croom et al., 2021](#)) over the past 10 years, spatially resolved spectroscopic bulge-disc decomposition has now become a possibility.

In the last few years, several studies have already successfully implemented the use of integral field units (IFUs) to extract stellar populations of different regimes in the galaxy. For instance, [Fraser-McKelvie et al., 2018](#) used the photometric decomposition of imaging data to identify the bulge and disc-dominated regions in S0 galaxies in the MaNGA survey, and [Barsanti et al., 2021](#) used a similar technique on S0 galaxies in the SAMI survey to measure their stellar populations.

An unfortunate drawback to these techniques is the fact that there exists a low level of contamination or overlap between the components, which can ultimately bias the stellar ages to be artificially younger or older when measured. In order to reduce this contamination, there have been several studies (which we discuss in detail below) that extend the idea of multi-waveband light profile fitting to the many wavelengths of IFU datacubes to cleanly isolate the light and the spectra of each component.

The first code to accomplish this is BUlge-Disc Decomposition of IFU data (BUDDI; [Johnston et al., 2017](#)), which creates wavelength-dependent models of each component by fitting the galaxy in each image slice of the IFU datacube. For a brief overview of BUDDI, readers can refer to Sect. 2.4 of this paper and for more details on the fitting process, readers can refer to [Johnston et al., 2022a](#). This allows a cleaner extraction of the spectra of the components with minimal contamination from either component on the other. BUDDI was first tested successfully on eight S0 galaxies in MUSE ([Johnston et al., 2021](#)), where the decomposition was made for the bulge, disc, and lens components. Another code that works along the same lines is C2D ([Méndez-Abreu et al., 2019a](#)), which has also been successfully tested with a bulge and disc decomposition on CALIFA galaxies ([Méndez-Abreu et al., 2019b](#); [Méndez-Abreu et al., 2021](#)).

Following these successful tests using improved techniques, the next step would be to extend the study of galaxy components to a more statistical sample to cover a better range of morphologies and stellar masses. The present study forms the third paper within the BUDDI-MaNGA framework. It mainly relies on the fits and catalogue built from a sub-sample of MaNGA galaxies in SDSS DR17, which decomposes the spectra of the galaxies into their bulge and disc components, along with the publicly available value-added catalogues (which provide additional information on the physical properties of the MaNGA galaxies based on different studies), and corresponding SDSS optical imaging data products that provide a range of ancillary information. This final sample of fits forms by far the largest statistical sample of IFU-based decomposition with 1452 galaxies containing bulge and disc spectra. The technical details of the methodology can be found in [Johnston et al. \(2022a\)](#), which describes the technique applied to SDSS-MaNGA DR15. A brief overview is provided in Sect. 2.4.2 along with the modifications implemented in the new version. In this paper, we turn our focus to reconstructing the stellar mass assembly histories of bulges and discs in spiral galaxies,

to understand the pathways through which they have built up their mass over cosmic times. Moreover, by comparing the stellar populations hosted in the bulges and discs of these galaxies, we explore the physical processes that have driven their evolution.

This paper is organised as follows. Sect. 2.3 outlines the data and catalogues used in this study, Sect. 2.4 gives a brief overview of the bulge-disc decomposition technique with BUDDI, along with the selection criteria for the final BUDDI-MaNGA DR17 sample. Sect. 2.5 describes the methodology we employed to estimate the stellar masses of bulges and discs, and the full-spectral fitting procedure of the resulting decomposed spectra to derive physical parameters of stellar populations. The main results of this work are presented in Sections 2.6 and 2.7, describing the trends observed in the mass assembly histories of both components as a function of different physical properties and the analysis of their stellar populations. Section 2.8 discusses the results in the context of previous related studies, and we draw our conclusions in Section 2.9. Throughout this work, unless stated otherwise, all magnitudes are relative to the AB system (Oke et al., 1983), and we have adopted the flat Λ CDM cosmology with $H_0 = 70 \text{ km s}^{-1} \text{ Mpc}^{-1}$, $\Omega_m = 0.3$, $\Omega_\Lambda = 0.7$.

2.3 Data and catalogues

In this section, we list the datasets and catalogues that we use throughout this paper.

2.3.1 SDSS

SDSS is an imaging and spectroscopic redshift survey, that employs the dedicated 2.5m Sloan Foundation telescope (Gunn et al., 2006) at Apache Point Observatory (APO) in New Mexico. SDSS has been an ongoing effort for over two decades to provide optical imaging for approximately one quarter of the sky in the Northern Galactic Cap. It provides deep photometry ($r < 22.5$) in five optical passbands: *ugriz* (Fukugita et al., 1996; Smith et al., 2002). In this work, we use the imaging data products from the SDSS Data Release 17 (Abdurro'uf et al., 2022).

2.3.2 The MaNGA IFU survey

This work centres on MaNGA (Mapping Nearby Galaxies at APO; Bundy et al., 2015) data released in the SDSS Data Release 17. MaNGA is an integral field spectroscopic survey, which is a part of the SDSS-IV surveys (Blanton et al., 2017). Using a modification of the BOSS spectrograph (Smee et al., 2013), the fibres are bundled into hexagons (Drory et al., 2015) marking different IFU sizes to cover the galaxies, ranging from 19 fibres to 127 fibres, with 12'' and 32'' diameters respectively. The final public data release holds a total of 10 127 galaxies within the redshift range $0.01 < z < 0.15$ (Yan et al., 2016), and a flat mass distribution within $10^9 - 10^{11} M_\odot$. The IFU size for each galaxy is selected such that it covers the galaxy out to $\sim 1.5R_e$ for ~ 66 per cent of the total galaxy sample, and out to $\sim 2.5R_e$ for the rest.

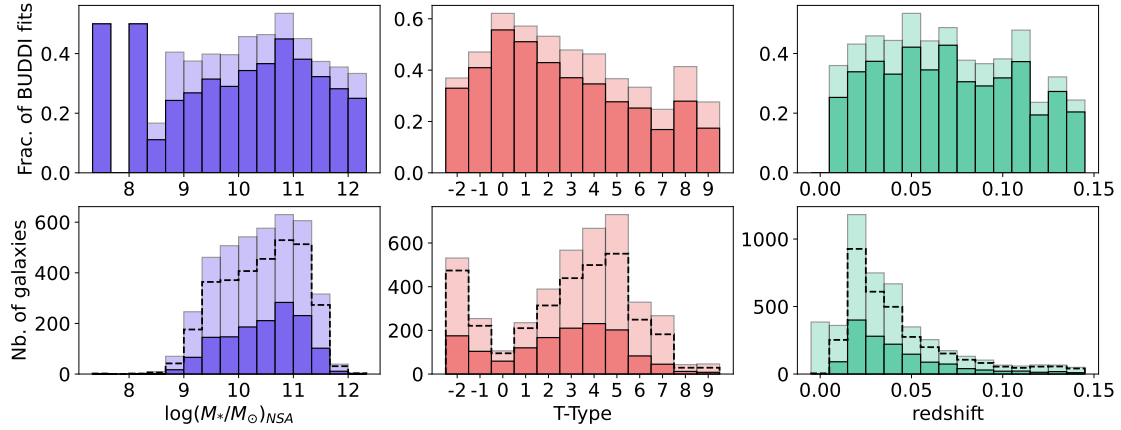


Figure 2.1: Histograms depicting the distributions of physical properties of different samples used in this study. Lower panels: Distributions of the galaxy stellar mass, morphological T-Type, and redshift in the successful fits in the new BUDDI-MaNGA DR17 sample, as defined in Sect 2.4.3 (darker shades), and for all the MaNGA galaxies observed with the 91 and 127 fibre IFUs (lighter shades). The dashed outlines depict the distributions of the galaxies that were successfully fit with PyMorph in the MPP-VAC-DR17, which determined the initial set of objects from which we built the BUDDI-MaNGA sample. The T-Types of the ellipticals and S0s from the VAC are reassigned indices of -2 and -1, respectively, for continuity in the distribution. Upper panels: Distributions of the fraction of successful BUDDI fits with respect to the PyMorph fits sample (lighter shades), and a fraction of successful BUDDI fits with respect to the MaNGA sample with the largest IFUs (darker shades).

2.3.3 Galaxy Zoo: 3D

The Zooniverse¹ crowd-sourcing platform was utilised by the MaNGA team to construct GZ:3D², a project where citizen scientists could contribute to creating spaxel maps identifying various sub-features in galaxies, such as galactic bars and spiral arms. Aside from this, they also identify and mark the presence of foreground stars and locate the central spaxels of the galaxy. These properties have been gathered into a set of masks available in the value-added catalogue, that has been described in greater depth in Masters et al. (2021), which we use to mask out foreground stars as described in Sect 2.4.2.

2.3.4 MaNGA PyMorph Value-Added Catalogue

The MaNGA PyMorph Value-Added Catalogue DR17 (MPP-VAC-DR17³; Domínguez Sánchez et al., 2022) is a table that provides photometric structural parameters for galaxies in SDSS-MaNGA DR17. These estimates come from modelling the 2D surface profiles of the SDSS galaxies using the PyMorph (Vikram et al., 2010; Meert et al., 2013; Meert et al., 2015; Meert et al., 2016) fitting software, which employs SExtractor (Bertin

¹ <https://www.zooniverse.org/lab>

² Available from https://www.sdss4.org/dr17/data_access/value-added-catalogs/?vac_id=galaxy-zoo-3d

³ Available from https://www.sdss4.org/dr17/data_access/value-added-catalogs/?vac_id=manga-pymorph-dr17-photometric-catalog

et al., 1996) and *Galfit* (Peng et al., 2002; Peng et al., 2011). This VAC provides separate estimates for the g, r, i bands of the SDSS images of 10 127 galaxies. The structural parameters were measured for both single Sérsic fits and Sérsic + Exponential (two components) fits. The catalogue additionally provides a flag where either or both fits failed, and in the case of galaxies that have successful fits with both models, denotes the best model preferred amongst them. This version of the VAC has been updated from the MPP-VAC-DR15 (Fischer et al., 2019), which was built on SDSS DR15, and Fischer et al. (2019) details the exact methodology and algorithm used in the PyMorph fits. We use these values as starting parameters for the BUDDI-MaNGA fits in an automated fashion.

2.3.5 MaNGA Visual Morphologies from SDSS and DESI images

This is a value-added catalogue⁴ provided with the MaNGA data products that provides visual morphological classification of the MaNGA DR17 galaxies based on the r -band images from SDSS and the Dark Energy Spectroscopy Instrument (DESI) Legacy Survey (Dey et al., 2019), using a new digital re-processing technique described in Vázquez-Mata et al. (2022). While the two widely used morphology catalogues are the Galaxy Zoo visual classifications (Masters et al., 2020) and the deep learning classifications in Domínguez Sánchez et al. (2018) and Domínguez Sánchez et al. (2022), the former has a significant fraction of galaxies that have no definitive classification, and the latter can be skewed by image quality. This VAC provides both Hubble types and the T-Type indices associated to each of them, along with bar identification. In this work, we use both indices simultaneously, but our interpretations are often based on the Hubble types.

2.3.6 The Nasa Sloan Atlas (NSA) catalogue

The NSA⁵ is a catalogue containing useful derived quantities including galaxy stellar mass, redshift, magnitudes and line flux measurements. The catalogue was built from SDSS DR8 photometry, combined with UV photometry from GALEX (Galaxy Evolution Explorer; Blanton et al., 2007). We use the NSA v1 catalogue, which extends out to $z = 0.15$, and covers the redshift range of the galaxies in MaNGA.

2.4 Galaxy decomposition in SDSS-MaNGA DR17

2.4.1 Input sample selection and data preparation

The input sample to our analysis is taken from the SDSS-MaNGA DR17, which consists of 11 273 galaxy datacubes in total, out of which 10 010 are unique galaxies with high-quality observations. From this, we select only those galaxies having the two largest IFU

⁴ Available from https://www.sdss4.org/dr17/data_access/value-added-catalogs/?vac_id=manga-visual-morphologies-from-sdss-and-desi-images

⁵ Available from <http://www.nsatlas.org>

sizes with 91 and 127 fibres, since [Johnston et al. \(2017\)](#) find that two-component fits to the galaxies observed with smaller IFU sizes (19, 37 and 61 fibres) become unreliable owing to their small fields of view and availability of spaxels. This leaves us with 4661 galaxies that can potentially be fit with either a single Sérsic, a Sérsic + Exponential model, or both.

From this sample, we further narrowed down our selection to the galaxies that were flagged to have successful fits with these models in the MPP-VAC-DR17 (readers can refer to Sect. 2.3.4). We also eliminate galaxies with non-physical fit parameters, where the R_e (effective radius) is less than 1 pixel in this catalogue, which results in 4051 objects. These parameters from the MPP-VAC-DR17 would serve as initial values for the `GalfitM` fits in BUDDI (readers can refer to Sect. 2.4.2).

For the fits to the datacubes, we further require a bad pixel mask, in order to mask any pixels in the rectangular fits files that were not covered by the hexagonal IFU bundles. This is provided as an extension in the MaNGA datacubes in their data releases. Additionally, this extension also includes sufficient masks of foreground stars, which were created by visual inspection by the MaNGA team and complemented by GZ:3D (readers can refer to Sect. 2.3.3 and 2.6.4). Using this information in the fitting procedure is the significant modification for improving the fits from the previous run on DR15 galaxies (readers can refer to Sect. 2.8).

To improve the fits, a point spread function (PSF) datacube was created for each galaxy to be convolved with the fit to each image in the datacube. The (reconstructed) PSF for the *griz* bands are also provided in the datacube, from which the PSF at each wavelength was created through interpolation. `GalfitM` and by extension, BUDDI, allows a sigma datacube to be provided in order to estimate the flux uncertainty in each pixel more accurately. Lastly, the MaNGA datacubes contain an inverse variance datacube (IVAR) from which we derive the sigma datacube as $1/\sqrt{IVAR}$.

2.4.2 Bulge-disc decomposition with BUDDI

The decomposition of the MaNGA galaxies into their bulge and disc components itself is done using BUDDI⁶, an IDL wrapper for `GalfitM`⁷ that can handle the many wavelengths of IFUs and uses all available data simultaneously in order to optimise this task.

As described in [Johnston et al. \(2017\)](#) and [Johnston et al. \(2022a\)](#), BUDDI starts by measuring and normalising the galaxy kinematics from the IFU datacubes. This step is important since `GalfitM` can only model symmetric structures, and failure to normalise the kinematics in this way can lead to artefacts in the final spectra. The Voronoi binning technique described in [Cappellari et al. \(2003\)](#) was used to bin the datacubes for this purpose. The kinematics of the binned spectra were measured with `pPXF`, making use of the Medium resolution INT Library of Empirical Spectra (MILES) stellar library ([Sánchez-Blázquez et al., 2006](#)) to determine the line-of-sight velocities and velocity

⁶ Available from <https://github.com/EvelynJ/BUDDI>

⁷ Available from <https://www.nottingham.ac.uk/astronomy/megamorph/>

dispersions. Following this, the spectrum in each spaxel was shifted to match the line-of-sight velocity of the galaxy centre, and broadened to match the maximum velocity dispersion in the galaxy. This way, the IFU cube is ideally set up for BUDDI.

The code then follows a three-step process to derive the spectra of each component:

- In the first step, a single broad-band image of the galaxy is created by stacking the entire datacube, and modelled with `GalfitM` with both a single Sérsic profile to model the galaxy as a whole, and a Sérsic + Exponential profile fitting the bulge and disc, respectively. The r -band structural parameters from the MPP-VAC-DR17 (Domínguez Sánchez et al., 2022) were used as the initial parameters in BUDDI, which also helped contain the fits to a reasonable sample eliminating irregular morphologies with no distinct bulges and discs. The MPP-VAC provides flags where either the single-component model (Sérsic) or the two-component model (Sérsic + Exponential) or both have failed (readers can refer to Sect. 2.3.4), which further constrains our sample to those galaxies whose surface brightness profiles can be sufficiently modelled.
- To better refine the fit parameters as a function of wavelength, specifically to derive the Chebyshev polynomials used in `GalfitM`, the datacube was rebinned in terms of wavelength into a series of ten narrow-band images, following the approach outlined in Johnston et al., 2022a. These ten images were again modelled with `GalfitM` by fixing the initial parameters to those derived in the previous step. Additionally, this step is where the variations due to wavelength are introduced through the above-mentioned Chebyshev polynomials. A polynomial of order 1 was selected for the parameters R_e , $n_{\text{Sérsic}}$, q , and PA , which forces them to be constant with wavelength. This is because Häußler et al. (2022) find that the colour differences that exist within galaxies are small compared to differences between the components, which makes accurate measurements difficult; therefore, using a first order polynomial to model the structural parameters allows us to derive the spectra of the bulge and disc components more easily.
- Finally, in a third and last step, BUDDI fixes all the structural parameters to those derived in the previous step, and by leaving only the magnitudes free, derives the component magnitudes in each individual image slice of the datacube. This allows us to cleanly extract the 1D spectra of each component.

2.4.3 Selection of final sample

With BUDDI, we obtained a sample of 2699 galaxies that were successfully fit with the SE model (67% of the parent sample with reasonable `PyMorph` parameters), that is, the fit converged on a final solution and did not crash. To refine this sample, we used the selection criteria outlined in Johnston et al. (2022a) and Johnston et al. (2022b), which led to a final sample of fits with acceptable structural parameters recovered in the BUDDI fits:

- (i) $\Delta mag_r \leq 2.5$

- (ii) $0.25'' \leq R_e \leq 50''$
- (iii) $0.205 \leq n_{\text{Sérsic}} \leq 7.95$
- (iv) $0.1 \leq q \leq 1$,

where Δmag_r is defined as the difference in the magnitudes over the r -band wavelength range between the Sérsic and exponential components, which corresponds to the fainter component accounting for 10% of the total light. R_e is the half-light radius, $n_{\text{Sérsic}}$ is the Sérsic index of the Sérsic component, and q is the axis ratio of both components. This selection criteria led to a sample of 1452 galaxies with good fits and physically reasonable fit parameters, for which the bulge and disc spectra have been extracted. Although single Sérsic (one-component) fits were also performed, they are not relevant to this particular study and are not discussed here. More details on the methodology, choice of selection criteria, and derived spectra can be found in [Johnston et al. \(2022a\)](#). Furthermore, Sect. 4.1 in [Johnston et al. \(2022a\)](#) details the common reasons why fits can fail with BUDDI.

Figure 2.1 shows the general overview of the BUDDI-MaNGA DR17 sample, with the distributions of galaxy stellar mass, T-Type, and redshift (darker shades in the histograms). The distributions for all the MaNGA galaxies that were observed with the 91 and 127 fibre IFUs are shown as the lighter histograms. From these, the galaxies that were successfully fit with a Sérsic + Exponential model with PyMorph in the MPP-VAC-DR17 are shown by the dashed black outlines. The upper panels show the corresponding fraction of successful BUDDI fits with respect to the PyMorph sample (lighter shades), and to the MaNGA sample (darker shades). These fractions allow us to easily identify any biases that may exist purely in our sample. The galaxy stellar masses and redshifts were taken from the NSA catalogue (readers can refer to Sect. 2.3.6), the T-Types from visual morphology value-added catalogue described in Sect. 2.3.5. The sample consists predominantly of galaxies within $2 \leq \text{T-Type} \leq 6$, which correspond to Sab - Sc type galaxies, with a peak at T-Type = 4 (Sbc, late-type spiral). The galaxy stellar masses of the sample show hints of a bimodality in the distribution, with a maximum peak in the high mass end at $M_* \sim 10^{11} M_\odot$, and a smaller peak in the lower mass end at $M_* \sim 10^{9.8} M_\odot$. The BUDDI-MaNGA sample closely traces the distributions of the PyMorph sample and the MaNGA sample. Moreover, the upper panels show no significant biases that are specific to the BUDDI-MaNGA sample that are not already due to the selection effect in the MaNGA and PyMorph samples.

2.4.4 Caveats

We acknowledge a few caveats in the spectro-photometric modelling which are related to the assumptions we have made.

- For one, we assume that the surface brightness profile of the disc is always purely exponential from the outskirts all the way to the centre of the galaxy. However, recent studies debate the validity of this premise. [Breda et al. \(2020a\)](#) found that

a significant fraction of the discs in their late-type galaxy sample in fact show a down-bending of their light profile within the radius of the bulge. Their analysis revealed that for a third of their sample, the bulge SED showed negative fluxes in the blue end of the spectrum when a standard exponential disc model was subtracted from the galaxy SED.

- We also make a simplistic assumption on the structural components of the galaxies to only have a well-defined bulge and disc. This might not reflect the true surface brightness profile of the complexity of components such as spiral arms and bars. For example, excluding a model for the bar can affect the structural parameters of the components, such as overestimating the bulge-to-disc ratio (B/D) and the Sérsic index of the bulge (Laurikainen et al., 2004). Erwin et al. (2021) find that modelling a barred galaxy with a bulge and disc overestimated the fraction of light from the bulge by a factor of 4 and 100 for their two galaxies. While this can have an impact on the extracted spectra, it is also important to note that the low spatial resolution of MaNGA does not permit us to isolate the bars clearly and model them as a separate component. Similarly, the presence of a nuclear bar in the central region of the galaxy could cause the bulge to appear more elongated if not taken into account, which can affect the estimation of bulge structural parameters. On that note, Méndez-Abreu et al. (2008) investigated the influence of nuclear bars by adding them to simulated images and studying their structural parameters through photometric decomposition, to observe if the bulges showed signs of elongation. They found that the majority of the bulges were in fact circular and not significantly impacted by the presence of a nuclear bar in their midst. Therefore, we expect these results to also hold in the present study.

Our assumptions for this work are primarily based on the work of Fischer et al. (2019) and Domínguez Sánchez et al. (2022), which as we mentioned earlier in Sect. 2.4.2, served as our initial parameters for the fits. However, testing the alternate or additional premises would require this large sample of galaxies to be fit on a case-by-case basis, which would defeat the purpose of an automated fitting procedure.

2.5 Methods

2.5.1 Estimating bulge and disc stellar masses

Due to the small field of view of the MaNGA IFUs, the light from the outskirts of the galaxies can often be lost. As a result, any mass estimates derived using the bulge and disc fluxes from BUDDI may be biased due to the loss of the light profile information in these outer regions.

Therefore, in this work, the masses of the bulges and discs were estimated through SED fitting to the photometry derived from SDSS imaging (Sect. 2.5.1.1). This data not only shows improved imaging resolution compared to the MaNGA data, but ensures broad-band photometry necessary for the SED fitting routines. For consistency, we feed

to `GalfitM` the GZ:3D foreground star masks that were created on the SDSS images, to align with the data preparation approach in BUDDI (readers can refer to Sect. 2.4.1). The exact approach we employ is explained below. An alternative approach employing the relation between optical colour and the stellar mass-to-light ratio was also explored, and will be detailed below in Sect. 2.5.1.2.

The SDSS images were modelled with two components using `GalfitM` with the structural parameters fixed to those derived in the BUDDI fits (readers can refer to Sect. 2.4.2), to derive the magnitudes in the *ugriz* bands. These magnitudes were fit with polynomials of order 5 which were allowed complete freedom as a function of wavelength (freedom in 5 bands). By fixing the structural parameters in this way we ensure that we are measuring the masses for the same components derived from the IFU datacubes, with the caveats discussed in Sect. 2.5.1.3. It must be noted that not all the galaxies in the final BUDDI-MaNGA Sérsic + Exponential sample (from Sect. 2.4.3) had a successful fit with `GalfitM` to the SDSS imaging data. From the 1452 selected galaxies in BUDDI, we were able to recover the fits for 1390 galaxies. From this, we further selected the galaxies that had $0.1 \leq (B/T)_r \leq 0.9$, which corresponds to the *r*-band magnitude selection we imposed in Sect. 2.4.3. With this in place, we have 1312 galaxies with reasonable fit parameters to both SDSS images and MaNGA datacubes, for which we can now perform SED fitting to retrieve their stellar masses. The resulting observed magnitudes were then converted into fluxes in units of μJy using a zero-point magnitude of 23.9, to be fed as input to the SED fitting code described below. Häußler et al. (2013) find that `GalfitM` underestimates the errors by a factor of $\sim 2 - 2.5$, and we increase all magnitude errors by a factor of 3 to be conservative, as suggested in Nedkova et al., 2021. This needs to be included in the SED fitting, since the codes heavily rely on the uncertainties, and a value has to be provided which is as realistic as possible.

2.5.1.1 BAGPIPES derived masses

The SED fitting was performed using Bayesian Analysis of Galaxies for Physical Inference and Parameter ESTimation (BAGPIPES⁸; Carnall et al., 2018). Based on Python, BAGPIPES is a versatile tool that can fit both observed photometric and spectroscopic SEDs simultaneously to complex galaxy model spectra to obtain a probability distribution function (PDF) for each key physical property that can be derived with it.

We set up the code to assume the stellar population synthesis models described in Bruzual et al. (2003), built with a Kroupa (2001b) initial mass function (IMF). Since our main objective with BAGPIPES was to estimate stellar masses, we simply model the stellar continuum imposed by the photometric bands, without providing spectroscopic information pertaining to emission lines. For our redshift range, the photometric bands provide reliable stellar mass estimates because they sample the Balmer break. For the fitting, we assume an exponentially declining SFH (τ model) of the form defined in

⁸ Available from <https://bagpipes.readthedocs.io/>

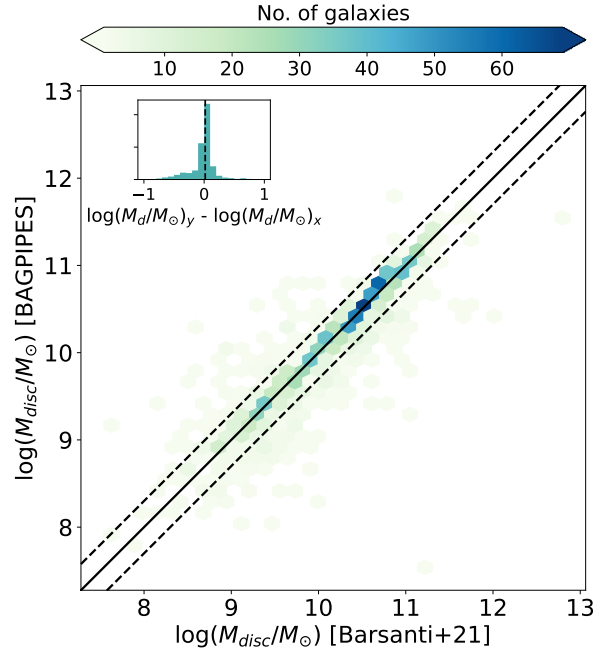


Figure 2.2: Density plot of the disc masses estimated by BAGPIPES and the colour-mass relation in Barsanti et al. (2021). The black diagonal line shows the 1:1 correspondence, and the dashed lines mark the ± 0.3 dex offset from it. The inset shows the distribution of the difference between each BAGPIPES estimate and the CMR estimate, with the black dashed vertical line marking the median offset.

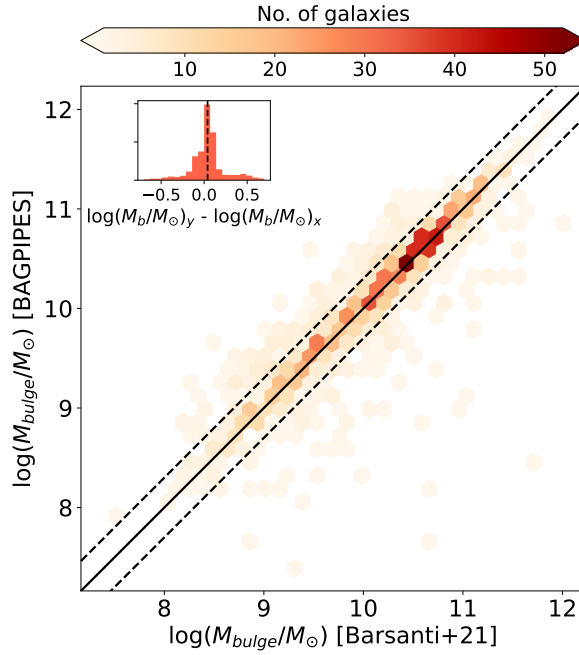


Figure 2.3: Similar to the density plot for Figure 2.2 but showing the bulge masses.

Carnall et al. (2019):

$$\text{SFR}(t) = \begin{cases} \frac{\exp(-t - T_0)}{\tau}, & t > T_0 \\ 0, & t < T_0 \end{cases}$$

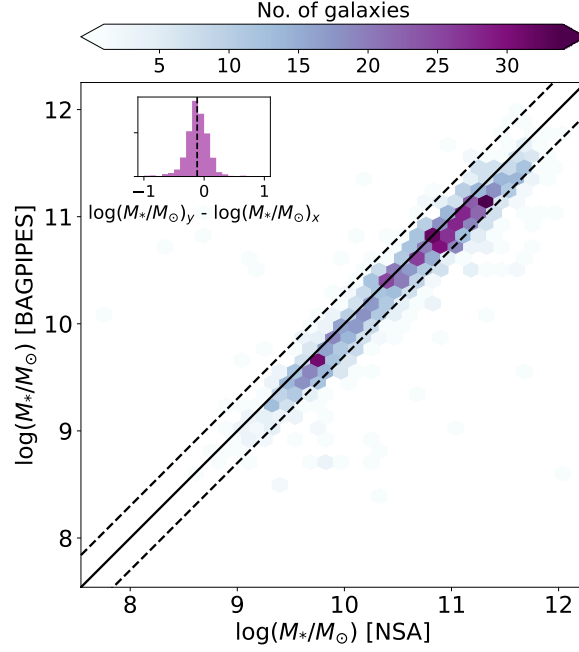


Figure 2.4: Similar to the density plot for Figure 2.2 but showing the total galaxy stellar masses.

where T_0 is the time at which star formation is expected to jump from its initial value of 0 to its maximum value, and τ is the e-folding timescale with which the star formation declines exponentially. BAGPIPES assumes a uniform prior for all parameters by default; imposing different priors may result in different estimates for the physical parameters and a detailed analysis can be found in [Carnall et al. \(2019\)](#). We allow the stellar ages to vary between 10 Myr and the age of the Universe, 13.8 Gyr. τ is allowed to vary between 100 Myr and the age of the Universe, while a solar metallicity of 0.02 is fixed. We assume a Calzetti dust attenuation law ([Calzetti, 2001](#)), allowing A_v to vary between 0 and 2 mag. The prior distributions for the parameters are taken to be flat, following the default setting in BAGPIPES. The redshifts of the galaxies are set and fixed to the estimates from the MSR-VAC-DR17 (MaNGA Spectroscopic Redshifts Value Added Catalog; [Talbot et al., 2018](#)). For the galaxies that do not have a spectroscopic redshift from this catalogue (344 objects), the photometric redshifts from the NSA catalogue were used instead. The Bayesian formalism integrated into BAGPIPES results in a posterior distribution for the stellar masses (and in principle for all physical parameters), leading to reliable uncertainty estimates. We take the median values as the parameter estimates, with the difference between the 16th and 84th percentiles as the uncertainties. We note that BAGPIPES fails in $\sim 4\%$ of the bulges and the discs, mostly due to unfeasible errors on the magnitudes estimated by GalfiTM, or due to a simplistic assumption of a parametric SFH for both components.

2.5.1.2 Mass estimates derived from the colour-mass relation

A final comparison set was generated estimating the stellar masses purely on the basis of their optical colours and observed magnitudes in a maximum of two bands, without

imposing any assumptions on the star-formation history or using stellar population synthesis models. We followed the prescription mentioned in [Barsanti et al. \(2021\)](#):

$$\log_{10}(M_*/M_\odot) = -0.4 i + 2 \log_{10}(D_L/10) - \log_{10}(1+z) + (1.2117 - 0.5893 z) + (0.7106 - 0.1467 z) \times (g - i) \quad (2.1)$$

where z is the galaxy redshift from NSA, and D_L is the luminosity distance in parsec. The resulting stellar masses of the bulges and discs estimated from both methods show excellent agreement and little scatter. Figures 2.2, 2.3, 2.4 show the comparison of these estimates (for the disc, bulge, and total mass respectively) with different methods, and it is clear the majority of them agree well with each other within 0.3 dex. The small scatter and offset can be attributed to the differences in the assumptions and the physics that go into the template fitting codes, as well as the fact that these codes make use of magnitudes in 5 bands and model the SED of the galaxies in the optical range, while the colour-mass relation only uses 2 magnitudes. We define the total galaxy mass for our sample as a simple sum of the bulge and disc stellar masses. In Figure 2.4, our estimates are compared to the total galaxy stellar masses in the NSA catalogue (converted to the cosmology parameters we assume in this paper), which were estimated from K-correction fits to Sérsic fluxes.

For this work, we use the BAGPIPES estimates of stellar masses whenever we have them, and the colour-mass relation estimates for the ones where BAGPIPES failed to fit the galaxy SED. The sample now contains 1312 objects with physically feasible component masses. It must be noted that only the BAGPIPES estimates have associated errors.

In order to study any trends related to morphology, we cross-match our catalogues with the MaNGA Visual Morphologies VAC (readers can refer to Sect. 2.3.5), which leads to sample of 1275 galaxies where we can study both mass and morphology trends. Figure 2.5 depicts the bulge-to-total ratio estimated from the r -band fluxes as a function of morphological T-Type and Hubble type (obtained from the VAC mentioned above) through violin plots. The violins are marked by a black box and whisker plot inside them, where the white circles denote the median $(B/T)_r$ for each type. The Sdm and Sm galaxies have very low numbers and wherever they are included in the analysis, it is important to note that those particular inferences are not statistically significant. Galaxies with irregular morphologies (Irr) and those with no classifications (NC) in the catalogue are excluded here. As would be expected, despite the large scatter in all morphologies, the median $(B/T)_r$ circles trace a trend starting with relatively high values for ellipticals and declining slowly with increasing type, flattening towards spirals. In the late-type spirals (Sd-Sm), our sample hits low-number statistics and begins to show an irregular trend. We note that all galaxies in our sample were run through BUDDI for a two-component decomposition prior to categorising their morphologies; therefore it appears that ellipticals have also successfully been decomposed into two components despite the traditional picture of a single (Sérsic)-component model. However, we expect it to be mostly an effect of forcing a two-component fit onto one-component objects. We note that from Sect. 2.6 onwards, our analysis is dedicated purely to spiral galaxies.

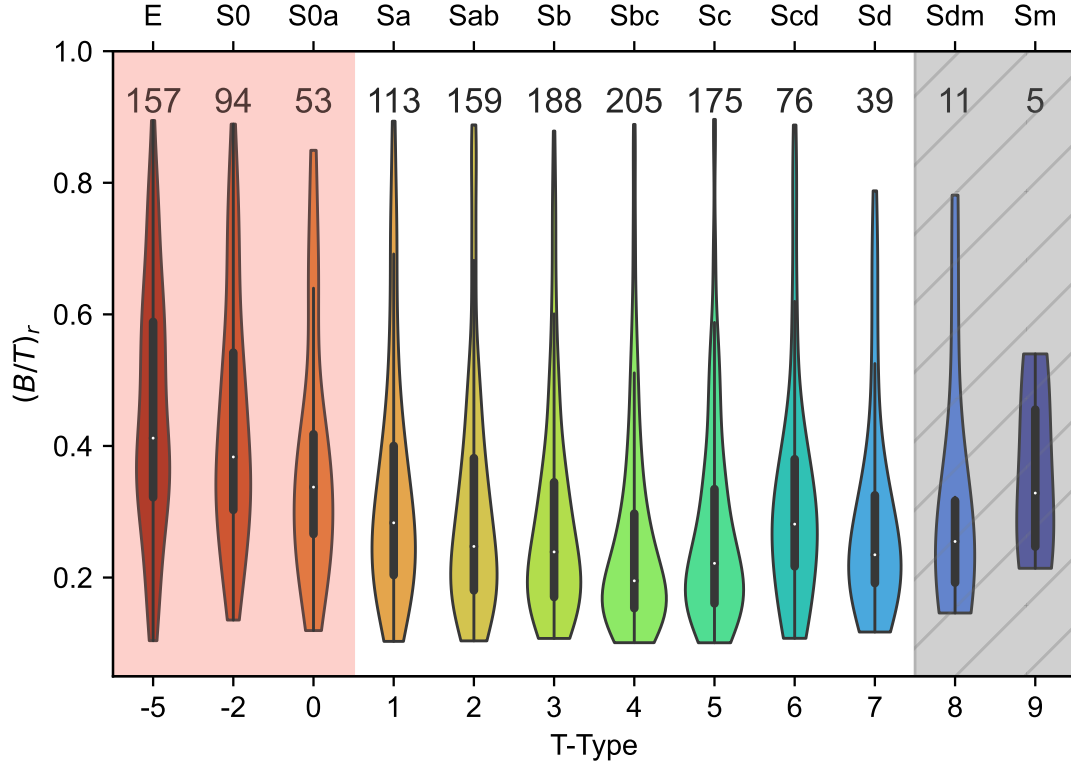


Figure 2.5: Bulge-to-total ratio of all galaxies in the r -band, as a function of morphology. The lower x -axis is labelled by the T-Type index, and the upper x -axis by the corresponding Hubble types. The inner parts of the violins contain a box and whisker plot. The white circles in the violin plots represent the median bulge-to-total ratios, while the thick black bar defines the interquartile (25th - 75th percentile) range of the distribution. The limits on the thin black bar extend to 1.5 times the interquartile range. The upper and lower ends of the violins mark the highest and lowest values of $(B/T)_r$ in each T-Type. The number of galaxies in each T-Type is denoted on top of its corresponding violin. The region shaded in red depicts the early-type galaxies (ETGs: E, S0, and S0a), that are not part of this analysis, which concentrates on the types with the white background. The ETGs will be discussed in a different publication. The region marked in grey with the late-type spiral galaxies (Sdm and Sm) are highlighted due to their very low numbers. Additionally, these are visually harder to separate as two distinct morphologies, and will be merged together in certain plots in the analysis.

Therefore, any possible physical motivation behind multiple components in elliptical galaxies will be investigated in future work.

2.5.1.3 Caveats on component stellar masses

There are some caveats with these derived component masses which should be discussed. Most importantly, these masses are derived, as explained above, by applying the structural parameters derived by the BUDDI fits on MaNGA data to the SDSS imaging data. However, the field of view of the MaNGA data is, by design, very small with an upper limit of $\sim 2.5R_e$ (readers can refer to Sect. 2.3.2), whereas it has been shown that a large field of view is critical in deriving accurate structural parameters, at least for components with high Sérsic index values (Häussler et al., 2007). This means that the structural parameters from the BUDDI fits only really apply to the central parts of the galaxies, and not necessarily to their outskirts. This can have a large impact on the photometry of the components, for example it is known that the bulge profile (usually Sérsic or de Vaucouleurs) dominates at large radii and obtaining an accurate sky measurement is vital to deriving good measurements of structural parameters (Häussler et al., 2007). Most importantly, the outskirts of a galaxy cannot be reliably taken into account in the absolute photometry, that is, the absolute mass scale can be somewhat compromised. Therefore, it should be remembered that the masses presented in this work for the bulges and discs represent the masses of the components that BUDDI identified and modelled as the bulges and discs, and thus may not correspond to the same components modelled in the same galaxies in other studies (Domínguez Sánchez et al., 2022; Mendel et al., 2013).

As a second effect, this of course also means that the photometry in general cannot represent the SEDs of the entire bulge or entire disc, potentially changing the bulge-to-disc mass ratio $(B/D)_{mass}$ or the bulge-to-total mass ratio $(B/T)_{mass}$ of the two components. Instead the component masses represent the bulge and disc as seen within the MaNGA field of view and assuming that their light profiles extend outside of this region in the same way. However, we have shown that our total masses agree well with masses derived by other means (Fig. 2.4). We emphasise that the main purposes of these derived masses is to examine global trends with component mass and not perform any detailed analysis with them. Therefore, the masses will not have an impact on the mass assembly histories themselves that are examined in this work (Sect. 2.6), and such uncertainties on the component masses are deemed not to be critical here.

2.5.2 Spectral fitting

With the stellar masses of the bulges and discs in place, we now turn our attention to analysing the stellar populations of the different components in order to build a comprehensive picture of how spiral galaxies have assembled their masses throughout their lifetimes. A sub-sample of types Sa - Sm consisting of 968 spiral galaxies will form the basis for the rest of the analysis in this paper. We focus on extracting the

mass-weighted stellar populations parameters through full spectrum fitting of the bulge and disc spectra of this BUDDI-MaNGA spiral galaxy sample using the penalised Pixel Fitting code pPXF (Cappellari et al., 2004; Cappellari, 2017). pPXF is an IDL and Python-based spectral fitting software that, when used in conjunction with a stellar spectral library, finds a linear combination of templates that best matches the observed spectrum after convolution with the line-of-sight velocity and velocity dispersion (LOSVD) of the galaxy. In this work, we opt for the Python implementation of pPXF v7.4.5⁹.

To fit the spectra, the MILES¹⁰ evolutionary stellar population synthesis (SPS) (Vazdekis et al., 2015) models based on the BaSTI isochrones (Pietrinferni et al., 2004; Pietrinferni et al., 2006; Pietrinferni et al., 2013) were chosen as the stellar template library mainly owing to its rich metallicity coverage. The MILES library contains 985 stars with a wavelength coverage between 3 500 and 7 000 Å, and a spectral resolution FWHM of 2.51 (Sánchez-Blázquez et al., 2006). We limit the fit to the spectral region between 4 700 and 6 700 (in the rest-frame), converting this range to the observed frame of each galaxy, such that it sufficiently covers the wavelength range between the H β and H α lines. We normalise the input fluxes, and set a constant noise over the spectral range, defined by the reciprocal of the derived S/N. The grid formed by the fixed stellar population parameters range from -2.27 dex to 0.4 dex in 12 steps for the metallicities [M/H], and from 30 Myr to 14 Gyr in 53 steps for stellar ages, making up a total of 636 template spectra. We assume a Kroupa Universal IMF (Kroupa, 2001b) with a slope of 1.3, and with no specific assumptions on the α -abundance for the SPS models. In order to account for the shape of the continuum and correct for spectral calibration inaccuracies, a multiplicative Legendre polynomial of order 8 was adopted, excluding the need for explicitly specifying a reddening curve (Cappellari, 2017). After masking out the [OI]5577 sky line, the stellar continuum is fit alongside the gas emission lines simultaneously.

During the fit, we also employ regularisation to reduce intrinsic degeneracies to the fit solutions, that might otherwise lead to discrete weights and a bursty star formation history. The regularisation step allows for the smoothing of the variation of SSP weights with similar ages and metallicities. The level of smoothing is determined by the user-defined regul parameter in pPXF. While regularisation is useful in the case of individual spectral fitting and mostly recovers star formation histories that are physically interpretable (such as a continuous star formation episode as opposed to a discrete one with spurious features), it does not come without its limitations. Shetty et al. (2015) and Norris et al. (2015) state that regularised fits do not prevent sharp jumps in the recovered star formation histories provided that such features are necessary to accurately fit the data, whether or not they are physically motivated. This situation may occur in cases where the spectrum is particularly noisy, leading to poor fits with the template spectra, or where the galaxy has undergone a small number of short bursts of star formation on timescales less than the difference in the age steps of the template spectra (readers

⁹ Available from <http://purl.org/cappellari/software>

¹⁰ Available from <http://miles.iac.es/pages/webtools.php>

can refer to [Zibetti et al. \(2024\)](#) for a detailed study on constraining the minimum age resolution that can be achieved using SPS models). The challenge in regularisation lies in maintaining a balance between fitting the data and achieving smoothness in the solution, which can introduce potential biases ([Cappellari, 2023](#)) such as sudden shifts or jumps in the recovered SFHs. Therefore, some level of discreteness is not completely unavoidable especially in the above-mentioned cases, and we exercise caution while interpreting them (readers can refer to Sect. 2.6.1.1).

The degree of smoothing for each spectrum was determined following the approach outlined in [Cappellari \(2017\)](#) and described here. An unregularised fit with fixed kinematics is performed first, followed by a noise scaling step such that $\chi^2/N_{DOF} = 1$ (DOF being the number of degrees of freedom in the fit). Then the fit is repeated over a range of user-defined regularisation values, and the optimal value is chosen when the increase in χ^2 , $\Delta\chi^2 = \sqrt{2 \times N_{DOF}}$. For some galaxies, however, this does not constrain the optimal regularisation value well, and we opt the criterion following [Shetty et al. \(2015\)](#). The modified criterion is now $\Delta\chi^2 = (\sqrt{2 \times N_{DOF}})/n$, where n is an integer that we allow to vary between $1 < n < 100$. The constraint over n that we have chosen is very liberal to allow fits to the spectra with very low S/N. We note that almost all of the component spectra with $n > 20$ do in fact have low $S/N < 30$. We did not discard any fits because the fraction of objects with high n values is very small compared to the entirety of the sample ($< 2\%$). It must be noted that the defined steps in stellar age in the synthetic template models are only an approximation as the models are based on averages of stars of similar ages and metallicities. In reality, star-formation is unpredictable and may occur on shorter timescales than defined in the models. Therefore, the resulting estimates derived from fitting these models might not be an absolute representation of the true star-formation activity in the galaxy components.

2.5.2.1 Mass-weighted stellar populations.

pPXF estimates the mean metallicities and mean stellar ages in the stellar population analysis from the derived template spectra weights:

$$\log(\text{age}) = \frac{\sum \omega_i \log(\text{age}_{\text{temp},i})}{\sum \omega_i} \quad (2.2)$$

$$[\text{M}/\text{H}] = \frac{\sum \omega_i [\text{M}/\text{H}]_{\text{temp},i}}{\sum \omega_i} \quad (2.3)$$

where ω_i is the weight of each (i^{th}) template, and $[\text{M}/\text{H}]_{\text{temp},i}$ and $\text{age}_{\text{temp},i}$ are the metallicity and stellar age of that same stellar template respectively. The weights ω_i in our analysis specifically represent the fractional contribution of each stellar template to the galaxy stellar mass M_* (mass fraction). pPXF recovers the ‘formed stellar masses’, which are associated with the zero-age mass distribution and do not include contributions from mass loss or supernova outflows (and are therefore expected to be higher than the present-day stellar masses).

2.5.2.2 Error analysis.

As in Johnston et al. (2022b), we performed the errors analysis on the mean metallicities and stellar ages estimates by adding a random noise to the best fit spectrum obtained in the previous analysis, until it results in the same S/N as the original spectrum. This new simulated spectrum is fit with pPXF with the same noise scaling and regularisation value as before. This simulation was repeated 50 times for each spectrum, and the errors are taken as the 16th-84th percentile range of the resulting distributions of each stellar populations parameter.

2.6 Galaxy mass assembly histories

With the mass weights obtained from pPXF, we can now reconstruct the mass assembly histories (MAHs) of the bulges and discs independently, by mapping out their cumulative mass assembly as a function of the lookback time. For this study, we turn our focus to the spiral galaxy sample of $1 \leq \text{T-Type} \leq 9$, which corresponds to Sa - Sm spiral galaxies. This sub-sample in BUDDI-MaNGA consists of 968 objects (Sect. 2.5.2) with successful pPXF fits to their component spectra and stellar mass estimates. For the rest of the paper that focusses on spectroscopic properties, these galaxies form the basis for the analysis. In Sect. 2.6.1, we present our results on the individual mass assembly histories and the global trends we observe in the bulges and discs of the sample, as a function of their respective stellar masses. In Sect. 2.6.2, we follow through with a better representation of mass-dependence using a mass-matched sample in every type. Finally in Sect. 2.6.3, we study the dependence of the morphological type on these mass assembly histories.

2.6.1 Individual and global trends: Component downsizing

In the sections that follow, we first investigate the trends shown by the mass assembly histories of the bulges and discs of each galaxy in different morphological types. We then emphasise these trends through quantifiable parameters that indicate the formation mode of the components. Finally, we study the global trends observed on average by these mass assembly histories.

2.6.1.1 Individual trends in bulge and disc mass assembly histories.

The individual MAHs of the components are plotted in Figure 2.6, in different bins of the T-Type: each row begins with the disc MAHs on the left, the bulge MAHs in the middle, and their respective stellar mass distributions on the right (blue for discs, red for bulges). The cumulative mass fraction assembled by each galaxy has been plotted against lookback time, which traces the star formation histories of galaxies across cosmic time. The cumulative mass fractions have been created by adding the normalised weights of the stellar spectra used in the pPXF fits at each age step from the oldest to the youngest stellar templates. Vertically, the plots step through increasing T-Types, starting

with Sa in the top row, to Sdm and Sm in the bottom. The MAHs of the bulges and discs in the left two panels are colour-coded as a function of their respective stellar masses, with the highest masses in red and the lowest masses in blue and purple. The thick black dot-dashed and dashed lines represent the mean MAH in high ($M > 10^{10} M_{\odot}$) and low ($M < 10^{10} M_{\odot}$) component mass bins. These mean MAHs are shown in red only for the Sa type galaxies, since they act as a reference against which the MAH trends of the following types can be compared.

From the dot-dashed curves in Figure 2.6, we observe that the more massive bulges assemble their stellar masses very early on within a short timescale, while the less massive bulges, for which the mean-stacked MAHs are shown as dashed curves, show a relatively delayed and longer-lasting mass assembly, an effect defined in Cowie et al. (1996) as ‘downsizing’ for galaxies as a whole. This effect is clearly visible even among the individual MAHs up to Sc type spirals, with a gradient from high masses in red and orange to low masses in green and blue - albeit the gradient being relatively stronger in bulges than in the discs. The morphological types later than Sc mostly host less massive bulges and discs (see the respective stellar mass distributions in column 3) with a large diversity in their MAHs, and a gradient is not clearly visible in either component for these. However, the large number of MAHs in these plots for each morphology makes the trend harder to see; for example, it can be made artificially weaker or stronger due to the number and order of the lines plotted. Especially in the latest T-Types, trends might become clearer when comparing average, or mass-matched samples. It must be noted that some of the individual MAHs appear to have sharp jumps over short timescales, which might imply extraordinarily high star formation rates seen in extreme starbursts. While this is a possibility, the discreteness can also be an effect of the limits of regularisation mentioned in Sect. 2.5.2. However, since these sharp jumps occur only in a few objects relative to the total number of objects in our analysis, we do not expect this to alter our statistical results. Furthermore, in order to better identify any trends present, the next subsections will explore the data further by calculating and comparing the timescales over which half the mass was created in each component (Sect. 2.6.1.2) and will consider the mean MAHs as a function of mass and morphology.

2.6.1.2 Half-mass formation times and mass build-up.

We quantify the individual mass assembly histories through the ‘half-mass formation time’ and a closely related parameter - the ‘half-mass formation timescale’. We define half-mass formation time as the lookback time ($LBT_{1/2}$) when 50% of the stellar mass had been built up. This parameter allows us to study which component assembled its stellar mass earlier. We define the half-mass formation timescale ($\tau_{1/2}$) as the difference between the lookback time when stellar mass assembly first occurred and when 50% of the mass had been built up. This parameter provides information on which component assembled its stellar mass faster. Figure 2.7 shows the comparison of the formation times of the bulge and the disc for each galaxy, colour-coded by the total stellar mass of the

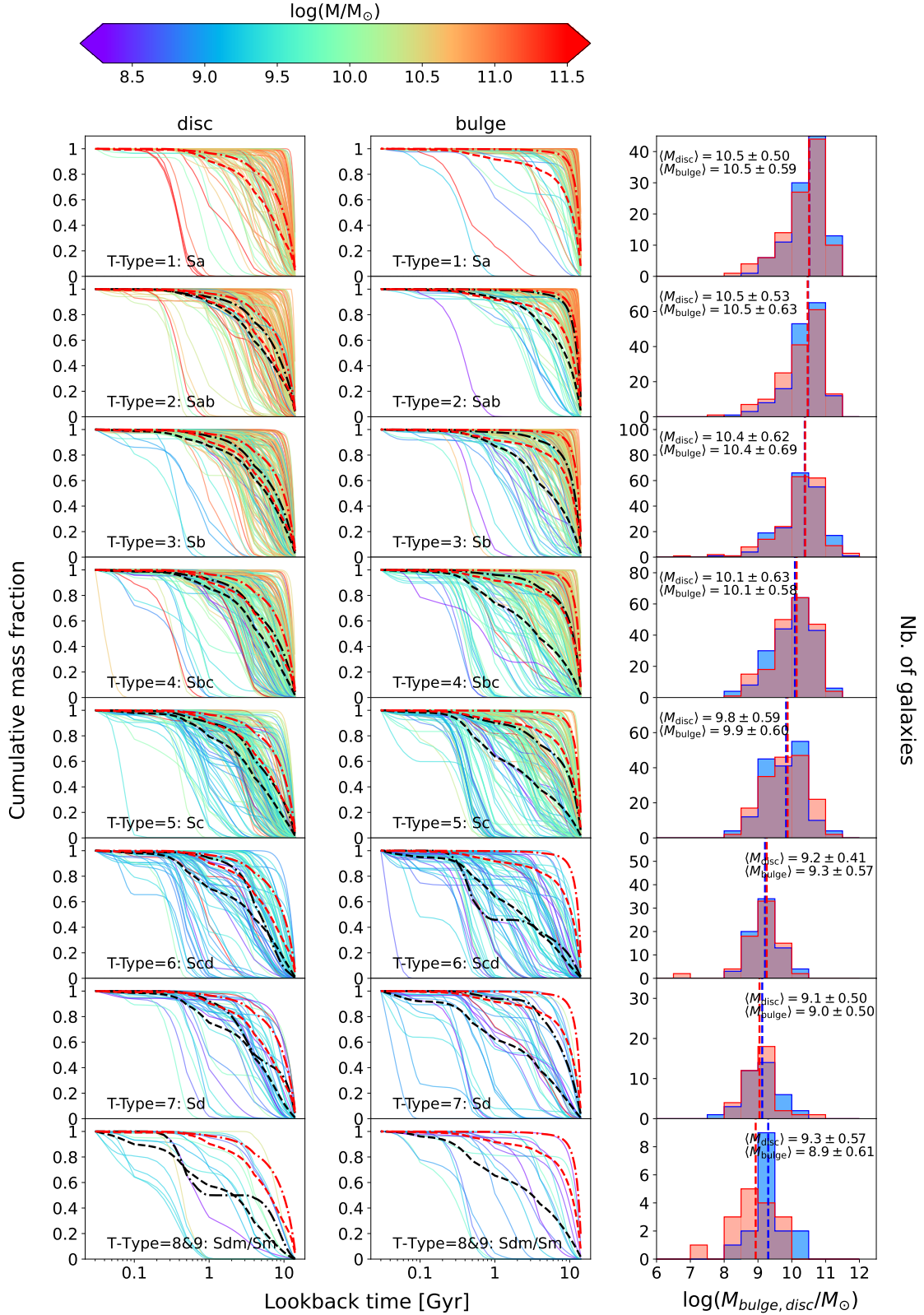


Figure 2.6: Individual and global trends of MAH in bulges and discs. Left and centre columns: Individual MAHs of spirals separated by increasing T-Types (from top to bottom). In each panel, the mean-stacked MAH for high-mass components ($M > 10^{10} M_{\odot}$) are shown as thick black dot-dashed curves, and low-mass components ($M < 10^{10} M_{\odot}$) as thick black dashed curves. These are depicted as red dot-dashed and dashed curves respectively for the Sa type (row 1), which also serves as a reference for all following types for easier visual comparison. Right-most column: Bulge and disc masses in red and blue, respectively, with their median masses shown by dotted lines.

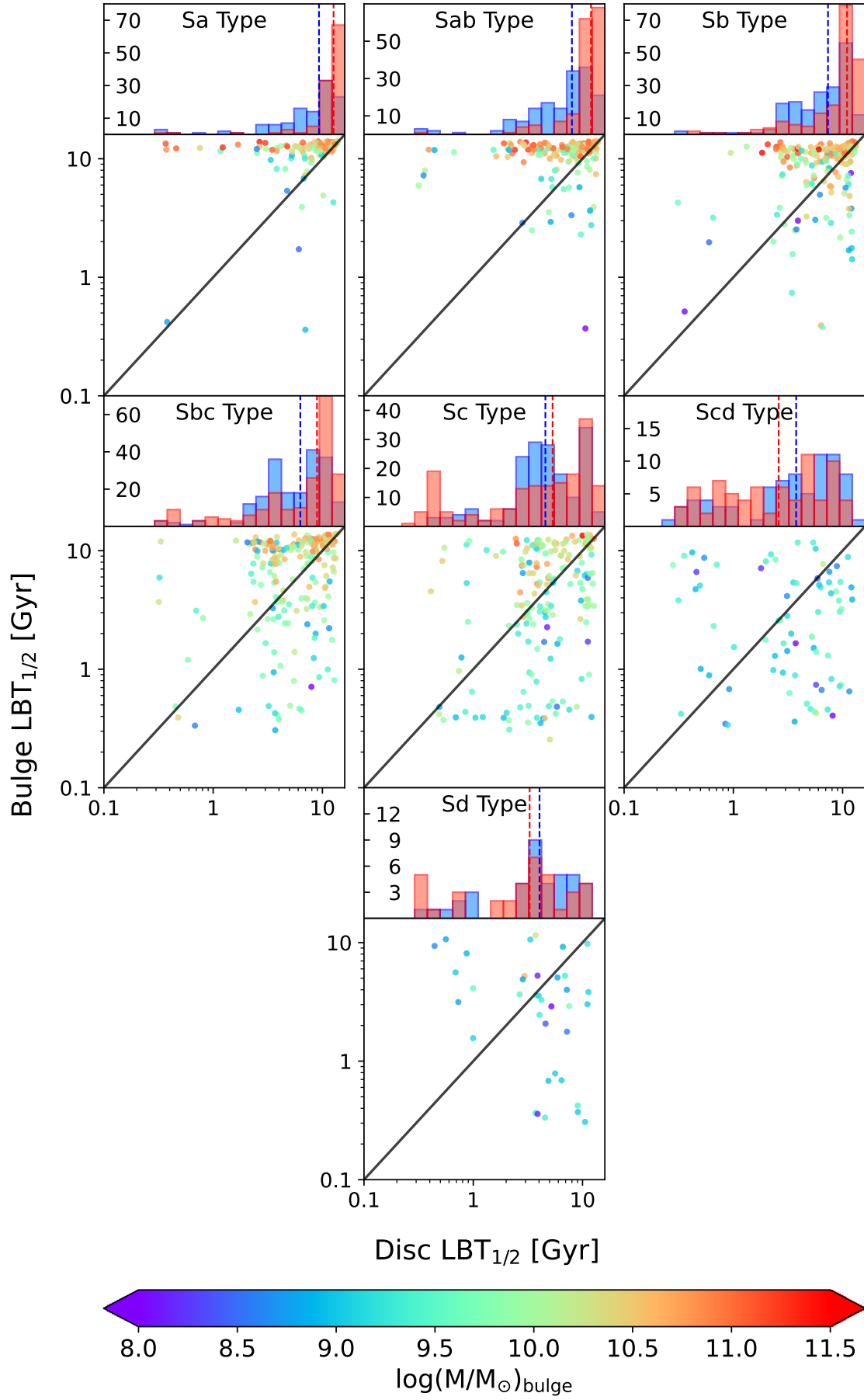


Figure 2.7: Formation time of the bulges and discs which marks the time it took to form 50 per cent of the stellar mass, colour-coded by the total stellar mass. The upper panels show the histogram of these formation times for the bulge and disc in red and blue respectively, with their median times in dashed lines.

galaxy. The solid black diagonal line marks the 1:1 correlation between them. The plots are split into seven panels in terms of their T-Types as in Figure 2.6, excluding the Sdm and Sm types due to low-number statistics. The histograms in the upper panels show the $LBT_{1/2}$ distributions of the bulge in red and the disc in blue, with their medians shown as the dotted lines. If bulge $LBT_{1/2} > \text{disc } LBT_{1/2}$, then the stars in the bulge assembled the majority of their masses before the disc, implying an inside-out assembly mode. Alternatively, galaxies with bulge $LBT_{1/2} < \text{disc } LBT_{1/2}$ would correspond to an outside-in formation mode, with the stars in the disc assembling the majority of its mass prior to the bulge.

We can see a clear trend with Hubble type in this plot. Starting with the Sa spirals, the majority of the galaxies fall under the inside-out assembly regime (above the 1:1 line). Stepping horizontally across the different T-Types up until Sc, this result follows through, with the exception that the fraction of outside-in assembled galaxies increases with each type with the above-mentioned effect becoming less pronounced; nevertheless, the inside-out mode is still dominant. On reaching the Scd and Sd types, there does not appear to be any preferred assembly mode, and the galaxies are more or less equally distributed in both regimes. However, it must be noted that these types have relatively fewer galaxies in comparison to the earlier types, and it is possible this equal distribution is an artefact of low-number statistics. The histograms in the upper panels additionally show that the median bulge half-mass formation time is always higher than the median disc half-mass formation time for galaxies from Sa - Sc types. The Scd and Sd types appear to show a median outside-in assembly mode. However, the latter shows nearly identical half-mass formation time histograms for both components, and the time window between the bulge and disc $LBT_{1/2}$ is quite narrow, suggesting instead that there was no preferred assembly mode.

With respect to the half-mass formation timescales, if bulge $\tau_{1/2} < \text{disc } \tau_{1/2}$, then the stars in the bulge assembled the majority of their masses in a shorter time span than the discs. On the other hand, if bulge $\tau_{1/2} > \text{disc } \tau_{1/2}$, then the disc stars assembled their masses faster than the bulge stars. From Figure D.1 in Appendix D, we can see a correlation between the two parameters $LBT_{1/2}$ and $\tau_{1/2}$. The same trends with morphology observed in Figure 2.7 are mirrored in Figure D.1, with the majority of Sa - Sc type spirals having assembled half of their bulge stellar masses faster than half of their disc masses. This fraction decreases, as we move from Sa towards Sc galaxies, whilst the fraction of galaxies showing the opposite trend increases. The later type Scd and Sd galaxies are equally distributed between those where the bulge stars assembled their mass faster than the disc stars, and those where the disc stellar mass assembly was faster. These trends are emphasised in the histograms (and the median bulge and disc $\tau_{1/2}$ lines) above each panel; additionally the time window between the bulges and discs is the highest for the Sa spirals, and becomes narrower with increasing type. These results tie in with our inferences from Figure 2.7, implying that a high fraction of bulges in Sa - Sc type spirals assemble half their stellar mass earlier (inside-out assembly) and in a shorter time span than the discs. The Scd and Sd types again suggest that the bulge

and disc stellar masses were assembled together or have no preference in the assembly mode, with nearly equal assembly timescales. This is consistent with our inferences from the individual MAHs described in Sect. 2.6.1.1.

2.6.1.3 Global trends in bulge and disc mass assembly histories.

To observe the mean global trends exhibited by the MAHs of the components (Fig. 2.6), the bulges and discs are split into two stellar mass bins at $10^{10} M_{\odot}$ (each by the component mass). The MAHs in each bin are then median-stacked, with the median of the galaxies with bulge and disc masses higher than $10^{10} M_{\odot}$ shown as the thick dot-dashed curve, and those lower than $10^{10} M_{\odot}$ shown as the thick dashed curve. The first row showing the Sa type spirals have the median MAHs marked in red, and point as a reference in each following panel with the different T-Types. For all other types, the median curves are shown in black, and can be directly compared to the earliest spiral type Sa, to more clearly see any trends with respect to Hubble type. Except for the latest Sdm and Sm type galaxies (bottom row), which do not contain high mass bulges, the downsizing trend is seen clearly especially in the bulges, where the MAH of both mass bins are very well separated, with the low mass bulges showing a slower mass build-up. On average, this downsizing appears to present itself in discs as well, albeit at a lower extent than the bulges. However, the high diversity observed in the MAHs requires a more narrow binning to better isolate the stellar mass dependence, that consequently also helps in matching the different T-Type sub-samples in their mass distributions (this will be addressed in the next section).

On comparing the median (black) MAHs with respect to the Sa type (red), the bulges in both the high and low mass bins shift slowly to the left but progressively with type (up until Sd), indicating a relatively slower build-up of stellar mass. The Sdm and Sm types in the final row simply do not host any bulges over $10^{10} M_{\odot}$, but the shift in the low mass bin is still evident. The discs also show this shift, although the median separation between the low and high mass bins are much smaller than for the bulges, and are more delayed and extended as seen earlier from the individual MAHs. While these plots already provide us with a good deal of information, we must note from the stellar mass distributions in the different T-Types (shown in column 3 of Fig. 2.6), that they are not mass-matched. Additionally, there is a large scatter in the MAHs for which a simple binning into high and low masses might not provide an accurate representation of their assembly at all masses. In the following sections, this will be addressed to better understand the true mass-dependence of the assembly histories of bulges and discs.

2.6.2 Dependence on component stellar mass

While stellar mass trends can already be seen in Figure 2.6, the density of MAH curves in the plots make it difficult to really assess the strength of these trends. Additionally, given the disparity amongst the stellar mass distributions of bulges and discs for the different T-Types (see column 3 in Fig. 2.6), it is important that they are optimally

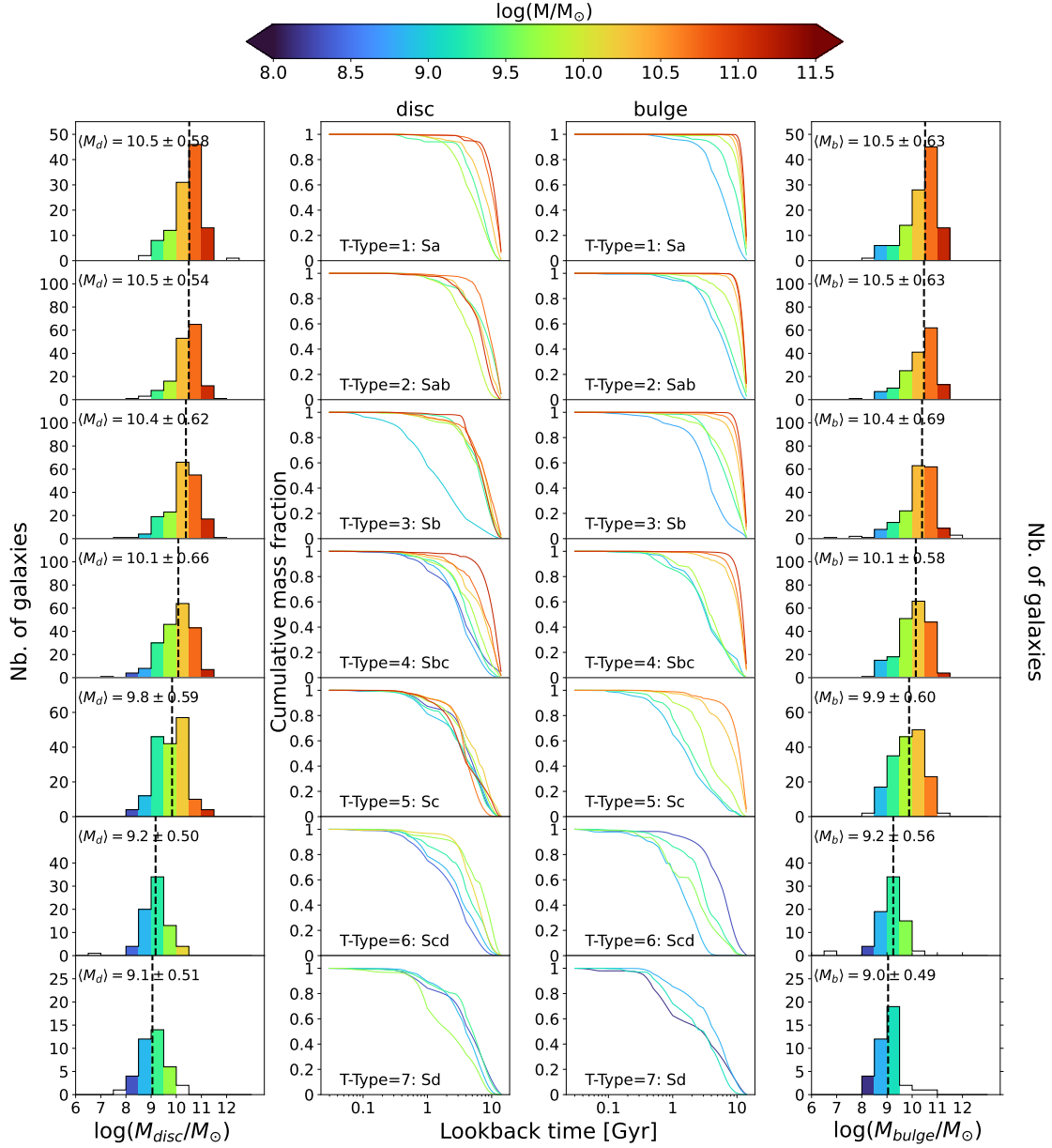


Figure 2.8: Dependence of MAH on component stellar mass. Left-most column: Disc mass distributions in increasing steps of morphological type (top to bottom panels). Right-most column: Bulge mass distributions in increasing steps of morphological type. The vertical dashed line is the median component stellar mass for each type. Centre columns: disc and bulge MAH curves stacked in every corresponding mass bin shown in the histograms. Histogram bins and MAH curves have the same colour-coding, marked by the median mass of bulges or discs in each bin. Bins containing 3 objects or less are shown in white on the histograms, and their corresponding MAH curves have been excluded.

matched to discard skewed or imbalanced inferences. In this section we will further investigate the effect of mass on the MAHs.

In order to look more closely at the dependence on the stellar mass of each component, we re-plotted Figure 2.6, but instead show the median-stacked MAH curves in 0.5 dex bins of logarithmic stellar mass. These binned curves are shown in the middle two columns in Figure 2.8, with the colours representing the median component mass within that bin. The MAH of any bin with 3 galaxies or less was not plotted to avoid effects of small number statistics. The left and right-most columns in this figure show the mass distribution histograms for the discs and bulges, respectively, using the same mass steps and colour-coding for each mass bin. The galaxies excluded in the MAH plots (bins with 3 objects or less) are still shown in the component mass distribution histograms in white. The black dashed line indicates the median of the respective component mass for each type, showing that both the mean bulge and disc mass becomes lower, moving from earlier to later type morphologies. This allows us to directly compare the stacked MAHs with their component distributions, and any type that does not have any objects in a particular bin simply does not show up in the plots in that corresponding colour. This allows our MAH plots to be mass-matched as we look at the curves of the same colour in different panels.

Starting with the **Sa type** spirals in the first row, we see the aforementioned downsizing effect clearly in the bulges as a smooth gradient. The bulges of intermediate - high mass (orange-red) have assembled their stars very early on (> 8 Gyr ago), and rapidly within a narrow timescale of the order of 1-2 Gyr. Moving to the low-mass bulges (green-blue), the mass assembly timescale increases successively, with them showing relatively prolonged star formation. Comparing to the discs in the same galaxies, this effect is still visible, but is strongly diluted. Overall, the most massive discs (red) do form first before the others; beyond this however, there is no consistent order to the disc assembly as a function of their mass. This result in both discs and bulges is seen again in **Sab type** spirals.

The downsizing trend is observed in **Sb type** spirals as well, but the bulges in the intermediate-high mass bins over $10^{10} M_{\odot}$ (orange-red) are more difficult to distinguish; they still do assemble earlier and faster than their less massive counterparts, however the order of assembly within these mass bins is less strict and harder to conclude. The discs might not show downsizing at the precision of the narrow mass bins, but the general trend of assembly still persists in the order of high-mass to intermediate-mass to low-mass discs (red-green-blue).

In the **Sbc type** spirals, the bulges continue to conform to this trend; additionally, at $\sim 10^{10} M_{\odot}$ (light green), there is a clear separation between high and low mass MAH curves - the more massive bulges (red-orange) appear to have assembled their stellar mass rapidly through a single star formation event. The less massive ones (green-blue) have taken longer over the course of 10 Gyr with more than one star formation episode, showing more extended assembly histories. This result complies well with the global mass assembly histories from the previous section, but this is the last morphological

type where the discs exhibit this trend.

The **Sc** type spiral bulges still show the downsizing trend for the intermediate-high mass bulges (orange-red), but for mass bins under $10^{9.5}M_{\odot}$, the MAH curves overlap and become harder to disentangle. The disc MAH curves are completely indistinguishable, where even the global downsizing effect begins to break down. Beyond this type, for the late **Scd** and **Sd** spirals, downsizing breaks down for both bulges and discs, and there appears to be no order in the stellar mass assembly of either component. These components show similar MAHs with longer delayed stellar mass assembly timescales with multiple star formation episodes. This might be a real result, or an effect of the faint bulges in these late-type spirals being technically difficult to recover. One must also note throughout these plots that objects below 10^9M_{\odot} and above $10^{11}M_{\odot}$ are rare compared to the other mass bins (see left-most and right-most columns in Fig. 2.8), and although their MAH curves are still shown, they are not statistically significant. We find that these global results of the mass-assembly histories and their stellar mass dependence obtained through spectra are in accordance with a similar (albeit less detailed) analysis with SDSS photometry, using the star-formation history parameter τ (the e-folding time). These results are presented in Appendix A.

The range of stellar mass assembly histories of the bulges and discs lends support to the idea that bulges residing in early and late-type spirals in the local Universe had been formed and grown through different mechanisms, and have a clear dependence on their stellar mass. The high-mass bulges in our sample always point to a fast and early mass assembly, which implies the formation of these entities through rapid or violent processes namely the monolithic collapse of a primordial gas cloud, or through major mergers. The low-mass bulges, on the other hand, are split between two cases: an assembly history that resembles the high-mass bulges (fast and early in Sa-Sab types), and one that resembles discs (slow or delayed, or both, with extended star formation episodes in Sb-Sd types). The latter suggests that the low-mass bulges were more likely formed from the discs through internal physical processes as well as environmental effects. While Fig. 2.8 displays the median-stacked mass assembly histories that help us identify statistically significant trends, Fig. 2.6 shows the signatures of both formation scenarios mentioned above in all morphologies, for each galaxy in the sample. It is also important to note that the presence of a composite-bulge system in some galaxies cannot be entirely discarded (Erwin et al., 2015), where the combined effects and properties are harder to disentangle, and could explain the range of mass assembly histories found in the bulges of spiral galaxies. Another theory that has been suggested in other studies is that a late-type galaxy bulge does not form purely through one of two scenarios but through a combination of both occurring on different timescales (Breda et al., 2018). A complement to this analysis by studying the stellar population properties of bulges and discs will be provided later in Sect. 2.7. In the line of the MAH analyses, the next step is to isolate the morphology trends, which is described in the following section.

2.6.3 Dependence on morphology

With the component masses binned the same way as in Sect. 2.6.2, we now separate the average mass assembly histories of the bulges and discs in each component stellar mass bin, as a function of morphological type (T-Type) in Figure 2.9. The bins increase in steps of 0.5 dex in logarithmic stellar mass vertically from top to bottom. In order to make the plots more readable and avoid over-plotting multiple curves, we bin the types into 4 major morphologies as Sa, Sab/Sb, Sbc/Sc, and Scd/Sd. The solid thick curves represent the bulge MAHs, and the thin dot-dashed lines represent the disc MAHs. In terms of morphological type, the Sa galaxies are marked in maroon, the Sab/Sb galaxies in orange, the Sbc/Sc galaxies in navy, and the Scd/Sd galaxies in grey.

In the lowest mass bin ($8 < \log(M/M_\odot) < 8.5$), the components do not appear to show any dependence with morphology - however, there are no Sa spiral discs in this mass bin. It might seem initially that despite a non-dependence on morphology, the discs have assembled their stellar masses prior to the bulges; however, this again might or might not be a skewed interpretation resulting from the fact that at these low masses, our sample simply has too few objects to statistically point to an outside-in assembly scenario.

The bulges do show a dependence on morphology - the Sa spirals consistently form first in all mass bins within $8.5 < \log(M/M_\odot) < 11$, followed by Sab/Sb, later by Sbc/Sc, and finally by the Scd/Sd types. With increasing mass, we also note that the timescale between formation of bulges of different morphologies becomes shorter at each step.

In the mass bin $9.5 < \log(M/M_\odot) < 10$, the morphology dependence of discs starts to appear, although there is significant overlap for a majority of their assembly histories especially at earlier lookback times when the age uncertainties dominate. In the mass bin $10 < \log(M/M_\odot) < 10.5$, this dependence becomes clearer and distinguishable between the early spirals and the late spirals (that is, the discs of types Sa-Sb have a clear earlier stellar mass assembly compared to types Sbc-Sd), although the morphology dependence is difficult to disentangle within these broader classifications. The dependence of the disc MAHs on morphology is best observed in the next two high-mass bins of $10.5 < \log(M/M_\odot) < 11$ and $11 < \log(M/M_\odot) < 11.5$, where the curves can be easily discerned and follow the same assembly order as the bulges as described earlier (Sa first, followed by Sab-Sb, then by Sbc-Sc). We note at these high masses of $\log(M/M_\odot) > 10.5$, our sample lacks components of the late Scd-Sd types, but nevertheless emphasise that still shows the same order of bulge and disc mass assembly in terms of morphology, for the ones that do exist. The final mass bin $11.5 < \log(M/M_\odot) < 12$ only contain galaxies of types Sab-Sb which show the general trend of an earlier bulge stellar mass assembly compared to the disc by several Gyr.

The downsizing trend is visibly justified looking at the decreasing assembly timescale with increasing mass steps, as the lines get steeper with increasing mass. The morphology dependence is evidently stronger for the bulges than the discs, where it only becomes apparent at higher masses.

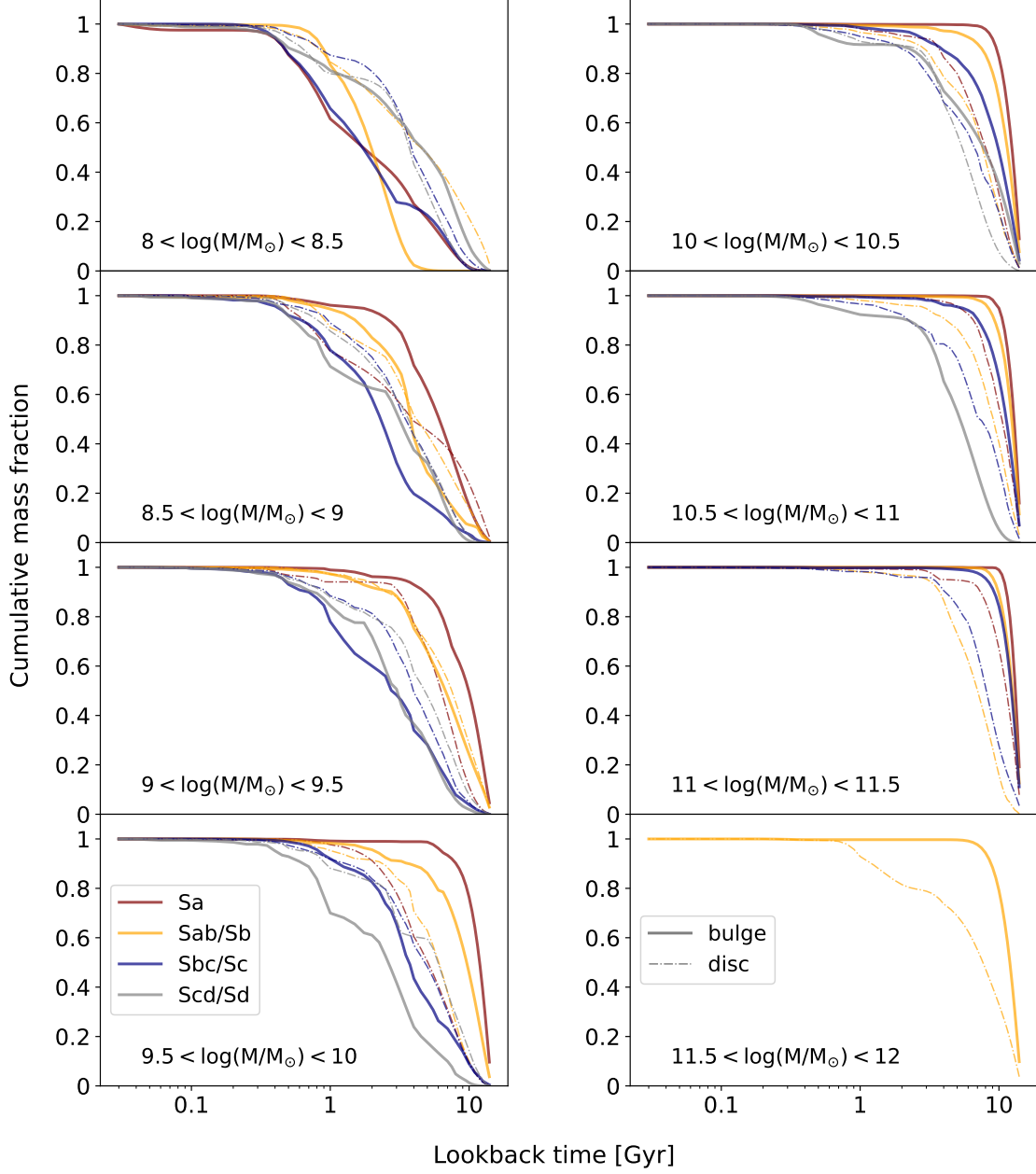


Figure 2.9: Dependence of MAH on morphology: Each panel is a stellar mass bin defined in the previous section, increasing vertically from top to bottom. The morphologies were binned and stacked to show median MAHs of types Sa (maroon), Sab/Sb (orange), Sbc/Sc (navy), and Scd/Sd (grey). The solid thick lines represent the bulges and the thin dot-dashed ones correspond to the discs.

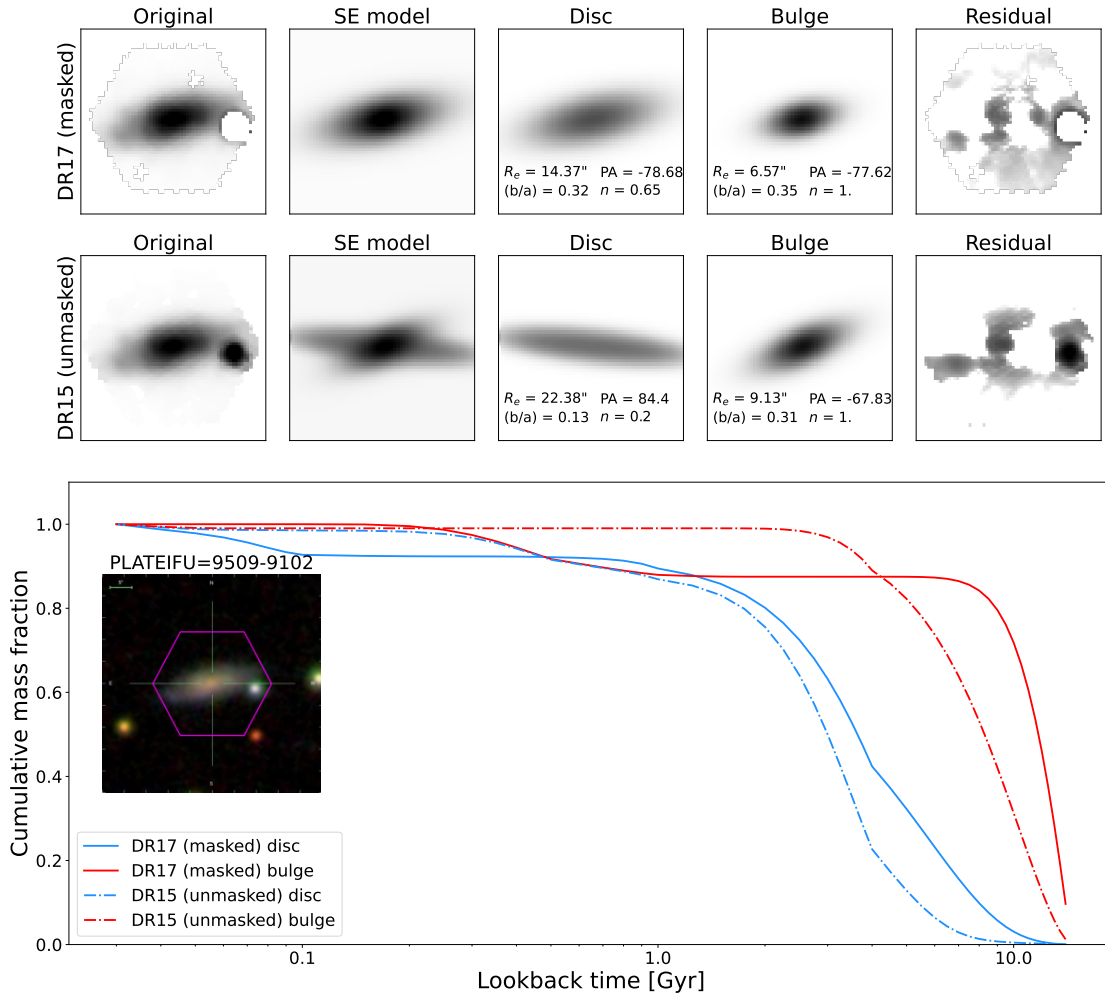


Figure 2.10: Bulge-disc decomposition of galaxy 9509-9102 from the previous BUDDI run on DR15 (second row) and current DR17, which includes a foreground star mask (upper row). The final panel shows the MAH of the bulge (red) and disc (blue) resulting from both fits (solid curves for DR17 and dot-dashed curves for DR15), along with an SDSS gri image of the galaxy with the MaNGA field of view (91 fibre IFU) superimposed in purple.

These results on the dependence of the mass assembly histories of bulges and discs on their respective stellar masses and morphologies, show that the primary driver is indeed the stellar mass. While the morphology definitively plays a role in determining the assembly mode, its dependence is relatively less substantial.

2.6.4 Effect of masking foreground stars

A significant improvement in the current DR17 version of BUDDI fits over the previous DR15 ones is that we have incorporated the masking of foreground stars in the field of view of the target MaNGA galaxies. In the fitting process with `GalfitM` (and by extension BUDDI), the magnitudes and structural parameters of the target galaxy can be altered due to the presence of a foreground star or a neighbouring galaxy if those are not taken into account properly. The Data Reduction Pipeline (DRP; Law et al., 2016) of all SDSS-MaNGA data releases includes foreground star masks that were created through

visual inspection by MaNGA team members. From DR15 however, these star masks were augmented by those created by citizen scientists in the Galaxy Zoo: 3D project (Masters et al., 2021). For more details on the project and the criteria used in identifying and creating foreground star masks, we refer the reader to Sect. 3.2 in Masters et al. (2021). The masks were created as a circle with a $2.5''$ radius (MaNGA PSF) around the clustered location marked by the volunteers. These masks identify and mask all stars that are visually deemed important enough to influence the output of the `GalfitM` fit significantly.

Figure 2.10 compares the masked and unmasked fit results and mass-assembly histories for the galaxy with MaNGA plate-IFU 9509-9102, which has an Sab type morphology. The upper row depicts the final BUDDI fits after the foreground star within the hexagonal field of view has been masked out, and the middle row shows the fits from the previous run where the star was included in the fitting process. The original datacube image is shown in the first column, followed by the combined Sérsic + Exponential model, the disc model, the bulge model, and finally the residual. All the images are collapsed along the wavelength direction to create the median white-light image. The fit parameters indicating the effective radius (R_e), the position angle (PA), the axis ratio (b/a), and the Sérsic index (n) for each component is shown in their respective panels. It is immediately apparent from these values, as well as the bulge model and the fit residuals, that the masking of this bright nearby star is essential to derive physically meaningful fit parameters, and consequently the spectra and MAHs. To show the effect of this mask on the MAHs, we compare the MAHs of the bulges and discs before and after masking out the star in the fits, in the lower-most panel in Figure 2.10. The solid blue and red curves indicates the MAHs of the disc and the bulge respectively, where masking is included, and the dot-dashed blue and red curves represent those where the star was not masked out. On the left, we also show the SDSS *gri* image of the galaxy with the hexagonal field of view superimposed on it.

From the disc model of the DR15 fit, it is clear that in the unmasked fit, `GalfitM` has tried to include the neighbouring star in the fit, resulting in an unusually extended light profile for the component, with a Sérsic index of 0.2 (which is also the lower limit of the fits) and R_e of $22.38''$ (which is the most unfeasible and significantly affected parameter). Moreover, the disc axis ratio ($b/a = 0.13$) suggests a highly edge-on galaxy, which is not the case as seen from the SDSS image and the MaNGA datacube. Since the foreground star appears very close to the disc, the fit has assumed it to be a significant part of the disc and has completely shifted the position angle of the disc in order to incorporate it. The bulge has also been modelled as an elongated component (with a large R_e of $9.13''$) that has incorporated the light from the true disc component of the galaxy.

In the new DR17 fit with the star masked out, `GalfitM` has modelled the bulge and the disc cleanly with a more physically motivated Sérsic indices of 1 and 0.65 respectively. The fit parameters of the discs are significantly changed compared to the DR15 fits. The position angle of the bulge and the disc have similar values as would be expected, as opposed to the DR15 fit, where they were oriented in opposite directions. The R_e for the

bulge and disc are also physically feasible with values of 6.75'' and 14.37'' respectively. Additionally, the estimated axis ratio for the disc is higher ($b/a = 0.32$) than for the unmasked fit, indicating the galaxy is not as edge-on as previously modelled. Finally, the combined SE fit has managed to cleanly model the light profile of the entire galaxy this time.

On comparing the MAHs between the two versions of the fits, we can see that although the general mass assembly order has not changed, they trace substantially different star formation histories. Moreover, through the unmasked fits, the stellar populations of both the bulge and disc are biased towards relatively younger stellar populations up to ~ 1 Gyr ago. With both the masked and unmasked fits, it appears that the bulge started assembling its mass first within a few Gyr after the Big Bang. The disc on the other hand, has had a more delayed and slower star formation starting after the bulge. However, for the unmasked fits, the bulge mass assembly history is more prolonged compared to one from the masked fits. Additionally, while the unmasked fits point to a single episode of star formation that built up the entire stellar mass of the bulge within a few Gyr, the masked fits instead show more recent star formation, as late as 0.3 Gyr ago. The disc mass assembly histories are similar for both the masked and unmasked fits up to a lookback time of ~ 0.5 Gyr, after which the new MAH suggests continued star formation leading up to current times, while the old MAH indicates that the stellar mass has already been built-up soon after.

The foreground star which is present at a different redshift than the target galaxy, adds a strong superimposed spectrum onto the disc spectrum due to their apparent proximity. The spectral features of the star would therefore appear in the disc spectrum at the wrong positions and can lead to a poor fit with pPXF. However, it must be noted that this example is not a global representation of all the galaxies in the sample with a foreground star, and that the results change depending on the apparent proximity of the star to the galaxy. We have visually inspected the effects of masking the star for ~ 100 randomly chosen objects from the GZ:3D catalogue, and find that in several cases where the star is at a sufficient distance from the bulge and the disc, even if it is present within the MaNGA field of view, only has a negligible effect on the MAHs. However, we rarely find cases where masking the star leads to a worse fit or poses a disadvantage. As such, we have decided to use the masked fits in all galaxies where they exist, for consistency. We observe that when the foreground star is in fact in close proximity to the galaxy such that it can affect the spectrum of either component, masking it out clearly improves the results of the fits. This agrees with the findings in Häussler et al., 2007. Therefore, masking foreground stars while fitting the galaxy components ultimately provides more accurate and physically motivated stellar populations and star formation histories.

2.7 Stellar population properties of bulges and discs

As described in Sect. 2.5.2, the mean mass-weighted stellar population properties of the bulges and discs were derived from pPXF after fitting the 'clean' spectra. In this

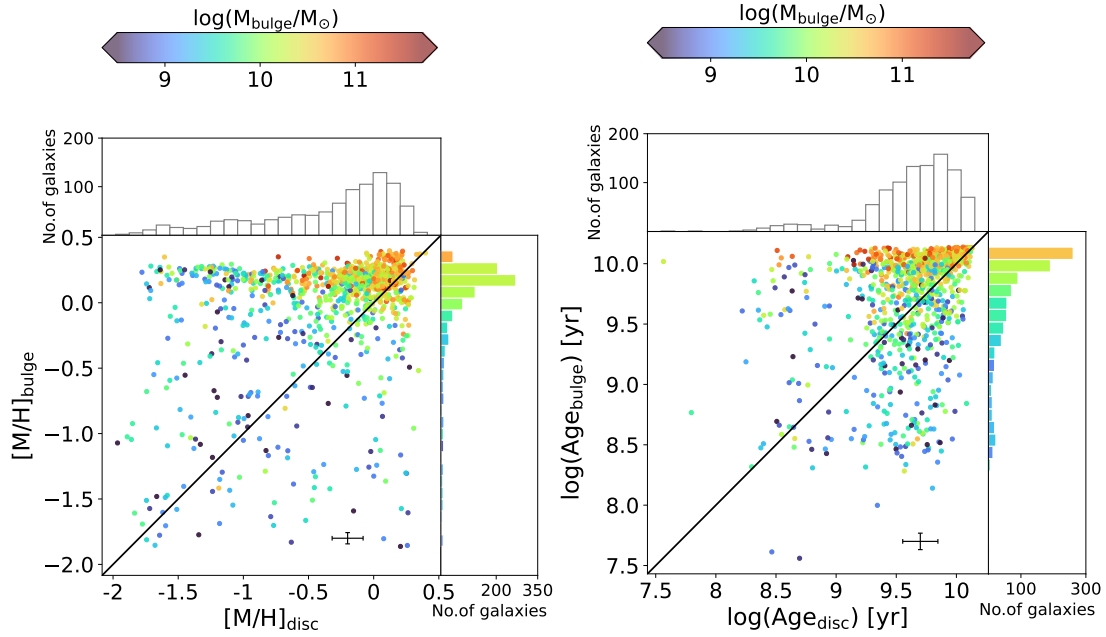


Figure 2.11: *Stellar population properties of bulges and discs along with their corresponding distributions. Left: Comparison of mean mass-weighted stellar metallicities of the bulges and discs, colour-coded by bulge stellar masses. Right: Same as the left panel, but for stellar ages. Joint histograms show the distributions in bulge and disc properties.*

section, we explore the dependence of these stellar population properties on stellar mass and morphology. In Figure 2.11, the upper panel compares the mean stellar metallicities of the bulges and the discs, colour-coded by the bulge mass. The error bars shown denote the median uncertainties for the sample as computed in Sect. 2.5.2.2. The black diagonal line marks the 1:1 correlation between them - above this line, the bulges have higher metallicities than the discs. The joint histograms show the distributions of the component metallicities (disc $[M/H]$ in the upper-joint panel and bulge $[M/H]$ in the right-joint panel). Furthermore, each bin in the bulge metallicities histogram is colour-coded by the median bulge mass in that bin, which allows us to highlight trends that might be hidden beneath the volume of points. The lower panel compares the mean logarithmic stellar ages of the bulges and discs in a similar way.

Figures 2.12 and 2.13 compare the stellar population properties of bulges and discs ($[M/H]$ in left panel of Fig. 2.12; ages in left panel of Fig. 2.13), colour-coded with respect to morphological type (early types in red to late types in blue). The violin plots in the next two panels study the stellar populations of the bulges and discs of each morphological type. The upper violins in red show the $[M/H]$ distributions (Fig. 2.12) and stellar age distributions (Fig. 2.13) of the bulges, while the lower violins in blue show those of the discs.

2.7.1 Trends in mass-weighted stellar metallicity

From Figure 2.11 (upper panel), for the whole spiral galaxy sample, we find that the bulges are in general more metal-rich. On average, we find the metallicity difference

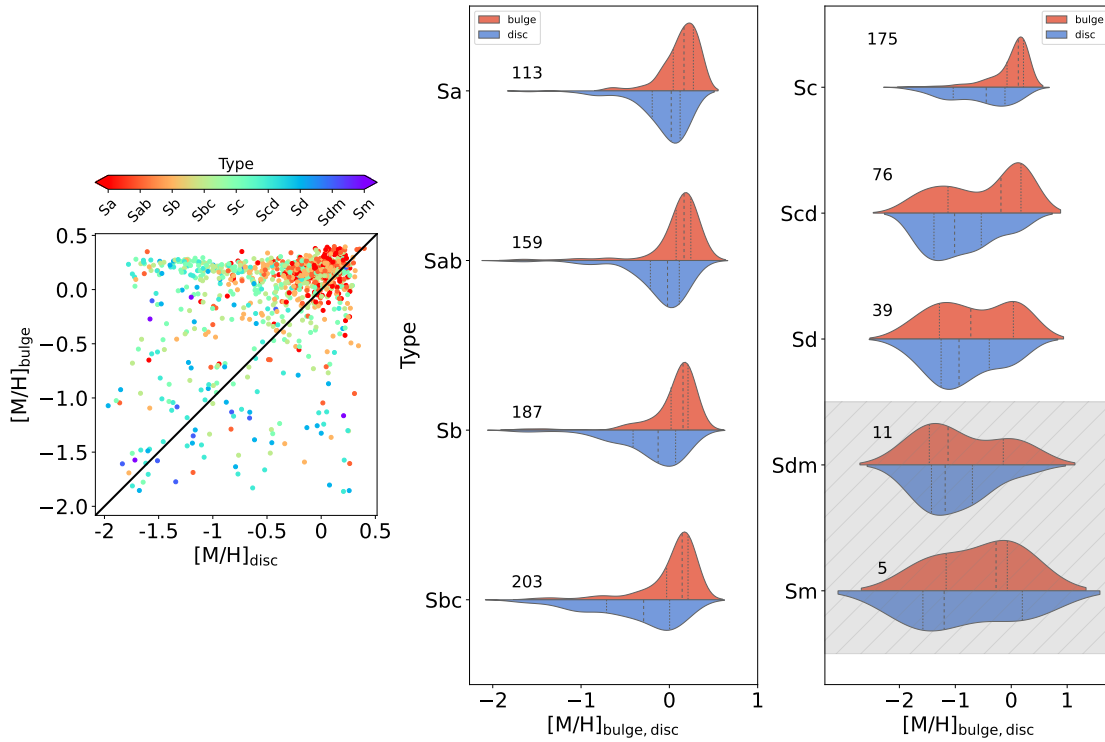


Figure 2.12: Comparison of bulge and disc metallicities and their dependence on morphology. Left panel: Bulge $[M/H]$ compared to disc $[M/H]$, colour-coded by the morphological type. The next two columns show split violin plots, with the upper half depicting the bulge metallicity distribution (red) and the lower half depicting the disc metallicity distribution (blue) in each type. The violin plots are marked with the median by the dashed black lines, and the quartiles are shown by the dotted lines. The grey shaded regions show the morphologies with very low-number statistics.

between the bulge and disc within the same galaxy to be ~ 0.34 dex. The high-mass bulges of $\sim M_{\text{bulge}} > 10^{10} M_{\odot}$ (red-orange points) almost all cluster above the 1:1 line, indicating these form the highest fraction of galaxies with bulges more metal-rich than discs. With decreasing bulge mass, the metallicities also appear to become lower, with those for the lowest masses of $M_{\text{bulge}} < 10^9 M_{\odot}$ (blue points) showing a broad range in metallicities. Below the 1:1 line, the majority of points show lower bulge masses. This trend is further highlighted by the right-joint histogram, where we can see that the bulge stellar metallicities correlate well with bulge stellar masses. The general trend is clear starting with the high-mass bulges (orange) on the high-metallicity end, towards the low-mass bulges (blue) on the low-metallicity end. These results emphasise the dependence of bulge stellar metallicities on the bulge mass, with the more massive bulges hosting more metal-rich stellar populations than the low-mass counterparts.

In Figure 2.12, the left panel shows that the majority of spirals (Sa - Sc types from red to light-blue) have the most metal-rich bulges and discs, and the bulges are significantly more metal-rich than the discs. However, due to the density of points and their plotting order, much of the trends are hidden. The violin plots in the figure provide a clearer depiction of the morphology dependence by splitting the metallicity distributions of the bulges and discs for each type. We note that the results mentioned above are

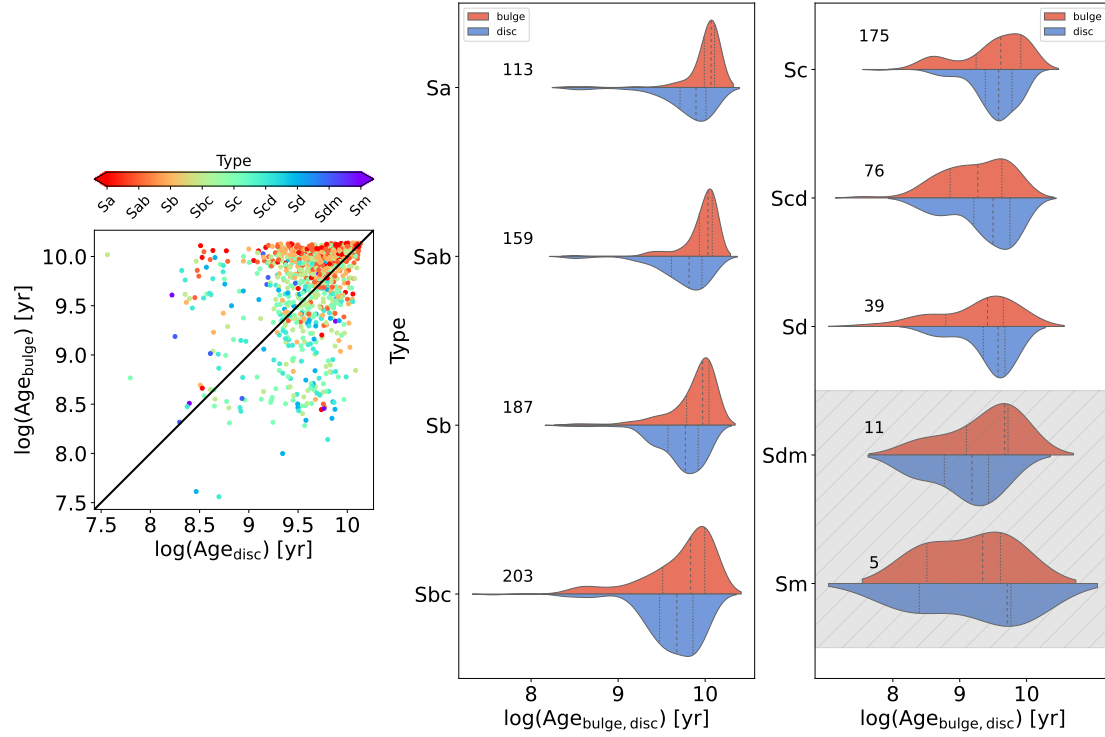


Figure 2.13: Comparison of bulge and disc stellar ages and their dependence on morphology. Left panel: Bulge $\log(\text{Age})$ compared to disc $\log(\text{Age})$, colour-coded by the morphological type. As in Figure 2.12 next two columns show split violin plots, with the upper half depicting the bulge age distribution (red) and the lower half depicting the disc age distribution (blue) in each type. The violin plots are marked with the median by the dashed black lines, and the quartiles are shown by the dotted lines. The grey shaded regions show the morphologies with very low-number statistics.

reproduced in the violin plots. For spiral galaxies from types Sa - Sc, the bulges are more-metal rich than the discs (shown by the median lines), with their difference increasing towards the later spiral galaxies (towards Sc). The discs start showing a wide range of metallicities and a clear tail towards lower values. For types later than this, the bulge metallicity distributions show a bimodality with peaks in the higher and lower $[M/H]$ ends, although for the very late types this result is limited by very low-number statistics (Sdm-Sm). However, the median trend still follows - although the bimodality in the bulges of late-type spirals is significant.

It can be seen in Figure 2.11 that $\sim 16\%$ of the discs and $\sim 7\%$ of the bulges of the spiral galaxies appear to have $[M/H] < -1$ dex. Such low metallicity ranges are more comparable to those found in low-mass galaxies ($M_* < 10^9 M_\odot$) than in spirals. There could be several potential reasons for these low metallicity estimates from pPXF. For example, in some cases, the S/N of the decomposed spectra are less than 20, which makes stellar population analysis with full spectral fitting more difficult (Zibetti et al., 2024). One potential cause of these noisy spectra could be particularly low or high bulge-to-total ratios. In this work, we considered the fits to be successful if the magnitude difference of the two components was between $0.1 \leq B/T_r \leq 0.9$. In photometric bulge-disc decomposition, the B/T light ratio is often selected to be more conservative (Häußler

et al., 2013; Nedkova et al., 2021; Häußler et al., 2022), where they recover very reliable structural parameters within $0.2 < B/T < 0.8$. While we justify our lower limit by using information from the entire wavelength range to derive a reliable fit, there can still be extreme cases where either the bulge or the disc component might be particularly faint, thus making it harder to measure the stellar populations reliably. Another effect that should be mentioned is the age-metallicity-extinction degeneracy. While full spectral fitting with pPXF is often considered to reduce this degeneracy relative to photometric colours or line strength indices, it may not remove the effect completely. Since the sample of galaxies presented here have spiral morphologies, a significant fraction of them likely contain dust discs. These dust discs might not be easily resolvable in the MaNGA data, but they could still affect the decomposed spectra by leading to artificially low values of metallicity. The above-mentioned effects can dominate individually in either component in the spectral fitting process or combined to a point that they cannot be disentangled. Therefore, we add a word of caution towards interpreting these estimates as absolutes. Even so, the general statistical trends we have highlighted hold despite the caveat.

2.7.2 Trends in mass-weighted stellar age

From Figure 2.11 (lower panel), the bulges are in general older than the discs. On average, we find the stellar age difference between the bulge and disc within the same galaxy to be ~ 1.7 Gyr. We see a clear trend with respect to the bulge ages, with the most massive bulges (red-orange points) being the oldest, which again cluster together above the 1:1 line. Moving towards intermediate and low-mass bulges, their ages become younger as well. This trend is emphasised in the right-joint histogram, starting with the high-mass bulges (orange) that are older, towards the low-mass bulges (blue) that are younger. The dependence of the stellar populations on bulge mass is stronger for the stellar ages than for the metallicities as shown in the histogram.

In Figure 2.13, the left panel shows clearly that the early spirals from Sa - Sb have the oldest components, and host bulges that are older than their corresponding discs. However for the later types from Sbc - Scd, the points appear to be spread out across a range of ages. There is a significant number of galaxies that lie below the 1:1 line, indicating the presence of a second population with discs older than their bulges. This result again follows through in the different T-Types shown by the violin plots in the next two panels. For types Sa-Sc, the bulges are consistently older than the discs on average, as shown by the median lines. Beyond this, the trend seems to shift with discs appearing to be older, until the very late-types where we hit too low numbers to reach conclusive results. The bulge distributions fall steeply off at the higher end of stellar ages, while showing a tail towards lower values. The discs show a broader range in stellar ages than the bulges (except for Scd and Sd types), reflecting their different, more extended star formation histories compared to the bulges. However, we note that the stellar age determination beyond 8 Gyr has been often found to be highly uncertain (Ibarra-Medel et al., 2016; Ibarra-Medel et al., 2019).

Although we do not show the dependence on disc mass in the plots, we find very similar general trends with more massive discs hosting older and more metal-rich populations compared to their low-mass counterparts. Finally, these trends in stellar population properties of the bulges and discs with both stellar mass and morphology reflect different formation mechanisms for each component. For instance, a high fraction of bulges are old and have high masses, and appear to have assembled the majority of their stellar masses early on in their lifetimes. However, a smaller but significant fraction of bulges and discs show the opposite trend, or show similar stellar populations in both, reflecting a slower mass assembly in these components. The possible reasons for this will be explored in the discussion.

2.8 Discussion

In the series of papers based on BUDDI-MaNGA, Paper I (Johnston et al., 2022a) introduces the project and describes the technical details behind modelling bulges and discs of galaxies from IFU datacubes in order to cleanly extract their spectra. Consequently, it provides an overview and characterisation of the first fits to the BUDDI-MaNGA sample built from DR15, along with statistical and reliability tests. Paper II (Johnston et al., 2022b) presents the first scientific results centred on the S0 galaxies in the BUDDI-MaNGA DR15 sample. It probes the stellar populations of the bulges and discs in these galaxies, and how their star formation histories trace their origins and evolutionary pathways. In this paper, we further build on our sample size with the final release of SDSS-MaNGA DR17 and improve the fits by masking the neighbouring foreground stars. We have nearly doubled the number of galaxies in this latest version to 1452 objects (with SE fits for all morphologies available) in the final sample, and undertake a follow-up study by tackling the sample with the highest morphological frequency: the spiral galaxies. Through full spectral fitting with pPXF, the mass-weighted stellar metallicities and stellar ages of the two individual components are estimated for 968 spiral galaxies, along with their mass assembly histories, to help unravel a picture of their formation and evolution. It must be noted that in both versions of the fits, there is an inherent selection bias towards the high-mass galaxies because our initial sample selection criterion is to use only those galaxies that were observed with the two largest IFU sizes (91 and 127 fibre IFUs), which consequently does not sample the low-mass systems (Johnston et al., 2022b) as well as the high-mass ones (see Fig. 2.1).

Our analyses and results target the mass-assembly histories of bulges and discs as a function of their respective stellar masses and morphology, emphasising the trends they exhibit individually as well as globally. We complement these results by analysing the properties of stellar populations hosted by bulges and discs and similarly their dependence on stellar mass and morphology. Throughout this paper, we only focus on the mass-weighted stellar populations, which trace the evolutionary history of the galaxies and are not badly affected or biased by recent star formation. In this section, we further explore these results from Sect. 2.6 and 2.7 and compare them

with several related works in literature. We examine the physical drivers behind the stellar populations and mass-assembly histories that we observe today in the bulges and discs of spiral galaxies, and how they fit into the broad picture of galaxy formation and evolution.

2.8.1 Implications on galaxy stellar populations

From Figures 2.12 and 2.13, we find that our sample can mostly be split up into two (major) different stellar populations - one with bulges that are older and more metal-rich than discs, and one with bulges that are younger and more-metal rich than discs - which are both discussed in detail below. In this section, we discuss certain trends in terms of the total galaxy stellar mass (defined here as the simple sum of bulge and disc stellar mass for a galaxy), so that it fits in the context of the literature.

Case I: Galaxies with older and more metal-rich bulges. For the full spiral galaxy sample, our results show that this sample is dominated by bulges that are more metal-rich than their disc counterparts. On average, $\sim 68\%$ of the spiral galaxies contain older bulges than the discs, $\sim 79\%$ contain more metal-rich bulges than the discs, $\sim 51\%$ contain both older and more metal-rich bulges. This trend agrees with many studies in literature for S0s and spirals (MacArthur et al., 2009; Sánchez-Blázquez et al., 2011; Johnston et al., 2012; Johnston et al., 2014; Sánchez-Blázquez et al., 2014; Goddard et al., 2017; Breda et al., 2018; Barsanti et al., 2021; Parikh et al., 2021; Johnston et al., 2022b). However, it must be noted that most of these studies compare the stellar populations of bulge and disc-dominated regions of the galaxy measured in terms of radii rather than the bulge-disc decomposition approach we take in this work.

Our stellar age and metallicity results also point to a dependence on total galaxy stellar mass. By dividing the sample into 4 mass bins, we find that $\sim 53\%$ of the galaxies in the lowest mass range $M_* < 10^9 M_\odot$, have older bulges than discs, although this bin only has 19 objects (low-number statistics). For $10^9 M_\odot < M_* < 10^{10} M_\odot$, this population makes up $\sim 40\%$ (the younger bulges dominating this mass range are discussed later in this section). In the mass bin $10^{10} M_\odot < M_* < 10^{11} M_\odot$, the fraction of older and more metal-rich bulges increases to 74% , and for galaxies with $M_* > 10^{11} M_\odot$, this further reaches a maximum at 96% .

A similar (total) galaxy stellar mass binning to investigate stellar metallicities shows that out of the galaxies with $M_* < 10^9 M_\odot$, $\sim 68\%$ host bulges that are more metal-rich than discs. This fraction increases with galaxy stellar mass, with $\sim 72\%$ in the mass bin $10^9 M_\odot < M_* < 10^{10} M_\odot$, $\sim 82\%$ in $10^{10} M_\odot < M_* < 10^{11} M_\odot$, and $\sim 87\%$ for galaxies with $M_* > 10^{11} M_\odot$.

The relatively high metallicity in the majority of the bulges can be explained on the basis of the depth of the gravitational potential well (Barone et al., 2020; Lah et al., 2023). The bulges, having a deeper potential well, can retain their metals more strongly than the discs, whose shallower potential makes it easier to lose their metals to the intergalactic

medium. The metallicity difference between the bulge and the disc $\Delta[M/H]_{\text{bulge-disc}}$ is fairly constant within their error bars, for galaxies of stellar masses over $10^{10}M_{\odot}$, but show no significant trend. Below this mass, our sample has relatively fewer galaxies, and shows a wider range in $\Delta[M/H]_{\text{bulge-disc}}$. This result also agrees with Domínguez Sánchez et al. (2020), where they find a lack of metallicity trends for galaxies over $3 \times 10^{10}M_{\odot}$. However, contrary to us, they find strong metallicity gradients for low-mass galaxies in their sample. For the very early type spirals (Sa and Sab), these stellar populations could potentially signal a phase of their evolution as they transform to S0 galaxies. S0s are considered to be an endpoint in the evolution of spiral galaxies once the gas has been used up or stripped away and the star formation truncated. However, in order to better understand this transformation, we must first understand the properties of the bulges and discs in the progenitor spirals, as we explore in this study. An inside-out quenching scenario has been proposed in Mendel et al. (2013), Tacchella et al. (2015), and Barsanti et al. (2021), where star formation is shut off first in the bulge as a result of AGN feedback or halo quenching through the mechanisms described in Sect. 2.2. The quenching phase then propagates outwards from the bulge across the disc, which eventually leads to a morphologically transformed galaxy - an S0 - with a bulge older than the disc.

Our sample of spiral galaxies shows older stellar ages for bulges than for the discs, for galaxies of stellar masses above $10^{10}M_{\odot}$. This agrees with results obtained in previous studies (Sánchez-Blázquez et al., 2014; Goddard et al., 2017; Fraser-McKelvie et al., 2018; Pak et al., 2021; Johnston et al., 2022b). This is often explained by the fact that discs have ongoing star-formation fuelled by accreting gas, while star-formation has long ceased in the bulge. Similar to the metallicity differences, for masses below $10^{10}M_{\odot}$, there are fewer galaxies but those show a wider range of stellar age differences between the bulge and the disc.

Case II: Galaxies with younger and more metal-rich bulges. As we noted in Sect. 2.7, although the older and more metal-rich bulges dominate our sample, there is a significant fraction of galaxies that host a different stellar population - with younger and more metal-rich stars in the bulge compared to the disc, forming $\sim 28\%$ of the sample. In our sample, this fraction appears to depend on morphology, and increases steadily with each type - with $\sim 5\%$ in Sa spirals and ending with $\sim 57\%$ in Scd spirals. This coincides well with the findings in Barsanti et al. (2021), where they study the stellar populations of bulges and discs of S0 galaxies. Bedregal et al. (2011) find that the presence of a galaxy population exhibiting a bulge that is younger and more metal-rich compared to its disc suggests that the bulge has experienced more recent star formation, fuelled by enriched material, in contrast to the disc where star formation activity has ceased. Along those lines, Johnston et al. (2014) suggest that the bulge in similar S0 galaxies has been fuelled by enriched gas, inducing more recent star formation activity there. They propose that while the disc is being quenched, the gas collapses towards the inner regions of the galaxy, and incites a final episode of star formation, which biases

their mean luminosity-weighted stellar populations in the bulge towards younger ages. Another possibility is presented in [Coelho et al. \(2011\)](#), where they find by comparing the ages and metallicities of bulges hosted by barred and non-barred galaxies, that bars play a significant role in funnelling gas from the disc along the bar towards the central bulge. This induces a new episode of star formation there, pushing the observed stellar populations towards younger ages. However, given the low spatial resolution and field of view in MaNGA, modelling reliably a third component representing the bar would prove difficult, especially in an automated fashion as for BUDDI-MaNGA. Therefore, we continue with the simple two-component model for this work. For further investigation on the properties of bars as an independent component of the galaxy, and the effect they could have on the relative stellar populations of bulges and discs would be better studied using other IFUs with a better spatial resolution such as MUSE. However, this is beyond the scope of the BUDDI-MaNGA project.

Another possible reason for this trend has been discussed and debated extensively in the literature as the presence of ‘pseudo-bulges’ in these galaxies. These disc-like pseudo-bulges are often the result of a steady and secular evolution of the disc over sufficiently long timescales with star forming episodes up to recent times, leading to the formation of a central bulge (although only named such because this component is more centrally concentrated than the disc) that mimics the properties of the precursory disc. These pseudo-bulges have been found to contain sufficient amounts of cold gas needed to build up its stellar mass through continued star formation, fuelling their internal evolution ([Gadotti et al., 2001](#); [Kormendy et al., 2008](#); [Peletier, 2008](#); [Erwin et al., 2015](#); [Kormendy, 2016](#)). Hence, these bulges would be expected to be relatively younger on average or have similar ages to their corresponding discs. In our work, we do not explicitly classify the bulges as classical or pseudo since most criteria in literature involves an arbitrary selection cut in Sérsic index, which can lead to significant mixing considering not all literature agree on the exact selection cut. Furthermore, [Häußler et al. \(2022\)](#) find that while modelling galaxies with Galfit and Galfit^M, the Sérsic index is the hardest structural parameter to accurately recover, and hence cannot be reliably used to separate different bulge types. We concede that bulges do not come in distinct classes, but rather exist on a spectrum with the possibility of more than one kind of bulge existing in a galaxy ([Erwin et al., 2015](#)). Furthermore, it is plausible that a fraction of the galaxies in our sample also host such a composite bulge system containing different stellar populations, although this is much harder to disentangle.

In that vein, [Breda et al. \(2018\)](#) determine the driving mechanisms behind the formation of bulges in late-type galaxies, and subsequently discuss the validity of the distinctness of classical and pseudobulges. Their sample consisted of 135 late-type galaxies in the CALIFA survey, on which 2D spectral modelling had been performed, alongside surface photometry of their corresponding SDSS images. In accordance to the results presented in this work, they find that the most massive bulges host the oldest and most metal-rich stellar populations. The mass-weighted stellar ages and metallicities of the bulges and discs showed a homologous increasing trend with the

galaxy stellar mass. For the lowest-mass galaxies, the bulges and the discs exhibited nearly indistinguishable stellar population properties. In the higher mass galaxies, the bulges were clearly older than the discs, having formed $\sim 2 - 3$ Gyr earlier (readers can refer to their Fig. 7), consistent with our results. On observing the difference between the stellar age of the bulges and the discs as a function of galaxy stellar mass, they found a strong positive trend. A weaker but significant positive trend was observed for the metallicity difference as a function of galaxy mass. They also find no evidence of an age bimodality that would confirm the existence of two distinct bulge populations; they imply instead that bulges and discs evolve parallel to each other. For a more exhaustive list of the various stellar populations gradients and trends observed in various studies, we refer the reader to the appendix in [Lah et al. \(2023\)](#).

2.8.2 Implications on galaxy assembly: downsizing and growth from the inside-out

We have studied the mass-assembly histories of bulges and discs of our spiral galaxy sample independently as a function of their respective component stellar masses and their morphologies (type). The bulges, especially in early-type spirals show a prominent downsizing trend, with the stellar populations in high-mass bulges having assembled notably earlier than those in their low-mass counterparts. In discs, the downsizing effect is diluted but still exists in the earlier types, and breaks down in the later types (Fig. 2.6 and Fig. 2.8). This downsizing trend we observe in our sample complies with the results of previous studies in a qualitative sense, although a direct quantitative comparison would not be possible owing to the differences in methodologies and galaxy samples employed in each study.

For all the spirals in our sample of (total) galaxy stellar mass $M_* < 10^9 M_\odot$, the discs appear to have assembled half their stellar masses approximately $0.12^{+7.3}_{-6.5}$ Gyr before the bulges did. Similarly, galaxies in the mass range $10^9 M_\odot < M_* < 10^{10} M_\odot$ on average have assembled half the mass in their discs $0.89^{+4.4}_{-5.4}$ Gyr before their bulges. These low mass galaxies are the most diverse in terms of their MAHs and therefore the median is only a rough estimate of the time window between bulge and disc mass assembly, but nevertheless points to an outside-in assembly scenario on average. However, considering the high uncertainties on recovering stellar ages beyond 8 Gyr ([Ibarra-Medel et al., 2016](#); [Ibarra-Medel et al., 2019](#)), some of these galaxies might inherently have gone through an inside-out assembly or simultaneous bulge and disc assembly, which is also suggested from the diversity of MAHs in the components of these low mass galaxies. Higher mass galaxies within the range $10^{10} M_\odot < M_* < 10^{11} M_\odot$ show a clear inside-out assembly mode with a half-mass formation time difference of $2.02^{+6.6}_{-1.8}$ Gyr. The inside-out assembly is the most pronounced in the galaxies of the highest stellar masses: $M_* > 10^{11} M_\odot$ with the discs having assembled half their masses by about $4.5^{+9}_{-0.9}$ Gyr on average after the bulges did. As we can see from the uncertainties denoted by the 16th and 84th percentiles of the timescale distribution, these median timescale estimates

are rough and do not represent the diversity of MAHs in their entirety. It must be noted at this point that while these MAHs trace the time when the stellar populations have assembled, they do not give us any information on their origin, that is, whether they are stars born in situ in the gravitational potential of the galaxy, or if they are ex situ stars accreted in mergers.

From Figure 2.9, our results indicate the MAHs of bulges and discs depend moreover on the morphological types. The later-type spiral galaxies show no clear distinction between the disc and bulge star formation histories, with a much lesser dependence on their stellar masses as compared to the early-type spirals. Additionally, these galaxies lie in the low-mass regime of our sample and could imply that their bulges and discs have varied mass assembly histories with either inside-out or outside-in modes. A single assembly mode might dominate consistently throughout the lifetime of a galaxy, or different modes might dominate at different epochs which is also implied by some bulge and disc MAHs transitioning after some Gyr. Some of these bulges and discs could have formed together from the same material, over similar extended timescales, with several bursts of star formation throughout their lifetime. However, there is also the possibility that these late-type galaxies are in fact bulge-less and our assigning two components consistently for all galaxies in the sample results in similar mass-assembly histories for these in particular. Although a quantitative flagging of galaxies that are best represented by a single-component model or a two-component model is beyond the scope of this paper, we plan to address this in future work.

The inferences from our study regarding the formation pathways of galaxies match those from Pérez et al. (2013), where their sample of galaxies were found to have grown their stellar mass from the inside-out. With 105 objects from the CALIFA survey, they employ the fossil record method to reconstruct spatial mass growth histories across cosmic time. The spectra were extracted in four spatial galaxy regions from the centre to the outskirts, defined as a function of the half-light radius R_{50} . This pivotal study was the first to present evidence of galaxy downsizing using integral field spectroscopy (IFS). The mass growth histories were quantified by the time it takes for 80% of the stellar mass to have been built up. They found that the outer-most regions of less massive galaxies had reached this mass fraction as recent as about 1 Gyr ago, while the more massive ones had reached the same fraction almost 5 Gyr ago - clearly indicating that the downsizing phenomenon depends on the galaxy stellar mass. Their results support the inside-out formation theory, where the stars had assembled in the inner regions much earlier than in the outer regions. However, at galaxy stellar masses $M_* < 10^{9.58} M_\odot$, they observe a transition to outside-in formation similar to that observed in dwarf galaxies. In the framework of formation pathways, they propose that the high-mass galaxies had grown their stellar masses in the inner regions first as a result of a merger event about 5 – 9 Gyr ago, while the lowest-mass galaxies had instead undergone a steady secular evolution, a result that is supported by our findings as well.

Our results also qualitatively confirm the findings in Ibarra-Medel et al. (2016), where the primary focus was of a similar nature to understand how galaxies assembled

their stellar masses, using SDSS-MaNGA DR13. With the spatial information available, they studied the mass growth histories (MGHs) at different radial regions up to $1.5R_e$, as a function of galaxy stellar mass and morphology. Moreover, they also probed the assembly as a function of other galaxy properties such as specific star formation rate and colour. The difference in methodology is that we use distinct bulge-disc decomposition cleanly separating out the spectra from each component, while they separate the galaxies into ‘inner’ and ‘outer’ regions in relation to the half-light radius. Nevertheless, they find that the more massive a galaxy is, the earlier is its assembly (quantified by the 50%, 70%, and 90% mass formation time, which they define as the LBT difference between the inner and outer regions when the MGH reaches these percentages of stellar mass). They also find a large diversity and scatter in the assembly histories of dwarf and low-mass galaxies, with more extended and episodic star formation. In terms of the assembly mode, the innermost regions of most of their galaxies had assembled their stellar populations before the outermost regions, pointing to the inside-out formation mode as in ours. Another difference between our analyses is that they study the dependence of MGHs on the galaxy stellar mass, while we note the dependence on the component stellar mass (how the bulges assemble as a function of bulge stellar mass, and similarly for the discs).

Another similar SDSS-MaNGA study is described in [Peterken et al. \(2020\)](#), where they built the spatially resolved star-formation histories using the full-spectrum fitting software STARLIGHT ([Cid Fernandes et al., 2005a](#)). Their approach involved creating time-slice maps, which allowed them to look at regions where stellar populations of any given stellar age are present. For their sample of 795 spiral galaxies, they again find clear evidence for inside-out galaxy growth, with a negative age gradient. The outskirts of the galaxies are consistently younger than the central regions in 80% of the sample for galaxies of stellar mass $M_* > 10^{10.22} M_\odot$. They complement this result by defining the formation time as when 95% of the total galaxy mass was assembled in each region of the time-slice, which decreases radially from the centre. This mode of galaxy growth becomes predominant at the highest masses, in line with our generalised results.

[Breda et al. \(2018\)](#) (described earlier in Sect. 2.8.1), in accordance to the results presented in this work, find that the most massive bulges are hosted by massive late-type galaxies ($M_* \gtrsim 10^{10.7} M_\odot$). They note that the timescale of mass assembly is shorter for the most massive bulges compared to the less massive ones, which assemble their masses over longer timescales. Furthermore, the high-mass bulges are found to be on average older than their low-mass counterparts by ~ 4 Gyr, where the galaxy component downsizing is clear. They also find evidence of the oldest bulges being hosted by the oldest discs. The authors suggest that bulge growth is driven by a combination of faster and earlier processes namely a monolithic collapse, and slower secular processes. In this scenario, the bulges and discs are expected to grow and evolve in an interwoven fashion, with the bulge assembling out of the parent or hosting disc. The bulge might then continue to grow through processes such as inward stellar migration. This interpretation also implies that the Sérsic index of the bulge increases with galaxy stellar mass, which is

mirrored in our study (Appendix B). We therefore observe that there are clear similarities in the results of the stellar population analysis and formation mechanisms of bulges observed in this study and the present one.

Our results also tie in with the findings in McDermid et al. (2015), where they present a similar analysis on the ETGs in the IFU survey ATLAS^{3D} (Cappellari et al., 2011). The goal of their work was not to study the bulge and disc components or the inner and outer regions of the galaxies, but rather their star formation histories and stellar populations as a whole, as a function of dynamical mass and environment. Nevertheless, they find that the SFH depends on the present day dynamical mass of the galaxy for their sample, and that global galaxy downsizing prevails - the more massive galaxies had been formed much earlier than the less massive galaxies. Furthermore, they also measure the mean SFR and SFR density which allowed them to conclude that in ETGs the less massive galaxies display more extended star formation histories, while in the most massive ones, the star formation rapidly falls off leading to quiescence. They quantify the stellar mass assembly by their half-mass formation time and find that their most massive galaxies ($10^{11.5}M_{\odot} < M_{\text{dyn}} < 10^{12}M_{\odot}$) have formed their stellar populations by 2 Gyr after the Big Bang. On the other hand, the least massive galaxies in their sample ($10^{9.5}M_{\odot} < M_{\text{dyn}} < 10^{10}M_{\odot}$) only finish assembling 50% of their masses by 8 Gyr after the Big Bang.

In line with ETGs, Johnston et al. (2022b) was a precursor to this work, which used BUDDI for bulge-disc decomposition of S0 galaxies in SDSS-MaNGA DR15, and whose procedure of estimating mass-weighted stellar populations and mass assembly histories using pPXF we have followed here. Consistent with the literature listed above and the current work, they find primarily an inside-out formation scenario for high-mass S0s with $M_{*} > 10^{10}M_{\odot}$. The bulges assemble their stellar populations first rapidly, and the disc follows with a diverse range of star formation histories extending up to recent times. In the lower-mass galaxies, they find no evidence of a consistent mass assembly mode, owing to the diversity in SFH. However, their results support downsizing in bulges with respect to the total galaxy stellar mass, while the discs show no evidence of this, at least in the S0 galaxies they examined. We also note that their sample size is much smaller, with only 78 galaxies, so these differing inferences could be real in that spiral galaxies and S0s inherently do not have the same assembly pathways, or instead just be the result of a lack of a statistically significant sample. While our results here support downsizing in both bulges and discs, albeit at a weaker level in the discs, they are studied in terms of the component masses and not the total galaxy stellar mass as they do.

More recently, a study based purely on imaging data from GAMA, (Bellstedt et al., 2023) found results that are in accordance with ours in this work. In their approach, they used ProFuse, which is another spectro-photometric technique (where the spectral aspect encompasses the UV to the far infrared) that models the 2D surface brightness profile of galaxy components in multiple wavelengths simultaneously and derives their stellar populations, by combining both structural decomposition and SED fitting. This technique is fairly similar in concept to BUDDI. With ProFuse, they model a sample of

7 000 galaxies in GAMA to study the cosmic star formation history (CSFH) of bulges and discs. They found that the stars in the discs had formed relatively recently within the last 8 Gyr. The bulges were found to host the oldest stellar populations, where a majority of the stellar mass had been formed 11.8 Gyr ago. The CSFH that were reconstructed with ProFuse (simultaneous profile fitting and SED fitting) was also consistent with that derived from SED fitting with ProSpect (each step done consequently). This agreement among the different techniques (including BUDDI) in deriving the general stellar populations of bulges and discs emphasises the reliability of all these techniques and our understanding of when the different components assembled their stellar masses.

To recap, previous IFS-based studies on inside-out galaxy assembly, and galaxy and component downsizing, and the dependence of these phenomena on stellar mass (Pérez et al., 2013; Breda et al., 2018; Johnston et al., 2022b) is consistent with the insights from the present study.

2.9 Conclusions

In summary, we have performed bulge-disc decomposition of integral-field spectroscopic observations and extracted the clean spectra of both components for 1452 galaxies in SDSS-MaNGA DR17. Following this, for the spiral galaxy sample of 968 objects, we derived the mean mass-weighted stellar populations hosted by each component through full spectral fitting using pPXF. With the mass weights obtained during the spectral fitting, we have traced the mass-assembly histories of the bulges and discs through cosmic time, and investigated their dependence on component mass and morphology. Our main findings are listed below:

- Through the fossil-record analysis, we find evidence of a clear global downsizing trend in terms of the component stellar masses, for spiral galaxies of types Sa-Sc. The effect is more prominent in bulges and is diluted in the discs. For the late-type spirals Scd-Sd, downsizing breaks down and the mass assembly becomes more random on average.
- We find that bulges on average assemble their stellar masses rapidly, possibly in a single episode of star formation, during the very early stages of their lifetime. The discs however take longer to assemble their masses with more delayed and extended star formation histories. This effect is also entangled with the morphology dependence, where with increasing types, the bulges also begin to show a larger fraction of extended mass assembly. By the latest spiral types Scd-Sd, almost all galaxies show similar delayed mass-assembly histories in their bulges and discs.
- The individual mass-assembly histories of the bulges and discs were quantified by the half-mass formation time, in which 50% of the stellar mass has been built up by the respective component. The MAHs had a clear dependence on both stellar masses and morphologies. From Sa-Sc types, the main mode of mass growth is from the inside out, and by separating into four total galaxy stellar mass bins,

we find this mode to be strongest in the most massive galaxies. For the late-type spirals Scd-Sd, it becomes harder to identify a specific formation mode and they rather show a large diversity in their MAHs, suggesting different epochs where different assembly modes are prevalent.

- The above-mentioned result is also complemented by stellar population analysis. The majority of spiral galaxies contain bulges that are older and more metal-rich than the discs. A smaller but significant fraction contain bulges that are younger and more metal-rich than their discs, and this trend becomes stronger with increasing morphological types.

In conclusion, this work is the third paper within the BUDDI-MaNGA project, where we present the results from the newest version of the fits with SDSS-MaNGA DR17. The galaxies were modelled with a Sérsic + Exponential profile for the bulge and disc, respectively, with the added advantage of incorporating masks for neighbouring foreground stars to improve the fits from the previous version described in Paper I and Paper II. This forms the largest sample to date of 1452 clean bulge and disc spectra derived from IFU datacubes, allowing detailed statistical analyses of their stellar populations. Our results suggest that spiral galaxies in general assemble their stellar mass through the inside-out pathway, but it is not the sole mode of assembly. Furthermore, our results also show two major stellar populations, with bulges being older or younger and more metal-rich than their discs, again suggesting more than one pathway of stellar mass assembly in spirals. This spectroscopic study of spirals is one of several within BUDDI-MaNGA, the goal of which is to better understand the formation and evolution of galaxy bulges and discs across a range of morphologies and stellar masses, and how they fit into the broader picture of galaxy evolution.

THE MANY FACES OF ELLIPTICAL GALAXIES: UNVEILING THE STRUCTURAL COMPLEXITY AND STELLAR HISTORIES

This Chapter is based on the paper submitted to the *Astronomy&Astrophysics* journal, titled “Dual-component stellar assembly histories in local elliptical galaxies via MUSE”.

3.1 Abstract

Elliptical galaxies often exhibit complex assembly histories, and are presumed to typically form through a combination of rapid, early star formation and subsequent accretion of material, often resulting from mergers with other galaxies. To investigate theories of spheroidal galaxy formation, the objective of this work is to analyse the star formation histories (SFHs) of a sample of three isolated elliptical galaxies in the local Universe observed with MUSE at $z < 0.06$. With BUDDI, we decompose the integral field unit (IFU) datacubes into two components with Sérsic profiles, which roughly correspond to the two phases of in-situ and ex-situ star formation. To constrain the mode of growth in these galaxies, we derived the mass and light-weighted stellar ages and metallicities, and created the 2D stellar population maps of each component using pPXF. We reconstructed the mass and light-weighted SFHs to constrain the contribution of different stellar populations to the mass and luminosity of the components through cosmic time. Our results show that the ellipticals in this sample have experienced an early and rapid phase of star formation either through monolithic dissipational collapse or gas-rich major mergers concentrated in the inner component, which contributes to $\sim 50\%$ of the galaxy stellar mass. The co-dominant outer component, however, had assembled the bulk of its stellar mass shortly after the inner component did, through accretion via dry mergers and possible gas accretion. This premise is supported by our observations of the inner component being primarily composed of old and metal-rich stars. The outer component has a combination of old and intermediate-age stars, with a moderate spread in metallicities. These results are analysed through the lens of the two-phase

scenario, a framework developed over the years to explain the formation histories of elliptical galaxies.

3.2 Introduction

Elliptical galaxies are a part of the early-type galaxies (ETG) that are characterised by their spheroidal appearance and seemingly featureless and plain morphology, lacking any intricate structure. In the local Universe, they are thought to be simple and massive entities that are “red and dead”, hosting old and quiescent stellar populations and meagre amounts of gas to support star formation. However, in reality, this morphology encompasses a wide range of stellar masses and physical sizes, from compact and dwarf ellipticals to the most massive giant ellipticals. Each type has distinct structural properties and surface brightness profiles, providing valuable insights into galaxy formation and evolution. The formation scenarios for elliptical galaxies highlight the complex interplay of physical processes, from rapid monolithic collapse to gradual hierarchical merging and accretion. For instance, an often-cited mechanism for the formation of massive ellipticals is gas-rich mergers between spiral galaxies (Toomre, 1977; Hopkins et al., 2008). These processes essentially shape the structure of the elliptical galaxies, and result in different stellar populations, stellar orbits, and kinematics. Modelling the surface brightness profiles of ellipticals is therefore a crucial step in uncovering their origins and evolutionary history (MacArthur et al., 2008; Vulcani et al., 2014; Spavone et al., 2017; Spavone et al., 2021).

Elliptical galaxies were traditionally modelled with a de Vaucouleurs profile (de Vaucouleurs, 1948), which is an $R^{1/4}$ law. This implies a galaxy with a central concentration which becomes more extended radially outward. While this captures the light profile of many ellipticals, improved instrumentation and spatial resolution over the years have revealed a large diversity of elliptical galaxies deviating from this law (Kormendy, 1977; King, 1978). The Sérsic profile (an $R^{1/n}$ law) was later introduced (Sérsic, 1968), which modelled the surface brightness of the ellipticals more effectively, especially the inner regions of the galaxies. This was possible due to the freedom allowed for the Sérsic index n , which reverts to the de Vaucouleurs profile at $n = 4$. This flexibility that is incorporated into the Sérsic law is crucial because although ellipticals are indeed known for their high central concentration, the degree of concentration can vary from galaxy to galaxy. However, even the Sérsic profile might not fully represent the complex substructure that ellipticals are now expected to exhibit (Huang et al., 2013a; Huang et al., 2013b; Lacerna et al., 2016), challenging the simple structure often assumed.

Deep imaging has allowed the observation of internal sub-structures in elliptical galaxies, including low surface brightness tidal features (van Dokkum, 2005; Tal et al., 2009; Lazar et al., 2023) stemming from their outskirts in cluster environments, or shells (Malin et al., 1980; Athanassoula et al., 1985; Colbert et al., 2001; Bílek et al., 2016) around the galaxies. Substructures in the central regions of ellipticals have also been observed at different redshifts, such as embedded nuclear discs (Graham et al., 2016;

Dullo et al., 2018; Lacerna et al., 2020; Deeley et al., 2023). Furthermore, ellipticals have been systematically observed to fall under one of two classes based on the steepness of their central surface brightness profiles: “core ellipticals” with nearly flat central light profiles and “cuspy ellipticals” with sharply peaked central light profiles. The core and cusp regions are considered to be photometrically distinct components of ellipticals (Huang et al., 2013a). This central component therefore deviates from the standard Sérsic law that attempts to describe the surface brightness profile of the entire elliptical galaxy with a single model, without accounting for the inner component. It is therefore important to decompose the components of deceptively simple elliptical galaxies to discern their physical relevance, their formation histories, and stellar populations. For instance, Huang et al. (2013a) found that their sample of 94 nearby elliptical galaxies in the Carnegie-Irvine Galaxy Survey (CGS) required three or even four components to optimise the modelling of the surface brightness profile. Apart from the structural analysis, a complementary study in Huang et al. (2013b) revealed the underlying physical implications of modelling multiple components. Similarly Lacerna et al. (2016) found that their sample of 89 local elliptical galaxies at $z < 0.08$ were best modelled with two to four components. More recently, Lima Neto et al. (2020) demonstrated that two or three components were required to model the ellipticals in the NGC 4104 fossil group. The mechanisms leading to the formation of each component are more complex than can be explained by one of the two simple scenarios involving dissipational processes as previously mentioned.

The two major pillars of elliptical galaxy formation scenarios are the rapid monolithic collapse and hierarchical clustering. Over the decades, both numerical simulations and observations have been able to satisfactorily explain the structure of elliptical galaxies based on these theories. In the monolithic collapse scenario (Larson, 1974; Chiosi et al., 2002), an elliptical galaxy is formed by the rapid gravitational collapse of a primordial gas cloud, followed by a substantial dissipation of energy. This theory predicts that ellipticals emerge at high redshifts ($z > 5$) directly from the gas, with in-situ stellar mass build-up, rather than from accretion of stars formed ex-situ (Ogando et al., 2005). The rapid monolithic collapse scenario has been corroborated by strong negative metallicity gradients observed in elliptical galaxies (Domínguez Sánchez et al., 2019; Parikh et al., 2019; Goddard et al., 2017; Riffel et al., 2023), owing to the fact that the metals created during supernova explosions are retained by a strong enough gravitational potential that pushes the metal-enhanced gas toward the centre of the galaxy where the new stars form at a higher metallicity compared to the outer regions of the galaxy. The hierarchical clustering scenario (Toomre et al., 1972; Cole et al., 2000; Hopkins, 2009; Avila-Reese et al., 2014) on the other hand, predicts that the present-day galaxies formed through major and minor mergers and accretion of galaxies over time. This theory has also been supported by simulations and observations where a flat or shallow metallicity gradient was exhibited by ellipticals (González Delgado et al., 2015; Taylor et al., 2017; Benedetti et al., 2023), instead of the steep negative gradient expected from the monolithic collapse. Pure merger events are presumed to obliterate traces of the previous stellar history of

the galaxy, including metallicity gradients.

To better explain the mixed outcomes of elliptical galaxy observations, a hybrid scenario was proposed (Kormendy, 1989), where both mechanisms play a role in the formation of these remarkably complex galaxies. In the last decades, a two-phase scenario has been gaining traction, challenging the classical pictures of elliptical galaxy formation from either mergers or dissipative gas collapse (Kormendy, 1989). The two-phase scenario (Oser et al., 2010; Johansson et al., 2012; Huang et al., 2013a; Huang et al., 2013b) suggests that the first phase of dissipational processes dominate at high redshift through cold accretion and wet mergers of gas-rich galaxies, and later at lower redshifts, the galactic evolution is driven by delayed non-dissipational dry mergers. The presence of “red nuggets” at high redshifts $z \geq 1.5$ detected in several studies (Cimatti et al., 2004; Daddi et al., 2005; Trujillo et al., 2007; Toft et al., 2007; van Dokkum et al., 2008; Damjanov et al., 2009) already indicate an early onset of rapid star formation that settles into a compact core. Moreover, a smaller population of red nuggets that have survived to the present day has been identified, which have evolved in isolation without perturbations or interactions (Ferré-Mateu et al., 2017; D’Ago et al., 2023; Siudek et al., 2023; Moura et al., 2024). Most of these red nuggets eventually accumulate more stellar mass by accreting and merging with smaller systems to acquire the structure that is observed in present-day elliptical galaxies (Miller et al., 1980; Naab et al., 2006; Oser et al., 2010; Oser et al., 2012), while some ellipticals seem to have preserved their compact high- z progenitor (Barbosa et al., 2021).

Given the intricate structure of elliptical galaxies as both observations and numerical simulations clearly support, we delve into the multiple-component context of these galaxies in this paper. We make use of integral field spectroscopy (IFS) with the Multi Unit Spectroscopic Explorer (MUSE) observations of three elliptical galaxies in the local Universe, and perform 2D spectro-photometric decomposition to retrieve their structural parameters, as well as to extract their spectra and stellar populations to interpret their physical significance. The decomposition of a sample of three galaxies serves as a pilot study for further exploring the diverse properties that are inherent to elliptical galaxies over a range of stellar masses, redshifts, and environments.

This paper is organised as follows. Sect. 3.3 outlines the data and instrument used in the IFS observations for this study. Sect. 3.4 describes the methods of galaxy decomposition with BUDDI, full spectral fitting with pPXF, and Voronoi binning with Vorbin. The results of this work are highlighted in Sect. 3.5 in the context of structural parameters, the stellar populations analysis, and star formation histories of each component. Sect. 3.6 provides a discussion on the physical implications and future directions of this study, and we draw our conclusions in Sect. 3.7. Throughout this work, we adopt a flat Λ CDM cosmology with $H_0 = 67.8 \text{ kms}^{-1}\text{Mpc}^{-1}$, $\Omega_m = 0.308$, $\Omega_\Lambda = 0.692$ (Planck Collaboration et al., 2016).

Table 3.1: The coordinates and properties of the three elliptical galaxies observed with MUSE.

Galaxy	RA (J2000)	DEC (J2000)	z	$\log M_* M_\odot$
J020536.18-081443.23	02:05:36.18	-08:14:43.23	0.0411	10.956
J205050.78-004350.85	20:50:50.78	-00:43:50.85	0.0571	11.277
J225546.96-085457.87	22:55:46.96	-08:54:57.84	0.0590	11.274

3.3 Data and observations

MUSE (Bacon et al., 2010b) is an optical integral-field spectrograph mounted at the 8.2m ESO Very Large Telescope (VLT) in Chile. It covers the nominal wavelength range of 4600 – 9350 Å with spectral sampling of 1.25 Å and a $1' \times 1'$ field of view, and spatial resolution of $0.2''/\text{pixel}$ in the Wide Field Mode (WFM). The MUSE spectrograph has a spectral resolving power ranging from $R \approx 1770$ at 4800 Å to $R \approx 3590$ at 9300 Å. The three ellipticals were observed under Program ID 099.B-0411 (PI. Johnston) between July and October 2017 using the wide field mode with no adaptive optics (WFM-NoAO-N). The targets initially proposed for observation consisted of 48 galaxies selected from SDSS DR7, representing all major Hubble types from Nair et al. (2010). The selected targets spanned a range of Sérsic indices, B/T ratios, with an inclination $\lesssim 40^\circ$ as derived from Simard et al. (2011), which allowed to clearly discern the components of the galaxies. Moreover, the sample was chosen to only include unbarred galaxies, with no signatures of recent interactions, such that each galaxy can be cleanly decomposed into its major components. However, being a filler programme observed under sub-optimal weather conditions, only a small set of five elliptical galaxies with a higher set priority were observed. From this, we consider only three galaxies suitable for analysis in this work, as the other two ellipticals were severely affected by the observing conditions, making their surface brightness profiles impossible to model. These galaxies were observed with exposure time of 960 seconds, each containing 3 – 6 dithered and rotated exposures. The sample analysed in this work consists of relatively isolated elliptical galaxies at $z < 0.06$, with stellar masses $\sim 10^{11} M_\odot$ from the Nasa Sloan Atlas (NSA)¹.

The data reduction was carried out using the ESO MUSE pipeline (v2.6, Weilbacher et al., 2020) in the ESO Recipe Execution Tool (EsoRex) environment (ESO CPL Development Team, 2015). The master bias, flat field and wavelength calibrations for each CCD were created from the associated raw calibrations, and were applied to the raw science and standard-star observations as part of the pre-processing steps. Flux calibration was carried out using the standard star observations from the same nights as the science data, with the sky continuum measured directly from the science exposures with subsequent background subtraction. The individual exposures were aligned to a common frame and stacked to produce the final datacube. To alleviate residual sky contamination, we

¹ Available from <http://www.nsatlas.org>

used the Zurich Atmosphere Purge code (ZAP, [Soto et al., 2016](#)). The coordinates and redshifts of the galaxies used in this analysis are listed in Table 3.1. For readability, these galaxies will henceforth be denoted as J020536 (MRK 1172), J205050, and J225546.

3.4 Methods

In this Section, we outline our methodology for decomposing the spectra of the elliptical galaxies using BUDDI, followed by fitting the resulting spectra with pPXF. Additionally, we detail the construction of 2D stellar population maps utilising the Voronoi tessellation technique with Vorbin.

3.4.1 Galaxy decomposition with BUDDI

The light profiles of the elliptical galaxies in this sample were modelled using (BUDDI; [Johnston et al., 2017](#)) and decomposed into different components to extract their individual spectra. This code is an IDL wrapper for GalfitTM ([Vika et al., 2013](#); [Häußler et al., 2013](#); [Vika et al., 2014b](#); [Häußler et al., 2022](#)), which is adapted to model multiple components in all the wavelength slices of IFU datacubes. The galaxies were each modelled at first with a single Sérsic profile, and the complexity in the model was introduced by subsequent addition of a second Sérsic component. A double Sérsic model with an additional Point Spread Function (PSF) component, and a triple Sérsic model were also tested, but they either did not yield meaningful results or failed to fit the galaxy (we refer the reader to Sect. 3.5.1 for details on the preferred choice of components). Therefore, throughout this study, we adopt the models based on single and double Sérsic light profiles. We refer the reader to [Johnston et al. \(2017\)](#) for the full details of the IFU decomposition with BUDDI, and present a brief overview here.

BUDDI requires some initial data preparation before starting the fitting process. This includes normalising the galaxy kinematics by measuring the line-of-sight (LOS) velocities (V) and velocity dispersions (σ), and introducing the following kinematics corrections: (i) broadening the spectrum of each spaxel to match the maximum LOS velocity dispersion, and (ii) shifting the spectrum to match the LOS velocity at the centre of the galaxy. The kinematics corrections eliminate any artefacts in the final spectral features induced by the variation in rotation and velocity dispersion across the galaxy. For this, the IFU datacube was first binned using the Voronoi tessellation technique implemented by the Vorbin Python package² package of [Cappellari et al. \(2003\)](#), with a target minimum $S/N = 50^{-1}$. Subsequently, the stellar kinematics were measured by full spectral fitting of the binned spectra using the penalised PiXel Fitting routine (pPXF³) of [Cappellari et al. \(2004\)](#). We use the single stellar population (SSP) models ([Vazdekis et al., 2010](#); [Vazdekis et al., 2015](#)) based on the Medium resolution INT Library of Empirical Spectra (MILES; [Sánchez-Blázquez et al., 2006](#)), constructed

² Available from <http://purl.org/cappellari/software>

³ See footnote 2

from the PADOVA2000 stellar evolutionary tracks (Girardi et al., 2000). The parameter space for the kinematics measurements spans stellar ages between 1 and 17.78 Gyr, and metallicities between -1.71 and 0.22, resulting in a total of 156 template spectra.

The setup for BUDDI requires the following input files:

- (i) The flux datacube, which has been log-rebinned in wavelength.
- (ii) The PSF datacube, also log-rebinned in wavelength. In all three datacubes, postage stamps of stars in the field of view were created and stacked at each wavelength. A Gaussian profile was used to model them, constructing the PSF datacube. The full-width half maxima (FWHM) of the PSFs in our sample range from $0.8'' - 1.4''$ at the central r -band wavelength of 6166 \AA .
- (iii) The bad pixel mask datacube, that identifies and masks the pixels with no valid flux values. This also includes the masking of any bright sources in the field of view which can affect the fitting of the light profile of the target galaxy.
- (iv) The sigma datacube, which is crucial for accurately determining the flux uncertainty in each individual pixel.

Once the datacubes are in place, the fitting process in BUDDI takes place in three major steps. We refer the reader to Johnston et al. (2017) and Johnston et al. (2022a) for details.

1. **Fitting the median “broad-band” image.** The datacube was collapsed in wavelength to a median-stacked white-light image. Within the BUDDI routine, this single image was fit using `GalfitM` with a single Sérsic component at first, and subsequently with two Sérsic components. The sky background amplitude and the gradient in x and y directions were allowed to be freely fit simultaneously - this was deemed necessary due to the inconducive observing conditions which had created a non-uniform sky background.
2. **Fitting the “narrow-band” images.** This step fine-tunes the Chebyshev polynomials in `GalfitM`, which model the dependence of structural parameters (R_e , n , b/a , PA) on wavelength for the galaxy in the single Sérsic model, and for both components in the double Sérsic model. The datacube was binned along wavelength into 10 “narrow-band” images (Johnston et al., 2022a; Johnston et al., 2022b; Jegatheesan et al., 2024) and fit simultaneously twice: first with complete freedom for the parameters (10th-order Chebyshev polynomial), and then manually choosing the appropriate polynomial order after visual inspection of the intermediate plots that BUDDI creates with the estimated structural parameters as a function of the wavelength. For each galaxy and component, the chosen polynomial orders for the parameters are listed below in Table 3.2: a first-order polynomial constrains the parameters to remain constant with wavelength, while a second-order polynomial allows for linear variation in wavelength. The magnitudes were allowed to have complete freedom during the fit, and the initial parameters were set to those measured in each preceding step.

Table 3.2: *Chebyshev polynomials introduced in the step fitting the narrow-band images of the datacube.*

Galaxy	Comp	R_e	n_{ser}	ba	PA
J020536	single	2	2	1	1
	inner	1	2	1	1
	outer	1	2	1	1
J205050	single	2	2	1	1
	inner	1	1	1	1
	outer	1	1	1	1
J225546	single	1	2	1	1
	inner	1	1	1	1
	outer	1	2	1	1

3. **Fitting each image slice of the datacube.** The final step makes use of the refined parameters from the previous narrow-band fits and keeps them fixed for each image slice while allowing only the magnitudes to vary in the fit. This estimates the magnitude, and therefore the flux of each component, in each image slice of the datacube, ultimately extracting their clean 1D spectra.

Having modelled the surface brightness of the galaxies with one, two, and three Sérsic profiles, we opted for the two-component models for all of them, which are shown in Figure 3.1. To unveil the physical properties and implications associated with the different components of elliptical galaxies, the clean spectrum of each component was extracted with BUDDI in order to perform the stellar populations analyses.

3.4.2 Spectral fitting for stellar population analysis

The spectra of the two components obtained from the previous step (Sect. 3.4.1) were fit using pPXF to derive the stellar metallicity $[M/H]$ and stellar age. The Python implementation of pPXF v9.1.1 was used in this work. pPXF finds a linear combination of stellar templates that best matches the input spectrum. For this study, both the mass-weighted and light-weighted stellar population properties were derived and analysed. The full spectral fitting method optimises the mass or light weights for each SSP spectrum in the template library, such that the observed spectrum is a combination of these weights (Cappellari et al., 2003; Cappellari, 2017; Cappellari, 2023).

The empirical library of stellar spectra employed is MILES (Vazdekis et al., 2015)⁴, along with the BaSTI isochrone models (Pietrinferni et al., 2004), which track stellar evolution. This choice of the stellar library is attributed to the vast coverage of stellar metallicities and ages, which is necessary for studying nearby galaxies in the local Universe, which can contain both old and young stars with low and high metallicities.

⁴ Available from <http://miles.iac.es/pages/webtools.php>

Restricting to the safe ranges defined in [Vazdekis et al. \(2010\)](#), the chosen stellar population parameters span a range from -1.79 to 0.26 dex for the metallicities $[M/H]$ and from 30 Myr to 14 Gyr for the ages, forming a combined total of 530 template spectra. Since each stellar template is normalised to $1M_{\odot}$, pPXF derives the mass weights by default. In order to estimate the light weights, the stellar templates are normalised by the V -band luminosity (5070 – 5950 Å), chosen such that the resulting properties favour more recent star formation episodes in the galaxy. The Universal Kroupa IMF ([Kroupa et al., 2002](#)) with a slope of 1.3 is assumed.

During the spectral fit with pPXF, an 8th-order multiplicative Legendre polynomial was used to correct for the shape of the continuum. Furthermore, the inclusion of a multiplicative polynomial in the fit also ensures that the spectral fit is independent of dust reddening, thereby eliminating the need to define a reddening curve explicitly within the pPXF routine ([Cappellari, 2017](#)). Additionally, the [OI]5577Å sky line is masked during the fit. The code allows fitting of emission lines simultaneously alongside the stellar continuum using a set of respective Gaussian templates representing the nebular emission. The spectral range for the fit is constrained to rest-frame 4700 – 6780 Å due to inconsistencies that can be introduced when using the full MUSE wavelength range ([Krajinović et al., 2015](#)). Moreover, this chosen range spans the important spectral features that are sensitive to stellar age and metallicity ($H\alpha$, $H\beta$, Mg_2 , and Fe) and aligns with the wavelength coverage in the MILES models.

The pPXF routine provides a solution to the ill-posed problem of extracting stellar population properties from observed spectra. The extensive span of the parameter space of the SSPs inevitably leads to non-unique solutions that are degenerate in metallicity or age. This is one of the commonly cited challenges in the fossil-record method with stellar population modelling and full spectral fitting, along with the imprecise age resolution for older populations with $t > 8$ Gyr ([Cid Fernandes et al., 2005b](#); [Riffel et al., 2009](#); [Ibarra-Medel et al., 2019](#); [Lacerna et al., 2020](#); [Riffel et al., 2024](#)). The solution incorporated within pPXF is regularisation, which is responsible for mitigating intrinsic degeneracies in the final solution. When a possible degeneracy is encountered, the inclusion of a regularisation term treats this by smearing out the weights of similar metallicities and ages, going from discrete weights that resemble a single stellar population to a solution with smooth weights that are more physically motivated in galaxies. The REGUL parameter within the routine sets the degree of smearing, following the prescription outlined in the pPXF user manual and in [Shetty et al. \(2015\)](#) and [Jegatheesan et al. \(2024\)](#). A word of caution is advised at this point while interpreting the star formation histories from full spectral fitting: star-formation is a stochastic and unpredictable process, which can occur at timescales shorter than those specified in the synthetic template models.

3.4.3 Voronoi binning for spatially resolved properties

As a complementary analysis, the stellar populations across the spaxels of the datacube were measured and visualised as a 2D map to study the properties of the inner and

outer regions of the galaxies. Given the variations in S/N across the spaxels in the MUSE datacube, we opted to employ Voronoi binning which ensures that a minimum user-defined S/N per bin is achieved throughout the galaxy. The size of the Voronoi bins adapt based on the corresponding S/N, which allows for the spaxels of low S/N to be handled effectively (Cappellari et al., 2003) by assigning them to larger bins, while high S/N spaxels, usually located in central galaxy regions, are assigned to smaller bins or left unchanged (Cappellari et al., 2003).

The Python implementation of the Vorbin package of Cappellari et al. (2003) was used to Voronoi bin the S/N in our galaxy datacubes. The continuum S/N was determined at a rest-frame wavelength of 5635 Å, in a region without any spectral features. According to Zibetti et al. (2024), a minimum spectral S/N of 20^{-1} is required to constrain stellar ages reliably from stellar population synthesis (SPS) models (see also Cid Fernandes et al., 2005b; Riffel et al., 2009). We therefore chose the constant S/N threshold to be more conservative at 50^{-1} , following Johnston et al. (2021) where it was proven sufficient to extract stellar populations. The binning is performed such that the total S/N of each assigned bin is above the set threshold, thereby optimising the usage of spaxels on the outskirts of the galaxy with low S/N in addition to the spaxels with high S/N in the core of the galaxy. Any foreground stars in the MUSE field of view or neighbouring objects were masked out wherever necessary, as well as the spaxels with $S/N < 3$ to discard noise-dominated spaxels and sky spaxels.

The spectra in each bin were then summed, and modelled with pPXF, following the prescription detailed in Sect. 3.4.2 in order to extract the mean stellar metallicities and stellar ages. We note that this technique provides only a general overview of the stellar population properties of the galaxy in a 2D map, and allows us to study these properties and any features in “inner” and “outer” regions of the galaxy. While this is useful as a confirmation analysis, it is not an exact alternative to IFU galaxy decomposition described in Sect. 3.4.1. The Voronoi binned maps represent the light of the different components superposed on each other as the total light in each spaxel, and therefore propagates in each bin. BUDDI on the other hand extracts the light from each underlying component of the galaxy, minimising the superposition.

3.5 Results

3.5.1 Component models and structural parameters

As described in Sect. 3.4.1, the galaxies were modelled with a single Sérsic profile at first, and then the complexity of the models were subsequently increased and tested using BUDDI in order to isolate any relevant substructure in elliptical galaxies presenting different physical and stellar population properties. We attempted to go as far as three components, including a double Sérsic profile with a PSF model, and a triple Sérsic component model, drawing from the findings in Huang et al. (2013a) and Huang et al. (2013b). However, adding a third component caused the fit to crash before completion

Table 3.3: Structural parameters and the flux contribution of each component relative to the total flux for the single-component model (“single”) and for each component of the two-component model (“inner” and “outer”) at the r -band central wavelength 6166 Å.

Galaxy	Comp	$\left(\frac{F_{comp}}{F_{total}}\right)_r$	R_e (kpc)	n_{ser}	$\frac{b}{a}$	PA (deg)
J020536	single		3.63	2.35	0.90	-2.26
	inner	0.34	1.41	1.21	0.95	6.05
	outer	0.66	6.67	1.43	0.85	-8.47
J205050	single		5.79	2.96	0.68	2.48
	inner	0.45	2.84	1.95	0.68	3.62
	outer	0.55	18.98	1.34	0.73	-4.74
J225546	single		6.88	2.71	0.64	-5.41
	inner	0.34	2.42	1.66	0.78	-11.76
	outer	0.64	12.16	1.55	0.50	-2.77

due to a forced attempt at fitting a non-existent component for two of the galaxies (J205050 and J225546). Adding a PSF component to the double Sérsic model did not cause the fits to fail, but did not contribute to a significant difference to the models and spectra. For J020536, the fit appeared to be successful with three Sérsic components, only considering the residual image and the estimated structural parameters. However, on closer inspection, the fit had in fact resulted in spectra with a distorted and erratic continuum, suggesting inaccuracies due to significant noise. Given the spatial resolution offered by MUSE and the sub-optimal observing conditions, a double Sérsic model was chosen to be the best fit for all three galaxies, which was decided after visual inspection of the fit residuals and the estimated structural parameters, along with the extracted spectra. The structural parameters estimated by BUDDI are listed in Table 3.3 and the fits to the galaxies in Figure 3.1.

Considering the two-component fits, the Sérsic indices of all the ellipticals were found to be less than 2 for both components, and therefore are not represented by de Vaucouleurs profiles. For J205050 and J225546, the components show $n_{inner} > n_{outer}$, while J020536 shows the opposite. The axis ratios of the inner component is higher than the outer component in J020536 and J225546, while J205050 has nearly equal axis ratios for both components. For the single Sérsic fit, the Sérsic index is significantly higher ($n > 2$) than either of the components of the double Sérsic fit. This higher Sérsic index reflects the attempt to fit both the steep and shallow light profiles dominating at different scales in the galaxy simultaneously. For a galaxy that has more than one component, this often results in an average value that does not represent either component accurately, but rather provides a compromise whilst fitting the entire galaxy, leading to the impression of a highly compact object. Similarly, this affects the sizes of the galaxies, with a single

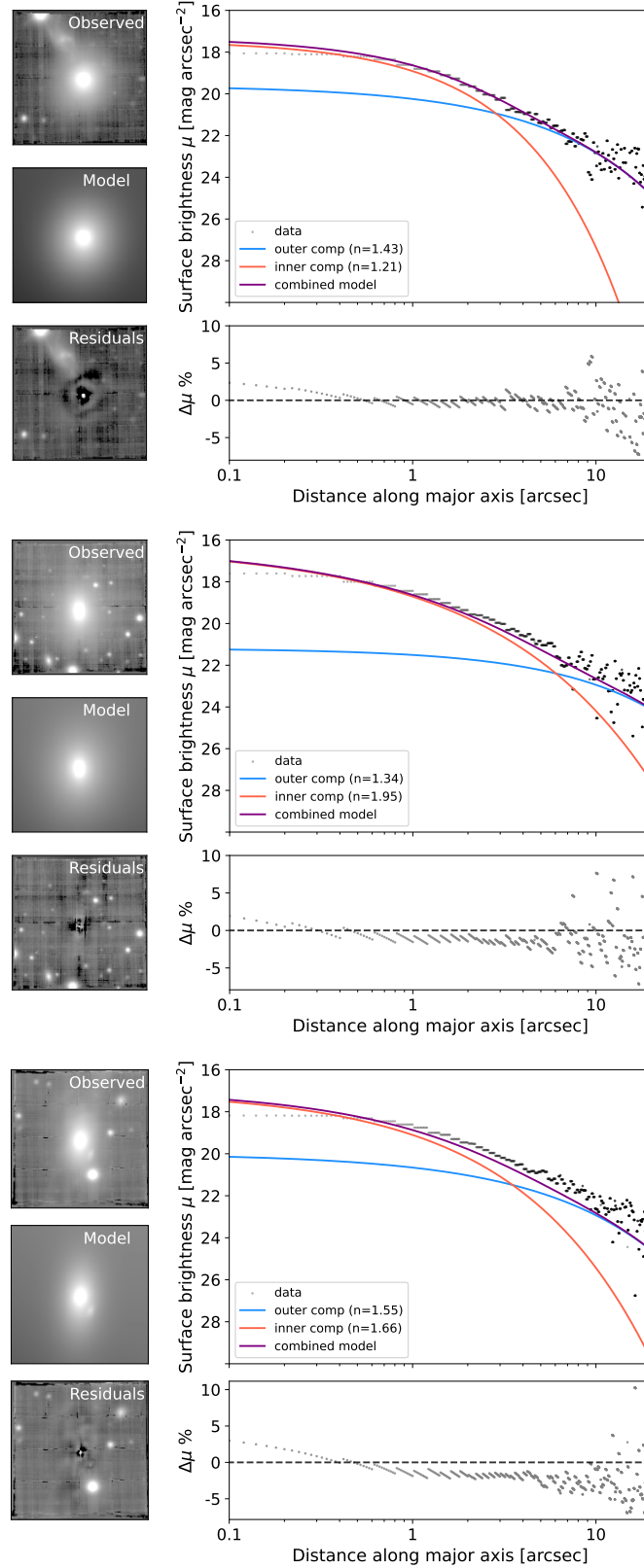


Figure 3.1: Fit to the median-stacked white-light image of the three ellipticals J020536, J205050, and J225546, from top to bottom. Left column: observed input image, the best-fit model, and the residual image. The images have all been scaled to the same flux for comparison. Upper right panel: 1D light profile of the galaxy at the central r -band wavelength along the major axis (black points), the Sérsic profiles of the inner (red line) and outer (blue line) components and the combined model (purple line). Lower right panel: residuals (in per cent) of the 1D data points and model as a function of distance along the major axis.

Sérsic fit yielding an R_e that falls between the R_e values of the two components.

As is evident from the white-light images of the three ellipticals in Figure 3.1, there are a number of foreground stars or neighbouring galaxies within the field of view, which have the potential to affect the component models if not accounted for. For example, another object can be clearly observed close to J020536. Lassen et al. (2021) concluded that this object was an irregular dwarf galaxy at $z = 0.04025$ that is interacting with J020536, creating a plume of irregular structure between both objects. The asymmetric distortion in the surface brightness caused by the interaction makes the dwarf galaxy difficult to model simultaneously with the target. To avoid the fit from crashing or modelling the wrong object, we mask this entire region out with a polygon, in addition to masking out the stars. However, we note that despite our efforts to mask out the interacting object, the overlap between the galaxies implies that the light contamination from the dwarf galaxy in J020536 cannot be entirely eliminated, especially at the outskirts. Similarly, there is a small galaxy that appears close in projection to J225546. However, with a redshift of 0.22, it is clear that this object is neither a satellite galaxy accreting onto the target nor interacting with it. It is rather a background galaxy along the same line of sight as the main galaxy. However, since the projection of this object appears to lie very much within the outer regions of the target galaxy itself, it was decided to model this as an additional component. Since the “neighbouring” background galaxy is an extended object, discerning the point where its light contribution reaches negligible levels becomes challenging, making it difficult to mask. Choosing the size of the mask can have a significant effect in modelling the light from the main galaxy. In this instance, the mask could either be inadequate to allow light from the outskirts to influence the fit to the target galaxy, or excessively large, resulting in substantial loss of light from the main galaxy. For these reasons, we elected to model the background galaxy, which helps to subtract its light contribution, providing a more reliable fit to the galaxy of interest as compared to masking it out (Häussler et al., 2007).

The two-component models of the galaxies as depicted in Figure 3.1 show a good fit, barring the very innermost regions. It must be noted that the seeing is indeed accounted for in these fits by convolving the flux datacubes with their PSF datacubes, but constructing an accurate PSF from IFU data presents a significant challenge. Therefore, these differences can alter the fit in the central regions of the galaxy, which is also why the Sérsic index is one of the most difficult parameters to estimate - the variation and behaviour of the light profile in the central few pixels makes it challenging to model this region (Häußler et al., 2022). This issue is seen reflected in the residuals, and is quantified in the 1D surface brightness profiles in the right panel. The lower right panel depicts the fraction of light that has been over- or under-subtracted from the r -band image slice as a function of the galactocentric distance along the major axis. The majority of the residuals lie within $\pm 5\%$ of the observed points. At the very central regions ($\lesssim 0.5$ kpc), the effect of using less robust PSF models can be seen. Alternatively, the profiles seem to resemble those of “core” elliptical galaxies (Trujillo et al., 2004; Thomas et al., 2014), characterised by a central flattening of the light profile. The higher scatter seen at

larger distances from the centre are likely due to the asymmetric sky background and the effect of low S/N in the outskirts, especially considering the profile was constructed from a single image slice. We note that the 1D and 2D surface brightness profiles are not a 1:1 correspondence, since the 2D models are for the median-stacked image, while the 1D observed profiles and models are built from the structural parameters interpolated to the r -band central wavelength at 6166 Å. Nevertheless, this serves as an example of the quality of the fits to the surface brightness of the galaxies.

3.5.2 Mean stellar populations

One of the main goals of this study is to investigate the physical significance of the two components that model the surface brightness profiles of elliptical galaxies, by examining their stellar properties. These dual-component models provide a more accurate representation than the single-component model that has been rooted in several decades of literature. The use of IFS allows us to study the stellar populations hosted by the two components, and identify any significant differences if they exist. This would ultimately help in correlating the stellar populations to physical mechanisms throughout the galaxies' lifetimes that have been driving the evolution of present-day classical ellipticals.

Figure 3.2 shows the stellar populations obtained from full spectral fitting with pPXF (see Sect. 3.4.2). The mean mass-weighted stellar metallicities [M/H] and the logarithmic stellar ages, are depicted in the upper panel, while the mean light-weighted properties are shown in the lower panel. The circles, squares, and triangles represent the three elliptical galaxies in the sample (J020536, J205050, and J225546 respectively), and the red and blue colours mark the inner and outer components derived from BUDDI in the two-component (Sérsic + Sérsic) models. The inner and outer components of the same galaxy are connected by the black lines for better readability. For comparison, the stellar population properties from the standard single component (Sérsic) model are shown in purple. Mass-weighted ages reflect the period when the majority of stellar mass was assembled and are less sensitive to the most luminous and younger stars; whereas light-weighted ages are influenced by recent star formation, which significantly impacts luminosity but contributes less to the overall mass (Hopkins, 2018).

The mean mass and light-weighted ages of the galaxies (single Sérsic) and their individual components (inner and outer components in the double Sérsic model) are all older than 9 Gyr, which typically places them in the category of long-term quiescent "classical ellipticals". The difference between the ages of the populations present in the inner and outer components ranges roughly between 1 and 5 Gyr. Plauchu-Frayn et al. (2012) define the star formation timescale $\Delta(t_*)$ as the difference between the mass-weighted and light-weighted stellar ages: $\Delta(t_*) = t_{MW} - t_{LW}$ Gyr. $\Delta(t_*)$ is high for objects that are continuously forming stars, while it is low for those that have ceased forming stars a long time ago. Following their definition, we compute $\Delta(t_*)$ for each component, as well as globally for each galaxy. Considering the ages of the galaxies as a whole, we

find $\Delta(t_*)$ to be negligible, of the order of a few 100 Myr, well within their uncertainties. This insignificant difference is typically expected for classical ellipticals when considered as a global property, implying that their stellar populations are homogeneous in age and would have formed and quenched at roughly similar early lookback times. The inner and outer components similarly show virtually imperceptible $\Delta(t_*)$ values. While we recognise that the mean light-weighted ages of J225546 appear to be slightly higher than the mass-weighted ages outside their error bounds, it is important to reiterate that one of the major caveats of the fossil-record method is that the stellar ages are indistinguishable for extremely old stellar populations. Furthermore, since the chosen isochrones of the SSP models used in the spectral fitting include ages up to ~ 14 Gyr, pPXF can estimate mass fractions at ages older than the Hubble time, depending on the assumed cosmology. Due to these limitations, we exercise caution in directly interpreting the individual absolute stellar ages and the star formation timescale. From the mean stellar ages, it is only clear that the $\Delta(t_*)$ values are low, and therefore suggest populations that are similar in age. However, the quantity $\Delta(t_*)$ is more related to intrinsic star formation and quenching in the galaxy, and less sensitive to dry mergers where stellar material is simply accreted without a subsequent star forming episode, unless the accreted galaxy itself is young. Therefore, the low values of the outer component do not necessarily confirm that the population was formed at the same time throughout the component, but could be attributed to stellar accretion from satellite galaxies that are approximately as old as the main galaxy.

The mean mass-weighted stellar metallicities of the galaxies indicate metal-rich stellar populations, with super-solar metal abundances ($[M/H]_{MW} > 0$). For the inner components, the metallicities are quite high compared to the global values for the galaxies. In contrast, the outer components signify metal-poor stellar populations, with sub-solar metal abundances ($[M/H]_{MW} < 0$). Compared to the outer components, the inner components are significantly more metal-enhanced by factors of 0.2 – 0.7 dex. Similarly, the light-weighted metallicities decrease inside-out, with the outer components showing less metal-enhanced stellar populations than their corresponding inner components by factors of 0.3 – 0.9 dex. The relative differences between the mass-weighted and the light-weighted metallicities $\Delta[M/H]_*$ are quite small, between 0 and 0.2 dex, with the highest differences exhibited by the outer components. These results align with the two-phase formation scenario where the inner component has likely assembled most of its stellar mass through in-situ bulk star formation when the interstellar medium was already enriched with metals, either through dissipative collapse of a gas cloud or through major mergers between gas-rich discs. The light-weighted metallicities exhibited by the outer components indicate that recent star formation episodes are associated with relatively metal-poor populations. This component would then accrete its stellar mass later in dry mergers of relatively metal-poor galaxies, such as dwarf galaxies, or through star formation resulting from relatively pristine gas inflow that dilutes the metal-enhanced interstellar medium.

Table 3.4: Mean mass and light-weighted stellar populations properties listing the stellar metallicities, ages, formation times τ_{50} and τ_{90} .

Mean mass-weighted stellar populations					
Galaxy	Comp	[M/H]	Age (Gyr)	τ_{50} (Gyr)	τ_{90} (Gyr)
J020536	single	0.063 ± 0.009	12.91 ± 0.180	13.42 ± 0.266	11.90 ± 1.138
	inner	0.138 ± 0.006	13.06 ± 0.164	13.50 ± 0.315	12.11 ± 0.894
	outer	-0.067 ± 0.021	10.69 ± 0.297	11.41 ± 0.902	8.28 ± 0.827
J205050	single	0.174 ± 0.004	13.61 ± 0.116	13.96 ± 0.063	13.17 ± 0.408
	inner	0.245 ± 0.004	13.80 ± 0.099	14.00 ± 0.025	13.55 ± 0.387
	outer	-0.426 ± 0.043	8.83 ± 0.553	9.26 ± 1.247	6.71 ± 0.905
J225546	single	0.035 ± 0.011	12.19 ± 0.200	12.81 ± 0.489	10.57 ± 1.125
	inner	0.132 ± 0.007	13.03 ± 0.222	13.50 ± 0.250	12.09 ± 0.826
	outer	-0.130 ± 0.024	12.13 ± 0.347	12.83 ± 0.565	10.41 ± 1.080
Mean light-weighted stellar populations					
Galaxy	Comp	[M/H]	Age (Gyr)	τ_{50} (Gyr)	τ_{90} (Gyr)
J020536	single	0.005 ± 0.042	12.25 ± 0.349	13.44 ± 0.355	11.86 ± 1.610
	inner	0.121 ± 0.006	13.03 ± 0.207	13.47 ± 0.345	12.06 ± 0.860
	outer	-0.222 ± 0.019	9.73 ± 0.492	10.73 ± 0.751	6.77 ± 1.394
J205050	single	0.166 ± 0.003	13.58 ± 0.143	13.94 ± 0.045	13.15 ± 0.453
	inner	0.239 ± 0.004	13.77 ± 0.112	14.00 ± 0.015	13.55 ± 0.378
	outer	-0.624 ± 0.029	8.87 ± 0.617	8.97 ± 1.093	7.25 ± 1.395
J225546	single	-0.031 ± 0.012	13.12 ± 0.347	13.57 ± 0.226	12.18 ± 1.113
	inner	0.118 ± 0.008	13.55 ± 0.200	13.93 ± 0.137	13.10 ± 0.805
	outer	-0.314 ± 0.024	12.59 ± 0.642	13.55 ± 0.557	10.51 ± 1.584

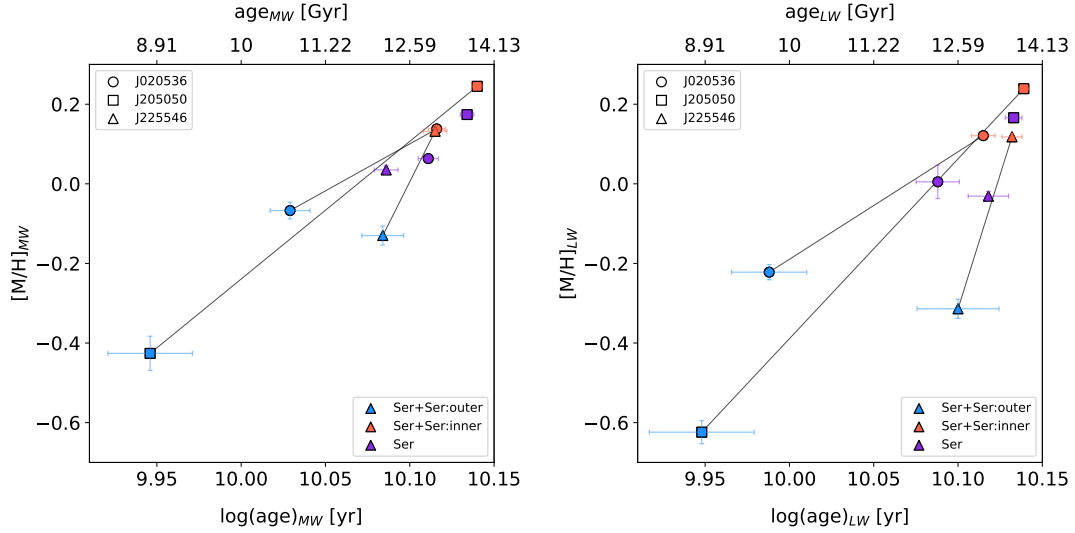


Figure 3.2: Left panel: Mass-weighted stellar populations showing the logarithmic stellar ages in years (lower x -axis) and their corresponding values in Gyr (upper x -axis), against stellar metallicities of the one-component and the two-component models. The three marker styles represent the three galaxies, while the colours represent the components - blue for the outer component of the double Sérsic model, red for the inner component, and purple for the single Sérsic component. The associated logarithmic error bars are also shown. Right panel: The same as the upper panel, but with light-weighted stellar populations instead.

3.5.3 Comparison with spatially resolved 2D stellar population maps

We also conducted a complementary stellar population analysis to compare the global properties described in Sect. 3.5.2. For this, the Voronoi binning technique was used to bin the IFU datacubes based on their S/N, and the spectra in each bin were summed together to retrieve a single spectrum with adequate S/N (we refer the reader to Sect. 3.4.3 for details). The binned spectra were then fit with pPXF using the same method detailed in Sect. 3.4.2. This technique allows us to create a 2D map of the stellar population properties and observe qualitatively any radial trends present in the galaxy. However, as stated in Sect. 3.4.3, these do not serve as a direct comparison to the results obtained with BUDDI due to the significant chance of mixing between different structural components. Nevertheless, these 2D maps offer an alternative way of comparing our results, albeit in a more generic way, and resemble more traditional analyses in the literature. The columns in Figure 3.3 represent the three elliptical galaxies, while each row shows a single stellar population property: mass-weighted age, light-weighted age, mass-weighted metallicity, and light-weighted metallicity in that order. The properties are mapped based on the colour bar above each plot, with the youngest ages and lowest metallicities in blue, and the oldest ages and the highest metallicities in red. The black contours mark the $1R_e$ and $2R_e$ ellipses for the inner (dashed) and outer (solid) components modelled in the two-component fit to each galaxy.

For galaxy J020536, the mass-weighted stellar age map shows a mildly negative gradient from the central region, corresponding to $1R_e$ of the inner component derived

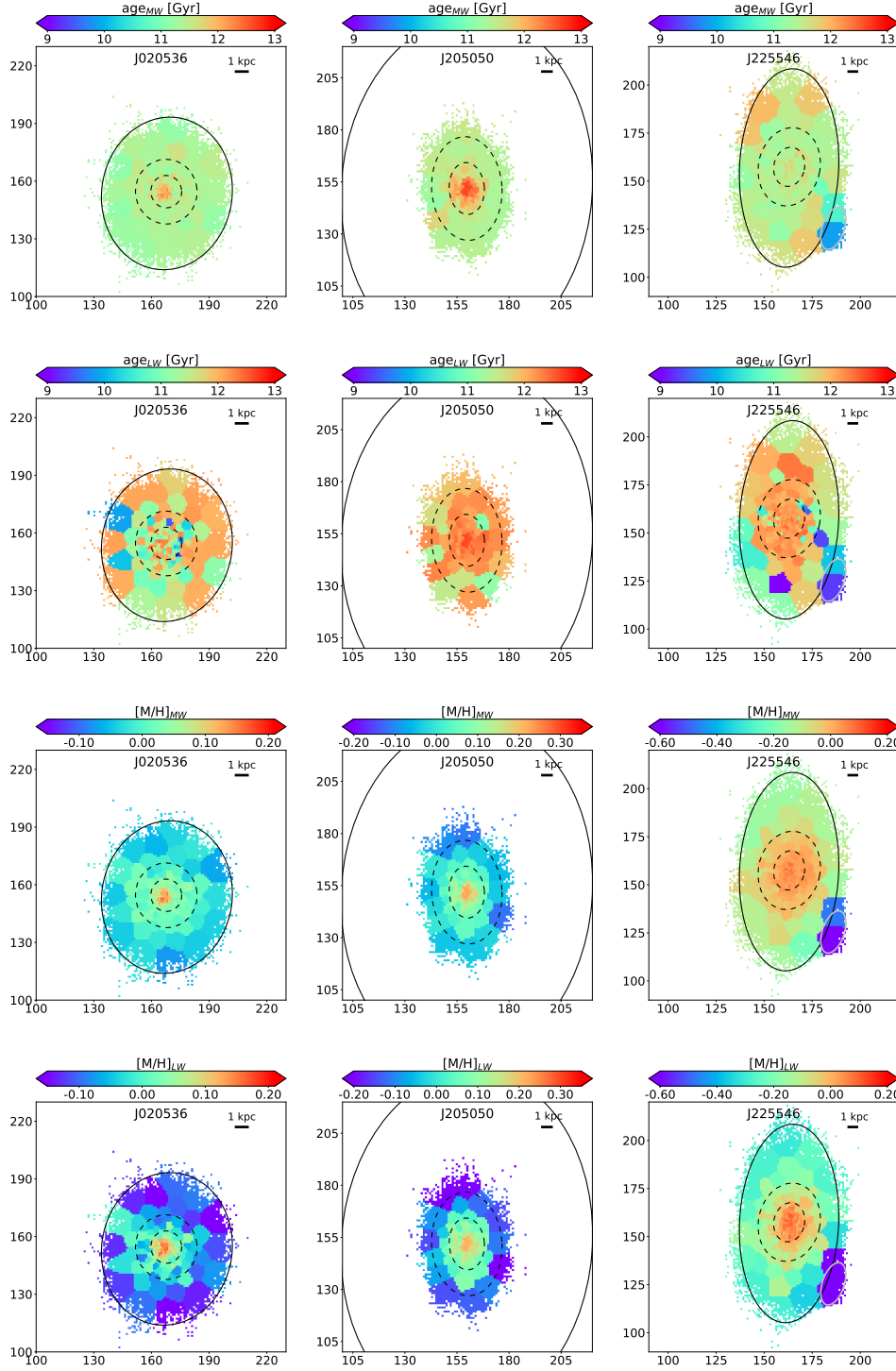


Figure 3.3: Voronoi-binned stellar populations for galaxies J020536, J205050, and J225546 from left to right. From top to bottom, the rows indicate the logarithmic mass-weighted stellar ages, the light-weighted ages, the mass-weighted metallicities, and the light-weighted metallicities. The colour bars for the ages have been displayed in Gyr for better clarity, and the scale bars in each plot mark 1 kpc. The $1R_e$ and $2R_e$ contours from BUDDI of the inner component are marked as dashed black ellipses, and only the $1R_e$ contour of the outer component is shown as solid black ellipses, since the $2R_e$ contours are beyond the extent of the mapped regions of the galaxy. For object J225546, an additional contour is shown in grey, which marks the $1R_e$ ellipse of the adjacent galaxy modelled together with the target.

from BUDDI, to the outskirts, corresponding to $1R_e$ of the outer component. We find the negative mass-weighted age gradients to be composed of a dominant old ($t \gtrsim 12$ Gyr) stellar population in the inner component, and a slightly younger but homogeneous population ($t \sim 11$ Gyr) on the outskirts. The light-weighted stellar age map however, does not appear to show any significant trends, similar to the findings of [Lassen et al. \(2021\)](#), where the spatially resolved light-weighted mean ages were derived through stellar population synthesis at the spaxel resolution. The mass-weighted and light-weighted stellar metallicity maps, on the other hand, show a very clear gradient from the centre to the outskirts. The core hosts the most metal-rich population in the galaxy, which becomes less enhanced moving radially outward towards the galactic outskirts. This trend is reflected in the inner component derived from BUDDI, with a negative gradient progressing from $1R_e$ to $2R_e$. This trend continues even moving toward $1R_e$ of the outer component, which hosts the least metal-enhanced populations in the galaxy. While both the mass-weighted and the light-weighted metallicity maps systematically show the same trend, the light-weighted map also appears to show less metal-enhanced populations compared to the mass-weighted map.

Likewise, J205050 appears to host a central core that is older than the rest of the galaxy, which also lies within $1R_e$. Beyond the central region, however, the mass-weighted stellar age map is mostly homogeneous. From the light-weighted age map, it is difficult to observe any gradient, there appear to be both younger and older stellar populations across the outer component of the galaxy, but the oldest populations are still clustered in the centre. Both the mass-weighted and light-weighted metallicity maps effectively mirror those presented in galaxy J020536. The central core shows relatively higher metallicities, with a decline moving radially outward, again reflected in the modelled components moving from $1R_e$ to $2R_e$ of the inner component. The trends exhibited in the light-weighted metallicity map are again only different in the sense that they are systematically less metal-enhanced than in the mass-weighted map.

The mass-weighted age map of J225546 does not indicate any substantial systematic trends, exhibiting both older stellar populations ($t \gtrsim 12$ Gyr) and slightly younger populations with differences hardly reaching 1 Gyr across different regions of the galaxy. The light-weighted age map similarly shows a diverse range of stellar ages across the galaxy. In both cases, the region south-west of the galaxy shows an anomalous population compared to the rest of the galaxy outskirts or the outer component. This area corresponds to the location of the galaxy at $z = 0.22$, where the Voronoi bins are dominated by its strong emission rather than J225546, causing this region to appear younger. The metallicity maps are consistent with the previously described galaxies, with the central region dominated by metal-rich stars, and a negative gradient with lower metallicity stars being hosted in the outskirts. Similarly, the most metal-enhanced regions in both the mass-weighted and light-weighted maps are hosted within $2R_e$ of the modelled inner component; although the negative gradient is steeper in the light-weighted map than it is in the mass-weighted map moving from $1R_e$ to $2R_e$. We also note that the neighbouring galaxy hosts relatively metal-poor stellar populations;

however analysing this galaxy is beyond the scope of this work.

3.5.4 Temporal mass and luminosity contributions from inner and outer components

The full spectral fitting process with pPXF returns a set of weights representing the relative contribution of each input SSP template to the optimised best-fit solution. From this, the 2D star formation history (SFH) of the galaxy components can be plotted on an age-[M/H] grid created from the stellar age and metallicity steps of the input stellar templates (see first and second columns in Figs. 3.4, 3.5, and 3.6). This proxy of SFH portrays the chemical evolution of the components through time, indicated by episodes of star formation. The 1D star formation histories (see third column in Figs. 3.4, 3.5, and 3.6) can then be constructed by cumulatively summing up the normalised weights over all the metallicities at each stellar age step in the grid, such that the total fraction is 1. In this study, since we analyse both mass-weighted and light-weighted stellar populations (Sect. 3.5.2), our reconstructed SFHs highlight the mass fraction and light fraction formed at different lookback times. The time evolution of the cumulative mass fraction provides insights into the stellar mass assembly history of the galaxy, such as whether it formed stars rapidly in the early universe or experienced prolonged star formation. The cumulative light fraction, on the other hand, highlights any recent star formation prominently since massive, young stars dominate the stellar luminosity of the galaxy and therefore have a higher impact on the light distribution when compared to the cumulative mass fraction. Furthermore, the light-weighted age distributions trace the most active phase of star formation in the galaxy.

Figures 3.4, 3.5, and 3.6 illustrate the 1D (right-most panels) and 2D (first and middle panels) star formation histories from the mass-weighted and the light-weighted stellar populations in the top and bottom rows, respectively. The 2D SFHs are depicted by the mass or light fractions in the age-[M/H] grid, with the weights coloured according to the colour bar on the right of each plot. In the 1D SFHs, the inner component is shown in red and the outer component in blue. The x -axis in both depictions is time, but for the 2D SFH, the time is denoted as the logarithmic stellar age in yr, while for the 1D SFH, this is instead denoted by the lookback time in Gyr. For galaxy J225546, there is an additional “component” coloured in grey, which is in fact the neighbouring galaxy described in Sect. 3.4.3. This is only depicted here to emphasise the reliability of BUDDI in modelling multiple inherent components and external galaxies simultaneously, and it does not play a part in the inferences from the study.

3.5.4.1 Mass fractions

The weights from pPXF measure the fractions of stellar populations that contribute to the total stellar mass of the galaxy or object of interest. As a preliminary overview, in Table 3.5, we compute the mass contributions from stars that are older than 8 Gyr (t_{old}), of intermediate ages between 4 and 8 Gyr (t_{inter}), and from stars that are younger than 3

Table 3.5: Mass fractions and light fractions estimated by pPXF. The fraction of contribution from the mass and luminosity of stellar populations that are old ($t > 8$ Gyr), of intermediate age ($4 < t < 8$ Gyr), and young ($t < 3$ Gyr).

Mass fractions (%)				
Galaxy	Comp	t_{old}	t_{inter}	t_{young}
J020536	single	99.96	0	0.04
	inner	100	0	0
	outer	88.34	11.58	0.08
J205050	single	100	0	0
	inner	100	0	0
	outer	64.13	35.83	0
J225546	single	99.58	0.42	0
	inner	100	0	0
	outer	98.01	1.99	1.50
Light fractions (%)				
Galaxy	Comp	t_{old}	t_{inter}	t_{young}
J020536	single	98.53	0	1.47
	inner	100	0	0
	outer	79.18	19.07	0.34
J205050	single	100	0	0
	inner	100	0	0
	outer	63.19	36.81	0
J225546	single	100	0	0
	inner	100	0	0
	outer	98.04	1.96	0

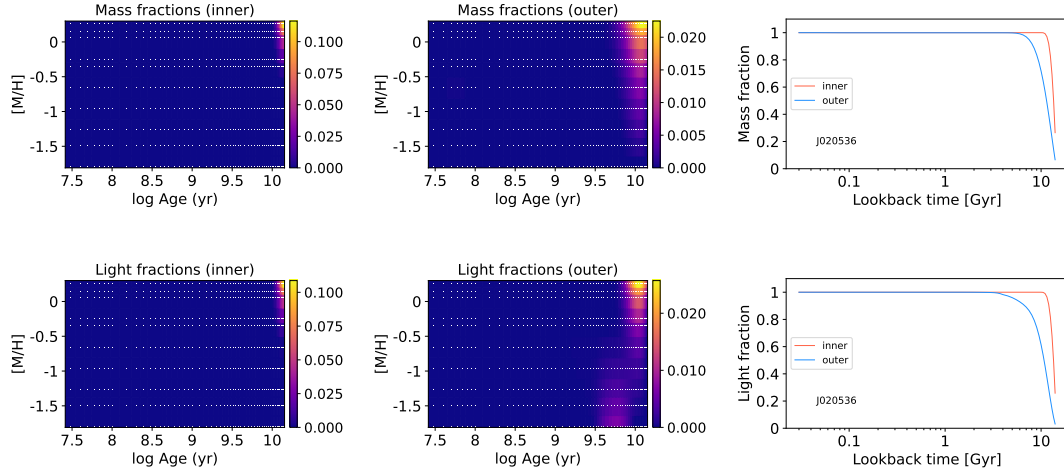


Figure 3.4: *Stellar populations in metallicity-age grids and their subsequent assembly histories for galaxy J020536.*

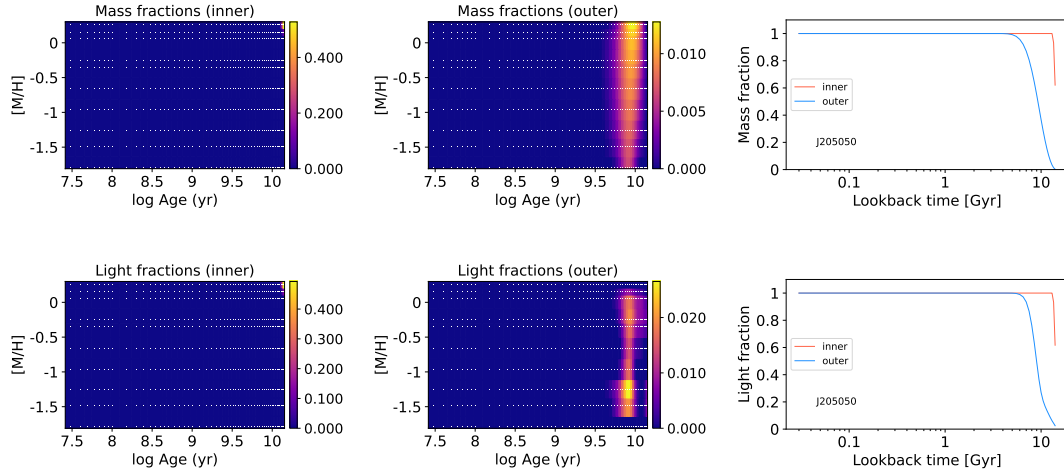


Figure 3.5: *Stellar populations in metallicity-age grids and their subsequent assembly histories for galaxy J205050.*

Gyr (t_{young}). These values are listed for the galaxy overall, and for the inner and outer components. Clearly, the majority of the mass of the ellipticals lies in stars older than 8 Gyr, in each component as well as collectively, making up over 85% of the mass for all except the outer component of J205050, which only contributes to 64%. The inner component appears to be entirely composed of such old stars, adding up to 100% of its mass. The fraction of stars younger than 3 Gyr is null or insignificant, except for the outer component of J225546, where they contribute mildly to 1.5% of the mass. This small fraction cannot be entirely ruled out as a consequence of the neighbouring object, which might not be completely deblended even when its profile is fit simultaneously with that of the target galaxy. The stars of intermediate age are prominent only in the outer component, varying from low to substantial in their mass contributions, between $\sim 2 - 35\%$. A more detailed analysis on the mass assembly of the components through cosmic time is described in the following Section.

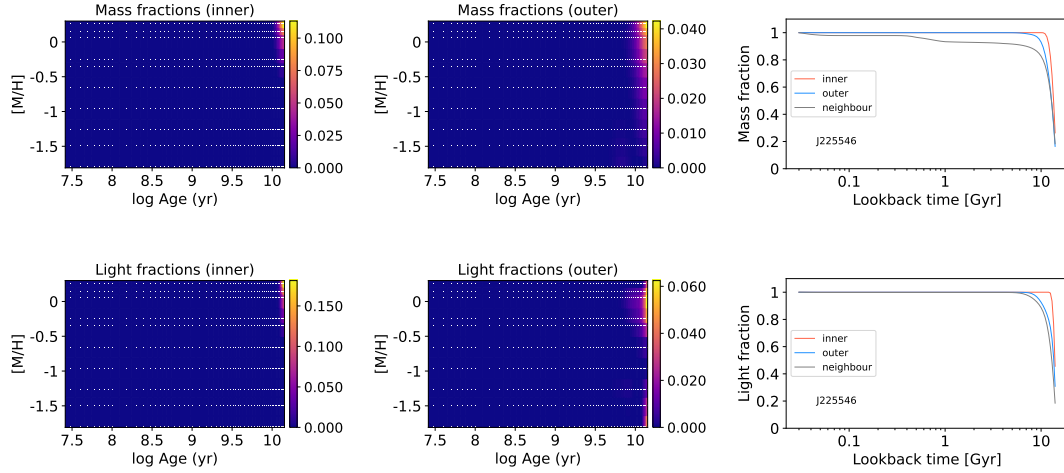


Figure 3.6: *Stellar populations in metallicity-age grids and their star formation histories for galaxy J225546.*

3.5.4.2 Star formation histories from mass fractions

The 2D SFHs built from the mass fractions in general illustrate a picture where the inner component of the elliptical galaxies are extremely old and have higher metallicities. These weights are concentrated in the upper right corner of the grid, with a minute spread in age ($t_{MW} > 10$ Gyr), while there is a relatively larger spread in metallicity for galaxies J020536 and J225546, between -0.5 and 0.3 dex. The outer component also shows a dominant old stellar population, with a relatively wider spread in age compared to the inner component, and an even greater spread in metallicity, with stellar populations spanning ages $\sim 4 - 14$ Gyr and the entire metallicity range of the grid. These are indicative of minor episodes of continuous and slower stellar mass assembly that have occurred after the primary peak of star formation, wherein different stellar populations have been accreted.

The 1D mass-weighted SFHs trace the cumulative mass assembly of each component through cosmic time. They complement the results from the 2D SFHs with a clear depiction of the inner component having assembled its stellar mass initially and swiftly within a very short timescale, forming the inner core of the galaxy. The peak mass assembly of the outer component exhibits a delay of several Gyr compared to the inner component, and has assembled its mass at a slower rate, over the course of a few Gyr, most likely growing its mass by continuous accretion during this time until attaining the present-day mass. The SFHs for the inner and outer components exhibit a flat slope from ~ 10 Gyr and ~ 5 Gyr ago respectively, up to $z = 0$, marking their quiescence during this period. This clearly points to an inside-out mass growth scenario for local elliptical galaxies.

Furthermore, the timescales τ_{50} and τ_{90} were measured from the cumulative mass fractions (Table 3.4). τ_{50} measures the lookback time when half of the present-day stellar mass had been assembled, while τ_{90} measures the same for 90% of the present-day mass, which is related to the onset of quenching in the galaxy (Ferré-Mateu et al.,

2018; Romero-Gómez et al., 2024), especially for retired quiescent galaxies. For all three ellipticals, the inner component had already formed half of their mass by ~ 13 Gyr ago, while the outer component had taken $\sim 1 - 5$ Gyr longer to assemble the same (with timescales of 2.09 Gyr, 4.74 Gyr, and 670 Myr for J020536, J205050, and J225546 respectively). Similarly, the inner component appears to have quenched its star formation activity as early as ~ 12 Gyr ago. The outer component, on the other hand, stopped forming stars only $\sim 6.5 - 10.5$ Gyr ago, roughly 3 – 5 Gyr after half the stellar mass had assembled. The relative contribution of the inner component to the total stellar mass was found to be 50% for all three galaxies, indicating that half of the stellar mass originates from the outer component. These collective findings demonstrate an early and rapid assembly of the majority of the stellar content within the inner component of the elliptical galaxies, which consequently appears to be a “co-dominant” component in terms of its influence on the present day total stellar mass. The longer assembly timescales attributed to the outer component, along with it hosting half of the galaxy stellar mass, imply a slower addition of stars well after the inner component has quenched its star formation.

3.5.4.3 Light fractions

Similar to the mass fractions described in Sect. 3.5.4.1, the light fractions are estimated by pPXF, from which the fraction of luminosity contributions of different stellar populations can be inferred. The luminosity of the galaxies is predominantly composed of an old stellar population ($t_{LW} > 8$ Gyr), contributing nearly 100% of the light on average. This is mirrored in both the inner and outer components as well, with the young stars of $t < 3$ Gyr having no contribution to the luminosity. The intermediate-age stars contribute substantially more to the outer components, accounting for $\sim 20 - 37\%$. The exception to this is the outer component of J225546, for which the intermediate stars only accounting for $\lesssim 2\%$ of the luminosity of the galaxy. The SFHs of each component are described in depth below, which puts into perspective these contributions to the galactic light across cosmic time. Based on the mass and light fractions of various stellar ages, the evident conclusion is that these ellipticals are indeed substantially evolved galaxies with no recent star formation.

3.5.4.4 Star formation histories from light fractions

The SFHs drawn from the light fractions as shown in the lower panels of Figures 3.4, 3.5, and 3.6 respectively, returned from the stellar population synthesis indicate how much of the galaxy light is dominated by stars created at different cosmic epochs. Since the light-weighting is performed with the V -band luminosity, the results also trace when star formation episodes had occurred during more recent times. τ_{50} and τ_{90} derived from the cumulative light fractions (Table 3.4) indicate the lookback time when the stars contributed to 50% and 90% respectively of the luminosity of the galaxy or its components. In this case, τ_{90} does not necessarily highlight the onset of quiescence,

but rather highlights the epoch when the stars contributed to 90% of the present-day luminosity. We find that the light-weighted 2D SFHs follow the trends observed in the mass-weighted SFHs, revealing a similar pattern in the history of star formation. In J205050, a significant portion of the light originates from stellar populations older than 5 Gyr, spanning a broad range of metallicities from super-solar to very sub-solar, reflecting a diverse range of stellar populations, similar to the mass-weighted 2D SFH. In contrast, the outer component of J225546 is dominated primarily by stars older than 10 Gyr, but with a wide spread in metallicities.

In galaxy J020536, the old metal-enhanced stars still dominate the luminosity of the inner component, suggesting that the bulk of the stellar mass assembly corresponds to a single significant star formation event more than 10 Gyr ago, which formed rapidly and very early on in the life of the Universe. This component appears to have formed the majority of its stars that now contribute to 90% of the luminosity 12 Gyr ago. In the outer component of J020536, there appears a smaller fraction of a younger stellar population aged ~ 4 Gyr with lower metallicities reaching sub-solar metal abundances. The outer component has taken an additional 5 Gyr to form or assemble the stars dominating 90% of the light. The 1D SFHs also show a long period of constant cumulative light fraction in the inner component, where it appears to have achieved quiescence and remained undisturbed by new star forming episodes or accretion in the last 4 Gyr.

The light fractions of J205050 similarly show a predominantly old and metal-enhanced light-weighted stellar population in the inner component, which similar to J020536, has undergone a rapid event of bulk star formation at early epochs. The τ_{90} lookback time, indicating the major star formation in this component, seems to have occurred and ceased roughly 13.5 Gyr ago, followed by a flat unperturbed quiescent slope leading to the present-day. The outer component, however, shows a delayed contribution to 90% of the luminosity, with most of these stars having formed around 7 Gyr ago. It has remained quiescent since then, with no significant star formation up to the present day.

Following this trend, the 2D light-weighted SFH of J225546 shows an inner component again dominated by the light of the old metal-rich stars at solar and super-solar metal abundances. The outer component consists of two distinct light-weighted stellar populations, one with old and metal-enhanced stars, and the other with similarly old but quite metal-poor stars reaching $[M/H]_{LW} < -1$ dex. The cumulative light fractions complement this with a clear indication that the peak of star formation in both the inner and outer components happened at earlier lookback times. The outer component followed after the principal star formation occurred, but the formation timescale between both components for this galaxy is not as substantial as for the other two galaxies, which is also evident from their τ_{90} , indicating a delay of roughly 3 Gyr.

The stellar population analyses and the reconstructed star formation histories support the two-phase scenario introduced in Sect. 3.2. The inner regions of the ellipticals ($R_e < 5$ kpc) could, in principle, be associated to the in-situ star formation within the galaxy as a result of dissipative collapse or major mergers very early on in their lifetimes. In contrast, the outer component ($6 < R_e < 20$ kpc in this sample), is likely a

combination of star formation formed in-situ from gas, with the majority of the stellar envelope having been accreted through dry mergers over longer timescales compared to the inner component. Regarding the former, [Choi et al. \(2024\)](#) find that in cosmological simulations, mergers can result in the accretion of gas from external galaxies. They also find signatures of smoothly accreted gas, particularly through the cooling of the galaxy halo, aligning with the findings of [Lagos et al. \(2015\)](#) in ETGs. In [Choi et al. \(2024\)](#), another origin is attributed to gas from the primary galaxy halo that has been recycled over generations of stellar evolution. While these processes were examined in the context of gas accretion in the inner regions of galaxies fuelling a supermassive black hole, a smaller fraction of the gas can be distributed over different regions, including the outskirts. On the other hand, the accretion of direct stellar material from dry mergers with external satellites of different metallicities occurs around the old, metal-rich core which undergoes minimal evolution since its star formation was quenched early on.

3.6 Discussion

In this work, we have decomposed three elliptical galaxies of $\log(M_*/M_\odot) \approx 11$, observed with MUSE, into an inner and outer component using the spectro-photometric code BUDDI. We have analysed the mass-weighted and light-weighted stellar populations of each component, and reconstructed their SFH to study the processes involved in their formation and subsequent quenching. The radial gradients of the stellar population properties were also measured as a complement to these analyses. In the following Section, these results will be explored in the context of the formation channels of present-day elliptical galaxies.

3.6.1 Multiple structural components in ellipticals: implications from surface brightness profiles

The notion that elliptical galaxies may consist of multiple components has been examined in several studies through 2D photometric decomposition, which are outlined in this Section. This work builds upon existing methods by incorporating the imaging and spectroscopic capabilities of integral field spectroscopy. The spectro-photometric decomposition technique with BUDDI not only models the surface brightness profiles of various components at each wavelength of an IFU datacube, but also enables a more accurate derivation of stellar populations from the resulting spectra compared to photometric colours, which often suffer from the age-metallicity degeneracy ([Worthey, 1999](#)).

[Huang et al. \(2013a\)](#) delve into investigating the possibility of multi-component ellipticals in a sample 94 local galaxies in the CGS survey. The high spatial resolution of deep optical images from this survey allowed for a reliable 2D decomposition of the ellipticals into 3-4 sub-components using GALFIT ([Peng et al., 2002](#); [Peng et al., 2011](#)) to study their structural properties in the V -band. They find that for a majority of their

sample, the surface brightness profiles are best modelled by three Sérsic components, representing a compact inner core, a middle component, and an outer extended envelope. The 2D residuals consistently improved with increasing complexity in the models. Interestingly, they report only a small fraction of their sample to be modelled with two components. Furthermore, they also suggest that their high-luminosity sample of ellipticals shows photometric signatures of being “core” ellipticals with a shallow slope within in the innermost component. [Lacerna et al. \(2016\)](#) report similar findings, noting a good fit with three Sérsic models for a sample of 89 isolated local elliptical galaxies from SDSS images. [Huang et al., 2013a](#) and [Huang et al., 2013b](#) link the inner and intermediate components to the phase of elliptical galaxy formation involving in-situ dissipative processes, while associating the outer component with a later stage of ex-situ star accretion through dry mergers. These findings and interpretations closely align with those presented in this work, despite differences in the number of components modelled.

Along these lines, [Spavone et al. \(2017\)](#) perform a detailed analysis of the surface brightness profiles of six massive ETGs in A VST Early-type GALaxy Survey (VEGAS) survey ([Capaccioli et al., 2015](#)). They adopt various profile combinations to identify the most accurate model. Four galaxies were effectively modelled using a Sérsic + exponential profile, whereas the remaining two were better represented by a double Sérsic model. Additionally, they find that a model consisting of two Sérsic profiles for the inner regions and an exponential profile for the outer region generally provides a good fit for all galaxies, which is their primary model for analysis. Following theoretical predictions, they conclude that the inner Sérsic profile represents a component formed by in-situ processes. The middle Sérsic profile represents the dominant component composed of a phase-mixed accreted component where the material has dynamically relaxed. The outer exponential profile was then associated with the unrelaxed accreted component, which often shows low surface brightness signatures of interactions, like shells or streams. From the 1D surface brightness profiles, they locate inflections that are indicative of physical transitions between the different components. A brief comparison with our 1D surface brightness profiles revealed that the inflection occurs at a galactocentric distance of $\sim 3.5 - 4$ kpc for the three ellipticals. The sizes of the inner “in-situ” component from our models lie within this apparent transition radius with $R_e \sim 1.5 - 3$ kpc. However, given the different model combinations used in both studies and the fact that our 1D surface brightness profiles are constructed solely from the r -band image slice of the datacube, we cannot conclusively determine if the inner component corresponds to the transition radius observed in the surface brightness profiles, as this radius can shift depending on the wavelength employed.

Despite the distinct methodologies, both the photometric and spectro-photometric models support the idea that the inner component is primarily shaped by in-situ star formation, while the outer component is dominated by ex-situ accretion, consistent with theoretical predictions and simulations.

3.6.2 Stellar population properties: inside-out formation and the two-phase scenario

Several studies in literature have investigated the mode of mass assembly in elliptical galaxies using IFS. However, most of these studies address this question by measuring the radial gradients of stellar age and metallicity. Our methodology instead measures the mean stellar population properties in each of the two “clean” components extracted with the spectro-photometric code BUDDI, where the mixing of light is mitigated between the components. Therefore, the comparisons that we make to literature in this Section are less specific to the measurements and techniques, and rather focus on the general results and implications to elliptical galaxy formation.

With the diverse range of methods and observations used to tackle this, there exists a broad variation in the stellar population results reported by different IFS-based studies. For instance, [González Delgado et al. \(2015\)](#) report elliptical galaxies in the Calar Alto Legacy Integral Field Area Survey (CALIFA) survey showing slight negative gradients in light-weighted age, with ~ 10 Gyr in the centre and dropping to ~ 5 Gyr at $1R_e$. A notable outcome by [Zibetti et al. \(2020\)](#) in their light-weighted stellar age analysis for 48 elliptical galaxies in CALIFA was the U-shaped profile in the inner regions within $0.4R_e$. The authors attribute this shape to a quenching process starting from the very central galactic regions. Otherwise, in contrast to the other studies, they find a slightly positive gradient up to $1.5R_e$, beyond which the slope flattened out. With the Mapping Nearby Galaxies at APO (MaNGA) survey, [Lacerna et al. \(2020\)](#) studied the stellar population properties of classical ellipticals, recently quenched ellipticals, and blue star-forming ellipticals independently. Our sample of ellipticals fall under the classical category, and we limit our comparisons to this sub-sample. They found moderately negative gradients in the light-weighted ages, and flat gradients in the mass-weighted ages. Similar flat age gradients were reported in [Parikh et al. \(2019\)](#), while weak negative age gradients were found in [Domínguez Sánchez et al. \(2019\)](#) for elliptical galaxies in MaNGA, and similarly in [Riffel et al. \(2023\)](#) for ETGs with MaNGA. A different study with MaNGA by [Goddard et al. \(2017\)](#) reported contrasting slightly positive gradients for ETGs, which include both ellipticals and S0s.

In principle, from these studies, a positive gradient in stellar age implies the galaxy has assembled its mass from the outside in. A negative gradient, on the other hand, suggests an inside-out mass growth, starting from the innermost regions of the present-day observed elliptical galaxy. Along those lines, the flat gradients observed in some works would indicate a more uniform mass growth throughout the galaxy. However, the stellar populations of galaxies, like most of their properties, are driven by a multitude of processes that are more likely to be interwoven rather than relying on a single mechanism. Our results from the stellar population analysis fall within the wide diversity of results that have been observed in the studies mentioned above. Both the mean mass-weighted and light-weighted stellar age differences between the inner and outer components were low to moderate ($\sim 1 - 5$ Gyr). For the three elliptical galaxies in this sample, this

observation insinuates a mild inside-out formation scenario for J020536 and J225546, and a more pronounced inside-out formation for J205050. This is qualitatively and globally similar to the moderately negative or flat gradients reported in a few of the aforementioned IFS-based studies. In the context of a two-component galaxy, the inner component would have formed stars earlier, while the star formation continued for a slightly longer period, building up the stellar mass on the outskirts. Such old stellar populations are typical for galaxies that have an early intense star formation in the inner component occurring in an extremely short timescale, which quench soon after a few Gyr. The relatively younger ages in the outer component could then be associated to accreted stars from satellite galaxies that are themselves quenched and are nearly as old as the main elliptical galaxy. At this point, we note again the high levels of degeneracy associated with stellar populations older than 8 Gyr, and it is important to be cautious when interpreting such old ages.

While the mean stellar ages offer some perspective into the growth mode of these galaxies, they are solely not enough to confirm this theory. The list of literature results described earlier in this Section additionally report results on the stellar metallicity analyses for their samples of ellipticals and ETGs. Most of the work done along these lines in the past with IFS have consistently reported negative metallicity gradients, with only the slope signifying their steepness varying between them. The exception is [González Delgado et al. \(2015\)](#), where they find nearly flat gradients in mass-weighted and light-weighted stellar metallicities for an elliptical galaxy sample in CALIFA. The reason for this discrepancy is not fully understood, and could be linked to the different methodologies employed in different studies. For an extensively shared sample, [Zibetti et al. \(2020\)](#) on the other hand, notice steeper gradients up to $1.5R_e$, after which the profiles transition to a flatter slope. Consistent with this, for their sample of classical ellipticals, [Lacerna et al. \(2020\)](#) find mildly steep gradients for the mass-weighted and light-weighted metallicities up to $1R_e$, beyond which the profiles flatten. Negative metallicity gradients are in accordance with the results presented [Parikh et al. \(2019\)](#), [Domínguez Sánchez et al. \(2019\)](#), and [Goddard et al. \(2017\)](#).

Based on these studies on stellar metallicity gradients, a negative slope points to one possible scenario of early dissipative collapse from a gas-rich cloud already enhanced with metals. The formation and metallicity profiles of ellipticals were investigated via simulations in [Kobayashi \(2004\)](#), where the relevant physical processes including radiative cooling, stellar feedback through SN and winds, and chemical enrichment models were incorporated. However, the AGN feedback often observed in massive galaxies was not considered. Under this simulated regime, they find that the radial metallicity gradients trace SFHs, and require a combination of both monolithic collapse and major mergers to adequately explain their variation. Moreover, they expect that subsequent major mergers tend to taper out the radial metallicity profiles, diminishing signatures of physical processes prior to the merger. If the progenitor mass ratios are high enough, the metallicity gradients can be completely destroyed and would appear flat in present-day observations. Additionally, the variation in metallicity gradients

can be triggered by late gas accretion in the outer regions, where a slower phase of star formation is then induced. With the inclusion of AGN feedback in [Taylor et al. \(2017\)](#), they reinforce the flattening of metallicity gradients by major mergers in massive galaxies, but the quenching induced by AGN makes it challenging to regenerate the gradients through later in-situ central star formation.

Our results show a substantial decrease in the metal enhancement for the outer component, compared to the metal-rich inner component, observed in both the mass-weighted and light-weighted properties. A clear negative radial gradient of metallicity is seen qualitatively in the 2D maps as well, with a decline from the central region of the galaxies. This points to an intense in-situ star formation phase in the inner component, that might have been influenced by major mergers. This is difficult to discern from our analysis since our estimates depict the mean stellar metallicity for each component, and therefore any information on gradients that might or might not exist within the inner component is lost. The decline in metallicity for the outer component, in tandem with the old stellar ages presented by these stellar populations, can be explained on the basis of accretion of ex-situ stars from old satellite galaxies that have formed their stars from metal-poor gas. In a dry merger, the ex-situ stars are deposited on the outskirts of the galaxy due to its lower binding energy compared to the in-situ formed stars ([Spavone et al., 2017](#)), causing accreted stars to dominate in the outer component. The combined stellar population properties presented in this work are therefore compatible with the two-phase scenario described in Sect. 3.2, with a preferred inside-out mass growth for the intermediate-mass ellipticals comprising our sample.

3.6.3 Star formation histories: stellar assembly across time

The star formation of ETGs has been extensively investigated in several works with IFS surveys, using a variety of techniques, from which some of the most relevant ones will be described in this Section. Similar to the stellar population gradients, our approach allows us to analyse the SFH of the inner and outer components of each elliptical galaxy, identifying the epochs of extensive star formation and quenching. These results from the literature, including ours from this study, align well with the two-phase scenario predicted in simulations of spheroid-dominated galaxies ([Naab et al., 2009](#); [Oser et al., 2010](#); [Johansson et al., 2012](#)).

Even from a cursory look, it would appear that the ellipticals in our sample fit the description of “red and dead” retired galaxies commonly referenced in literature. This impression is supported by the cumulative star formation histories (Fig. 3.4, 3.5, and 3.6), which reveal a significant early and rapid assembly of stellar mass for the inner component, heavily influencing its mass and luminosity. Similarly, the outer component exhibits a concentrated period of star formation in its early life, resulting in the majority of its stellar mass and luminosity. We surmise that the inner and outer components represent the in-situ and ex-situ components respectively, motivated by similar works described in [Huang et al. \(2013b\)](#), [Huang et al. \(2013a\)](#), [Spavone et al. \(2017\)](#), and

Spavone et al. (2021). Following the initial burst of star formation, the mass assembly histories of both components allude to rather quiescent ellipticals where there has been no significant build-up of stellar mass over roughly the last 8 Gyr. The star formation histories that account for the luminosity contributions by the stellar populations in each component depict a slightly nuanced picture. The majority of the light does indeed originate from the initial rapid star formation episode shortly after the Big Bang, and we find no indications of younger stellar populations contributing to the stellar mass or luminosity of any of the galaxies.

The star formation histories of the outer components are relatively more extended than those of the inner components, with the peak of star formation and mass assembly shifted towards relatively recent epochs. However, from Table 3.5, for galaxies J020536 and J205050, the contribution of stars younger than 3 Gyr to the stellar mass or luminosity is still entirely negligible. The fraction of intermediate-age stars is however quite substantial next to the oldest stars, suggesting this population either formed in-situ later in time or was accreted as an ex-situ population through dry mergers with relatively younger satellite galaxies aged between 4 and 8 Gyr old. Such a blend of old and intermediate-age stars were measured for dwarf elliptical galaxies in the Virgo and Fornax galaxy clusters (Geha et al., 2003; Michielsen et al., 2008), and in the Local Group (Geha et al., 2015). The unperturbed nature of the quiescence of these elliptical galaxies provide additional evidence that they are classical “red and dead” objects in the local Universe, where both in-situ and ex-situ star formation have ceased several Gyr ago. In that vein, the following segments of the discussion outline other studies in literature that have investigated the assembly histories of elliptical galaxies through various observations and techniques.

Lacerna et al. (2020) analysed the integrated star formation histories of 251 classical elliptical galaxies in MaNGA. They find that these galaxies had built up 70% of their stellar masses between 8 and 11 Gyr ago, and 90% of their masses by 5 Gyr ago at the latest. In conjunction with their results on the stellar population gradients (we refer the reader to Sect. 3.6.2), they predict that in the earliest stages of elliptical galaxy formation, star formation and the resulting stellar populations were relatively uniform across both the inner and outer regions. It was only in subsequent epochs that the outer regions started forming their stars after the inner regions did. Moreover, by analysing the specific star formation rates of the galaxies, they conclude that, following an initial phase of substantial homogeneous star formation, classical ellipticals continue to grow from the inside out and are subsequently quenched in the same manner. This was naturally explained on the basis of an intense burst of significant star formation, followed by rapid gas consumption, leading to a swift quenching of star formation. Nevertheless, they recognise the role of dry mergers where ex-situ stars can be accreted on to the main elliptical, and continue its stellar mass assembly. Despite the methodology and sample used being entirely different to theirs, the inferences we present are remarkably similar in the context of the two-phase formation scenario for early-type galaxies. However, it is important to note that the fossil-record method does not directly characterise a given

stellar population as having formed via in-situ or ex-situ processes.

A study by [González Delgado et al. \(2017\)](#) employs the fossil-record method to reconstruct the spatially resolved 2D SFHs of galaxies spanning a wide variety of morphologies in the CALIFA survey. Similar to Table 3.5 in this work, they report the fractions of the stars in different stellar age bins which contribute to the luminosity of the galaxy. They find that $\sim 3\%$ of stars younger than 1 Gyr contribute to the light from the outer regions of ellipticals, while the older stars with ages over 4 Gyr dominate with $\sim 86\%$ of the populations. In the inner regions, that fraction increases to 96% for the older stars, and 1% for the younger population. We note that this is slightly in contrast to our sample, which reveals no traces of young stellar populations in the inner components. The contributions to the stellar mass follow the same pattern in the inner and outer regions. Furthermore, they find evidence of an extended phase of star formation since 4 Gyr ago, and signs of the outer regions of ellipticals that are actively forming stars after the quiescent phase.

Another sample of nearby ETGs from the ATLAS^{3D} survey ([Cappellari et al., 2011](#)) were investigated in [McDermid et al. \(2015\)](#), where they measure the spatially resolved stellar populations and integrated star formation histories within $1R_e$ of the galaxies. Assessing this region within $1R_e$ across the galaxies in our sample (see Table 3.3), we note that this would result in a loss of information about the outskirts or the outer component, which extend to at least twice the R_e from the single Sérsic model. They find that roughly half the present-day stellar mass was already assembled as early as 2 Gyr after the Big Bang. The most massive present-day ETGs with $M_* > 10^{10.5} M_\odot$ host these old stars, and had built up 90% of the stellar mass by $z \sim 2$, which corresponds to a lookback time of approximately 10.5 Gyr ago under the cosmology defined in Sect. 3.2. They attribute their results to the picture where the old and metal-rich ETGs were formed from an early dissipative process at high redshifts, which is followed by a phase of quenching. Subsequently, stellar accretion takes over as the dominant mechanism of stellar mass growth, aligning with the two-phase scenario of formation.

The importance of ex-situ stars that have been accreted by early-type galaxies in their later stages has been demonstrated by observations and simulations, particularly with the IFS surveys. The metallicity and age distributions and profiles are often exploited to estimate the fraction of ex-situ accreted stars in an ETG. For instance, [Oyarzún et al. \(2019\)](#) measure the ex-situ stellar mass fractions of ETGs in the MaNGA survey. They find that for ETGs of $M_* \gtrsim 10^{11.5} M_\odot$, ex-situ stars make up to 80% of their stellar mass, at a galactocentric distance of $\sim 2R_e$. Similarly, using a combination of full-spectral fitting and galaxy evolution models, [Davison et al. \(2021\)](#) identify ex-situ stars in ETGs observed with MUSE, and report that the fraction of accreted stars increases with galactocentric radius, with values ranging between ~ 30 and 100% at $\sim 2R_e$. [Spavone et al. \(2021\)](#) present deep imaging of three massive galaxies from the VEGAS survey, combined with MUSE observations. This study correlates the structural components from imaging with the kinematics and stellar populations from IFS analysis, to explore the mass assembly histories of these galaxies. They find ex-situ mass fractions of 77%,

86%, and 89%, indicating that accretion is the primary contributor to the stellar mass. Our results align with the ranges reported by some of these studies, indicating that 50% of the stellar mass was accreted from external galaxies, forming a second “co-dominant” component in the context of a dual-component picture of elliptical galaxies.

3.7 Summary and conclusions

In summary, this study was primarily focused on the identification of the different components present in elliptical galaxies of intermediate stellar mass in the local Universe. For a sample of three galaxies observed with MUSE, we successfully modelled the surface brightness profiles adopting two Sérsic components, representing an inner and an outer component, using the spectro-photometric decomposition code BUDDI. After this, the full-spectral fitting software pPXF was used to fit the cleanly extracted spectra and estimate the mass-weighted and light-weighted stellar populations of each component, and subsequently their star formation histories. Spatially resolved 2D stellar population maps were constructed after binning the datacubes to achieve a sufficient minimum S/N threshold using the Voronoi tessellation method. We investigated the physical properties of each component to constrain the formation scenarios and the mode of stellar mass growth in local elliptical galaxies. While similar studies with photometric decomposition on data from imaging surveys have been conducted, this approach of using IFS to model multiple components in datacubes is relatively new and offers a different perspective of exploring elliptical galaxy formation and evolution. The main conclusions of our study are listed below:

- The best fit for the surface brightness profiles of the elliptical galaxies in this sample was achieved using two Sérsic components with distinct properties, referred to as the “inner” and “outer” components.
- The stellar population analysis of the inner and outer components and the spatial maps reveal an inside-out formation and growth mode in ellipticals. The majority of the stellar populations are older than 8 Gyr for both components (100% for the inner component, and $\gtrsim 65\%$ for the outer component), from both the mass and light-weighted ages. The inner components are generally more metal-enhanced compared to the outer components.
- The reconstructed SFHs highlight an inner component that has formed and assembled the bulk of its stars in the earliest epochs of the Universe, before $z \sim 2$. This component is expected to have formed from interlinked physical processes: monolithic dissipational collapse and major mergers, forming a central core hosting the oldest stellar populations. The outer component, however, aligns more with accretion events from past dry mergers, where old metal-poor stars have been deposited on the outskirts. This process continues to build the stellar mass of the ellipticals without having to undergo a new phase of star formation. The fraction of mass and luminosity contributed by the different stellar populations in the two

components further confirms the two-phase assembly mode.

- The mass weights from pPXF additionally provide information about the formation (τ_{50}) and quenching (τ_{90}) lookback times, which show that half of the present-day stellar mass in our sample had already assembled ~ 12 Gyr ago, and had undergone quenching around ~ 5 Gyr ago at the latest. The light-weighted properties show similar trends, except τ_{90} , which indicates a more extended star formation history in the outer component, with 90% of the light contribution coming from lookback times as recent as ~ 5 Gyr ago.

In conclusion, our method of decomposing the multiple components of elliptical galaxies has helped trace back the signatures of the physical processes involved in their formation and evolution across cosmic time. This serves as an initial pilot study, which can be extended to a more statistical sample such as the ellipticals in BUDDI-MaNGA (e.g. [Jegatheesan et al., 2024](#)) to better constrain the formation pathways. Possible future follow-up work involves capturing the extremely low-surface brightness stellar halos of elliptical galaxies and modelling their components ([Johnston et al., 2018](#)). Additionally, studying a more representative sample of local ellipticals, encompassing a range of masses from dwarf to giant ellipticals, variations in star formation activity, and in different environments, would provide a comprehensive understanding of the formation and evolution of these galaxies.

SUMMARY AND FINAL REMARKS

Over the years, vast imaging studies have allowed highly statistical analyses of galaxies and their components, but are limited by their wavelength coverage. To this end, the advent of integral field units providing wide field, high spatial resolution spectrographs in the past decade has revolutionised the field of galaxy evolution. With spatially resolved spectra across whole galaxies, we can study the stellar populations residing in different regions of the galaxies. The well resolved IFS data like MUSE do not offer statistics as opposed to imaging, but are best used to perform detailed analyses of the components of individual galaxies. MaNGA combines these two courses of action by providing a large sample with the detailed IFU information. Since the introduction of IFUs, there have been studies revolving around the spectra of different galaxy components. However, these studies with IFUs are however still affected by the contamination of the light from any component on the others, and therefore the next step in galaxy evolution studies with IFUs is to isolate cleanly the light from each component to extract and study their clean spectra. BUDDI has been the first code to successfully achieve this, and the projects developed within the BUDDI framework will contribute significantly to our understanding of the formation and evolution of galaxies by combining state of the art observations with this novel technique. The projects in this thesis explored different galaxy morphologies using BUDDI, both for individual galaxies as well as for statistical samples, with which we hope to have addressed some of the key questions in this field. In this thesis, I present a comprehensive analysis of galaxy formation scenarios through the spectro-photometric decomposition of the structural components of spiral and elliptical galaxies.

The major structural components of spiral galaxies include a bulge and a disc, whose physical properties can vary across the range of morphological sub-types often categorised under the Hubble - de Vaucouleurs scheme. After decomposing the light profile of the 968 spiral galaxy datacubes presented in the BUDDI-MaNGA sample into their constituents as a Sérsic bulge and an Exponential disc, I performed stellar population synthesis using the full spectral fitting tool pPXF. The mass weights that were returned by the software as a result of the fitting procedure, contain hidden insights from the spectra of each component. I used the weights not only to derive the

mean mass-weighted stellar populations, but also to reconstruct the mass-assembly histories across cosmic time. The study focussed on analysing these properties and their dependence on stellar mass and morphology of the respective components. With the combination of these decomposition and archaeological methods, the primary result I find is the downsizing effect for Sa-Sc type galaxies, which becomes stronger for the bulges the earlier the morphological type is, while the effect is weaker for the discs. In Scd-Sd types, I no longer find any indication of downsizing for either the bulges or the discs. The next crucial result I find is the rapid assembly of bulge stellar mass at very early times in the cosmic history of the galaxy, and the more extended and sometimes delayed stellar assembly of discs. However, the mass-assembly histories appeared more and more extended with later morphological types. I find that the early-type spirals were predominantly formed in an inside-out manner, while a consistent scenario was harder to observe in late-type spirals, demonstrating that spiral galaxies as a whole cannot be represented by a universal formation mechanism. The stellar population analysis of various spiral morphologies indicated the presence of older and metal-rich bulges, with a smaller fraction of younger and metal-rich population compared to those found in the discs, showing a similar increasing trend with morphology.

In the case of the elliptical galaxy study, given their intricate structure as both observations and numerical simulations clearly support, I delved into the multiple-component context of these galaxies in this project. IFS and structural decomposition with BUDDI take the stage once more, but this time with MUSE observations of three elliptical galaxies in the local Universe. The goal was to extract the spectra and stellar populations to interpret their physical significance, if ellipticals were found to host more than one major component. This project is motivated by the fits in BUDDI-MaNGA, where ~ 160 elliptical galaxies had been fit successfully with a Sérsic+Exponential model, with physically valid structural parameters (see Appendix E). Given that the field of view of MaNGA might not always capture the outer regions of a galaxy, this was best investigated with MUSE, which has finer spatial resolution and FoV that allowed us to capture the light from the entire galaxy. In the current study with MUSE, I did not constrain the outer component to be exponential. Instead the galaxies were modelled with two Sérsic profiles simultaneously, and I labelled them as an inner and outer component. The dual-component nature of ellipticals emerged from this technique, and revealed a clear inside-out formation and growth. Through the spectral analysis, these ellipticals were determined to host consistently old and relatively metal-enhanced stellar populations which had quenched the galaxies long since their initial burst of star formation. The findings of this study showed evidences of a rapid dissipational collapse in the earliest stages of galaxy formation, which was followed by a steady supply of stellar material for the next several Gyr through accretion of ex-situ populations in dry mergers. The combination of these results corroborate the two-phase scenario of massive early-type galaxies, which naturally emerge within the two distinct structural components of the ellipticals in the sample.

4.1 Future perspectives

In this Section, I would like to highlight some potential project objectives that can be undertaken in the future, under the umbrella of galaxy structural decomposition especially in the current era of integral field spectroscopy. Being one of the two only codes until now that have leveraged this utility in IFS, BUDDI offers a unique and novel perspective in exploring the complexities of galaxy formation through their structural building blocks.

BUDDI-MaNGA: To bar or not to bar? With roughly half of the spiral galaxies and one-third of S0 galaxies in the local Universe hosting bars in their central regions in addition to a bulge, the next ideal progression in BUDDI-MaNGA would be to increase the complexity of the existing fits. Bars have been found to play an important role throughout the evolution of disc galaxies, for instance, in funnelling gas towards central regions to induce nuclear starbursts, and sometimes subsequent AGN activity, triggering the quenching of the galaxy. A bar with older and metal-rich stellar populations can cause the galaxy to appear redder than their unbarred counterparts. While a bulge-disc decomposition separates out the light contributions from the major underlying components, this implies that in barred galaxies, the light from the bar could be distributed between the bulge and disc components. This can potentially bias the stellar population properties, particularly in a disc that would otherwise be dominated by young, blue stars. Moreover, with bars being prevalent in early-type and high-mass galaxies, a comparison of a mass-matched sample of S0 and spiral galaxies to analyse the stellar populations and mass-assembly histories of the bulges, discs, and bars would be prudent in constraining the evolutionary pathways of disc galaxies. Testing the inclusion of a bar component for this sample was not possible during the thesis, and requires modelling simulated MaNGA datacubes to fully comprehend the feasibility and limitations of this step, accounting for the lower spatial resolution of MaNGA datacubes. The light profiles of bars are often expected to follow the parametric Sérsic function fixed with a Sérsic index of 0.5, or a Ferrer profile which can model symmetric features with a truncated light profile; and both these profiles are allowed in `GalfitM`. Furthermore, since `GalaxyZoo:3D` provides pixel-level positional data identifying where bars are located within MaNGA galaxies, it offers an excellent starting point to test the distinction between barred and unbarred disc galaxies.

Uncovering ellipticals with MUSE and MaNGA: A tale of two instruments. While Chapter 3 served as a pilot study to reconcile the dual-component nature of elliptical galaxies with the two-phase formation scenario of massive elliptical galaxies, the story does not end there, and requires a larger representative sample to constrain the structural diversity and complexity exhibited by ellipticals. The sample used in this thesis consisted of plain retired galaxies that have long ceased their star formation. This is indeed representative of a sub-population of “red and dead” ellipticals, but not of

all elliptical galaxies in the local Universe, as described in Chapter 1. By increasing the sample size in the MUSE study to include blue star-forming ellipticals and recently-quenched ellipticals (either from archival data or new observations), as well as to those that have been determined photometrically to contain embedded nuclear discs, a deeper analysis can be conducted in alliance with kinematical studies. Star formation and any faint tidal features caused by mergers in recently-quenched ellipticals show signatures of kinematic features or disturbances. Along those lines, a dwarf elliptical galaxy with an embedded disc would not follow the two-phase scenario of formation, if they are found to host diametrically different stellar populations as compared to the inner components of massive quiescent elliptical galaxies. Furthermore, MUSE observations of elliptical galaxies can potentially be accompanied by a smaller but deeper pointing at a region that extends beyond $3 - 4 R_e$ of the main body of the galaxy to collect a fraction of the stellar halo light, to analyse the stellar populations in this region. In principle, this approach would allow the decomposition of the main body of the elliptical, but not for the halo, but would nevertheless provide vital clues into the assembly of the galaxy in an even more comprehensive fashion.

The case-by-case approach of MUSE sampled galaxies could be complemented by a statistical refinement of the two-component fits of ellipticals in the BUDDI-MaNGA sample. While the current version forces the extended component of all galaxy morphologies to be modelled by an exponential profile, this constraint can be loosened by isolating only the elliptical galaxies in MaNGA and performing the fits again with two or three Sérsic components, following the results of Chapter 3. The spatial resolution of MaNGA might not allow for the deeper analyses that are possible with MUSE, it offers a balance between a highly statistical photometric survey and deep individual observations with high-resolution IFS instruments. These future perspectives highlighted in this Section have clear objectives and are entirely feasible with existing IFS data or with newer observations.

In conclusion, the research conducted in this thesis under the framework of spectrophotometric galaxy decomposition contributes to our understanding of galaxy formation and evolution by offering a more detailed picture of the assembly histories, structural components, and stellar populations of spirals and ellipticals. Similarly, the future projects that can be conducted within this framework have equally important potential in understanding the diversity of galaxies in the nearby Universe. It reinforces the notion that galaxy evolution is a multifaceted process, shaped by a complex web of interrelated mechanisms that continue to be uncovered. This work sheds further light on the rich and intricate dynamics that have shaped galaxies into the systems we observe today.

BIBLIOGRAPHY

- Abdurro'uf et al. (Apr. 2022). "The Seventeenth Data Release of the Sloan Digital Sky Surveys: Complete Release of MaNGA, MaStar, and APOGEE-2 Data". In: 259.2, 35, p. 35. doi: 10.3847/1538-4365/ac4414. arXiv: 2112.02026 [astro-ph.GA].
- Afanasiev, V. L. and A. V. Moiseev (Mar. 2005). "The SCORPIO Universal Focal Reducer of the 6-m Telescope". In: *Astronomy Letters* 31.3, pp. 194–204. doi: 10.1134/1.1883351. arXiv: astro-ph/0502095 [astro-ph].
- Athanassoula, E. and A. Bosma (Jan. 1985). "Shells and rings around galaxies." In: 23, pp. 147–168. doi: 10.1146/annurev.aa.23.090185.001051.
- Avila-Reese, Vladimir, Jesús Zavala, and Ivan Lacerna (June 2014). "The growth of galactic bulges through mergers in Λ cold dark matter haloes revisited - II. Morphological mix evolution". In: 441.1, pp. 417–430. doi: 10.1093/mnras/stu382. arXiv: 1311.3163 [astro-ph.CO].
- Bacon, R. et al. (July 2010a). "The MUSE second-generation VLT instrument". In: 7735, p. 773508. doi: 10.1117/12.856027.
- Bacon, R. et al. (July 2010b). "The MUSE second-generation VLT instrument". In: *Ground-based and Airborne Instrumentation for Astronomy III*. Ed. by Ian S. McLean, Suzanne K. Ramsay, and Hideki Takami. Vol. 7735. Society of Photo-Optical Instrumentation Engineers (SPIE) Conference Series, 773508, p. 773508. doi: 10.1117/12.856027. arXiv: 2211.16795 [astro-ph.IM].
- Baldry, I. K. et al. (Mar. 2018a). "Galaxy And Mass Assembly: the G02 field, Herschel-ATLAS target selection and data release 3". In: 474.3, pp. 3875–3888. doi: 10.1093/mnras/stx3042. arXiv: 1711.09139 [astro-ph.GA].
- (Mar. 2018b). "Galaxy And Mass Assembly: the G02 field, Herschel-ATLAS target selection and data release 3". In: 474.3, pp. 3875–3888. doi: 10.1093/mnras/stx3042. arXiv: 1711.09139 [astro-ph.GA].
- Baldwin, J. A., M. M. Phillips, and R. Terlevich (Feb. 1981). "Classification parameters for the emission-line spectra of extragalactic objects." In: 93, pp. 5–19. doi: 10.1086/130766.
- Barbosa, C. E., C. Spiniello, M. Arnaboldi, L. Coccato, M. Hilker, and T. Richtler (May 2021). "A preserved high- z compact progenitor in the heart of NGC 3311 revealed with MUSE 2D stellar population analysis". In: 649, A93, A93. doi: 10.1051/0004-6361/202039809. arXiv: 2012.11609 [astro-ph.GA].
- Barden, Marco, Boris Häußler, Chien Y. Peng, Daniel H. McIntosh, and Yicheng Guo (May 2012). "GALAPAGOS: from pixels to parameters". In: 422.1, pp. 449–468. doi: 10.1111/j.1365-2966.2012.20619.x. arXiv: 1203.1831 [astro-ph.IM].

- Barone, Tania M., Francesco D'Eugenio, Matthew Colless, and Nicholas Scott (July 2020). "Gravitational Potential and Surface Density Drive Stellar Populations. II. Star-forming Galaxies". In: 898.1, 62, p. 62. doi: 10.3847/1538-4357/ab9951. arXiv: 2006.00720 [astro-ph.GA].
- Barsanti, S. et al. (Jan. 2021). "The SAMI Galaxy Survey: Bulge and Disk Stellar Population Properties in Cluster Galaxies". In: 906.2, 100, p. 100. doi: 10.3847/1538-4357/abc956. arXiv: 2011.04873 [astro-ph.GA].
- Bedregal, A. G., N. Cardiel, A. Aragón-Salamanca, and M. R. Merrifield (Aug. 2011). "Stellar population gradients in Fornax cluster S0 galaxies: connecting bulge and disc evolution". In: 415.3, pp. 2063–2080. doi: 10.1111/j.1365-2966.2011.18752.x. arXiv: 1103.4378 [astro-ph.CO].
- Bellstedt, Sabine, Aaron SG Robotham, Simon P Driver, Claudia del P Lagos, Luke JM Davies, and Robin HW Cook (2023). "Resolving cosmic star formation histories of present-day bulges, disks, and spheroids with ProFUSE". In: *arXiv preprint arXiv:2307.02788*.
- Benedetti, João P. V. et al. (June 2023). "Digging deeper into NGC 6868 I: Stellar population". In: 522.2, pp. 2570–2583. doi: 10.1093/mnras/stad1148. arXiv: 2304.11194 [astro-ph.GA].
- Benitez, N. et al. (Mar. 2014). "J-PAS: The Javalambre-Physics of the Accelerated Universe Astrophysical Survey". In: *arXiv e-prints*, arXiv:1403.5237, arXiv:1403.5237. doi: 10.48550/arXiv.1403.5237. arXiv: 1403.5237 [astro-ph.CO].
- Bertelli, G., A. Bressan, C. Chiosi, Y. K. Ng, and S. Ortolani (Jan. 1994). "CMDs of three regions toward the Galactic Centre." In: 65, pp. 689–692.
- Bertelli, G., L. Girardi, P. Marigo, and E. Nasi (June 2008). "Scaled solar tracks and isochrones in a large region of the Z-Y plane. I. From the ZAMS to the TP-AGB end for 0.15-2.5 $[M]_{\odot}$ stars". In: 484.3, pp. 815–830. doi: 10.1051/0004-6361/20079165. arXiv: 0803.1460 [astro-ph].
- Bertin, E. and S. Arnouts (June 1996). "SExtractor: Software for source extraction." In: 117, pp. 393–404. doi: 10.1051/aas:1996164.
- Bílek, M., J. -C. Cuillandre, S. Gwyn, I. Ebrov, K. Bartořkov, B. Jungwiert, and L. Jlkov (Apr. 2016). "Deep imaging of the shell elliptical galaxy NGC 3923 with MegaCam". In: 588, A77, A77. doi: 10.1051/0004-6361/201526608. arXiv: 1505.07146 [astro-ph.GA].
- Blanton, Michael R. and Sam Roweis (Feb. 2007). "K-Corrections and Filter Transformations in the Ultraviolet, Optical, and Near-Infrared". In: 133.2, pp. 734–754. doi: 10.1086/510127. arXiv: astro-ph/0606170 [astro-ph].
- Blanton, Michael R. et al. (July 2017). "Sloan Digital Sky Survey IV: Mapping the Milky Way, Nearby Galaxies, and the Distant Universe". In: 154.1, 28, p. 28. doi: 10.3847/1538-3881/aa7567. arXiv: 1703.00052 [astro-ph.GA].
- Breda, Iris and Polychronis Papaderos (June 2018). "The continuous rise of bulges out of galactic disks". In: 614, A48, A48. doi: 10.1051/0004-6361/201731705. arXiv: 1712.05354 [astro-ph.GA].
- Breda, Iris, Polychronis Papaderos, and Jean-Michel Gomes (Aug. 2020a). "Indications of the invalidity of the exponentiality of the disk within bulges of spiral galaxies". In: 640, A20, A20. doi: 10.1051/0004-6361/202037889. arXiv: 2006.02307 [astro-ph.GA].

- Breda, Iris et al. (Mar. 2020b). “Stellar age gradients and inside-out star formation quenching in galaxy bulges”. In: 635, A177, A177. doi: 10.1051/0004-6361/201937193. arXiv: 2001.05738 [astro-ph.GA].
- Bromm, Volker, Paolo S. Coppi, and Richard B. Larson (Jan. 2002). “The Formation of the First Stars. I. The Primordial Star-forming Cloud”. In: 564.1, pp. 23–51. doi: 10.1086/323947. arXiv: astro-ph/0102503 [astro-ph].
- Bruzual, G. and S. Charlot (Oct. 2003). “Stellar population synthesis at the resolution of 2003”. In: 344.4, pp. 1000–1028. doi: 10.1046/j.1365-8711.2003.06897.x. arXiv: astro-ph/0309134 [astro-ph].
- Bryant, J. J. et al. (Mar. 2015). “The SAMI Galaxy Survey: instrument specification and target selection”. In: 447.3, pp. 2857–2879. doi: 10.1093/mnras/stu2635. arXiv: 1407.7335 [astro-ph.GA].
- Bundy, Kevin et al. (Jan. 2015). “Overview of the SDSS-IV MaNGA Survey: Mapping nearby Galaxies at Apache Point Observatory”. In: 798.1, 7, p. 7. doi: 10.1088/0004-637X/798/1/7. arXiv: 1412.1482 [astro-ph.GA].
- Calzetti, Daniela (Dec. 2001). “The Dust Opacity of Star-forming Galaxies”. In: 113.790, pp. 1449–1485. doi: 10.1086/324269. arXiv: astro-ph/0109035 [astro-ph].
- Capaccioli, Massimo et al. (Sept. 2015). “VEGAS: A VST Early-type GALaxy Survey. I. Presentation, wide-field surface photometry, and substructures in NGC 4472”. In: 581, A10, A10. doi: 10.1051/0004-6361/201526252. arXiv: 1507.01336 [astro-ph.GA].
- Cappellari, Michele (Apr. 2017). “Improving the full spectrum fitting method: accurate convolution with Gauss-Hermite functions”. In: 466.1, pp. 798–811. doi: 10.1093/mnras/stw3020. arXiv: 1607.08538 [astro-ph.GA].
- (Dec. 2023). “Full spectrum fitting with photometry in PPXF: stellar population versus dynamical masses, non-parametric star formation history and metallicity for 3200 LEGA-C galaxies at redshift $z \approx 0.8$ ”. In: 526.3, pp. 3273–3300. doi: 10.1093/mnras/stad2597. arXiv: 2208.14974 [astro-ph.GA].
- Cappellari, Michele and Yannick Copin (June 2003). “Adaptive spatial binning of integral-field spectroscopic data using Voronoi tessellations”. In: 342.2, pp. 345–354. doi: 10.1046/j.1365-8711.2003.06541.x. arXiv: astro-ph/0302262 [astro-ph].
- Cappellari, Michele and Eric Emsellem (Feb. 2004). “Parametric Recovery of Line-of-Sight Velocity Distributions from Absorption-Line Spectra of Galaxies via Penalized Likelihood”. In: 116.816, pp. 138–147. doi: 10.1086/381875. arXiv: astro-ph/0312201 [astro-ph].
- Cappellari, Michele et al. (May 2011). “The ATLAS^{3D} project - I. A volume-limited sample of 260 nearby early-type galaxies: science goals and selection criteria”. In: 413.2, pp. 813–836. doi: 10.1111/j.1365-2966.2010.18174.x. arXiv: 1012.1551 [astro-ph.CO].
- Carnall, A. C., R. J. McLure, J. S. Dunlop, and R. Davé (Nov. 2018). “Inferring the star formation histories of massive quiescent galaxies with BAGPIPES: evidence for multiple quenching mechanisms”. In: 480.4, pp. 4379–4401. doi: 10.1093/mnras/sty2169. arXiv: 1712.04452 [astro-ph.GA].

- Carnall, Adam C., Joel Leja, Benjamin D. Johnson, Ross J. McLure, James S. Dunlop, and Charlie Conroy (Mar. 2019). “How to Measure Galaxy Star Formation Histories. I. Parametric Models”. In: 873.1, 44, p. 44. doi: 10.3847/1538-4357/ab04a2. arXiv: 1811.03635 [astro-ph.GA].
- Chabrier, Gilles (July 2003). “Galactic Stellar and Substellar Initial Mass Function”. In: 115.809, pp. 763–795. doi: 10.1086/376392. arXiv: astro-ph/0304382 [astro-ph].
- Chen, Yanping, Scott Trager, Reynier Peletier, and Ariane Lançon (Dec. 2011). “XSL: The X-Shooter Spectral Library”. In: *Journal of Physics Conference Series*. Vol. 328. Journal of Physics Conference Series. IOP, 012023, p. 012023. doi: 10.1088/1742-6596/328/1/012023. arXiv: 1112.3651 [astro-ph.GA].
- Chiosi, Cesare and Giovanni Carraro (Sept. 2002). “Formation and evolution of elliptical galaxies”. In: 335.2, pp. 335–357. doi: 10.1046/j.1365-8711.2002.05590.x.
- Choi, Ena, Rachel S. Somerville, Jeremiah P. Ostriker, Michaela Hirschmann, and Thorsten Naab (Mar. 2024). “The Origins of Gas Accreted by Supermassive Black Holes: The Importance of Recycled Gas”. In: 964.1, 54, p. 54. doi: 10.3847/1538-4357/ad245a. arXiv: 2312.08449 [astro-ph.GA].
- Cid Fernandes, Roberto, Abílio Mateus, Laerte Sodr , Gra yna Stasi ska, and Jean M. Gomes (Apr. 2005a). “Semi-empirical analysis of Sloan Digital Sky Survey galaxies - I. Spectral synthesis method”. In: 358.2, pp. 363–378. doi: 10.1111/j.1365-2966.2005.08752.x. arXiv: astro-ph/0412481 [astro-ph].
- (Apr. 2005b). “Semi-empirical analysis of Sloan Digital Sky Survey galaxies - I. Spectral synthesis method”. In: 358.2, pp. 363–378. doi: 10.1111/j.1365-2966.2005.08752.x. arXiv: astro-ph/0412481 [astro-ph].
- Cimatti, A. et al. (Dec. 2004). “Unveiling Old Massive Spheroidal Galaxies in the Young Universe”. In: *The Messenger* 118, pp. 51–54.
- Coccato, L., L. Morelli, E. M. Corsini, L. Buson, A. Pizzella, D. Vergani, and F. Bertola (Mar. 2011). “Dating the formation of the counter-rotating stellar disc in the spiral galaxy NGC 5719 by disentangling its stellar populations”. In: 412.1, pp. L113–L117. doi: 10.1111/j.1745-3933.2011.01016.x. arXiv: 1101.3092 [astro-ph.GA].
- Coelho, P., G. Bruzual, S. Charlot, A. Weiss, B. Barbuy, and J. W. Ferguson (Dec. 2007). “Spectral models for solar-scaled and α -enhanced stellar populations”. In: 382.2, pp. 498–514. doi: 10.1111/j.1365-2966.2007.12364.x. arXiv: 0708.2790 [astro-ph].
- Coelho, P. and D. A. Gadotti (Dec. 2011). “Bars Rejuvenating Bulges? Evidence from Stellar Population Analysis”. In: 743.1, L13, p. L13. doi: 10.1088/2041-8205/743/1/L13. arXiv: 1111.1736 [astro-ph.CO].
- Coelho, P. R. T. (May 2014). “A new library of theoretical stellar spectra with scaled-solar and α -enhanced mixtures”. In: 440.2, pp. 1027–1043. doi: 10.1093/mnras/stu365. arXiv: 1404.3243 [astro-ph.SR].
- Colbert, James W., John S. Mulchaey, and Ann I. Zabludoff (Feb. 2001). “The Optical and Near-Infrared Morphologies of Isolated Early-Type Galaxies”. In: 121.2, pp. 808–819. doi: 10.1086/318758. arXiv: astro-ph/0010534 [astro-ph].

- Cole, Shaun, Cedric G. Lacey, Carlton M. Baugh, and Carlos S. Frenk (Nov. 2000). “Hierarchical galaxy formation”. In: 319.1, pp. 168–204. doi: 10.1046/j.1365-8711.2000.03879.x. arXiv: astro-ph/0007281 [astro-ph].
- Conroy, Charlie (Aug. 2013). “Modeling the Panchromatic Spectral Energy Distributions of Galaxies”. In: 51.1, pp. 393–455. doi: 10.1146/annurev-astro-082812-141017. arXiv: 1301.7095 [astro-ph.CO].
- Cowie, Lennox L., Antoinette Songaila, Esther M. Hu, and J. G. Cohen (Sept. 1996). “New Insight on Galaxy Formation and Evolution From Keck Spectroscopy of the Hawaii Deep Fields”. In: 112, p. 839. doi: 10.1086/118058. arXiv: astro-ph/9606079 [astro-ph].
- Croom, Scott M. et al. (July 2021). “The SAMI Galaxy Survey: the third and final data release”. In: 505.1, pp. 991–1016. doi: 10.1093/mnras/stab229. arXiv: 2101.12224 [astro-ph.GA].
- D’Ago, G. et al. (Apr. 2023). “INSPIRE: INvestigating Stellar Population In RElics. III. Second data release (DR2): testing the systematics on the stellar velocity dispersion”. In: 672, A17, A17. doi: 10.1051/0004-6361/202245542. arXiv: 2302.05453 [astro-ph.GA].
- Daddi, E. et al. (June 2005). “Passively Evolving Early-Type Galaxies at $1.4 < z < 2.5$ in the Hubble Ultra Deep Field”. In: 626.2, pp. 680–697. doi: 10.1086/430104. arXiv: astro-ph/0503102 [astro-ph].
- Damjanov, Ivana et al. (Apr. 2009). “Red Nuggets at $z \sim 1.5$: Compact Passive Galaxies and the Formation of the Kormendy Relation”. In: 695.1, pp. 101–115. doi: 10.1088/0004-637X/695/1/101. arXiv: 0807.1744 [astro-ph].
- Davison, Thomas A., Mark A. Norris, Ryan Leaman, Harald Kuntschner, Alina Boecker, and Glenn van de Ven (Oct. 2021). “Mapping accreted stars in early-type galaxies across the mass-size plane”. In: 507.2, pp. 3089–3112. doi: 10.1093/mnras/stab2362. arXiv: 2108.06160 [astro-ph.GA].
- de Vaucouleurs, Gerard (Jan. 1948). “Recherches sur les Nebuleuses Extragalactiques”. In: *Annales d’Astrophysique* 11, p. 247.
- Deeley, Simon, Michael J. Drinkwater, Sarah M. Sweet, Kenji Bekki, Warrick J. Couch, and Duncan A. Forbes (Oct. 2023). “The formation pathways of compact elliptical galaxies”. In: 525.1, pp. 1192–1209. doi: 10.1093/mnras/stad2313. arXiv: 2308.00305 [astro-ph.GA].
- Dey, Arjun et al. (May 2019). “Overview of the DESI Legacy Imaging Surveys”. In: 157.5, 168, p. 168. doi: 10.3847/1538-3881/ab089d. arXiv: 1804.08657 [astro-ph.IM].
- Dickinson, Mark, Mauro Giavalisco, and GOODS Team (Jan. 2003a). “The Great Observatories Origins Deep Survey”. In: *The Mass of Galaxies at Low and High Redshift*. Ed. by Ralf Bender and Alvio Renzini, p. 324. doi: 10.1007/10899892_78. arXiv: astro-ph/0204213 [astro-ph].
- (Jan. 2003b). “The Great Observatories Origins Deep Survey”. In: *The Mass of Galaxies at Low and High Redshift*. Ed. by Ralf Bender and Alvio Renzini, p. 324. doi: 10.1007/10899892_78. arXiv: astro-ph/0204213 [astro-ph].
- Domínguez Sánchez, H., M. Bernardi, J. R. Brownstein, N. Drory, and R. K. Sheth (Nov. 2019). “Galaxy properties as revealed by MaNGA - I. Constraints on IMF and M_*/L gradients in ellipticals”. In: 489.4, pp. 5612–5632. doi: 10.1093/mnras/stz2414. arXiv: 1904.11992 [astro-ph.GA].

- Domínguez Sánchez, H., M. Bernardi, F. Nikakhtar, B. Margalef-Bentabol, and R. K. Sheth (July 2020). “Galaxy properties as revealed by MaNGA - III. Kinematic profiles and stellar population gradients in S0s”. In: 495.3, pp. 2894–2908. doi: 10.1093/mnras/staa1364. arXiv: 2005.07693 [astro-ph.GA].
- Domínguez Sánchez, H., M. Huertas-Company, M. Bernardi, D. Tuccillo, and J. L. Fischer (Feb. 2018). “Improving galaxy morphologies for SDSS with Deep Learning”. In: 476.3, pp. 3661–3676. doi: 10.1093/mnras/sty338. arXiv: 1711.05744 [astro-ph.GA].
- Domínguez Sánchez, H., B. Margalef, M. Bernardi, and M. Huertas-Company (Jan. 2022). “SDSS-IV DR17: final release of MaNGA PyMorph photometric and deep-learning morphological catalogues”. In: 509.3, pp. 4024–4036. doi: 10.1093/mnras/stab3089. arXiv: 2110.10694 [astro-ph.GA].
- Dressler, A. (Mar. 1980). “Galaxy morphology in rich clusters: implications for the formation and evolution of galaxies.” In: 236, pp. 351–365. doi: 10.1086/157753.
- Driver, S. P. et al. (May 2011a). “Galaxy and Mass Assembly (GAMA): survey diagnostics and core data release”. In: 413.2, pp. 971–995. doi: 10.1111/j.1365-2966.2010.18188.x. arXiv: 1009.0614 [astro-ph.CO].
- (May 2011b). “Galaxy and Mass Assembly (GAMA): survey diagnostics and core data release”. In: 413.2, pp. 971–995. doi: 10.1111/j.1365-2966.2010.18188.x. arXiv: 1009.0614 [astro-ph.CO].
- Drory, N. et al. (Feb. 2015). “The MaNGA Integral Field Unit Fiber Feed System for the Sloan 2.5 m Telescope”. In: 149.2, 77, p. 77. doi: 10.1088/0004-6256/149/2/77. arXiv: 1412.1535 [astro-ph.IM].
- Dullo, Bililign T. et al. (Apr. 2018). “The nuclear activity and central structure of the elliptical galaxy NGC 5322”. In: 475.4, pp. 4670–4682. doi: 10.1093/mnras/sty069. arXiv: 1801.03660 [astro-ph.GA].
- Elmegreen, Bruce G., Frédéric Bournaud, and Debra Meloy Elmegreen (Nov. 2008). “Bulge Formation by the Coalescence of Giant Clumps in Primordial Disk Galaxies”. In: 688.1, pp. 67–77. doi: 10.1086/592190. arXiv: 0808.0716 [astro-ph].
- Elmegreen, Debra Meloy, Bruce G. Elmegreen, Jay A. Frogel, Paul B. Eskridge, Richard W. Pogge, Andrew Gallagher, and Joel Iams (Aug. 2002). “Arm Structure in Anemic Spiral Galaxies”. In: 124.2, pp. 777–781. doi: 10.1086/341613. arXiv: astro-ph/0205105 [astro-ph].
- Erwin, Peter et al. (Feb. 2015). “Composite bulges: the coexistence of classical bulges and discy pseudo-bulges in S0 and spiral galaxies”. In: 446.4, pp. 4039–4077. doi: 10.1093/mnras/stu2376. arXiv: 1411.2599 [astro-ph.GA].
- Erwin, Peter et al. (Apr. 2021). “Composite bulges - II. Classical bulges and nuclear discs in barred galaxies: the contrasting cases of NGC 4608 and NGC 4643”. In: 502.2, pp. 2446–2473. doi: 10.1093/mnras/stab126. arXiv: 2101.05321 [astro-ph.GA].
- ESO CPL Development Team (Apr. 2015). *EsoRex: ESO Recipe Execution Tool*. Astrophysics Source Code Library, record ascl:1504.003.

- Fabbro, S., K. A. Venn, T. O'Briain, S. Bialek, C. L. Kielty, F. Jahandar, and S. Monty (Apr. 2018). "An application of deep learning in the analysis of stellar spectra". In: 475.3, pp. 2978–2993. doi: 10.1093/mnras/stx3298. arXiv: 1709.09182 [astro-ph.IM].
- Faber, S. M. (Sept. 1972). "Quadratic programming applied to the problem of galaxy population synthesis." In: 20, p. 361.
- Fall, S. M. and G. Efstathiou (Oct. 1980). "Formation and rotation of disc galaxies with haloes." In: 193, pp. 189–206. doi: 10.1093/mnras/193.2.189.
- Fang, Taotao and Renyue Cen (Dec. 2004). "The Transition from Population III to Population II Stars". In: 616.2, pp. L87–L90. doi: 10.1086/426786. arXiv: astro-ph/0405565 [astro-ph].
- Ferré-Mateu, Anna, Ignacio Trujillo, Ignacio Martín-Navarro, Alexandre Vazdekis, Mar Mezcua, Marc Balcells, and Lilian Domínguez (May 2017). "Two new confirmed massive relic galaxies: red nuggets in the present-day Universe". In: 467.2, pp. 1929–1939. doi: 10.1093/mnras/stx171. arXiv: 1701.05197 [astro-ph.GA].
- Ferré-Mateu, Anna et al. (Oct. 2018). "Origins of ultradiffuse galaxies in the Coma cluster - II. Constraints from their stellar populations". In: 479.4, pp. 4891–4906. doi: 10.1093/mnras/sty1597. arXiv: 1801.09695 [astro-ph.GA].
- Fischer, J. -L., H. Domínguez Sánchez, and M. Bernardi (Feb. 2019). "SDSS-IV MaNGA PyMorph Photometric and Deep Learning Morphological Catalogues and implications for bulge properties and stellar angular momentum". In: 483.2, pp. 2057–2077. doi: 10.1093/mnras/sty3135. arXiv: 1811.02580 [astro-ph.GA].
- Fisher, David, Marijn Franx, and Garth Illingworth (Mar. 1996). "Line Strengths and Line-Strength Gradients in S0 Galaxies". In: 459, p. 110. doi: 10.1086/176873.
- Fisher, David B. and Niv Drory (Aug. 2008). "The Structure of Classical Bulges and Pseudobulges: the Link Between Pseudobulges and SÉRSIC Index". In: 136.2, pp. 773–839. doi: 10.1088/0004-6256/136/2/773. arXiv: 0805.4206 [astro-ph].
- Fraser-McKelvie, Amelia, Alfonso Aragón-Salamanca, Michael Merrifield, Martha Tabor, Mariangela Bernardi, Niv Drory, Taniya Parikh, and Maria Argudo-Fernández (Dec. 2018). "SDSS-IV MaNGA: the formation sequence of S0 galaxies". In: 481.4, pp. 5580–5591. doi: 10.1093/mnras/sty2563. arXiv: 1809.04336 [astro-ph.GA].
- Freeman, K. C. (June 1970). "On the Disks of Spiral and S0 Galaxies". In: 160, p. 811. doi: 10.1086/150474.
- Fukugita, M., T. Ichikawa, J. E. Gunn, M. Doi, K. Shimasaku, and D. P. Schneider (Apr. 1996). "The Sloan Digital Sky Survey Photometric System". In: 111, p. 1748. doi: 10.1086/117915.
- Gadotti, D. A. and S. dos Anjos (Sept. 2001). "Homogenization of the Stellar Population along Late-Type Spiral Galaxies". In: 122.3, pp. 1298–1318. doi: 10.1086/322126. arXiv: astro-ph/0106303 [astro-ph].
- Gallagher John S., III and Deidre A. Hunter (Jan. 1984). "Structure and Evolution of Irregular Galaxies". In: 22, pp. 37–74. doi: 10.1146/annurev.aa.22.090184.000345.
- Ge, Junqiang, Renbin Yan, Michele Cappellari, Shude Mao, Hongyu Li, and Youjun Lu (Aug. 2018). "Recovering stellar population parameters via two full-spectrum fitting algorithms in the

absence of model uncertainties". In: 478.2, pp. 2633–2649. doi: 10.1093/mnras/sty1245. arXiv: 1805.03972 [astro-ph.GA].

Geha, M., P. Guhathakurta, and R. P. van der Marel (Oct. 2003). "Internal Dynamics, Structure, and Formation of Dwarf Elliptical Galaxies. II. Rotating versus Nonrotating Dwarfs". In: 126.4, pp. 1794–1810. doi: 10.1086/377624. arXiv: astro-ph/0304537 [astro-ph].

Geha, M., D. Weisz, A. Grocholski, A. Dolphin, R. P. van der Marel, and P. Guhathakurta (Oct. 2015). "HST/ACS Direct Ages of the Dwarf Elliptical Galaxies NGC 147 and NGC 185". In: 811.2, 114, p. 114. doi: 10.1088/0004-637X/811/2/114. arXiv: 1503.06526 [astro-ph.GA].

Giavalisco, M. et al. (Jan. 2004a). "The Great Observatories Origins Deep Survey: Initial Results from Optical and Near-Infrared Imaging". In: 600.2, pp. L93–L98. doi: 10.1086/379232. arXiv: astro-ph/0309105 [astro-ph].

— (Jan. 2004b). "The Great Observatories Origins Deep Survey: Initial Results from Optical and Near-Infrared Imaging". In: 600.2, pp. L93–L98. doi: 10.1086/379232. arXiv: astro-ph/0309105 [astro-ph].

Girardi, L., A. Bressan, G. Bertelli, and C. Chiosi (Feb. 2000). "Evolutionary tracks and isochrones for low- and intermediate-mass stars: From 0.15 to 7 M_{sun} , and from $Z=0.0004$ to 0.03". In: 141, pp. 371–383. doi: 10.1051/aas:2000126. arXiv: astro-ph/9910164 [astro-ph].

Goddard, D. et al. (Apr. 2017). "SDSS-IV MaNGA: Spatially resolved star formation histories in galaxies as a function of galaxy mass and type". In: 466.4, pp. 4731–4758. doi: 10.1093/mnras/stw3371. arXiv: 1612.01546 [astro-ph.GA].

Gomes, J. M. and P. Papaderos (July 2017). "Fitting Analysis using Differential evolution Optimization (FADO): Spectral population synthesis through genetic optimization under self-consistency boundary conditions". In: 603, A63, A63. doi: 10.1051/0004-6361/201628986. arXiv: 1704.03922 [astro-ph.GA].

González Delgado, R. M. et al. (Sept. 2015). "The CALIFA survey across the Hubble sequence. Spatially resolved stellar population properties in galaxies". In: 581, A103, A103. doi: 10.1051/0004-6361/201525938. arXiv: 1506.04157 [astro-ph.GA].

González Delgado, R. M. et al. (Nov. 2017). "Spatially-resolved star formation histories of CALIFA galaxies. Implications for galaxy formation". In: 607, A128, A128. doi: 10.1051/0004-6361/201730883. arXiv: 1706.06119 [astro-ph.GA].

Graham, Alister W., Bogdan C. Ciambur, and Giulia A. D. Savorgnan (Nov. 2016). "Disky Elliptical Galaxies and the Allegedly Over-massive Black Hole in the Compact "ES" Galaxy NGC 1271". In: 831.2, 132, p. 132. doi: 10.3847/0004-637X/831/2/132. arXiv: 1608.00711 [astro-ph.GA].

Grogin, Norman A. et al. (Dec. 2011). "CANDELS: The Cosmic Assembly Near-infrared Deep Extragalactic Legacy Survey". In: 197.2, 35, p. 35. doi: 10.1088/0067-0049/197/2/35. arXiv: 1105.3753 [astro-ph.CO].

Gunn, James E. and III Gott J. Richard (Aug. 1972). "On the Infall of Matter Into Clusters of Galaxies and Some Effects on Their Evolution". In: 176, p. 1. doi: 10.1086/151605.

Gunn, James E. et al. (Apr. 2006). "The 2.5 m Telescope of the Sloan Digital Sky Survey". In: 131.4, pp. 2332–2359. doi: 10.1086/500975. arXiv: astro-ph/0602326 [astro-ph].

- Häußler, Boris et al. (Mar. 2013). “MegaMorph - multiwavelength measurement of galaxy structure: complete Sérsic profile information from modern surveys”. In: 430.1, pp. 330–369. doi: 10.1093/mnras/sts633. arXiv: 1212.3332 [astro-ph.CO].
- Häußler, Boris et al. (Aug. 2022). “GALAPAGOS-2/GALFITM/GAMA - Multi-wavelength measurement of galaxy structure: Separating the properties of spheroid and disk components in modern surveys”. In: 664, A92, A92. doi: 10.1051/0004-6361/202142935. arXiv: 2204.05907 [astro-ph.GA].
- Häussler, Boris et al. (Oct. 2007). “GEMS: Galaxy Fitting Catalogs and Testing Parametric Galaxy Fitting Codes: GALFIT and GIM2D”. In: 172.2, pp. 615–633. doi: 10.1086/518836.
- Hook, I. M., Inger Jørgensen, J. R. Allington-Smith, R. L. Davies, N. Metcalfe, R. G. Murowinski, and D. Crampton (May 2004). “The Gemini-North Multi-Object Spectrograph: Performance in Imaging, Long-Slit, and Multi-Object Spectroscopic Modes”. In: 116.819, pp. 425–440. doi: 10.1086/383624.
- Hopkins, A. M. (Nov. 2018). “The Dawes Review 8: Measuring the Stellar Initial Mass Function”. In: 35, e039, e039. doi: 10.1017/pasa.2018.29. arXiv: 1807.09949 [astro-ph.GA].
- Hopkins, P. F. (Dec. 2009). “How Do Disks Survive Mergers?” In: *Galaxy Evolution: Emerging Insights and Future Challenges*. Ed. by S. Jogee, I. Marinova, L. Hao, and G. A. Blanc. Vol. 419. Astronomical Society of the Pacific Conference Series, p. 228.
- Hopkins, Philip, Lars Hernquist, Thomas J. Cox, and Dušan Kereš (Apr. 2008). “A Cosmological Framework for the Co-Evolution of Quasars, Supermassive Black Holes, and Elliptical Galaxies. I. Galaxy Mergers and Quasar Activity”. In: 175.2, pp. 356–389. doi: 10.1086/524362. arXiv: 0706.1243 [astro-ph].
- Huang, Song, Luis C. Ho, Chien Y. Peng, Zhao-Yu Li, and Aaron J. Barth (May 2013a). “Fossil Evidence for the Two-phase Formation of Elliptical Galaxies”. In: 768.2, L28, p. L28. doi: 10.1088/2041-8205/768/2/L28. arXiv: 1304.2299 [astro-ph.CO].
- (Mar. 2013b). “The Carnegie-Irvine Galaxy Survey. III. The Three-component Structure of Nearby Elliptical Galaxies”. In: 766.1, 47, p. 47. doi: 10.1088/0004-637X/766/1/47. arXiv: 1212.2639 [astro-ph.CO].
- Hubble, Edwin (Mar. 1929). “A Relation between Distance and Radial Velocity among Extra-Galactic Nebulae”. In: *Proceedings of the National Academy of Science* 15.3, pp. 168–173. doi: 10.1073/pnas.15.3.168.
- (Jan. 1926). “No. 324. Extra-galactic nebulae.” In: *Contributions from the Mount Wilson Observatory / Carnegie Institution of Washington* 324, pp. 1–49.
- Ibarra-Medel, Héctor J., Vladimir Avila-Reese, Sebastián F. Sánchez, Alejandro González-Samaniego, and Aldo Rodríguez-Puebla (Mar. 2019). “Optical integral field spectroscopy observations applied to simulated galaxies: testing the fossil record method”. In: 483.4, pp. 4525–4550. doi: 10.1093/mnras/sty3256. arXiv: 1811.04856 [astro-ph.GA].
- Ibarra-Medel, Héctor J. et al. (Dec. 2016). “SDSS IV MaNGA: the global and local stellar mass assembly histories of galaxies”. In: 463.3, pp. 2799–2818. doi: 10.1093/mnras/stw2126. arXiv: 1609.01304 [astro-ph.GA].

- Icke, V. (Mar. 1985). “Distant encounters between disk galaxies and the origin of S 0 spirals”. In: 144.1, pp. 115–123.
- Jegatheesan, Keerthana, Evelyn J. Johnston, Boris Häußler, and Kalina V. Nedkova (Apr. 2024). “BUDDI-MaNGA. III. The mass-assembly histories of bulges and discs of spiral galaxies”. In: 684, A32, A32. doi: 10.1051/0004-6361/202347372. arXiv: 2402.00959 [astro-ph.GA].
- Johansson, Peter H., Thorsten Naab, and Jeremiah P. Ostriker (Aug. 2012). “Forming Early-type Galaxies in Λ CDM Simulations. I. Assembly Histories”. In: 754.2, 115, p. 115. doi: 10.1088/0004-637X/754/2/115. arXiv: 1202.3441 [astro-ph.CO].
- Johnston, E. J., A. Aragón-Salamanca, M. R. Merrifield, and A. G. Bedregal (May 2012). “Spectroscopic bulge-disc decomposition: a new method to study the evolution of lenticular galaxies”. In: 422.3, pp. 2590–2599. doi: 10.1111/j.1365-2966.2012.20813.x. arXiv: 1202.6064 [astro-ph.CO].
- Johnston, Evelyn J., Alfonso Aragón-Salamanca, and Michael R. Merrifield (June 2014). “The origin of S0s in clusters: evidence from the bulge and disc star formation histories”. In: 441.1, pp. 333–342. doi: 10.1093/mnras/stu582. arXiv: 1403.5561 [astro-ph.GA].
- Johnston, Evelyn J., Boris Häußler, and Keerthana Jegatheesan (Aug. 2022a). “BUDDI-MaNGA I: A statistical sample of cleanly decomposed bulge and disc spectra”. In: 514.4, pp. 6120–6140. doi: 10.1093/mnras/stac1725. arXiv: 2206.08877 [astro-ph.GA].
- Johnston, Evelyn J., Michael Merrifield, and Alfonso Aragón-Salamanca (Aug. 2018). “Spectroscopic decomposition of the galaxy and halo of the cD galaxy NGC 3311”. In: 478.3, pp. 4255–4267. doi: 10.1093/mnras/sty1342. arXiv: 1805.06913 [astro-ph.GA].
- Johnston, Evelyn J., Michael R. Merrifield, Alfonso Aragón-Salamanca, and Michele Cappellari (Jan. 2013). “Disentangling the stellar populations in the counter-rotating disc galaxy NGC 4550”. In: 428.2, pp. 1296–1302. doi: 10.1093/mnras/sts121. arXiv: 1210.0535 [astro-ph.CO].
- Johnston, Evelyn J. et al. (Feb. 2017). “SDSS-IV MaNGA: bulge-disc decomposition of IFU data cubes (BUDDI)”. In: 465.2, pp. 2317–2341. doi: 10.1093/mnras/stw2823. arXiv: 1611.00609 [astro-ph.GA].
- Johnston, Evelyn J. et al. (Jan. 2021). “Formation of S0s in extreme environments II: The star-formation histories of bulges, discs, and lenses”. In: 500.3, pp. 4193–4212. doi: 10.1093/mnras/staa2838. arXiv: 2009.05548 [astro-ph.GA].
- Johnston, Evelyn J. et al. (Aug. 2022b). “BUDDI-MaNGA II: the star-formation histories of bulges and discs of S0s”. In: 514.4, pp. 6141–6156. doi: 10.1093/mnras/stac1447. arXiv: 2206.08878 [astro-ph.GA].
- Karlsson, Torgny, Volker Bromm, and Joss Bland-Hawthorn (Apr. 2013). “Pregalactic metal enrichment: The chemical signatures of the first stars”. In: *Reviews of Modern Physics* 85.2, pp. 809–848. doi: 10.1103/RevModPhys.85.809. arXiv: 1101.4024 [astro-ph.CO].
- Katz, Harley, Taysun Kimm, Richard S. Ellis, Julien Devriendt, and Adrienne Slyz (Sept. 2023). “The challenges of identifying Population III stars in the early Universe”. In: 524.1, pp. 351–360. doi: 10.1093/mnras/stad1903. arXiv: 2207.04751 [astro-ph.GA].
- Katz, Neal, Dusan Keres, Romeel Dave, and David H Weinberg (2003). “How do galaxies get their gas?” In: *The IGM/Galaxy Connection*. Springer, pp. 185–192.

Kennicutt Jr, Robert C (1998). “The global Schmidt law in star-forming galaxies”. In: *The Astrophysical Journal* 498.2, p. 541.

Kewley, Lisa J., Brent Groves, Guinevere Kauffmann, and Tim Heckman (Nov. 2006). “The host galaxies and classification of active galactic nuclei”. In: 372.3, pp. 961–976. doi: 10.1111/j.1365-2966.2006.10859.x. arXiv: astro-ph/0605681 [astro-ph].

Khochfar, S. and A. Burkert (Nov. 2003). “The Importance of Spheroidal and Mixed Mergers for Early-Type Galaxy Formation”. In: 597.2, pp. L117–L120. doi: 10.1086/379845. arXiv: astro-ph/0303529 [astro-ph].

King, I. R. (May 1978). “Surface photometry of elliptical galaxies.” In: 222, pp. 1–13. doi: 10.1086/156115.

Kobayashi, Chiaki (Jan. 2004). “GRAPE-SPH chemodynamical simulation of elliptical galaxies - I. Evolution of metallicity gradients”. In: 347.3, pp. 740–758. doi: 10.1111/j.1365-2966.2004.07258.x. arXiv: astro-ph/0310160 [astro-ph].

Koekemoer, Anton M. et al. (Dec. 2011). “CANDELS: The Cosmic Assembly Near-infrared Deep Extragalactic Legacy Survey—The Hubble Space Telescope Observations, Imaging Data Products, and Mosaics”. In: 197.2, 36, p. 36. doi: 10.1088/0067-0049/197/2/36. arXiv: 1105.3754 [astro-ph.CO].

Kormendy, J. (Oct. 1977). “Brightness distributions in compact and normal galaxies. III. Decomposition of observed profiles in spheroid and disk components.” In: 217, pp. 406–419. doi: 10.1086/155589.

Kormendy, J. and D. B. Fisher (Oct. 2008). “Secular Evolution in Disk Galaxies: Pseudobulge Growth and the Formation of Spheroidal Galaxies”. In: *Formation and Evolution of Galaxy Disks*. Ed. by J. G. Funes and E. M. Corsini. Vol. 396. Astronomical Society of the Pacific Conference Series, p. 297. doi: 10.48550/arXiv.0810.2534. arXiv: 0810.2534 [astro-ph].

Kormendy, John (July 1989). “Did Elliptical Galaxies Form by Mergers or by Dissipative Collapse?” In: 342, p. L63. doi: 10.1086/185485.

— (Jan. 2016). “Elliptical Galaxies and Bulges of Disc Galaxies: Summary of Progress and Outstanding Issues”. In: *Galactic Bulges*. Ed. by Eija Laurikainen, Reynier Peletier, and Dimitri Gadotti. Vol. 418. Astrophysics and Space Science Library, p. 431. doi: 10.1007/978-3-319-19378-6_16. arXiv: 1504.03330 [astro-ph.GA].

Kormendy, John and Jr. Kennicutt Robert C. (Sept. 2004). “Secular Evolution and the Formation of Pseudobulges in Disk Galaxies”. In: 42.1, pp. 603–683. doi: 10.1146/annurev.astro.42.053102.134024. arXiv: astro-ph/0407343 [astro-ph].

Krajnović, Davor et al. (Sept. 2015). “Unveiling the counter-rotating nature of the kinematically distinct core in NGC 5813 with MUSE”. In: 452.1, pp. 2–18. doi: 10.1093/mnras/stv958. arXiv: 1505.06226 [astro-ph.GA].

Kronberger, T., W. Kapferer, C. Ferrari, S. Unterguggenberger, and S. Schindler (Apr. 2008). “On the influence of ram-pressure stripping on the star formation of simulated spiral galaxies”. In: 481.2, pp. 337–343. doi: 10.1051/0004-6361:20078904. arXiv: 0801.3759 [astro-ph].

Kroupa, P. (Jan. 2001a). “The Local Stellar Initial Mass Function”. In: *Dynamics of Star Clusters and the Milky Way*. Ed. by S. Deiters, B. Fuchs, A. Just, R. Spurzem, and R. Wielen. Vol. 228.

Astronomical Society of the Pacific Conference Series, p. 187. doi: 10.48550/arXiv.astro-ph/0011328. arXiv: astro-ph/0011328 [astro-ph].

Kroupa, P. and C. M. Boily (Nov. 2002). “On the mass function of star clusters”. In: 336.4, pp. 1188–1194. doi: 10.1046/j.1365-8711.2002.05848.x. arXiv: astro-ph/0207514 [astro-ph].

Kroupa, Pavel (Apr. 2001b). “On the variation of the initial mass function”. In: 322.2, pp. 231–246. doi: 10.1046/j.1365-8711.2001.04022.x. arXiv: astro-ph/0009005 [astro-ph].

Kurucz, R. L. (Jan. 1992). “Model Atmospheres for Population Synthesis”. In: *The Stellar Populations of Galaxies*. Ed. by Beatriz Barbuy and Alvio Renzini. Vol. 149. IAU Symposium, p. 225.

Lacerna, I., H. M. Hernández-Toledo, V. Avila-Reese, J. Abonza-Sane, and A. del Olmo (Apr. 2016). “Isolated elliptical galaxies in the local Universe”. In: 588, A79, A79. doi: 10.1051/0004-6361/201527844. arXiv: 1511.08809 [astro-ph.GA].

Lacerna, I., H. Ibarra-Medel, V. Avila-Reese, H. M. Hernández-Toledo, J. A. Vázquez-Mata, and S. F. Sánchez (Dec. 2020). “SDSS-IV MaNGA: Global and local stellar population properties of elliptical galaxies”. In: 644, A117, A117. doi: 10.1051/0004-6361/202037503. arXiv: 2001.05506 [astro-ph.GA].

Lagos, Claudia del P., Nelson D. Padilla, Timothy A. Davis, Cedric G. Lacey, Carlton M. Baugh, Violeta Gonzalez-Perez, Martin A. Zwaan, and Sergio Contreras (Apr. 2015). “The origin of the atomic and molecular gas contents of early-type galaxies - II. Misaligned gas accretion”. In: 448.2, pp. 1271–1287. doi: 10.1093/mnras/stu2763. arXiv: 1410.5437 [astro-ph.GA].

Lah, Philip, Nicholas Scott, Tania M. Barone, A. S. G. Robotham, Francesco D’Eugenio, Matthew Colless, and Sarah Casura (Jan. 2023). “Comparison of the stellar populations of bulges and discs using the MaNGA survey”. In: 40, e002, e002. doi: 10.1017/pasa.2022.58. arXiv: 2212.06284 [astro-ph.GA].

Lançon, A., P. H. Hauschildt, D. Ladjal, and M. Mouhcine (June 2007). “Near-IR spectra of red supergiants and giants. I. Models with solar and with mixing-induced surface abundance ratios”. In: 468.1, pp. 205–220. doi: 10.1051/0004-6361:20065824. arXiv: 0704.2120 [astro-ph].

Larson, R. B. (Oct. 1976). “Galaxy Formation and Young Galaxies”. In: *Comments on Astrophysics* 6, p. 139.

Larson, R. B., B. M. Tinsley, and C. N. Caldwell (May 1980). “The evolution of disk galaxies and the origin of S0 galaxies”. In: 237, pp. 692–707. doi: 10.1086/157917.

Larson, Richard B. (Mar. 1974). “Dynamical models for the formation and evolution of spherical galaxies”. In: 166, pp. 585–616. doi: 10.1093/mnras/166.3.585.

Lassen, Augusto E., Rogerio Riffel, Ana L. Chies-Santos, Evelyn Johnston, Boris Häußler, Gabriel M. Azevedo, Daniel Ruschel-Dutra, and Rogemar A. Riffel (Sept. 2021). “The metal-poor dwarf irregular galaxy candidate next to Mrk 1172”. In: 506.3, pp. 3527–3539. doi: 10.1093/mnras/stab1838. arXiv: 2106.14925 [astro-ph.GA].

Laurikainen, Eija, Heikki Salo, Ronald Buta, and Sergiy Vasylyev (Dec. 2004). “Bar-induced perturbation strengths of the galaxies in the Ohio State University Bright Galaxy Survey - I”. In: 355.4, pp. 1251–1271. doi: 10.1111/j.1365-2966.2004.08410.x. arXiv: astro-ph/0409503 [astro-ph].

- Law, David R. et al. (Oct. 2016). “The Data Reduction Pipeline for the SDSS-IV MaNGA IFU Galaxy Survey”. In: 152.4, 83, p. 83. doi: 10.3847/0004-6256/152/4/83. arXiv: 1607.08619 [astro-ph.IM].
- Lazar, I., S. Kaviraj, G. Martin, C. Laigle, A. Watkins, and R. A. Jackson (Apr. 2023). “Relaxed blue ellipticals: accretion-driven stellar growth is a key evolutionary channel for low mass elliptical galaxies”. In: 520.2, pp. 2109–2120. doi: 10.1093/mnras/stad224. arXiv: 2302.06631 [astro-ph.GA].
- Le Borgne, J. -F. et al. (May 2003). “STELIB: A library of stellar spectra at $R \sim 2000$ ”. In: 402, pp. 433–442. doi: 10.1051/0004-6361:20030243. arXiv: astro-ph/0302334 [astro-ph].
- Lejeune, T. and D. Schaerer (Feb. 2001). “Database of Geneva stellar evolution tracks and isochrones for (UBV)_J(RI)_C JHKLL’M, HST-WFPC2, Geneva and Washington photometric systems”. In: 366, pp. 538–546. doi: 10.1051/0004-6361:20000214. arXiv: astro-ph/0011497 [astro-ph].
- Li, Cheng et al. (May 2015). “P-MaNGA: Gradients in Recent Star Formation Histories as Diagnostics for Galaxy Growth and Death”. In: 804.2, 125, p. 125. doi: 10.1088/0004-637X/804/2/125. arXiv: 1502.07040 [astro-ph.GA].
- Li, R., N. R. Napolitano, N. Roy, C. Tortora, F. La Barbera, A. Sonnenfeld, C. Qiu, and S. Liu (Apr. 2022). “Galaxy Light Profile Convolutional Neural Networks (GaLNet). I. Fast and Accurate Structural Parameters for Billion-galaxy Samples”. In: 929.2, 152, p. 152. doi: 10.3847/1538-4357/ac5ea0. arXiv: 2111.05434 [astro-ph.GA].
- Lima Neto, G. B., F. Durret, T. F. Laganá, R. E. G. Machado, N. Martinet, J. -C. Cuillandre, and C. Adami (Sept. 2020). “NGC 4104: A shell galaxy in a forming fossil group”. In: 641, A95, A95. doi: 10.1051/0004-6361/201936098. arXiv: 2006.13941 [astro-ph.GA].
- Liske, J. et al. (Sept. 2015a). “Galaxy And Mass Assembly (GAMA): end of survey report and data release 2”. In: 452.2, pp. 2087–2126. doi: 10.1093/mnras/stv1436. arXiv: 1506.08222 [astro-ph.GA].
- (Sept. 2015b). “Galaxy And Mass Assembly (GAMA): end of survey report and data release 2”. In: 452.2, pp. 2087–2126. doi: 10.1093/mnras/stv1436. arXiv: 1506.08222 [astro-ph.GA].
- MacArthur, Lauren A., Richard S. Ellis, Tommaso Treu, Vivian U, Kevin Bundy, and Sean Moran (June 2008). “The Evolutionary History of Galactic Bulges: Photometric and Spectroscopic Studies of Distant Spheroids in the GOODS Fields”. In: 680.1, pp. 70–91. doi: 10.1086/587887. arXiv: 0711.0238 [astro-ph].
- MacArthur, Lauren A., J. Jesús González, and Stéphane Courteau (May 2009). “Stellar population and kinematic profiles in spiral bulges and discs: population synthesis of integrated spectra”. In: 395.1, pp. 28–63. doi: 10.1111/j.1365-2966.2009.14519.x. arXiv: 0901.4135 [astro-ph.CO].
- Maio, Umberto, Benedetta Ciardi, Klaus Dolag, Luca Tornatore, and Sadegh Khochfar (Sept. 2010). “The transition from population III to population II-I star formation”. In: 407.2, pp. 1003–1015. doi: 10.1111/j.1365-2966.2010.17003.x. arXiv: 1003.4992 [astro-ph.CO].
- Malin, D. F. and D. Carter (June 1980). “Giant shells around normal elliptical galaxies”. In: 285.5767, pp. 643–645. doi: 10.1038/285643a0.

- Maller, Ariyeh H., Avishai Dekel, and Rachel Somerville (Jan. 2002). “Modelling angular-momentum history in dark-matter haloes”. In: 329.2, pp. 423–430. doi: 10.1046/j.1365-8711.2002.04983.x. arXiv: astro-ph/0105168 [astro-ph].
- Marigo, P., L. Girardi, A. Bressan, M. A. T. Groenewegen, L. Silva, and G. L. Granato (May 2008). “Evolution of asymptotic giant branch stars. II. Optical to far-infrared isochrones with improved TP-AGB models”. In: 482.3, pp. 883–905. doi: 10.1051/0004-6361:20078467. arXiv: 0711.4922 [astro-ph].
- Martins, Lucimara P., Rosa M. González Delgado, Claus Leitherer, Miguel Cerviño, and Peter Hauschildt (Mar. 2005). “A high-resolution stellar library for evolutionary population synthesis”. In: 358.1, pp. 49–65. doi: 10.1111/j.1365-2966.2005.08703.x. arXiv: astro-ph/0501225 [astro-ph].
- Mas-Hesse, J. Miguel and Daniel Kunth (Sept. 1999). “A comprehensive study of intense star formation bursts in irregular and compact galaxies”. In: 349, pp. 765–795. doi: 10.48550/arXiv.astro-ph/9812072. arXiv: astro-ph/9812072 [astro-ph].
- Masters, Karen L. and Galaxy Zoo Team (Jan. 2020). “Twelve years of Galaxy Zoo”. In: *Galactic Dynamics in the Era of Large Surveys*. Ed. by Monica Valluri and J. A. Sellwood. Vol. 353, pp. 205–212. doi: 10.1017/S1743921319008615. arXiv: 1910.08177 [astro-ph.GA].
- Masters, Karen L. et al. (Nov. 2021). “Galaxy Zoo: 3D - crowdsourced bar, spiral, and foreground star masks for MaNGA target galaxies”. In: 507.3, pp. 3923–3935. doi: 10.1093/mnras/stab2282. arXiv: 2108.02065 [astro-ph.GA].
- McDermid, Richard M. et al. (Apr. 2015). “The ATLAS^{3D} Project - XXX. Star formation histories and stellar population scaling relations of early-type galaxies”. In: 448.4, pp. 3484–3513. doi: 10.1093/mnras/stv105. arXiv: 1501.03723 [astro-ph.GA].
- McIntosh, Daniel H. et al. (July 2014). “A new population of recently quenched elliptical galaxies in the SDSS”. In: 442.1, pp. 533–557. doi: 10.1093/mnras/stu808. arXiv: 1308.0054 [astro-ph.GA].
- Meert, Alan, Vinu Vikram, and Mariangela Bernardi (Aug. 2013). “Simulations of single- and two-component galaxy decompositions for spectroscopically selected galaxies from the Sloan Digital Sky Survey”. In: 433.2, pp. 1344–1361. doi: 10.1093/mnras/stt822. arXiv: 1211.6123 [astro-ph.CO].
- (Feb. 2015). “A catalogue of 2D photometric decompositions in the SDSS-DR7 spectroscopic main galaxy sample: preferred models and systematics”. In: 446.4, pp. 3943–3974. doi: 10.1093/mnras/stu2333. arXiv: 1406.4179 [astro-ph.GA].
- (Jan. 2016). “A catalogue of two-dimensional photometric decompositions in the SDSS-DR7 spectroscopic main galaxy sample: extension to g and I bands”. In: 455.3, pp. 2440–2452. doi: 10.1093/mnras/stv2475. arXiv: 1510.07631 [astro-ph.GA].
- Mendel, J. Trevor, Luc Simard, Sara L. Ellison, and David R. Patton (Mar. 2013). “Towards a physical picture of star formation quenching: the photometric properties of recently quenched galaxies in the Sloan Digital Sky Survey”. In: 429.3, pp. 2212–2227. doi: 10.1093/mnras/sts489. arXiv: 1211.6115 [astro-ph.CO].

- Mendel, J. Trevor, Luc Simard, Michael Palmer, Sara L. Ellison, and David R. Patton (Jan. 2014). “A Catalog of Bulge, Disk, and Total Stellar Mass Estimates for the Sloan Digital Sky Survey”. In: 210.1, 3, p. 3. doi: 10.1088/0067-0049/210/1/3. arXiv: 1310.8304 [astro-ph.CO].
- Méndez-Abreu, J., J. A. L. Aguerri, E. M. Corsini, and E. Simonneau (Oct. 2008). “The Intrinsic Equatorial Ellipticity of Bulges”. In: *Formation and Evolution of Galaxy Disks*. Ed. by J. G. Funes and E. M. Corsini. Vol. 396. Astronomical Society of the Pacific Conference Series, p. 79.
- Méndez-Abreu, J., A. de Lorenzo-Cáceres, and S. F. Sánchez (June 2021). “The origin of bulges and discs in the CALIFA survey - I. Morphological evolution”. In: 504.2, pp. 3058–3073. doi: 10.1093/mnras/stab1064. arXiv: 2104.07743 [astro-ph.GA].
- Méndez-Abreu, J., S. F. Sánchez, and A. de Lorenzo-Cáceres (Apr. 2019a). “Spectro-photometric decomposition of galaxy structural components”. In: 484.3, pp. 4298–4314. doi: 10.1093/mnras/stz276. arXiv: 1901.08075 [astro-ph.GA].
- (Sept. 2019b). “Star formation in CALIFA early-type galaxies: a matter of discs”. In: 488.1, pp. L80–L84. doi: 10.1093/mnrasl/slz103. arXiv: 1906.10759 [astro-ph.GA].
- Michielsen, D. et al. (Apr. 2008). “The relation between stellar populations, structure and environment for dwarf elliptical galaxies from the MAGPOP-ITP”. In: 385.3, pp. 1374–1392. doi: 10.1111/j.1365-2966.2008.12846.x. arXiv: 0712.2017 [astro-ph].
- Mihos, J. Christopher and Lars Hernquist (Apr. 1994). “Triggering of Starbursts in Galaxies by Minor Mergers”. In: 425, p. L13. doi: 10.1086/187299.
- Miller, R. H. and B. F. Smith (Jan. 1980). “Galaxy collisions - A preliminary study”. In: 235, pp. 421–436. doi: 10.1086/157646.
- Moore, Ben, Neal Katz, George Lake, Alan Dressler, and Augustus Oemler (Feb. 1996). “Galaxy harassment and the evolution of clusters of galaxies”. In: 379.6566, pp. 613–616. doi: 10.1038/379613a0. arXiv: astro-ph/9510034 [astro-ph].
- Morgan, W. W. (Dec. 1956). “The Integrated Spectral Types of Globular Clusters”. In: 68.405, p. 509. doi: 10.1086/126988.
- Moura, Micheli T., Ana L. Chies-Santos, Cristina Furlanetto, Ling Zhu, and Marco A. Canossa-Gosteinski (Feb. 2024). “The internal dynamics and environments of Relics and compact massive ETGs with TNG50”. In: 528.1, pp. 353–364. doi: 10.1093/mnras/stae013. arXiv: 2401.02798 [astro-ph.GA].
- Naab, Thorsten, Peter H. Johansson, and Jeremiah P. Ostriker (July 2009). “Minor Mergers and the Size Evolution of Elliptical Galaxies”. In: 699.2, pp. L178–L182. doi: 10.1088/0004-637X/699/2/L178. arXiv: 0903.1636 [astro-ph.CO].
- Naab, Thorsten, Sadegh Khochfar, and Andreas Burkert (Jan. 2006). “Properties of Early-Type, Dry Galaxy Mergers and the Origin of Massive Elliptical Galaxies”. In: 636.2, pp. L81–L84. doi: 10.1086/500205. arXiv: astro-ph/0509667 [astro-ph].
- Nair, Preethi B. and Roberto G. Abraham (Feb. 2010). “A Catalog of Detailed Visual Morphological Classifications for 14,034 Galaxies in the Sloan Digital Sky Survey”. In: 186.2, pp. 427–456. doi: 10.1088/0067-0049/186/2/427. arXiv: 1001.2401 [astro-ph.CO].

- Nedkova, Kalina V. et al. (Sept. 2021). "Extending the evolution of the stellar mass-size relation at $z \leq 2$ to low stellar mass galaxies from HFF and CANDELS". In: 506.1, pp. 928–956. doi: 10.1093/mnras/stab1744. arXiv: 2106.07663 [astro-ph.GA].
- Norris, Mark A., Carlos G. Escudero, Favio R. Faifer, Sheila J. Kannappan, Juan Carlos Forte, and Remco C. E. van den Bosch (Aug. 2015). "An extended star formation history in an ultra-compact dwarf". In: 451.4, pp. 3615–3626. doi: 10.1093/mnras/stv1221. arXiv: 1506.00004 [astro-ph.GA].
- Ocvirk, P., C. Pichon, A. Lançon, and E. Thiébaud (Jan. 2006). "STECKMAP: STEllar Content and Kinematics from high resolution galactic spectra via Maximum A Posteriori". In: 365.1, pp. 74–84. doi: 10.1111/j.1365-2966.2005.09323.x. arXiv: astro-ph/0507002 [astro-ph].
- Ogando, Ricardo L. C., Marcio A. G. Maia, Cristina Chiappini, Paulo S. Pellegrini, Ricardo P. Schiavon, and Luiz N. da Costa (Oct. 2005). "Do Observed Metallicity Gradients of Early-Type Galaxies Support a Hybrid Formation Scenario?" In: 632.2, pp. L61–L64. doi: 10.1086/497824. arXiv: astro-ph/0509142 [astro-ph].
- Oke, J. B. and J. E. Gunn (Mar. 1983). "Secondary standard stars for absolute spectrophotometry." In: 266, pp. 713–717. doi: 10.1086/160817.
- Oser, Ludwig, Thorsten Naab, Jeremiah P. Ostriker, and Peter H. Johansson (Jan. 2012). "The Cosmological Size and Velocity Dispersion Evolution of Massive Early-type Galaxies". In: 744.1, 63, p. 63. doi: 10.1088/0004-637X/744/1/63. arXiv: 1106.5490 [astro-ph.CO].
- Oser, Ludwig, Jeremiah P. Ostriker, Thorsten Naab, Peter H. Johansson, and Andreas Burkert (Dec. 2010). "The Two Phases of Galaxy Formation". In: 725.2, pp. 2312–2323. doi: 10.1088/0004-637X/725/2/2312. arXiv: 1010.1381 [astro-ph.CO].
- Oyarzún, Grecco A. et al. (Aug. 2019). "Signatures of Stellar Accretion in MaNGA Early-type Galaxies". In: 880.2, 111, p. 111. doi: 10.3847/1538-4357/ab297c. arXiv: 1906.05298 [astro-ph.GA].
- Pak, Mina, Joon Hyeop Lee, Hyunjin Jeong, Suk Kim, Rory Smith, and Hye-Ran Lee (Aug. 2019). "Stellar Populations of Nine Passive Spiral Galaxies from the CALIFA Survey: Are They Progenitors of S0s?" In: 880.2, 149, p. 149. doi: 10.3847/1538-4357/ab2ad6. arXiv: 1906.07484 [astro-ph.GA].
- Pak, Mina, Joon Hyeop Lee, Sree Oh, Francesco D'Eugenio, Matthew Colless, Hyunjin Jeong, and Woong-Seob Jeong (Nov. 2021). "Stellar Populations of Spectroscopically Decomposed Bulge-Disk for S0 Galaxies from the CALIFA Survey". In: 921.1, 49, p. 49. doi: 10.3847/1538-4357/ac1ba1. arXiv: 2108.05014 [astro-ph.GA].
- Parikh, Taniya, Daniel Thomas, Claudia Maraston, Kyle B. Westfall, Brett H. Andrews, Nicholas Fraser Boardman, Niv Drory, and Grecco Oyarzun (Apr. 2021). "SDSS-IV MaNGA: radial gradients in stellar population properties of early-type and late-type galaxies". In: 502.4, pp. 5508–5527. doi: 10.1093/mnras/stab449. arXiv: 2102.06703 [astro-ph.GA].
- Parikh, Taniya et al. (Mar. 2019). "SDSS-IV MaNGA: local and global chemical abundance patterns in early-type galaxies". In: 483.3, pp. 3420–3436. doi: 10.1093/mnras/sty3339. arXiv: 1812.02753 [astro-ph.GA].
- Peebles, P. J. E. (Feb. 1969). "Origin of the Angular Momentum of Galaxies". In: 155, p. 393. doi: 10.1086/149876.

Peletier, R. F. (June 2008). “On Classical and Pseudo-bulges: The Nature of Bulges of Early-type Spirals”. In: *Pathways Through an Eclectic Universe*. Ed. by J. H. Knapen, T. J. Mahoney, and A. Vazdekis. Vol. 390. Astronomical Society of the Pacific Conference Series, p. 232. doi: 10.48550/arXiv.0707.4063. arXiv: 0707.4063 [astro-ph].

Peng, Chien Y., Luis C. Ho, Chris D. Impey, and Hans-Walter Rix (July 2002). “Detailed Structural Decomposition of Galaxy Images”. In: 124.1, pp. 266–293. doi: 10.1086/340952. arXiv: astro-ph/0204182 [astro-ph].

— (Apr. 2011). *GALFIT: Detailed Structural Decomposition of Galaxy Images*. Astrophysics Source Code Library, record ascl:1104.010. ascl: 1104.010.

Pérez, E. et al. (Feb. 2013). “The Evolution of Galaxies Resolved in Space and Time: A View of Inside-out Growth from the CALIFA Survey”. In: 764.1, L1, p. L1. doi: 10.1088/2041-8205/764/1/L1. arXiv: 1301.1679 [astro-ph.CO].

Peterken, Thomas, Michael Merrifield, Alfonso Aragón-Salamanca, Amelia Fraser-McKelvie, Vladimir Avila-Reese, Rogério Riffel, Johan Knapen, and Niv Drory (Jan. 2020). “SDSS-IV MaNGA: Excavating the fossil record of stellar populations in spiral galaxies”. In: 495.3, pp. 3387–3402. doi: 10.1093/mnras/staa1303. arXiv: 2005.03012 [astro-ph.GA].

Pfeffer, Joel, Mitchell K. Cavanagh, Kenji Bekki, Warrick J. Couch, Michael J. Drinkwater, Duncan A. Forbes, and Bärbel S. Koribalski (Feb. 2023). “The galaxy morphology-density relation in the EAGLE simulation”. In: 518.4, pp. 5260–5278. doi: 10.1093/mnras/stac3466. arXiv: 2212.08748 [astro-ph.GA].

Pietrinferni, Adriano, Santi Cassisi, Maurizio Salaris, and Fiorella Castelli (Sept. 2004). “A Large Stellar Evolution Database for Population Synthesis Studies. I. Scaled Solar Models and Isochrones”. In: 612.1, pp. 168–190. doi: 10.1086/422498. arXiv: astro-ph/0405193 [astro-ph].

— (May 2006). “A Large Stellar Evolution Database for Population Synthesis Studies. II. Stellar Models and Isochrones for an α -enhanced Metal Distribution”. In: 642.2, pp. 797–812. doi: 10.1086/501344. arXiv: astro-ph/0603721 [astro-ph].

Pietrinferni, Adriano, Santi Cassisi, Maurizio Salaris, and Sebastian Hidalgo (Oct. 2013). “The BaSTI Stellar Evolution Database: models for extremely metal-poor and super-metal-rich stellar populations”. In: 558, A46, A46. doi: 10.1051/0004-6361/201321950. arXiv: 1308.3850 [astro-ph.SR].

Planck Collaboration et al. (Sept. 2016). “Planck 2015 results. XIII. Cosmological parameters”. In: 594, A13, A13. doi: 10.1051/0004-6361/201525830. arXiv: 1502.01589 [astro-ph.CO].

Plauchu-Frayn, I., A. Del Olmo, R. Coziol, and J. P. Torres-Papaqui (Oct. 2012). “The star formation histories of Hickson compact group galaxies”. In: 546, A48, A48. doi: 10.1051/0004-6361/201219916. arXiv: 1208.1756 [astro-ph.CO].

Prugniel, Ph. and C. Soubiran (Apr. 2001). “A database of high and medium-resolution stellar spectra”. In: 369, pp. 1048–1057. doi: 10.1051/0004-6361:20010163. arXiv: astro-ph/0101378 [astro-ph].

Qiu, Chen et al. (June 2023). “Galaxy Light profile neural Networks (GaLNet). II. Bulge-Disc decomposition in optical space-based observations”. In: *arXiv e-prints*, arXiv:2306.05909, arXiv:2306.05909. doi: 10.48550/arXiv.2306.05909. arXiv: 2306.05909 [astro-ph.GA].

- Riffel, R., M. G. Pastoriza, A. Rodríguez-Ardila, and C. Bonatto (Nov. 2009). “Probing the near-infrared stellar population of Seyfert galaxies”. In: 400.1, pp. 273–290. doi: 10.1111/j.1365-2966.2009.15448.x. arXiv: 0907.4144 [astro-ph.CO].
- Riffel, Rogério et al. (Oct. 2023). “Mapping the stellar population and gas excitation of MaNGA galaxies with MEGACUBES. Results for AGN versus control sample”. In: 524.4, pp. 5640–5657. doi: 10.1093/mnras/stad2234. arXiv: 2307.11474 [astro-ph.GA].
- Riffel, Rogério et al. (June 2024). “Observational constraints on the stellar recycled gas in active galactic nuclei feeding”. In: 531.1, pp. 554–574. doi: 10.1093/mnras/stae1192. arXiv: 2405.00634 [astro-ph.GA].
- Robotham, A. S. G., D. S. Taranu, R. Tobar, A. Moffett, and S. P. Driver (Apr. 2017). “PROFIT: Bayesian profile fitting of galaxy images”. In: 466.2, pp. 1513–1541. doi: 10.1093/mnras/stw3039. arXiv: 1611.08586 [astro-ph.IM].
- Romero-Gómez, J., Reynier F. Peletier, J. A. L. Aguerri, and R. Smith (Apr. 2024). “Are early-type galaxies quenched by present-day environment? A study of dwarfs in the Fornax Cluster”. In: *arXiv e-prints*, arXiv:2404.15519, arXiv:2404.15519. doi: 10.48550/arXiv.2404.15519. arXiv: 2404.15519 [astro-ph.GA].
- Salpeter, Edwin E. (Jan. 1955). “The Luminosity Function and Stellar Evolution.” In: 121, p. 161. doi: 10.1086/145971.
- Sánchez, S. F. et al. (Feb. 2012). “CALIFA, the Calar Alto Legacy Integral Field Area survey. I. Survey presentation”. In: 538, A8, A8. doi: 10.1051/0004-6361/201117353. arXiv: 1111.0962 [astro-ph.CO].
- Sánchez, S. F. et al. (Apr. 2016). “Pipe3D, a pipeline to analyze Integral Field Spectroscopy Data: I. New fitting philosophy of FIT3D”. In: 52, pp. 21–53. doi: 10.48550/arXiv.1509.08552. arXiv: 1509.08552 [astro-ph.IM].
- Sánchez-Blázquez, P., P. Ocvirk, B. K. Gibson, I. Pérez, and R. F. Peletier (July 2011). “Star formation history of barred disc galaxies”. In: 415.1, pp. 709–731. doi: 10.1111/j.1365-2966.2011.18749.x. arXiv: 1103.3796 [astro-ph.CO].
- Sánchez-Blázquez, P. et al. (Sept. 2006). “Medium-resolution Isaac Newton Telescope library of empirical spectra”. In: 371.2, pp. 703–718. doi: 10.1111/j.1365-2966.2006.10699.x. arXiv: astro-ph/0607009 [astro-ph].
- Sánchez-Blázquez, P. et al. (Oct. 2014). “Stellar population gradients in galaxy discs from the CALIFA survey. The influence of bars”. In: 570, A6, A6. doi: 10.1051/0004-6361/201423635. arXiv: 1407.0002 [astro-ph.GA].
- Sandage, Allan (1961). *The Hubble Atlas of Galaxies*.
- Scoville, N. et al. (Sept. 2007a). “The Cosmic Evolution Survey (COSMOS): Overview”. In: 172.1, pp. 1–8. doi: 10.1086/516585. arXiv: astro-ph/0612305 [astro-ph].
- (Sept. 2007b). “The Cosmic Evolution Survey (COSMOS): Overview”. In: 172.1, pp. 1–8. doi: 10.1086/516585. arXiv: astro-ph/0612305 [astro-ph].
- Sersic, Jose Luis (1968). *Atlas de Galaxias Australes*.

- Shetty, Shravan and Michele Cappellari (Dec. 2015). "Observed trend in the star formation history and the dark matter fraction of galaxies at redshift $z \approx 0.8$ ". In: 454.2, pp. 1332–1357. doi: 10.1093/mnras/stv1948. arXiv: 1508.05009 [astro-ph.GA].
- Sil'Chenko, O. K. (Apr. 2006). "Evolution of the central parts of S0 galaxies". In: *Astronomical and Astrophysical Transactions* 25.2, pp. 199–203. doi: 10.1080/10556790600895992.
- Sil'chenko, O. K., I. S. Proshina, A. P. Shulga, and S. E. Kuposov (Nov. 2012). "Ages and abundances in large-scale stellar discs of nearby S0 galaxies". In: 427.1, pp. 790–805. doi: 10.1111/j.1365-2966.2012.21990.x. arXiv: 1209.0606 [astro-ph.CO].
- Silk, J. (Feb. 1977). "On the fragmentation of cosmic gas clouds. I. The formation of galaxies and the first generation of stars." In: 211, pp. 638–648. doi: 10.1086/154972.
- Simard, Luc, J. Trevor Mendel, David R. Patton, Sara L. Ellison, and Alan W. McConnachie (Sept. 2011). "A Catalog of Bulge+disk Decompositions and Updated Photometry for 1.12 Million Galaxies in the Sloan Digital Sky Survey". In: 196.1, 11, p. 11. doi: 10.1088/0067-0049/196/1/11. arXiv: 1107.1518 [astro-ph.CO].
- Simard, Luc et al. (Sept. 2002). "The DEEP Groth Strip Survey. II. Hubble Space Telescope Structural Parameters of Galaxies in the Groth Strip". In: 142.1, pp. 1–33. doi: 10.1086/341399. arXiv: astro-ph/0205025 [astro-ph].
- Siudek, M. et al. (Aug. 2023). "Environments of red nuggets at z 0.7 from the VIPERS survey". In: 523.3, pp. 4294–4308. doi: 10.1093/mnras/stad1685. arXiv: 2306.03230 [astro-ph.GA].
- Smee, Stephen A. et al. (Aug. 2013). "The Multi-object, Fiber-fed Spectrographs for the Sloan Digital Sky Survey and the Baryon Oscillation Spectroscopic Survey". In: 146.2, 32, p. 32. doi: 10.1088/0004-6256/146/2/32. arXiv: 1208.2233 [astro-ph.IM].
- Smith, J. Allyn et al. (Apr. 2002). "The u'g'r'i'z' Standard-Star System". In: 123.4, pp. 2121–2144. doi: 10.1086/339311. arXiv: astro-ph/0201143 [astro-ph].
- Soto, Kurt T., Simon J. Lilly, Roland Bacon, Johan Richard, and Simon Conseil (May 2016). "ZAP - enhanced PCA sky subtraction for integral field spectroscopy". In: 458.3, pp. 3210–3220. doi: 10.1093/mnras/stw474. arXiv: 1602.08037 [astro-ph.IM].
- Spavone, Marilena, Davor Krajnović, Eric Emsellem, Enrichetta Iodice, and Mark den Brok (May 2021). "Assembly history of massive galaxies. A pilot project with VEGAS deep imaging and M3G integral field spectroscopy". In: 649, A161, A161. doi: 10.1051/0004-6361/202040186. arXiv: 2103.07478 [astro-ph.GA].
- Spavone, Marilena et al. (July 2017). "A Photometric Study of Giant Ellipticals and Their Stellar Halos With VST". In: *Galaxies* 5.3, 31, p. 31. doi: 10.3390/galaxies5030031.
- Spinrad, Hyron (Nov. 1972). "A Comparison of Spectral Scans of Some E and so Galaxies". In: 177, p. 285. doi: 10.1086/151707.
- Tacchella, S. et al. (Apr. 2015). "Evidence for mature bulges and an inside-out quenching phase 3 billion years after the Big Bang". In: *Science* 348.6232, pp. 314–317. doi: 10.1126/science.1261094. arXiv: 1504.04021 [astro-ph.GA].
- Tal, Tomer, Pieter G. van Dokkum, Jenica Nelan, and Rachel Bezanson (Nov. 2009). "The Frequency of Tidal Features Associated with Nearby Luminous Elliptical Galaxies From a

- Statistically Complete Sample". In: 138.5, pp. 1417–1427. doi: 10.1088/0004-6256/138/5/1417. arXiv: 0908.1382 [astro-ph.CO].
- Talbot, Michael S. et al. (Mar. 2018). "SDSS-IV MaNGA: the spectroscopic discovery of strongly lensed galaxies". In: 477.1, pp. 195–209. doi: 10.1093/mnras/sty653. arXiv: 1803.03604 [astro-ph.GA].
- Taylor, Philip and Chiaki Kobayashi (Nov. 2017). "The metallicity and elemental abundance gradients of simulated galaxies and their environmental dependence". In: 471.4, pp. 3856–3870. doi: 10.1093/mnras/stx1860. arXiv: 1707.06488 [astro-ph.GA].
- Thielemann, F.-K., F. Brachwitz, P. Höflich, G. Martinez-Pinedo, and K. Nomoto (May 2004). "The physics of type Ia supernovae". In: 48.7-8, pp. 605–610. doi: 10.1016/j.newar.2003.12.038.
- Thomas, J., R. P. Saglia, R. Bender, P. Erwin, and M. Fabricius (Feb. 2014). "The Dynamical Fingerprint of Core Scouring in Massive Elliptical Galaxies". In: 782.1, 39, p. 39. doi: 10.1088/0004-637X/782/1/39. arXiv: 1311.3783 [astro-ph.GA].
- Tinsley, Beatrice M. (Feb. 1968). "Evolution of the Stars and Gas in Galaxies". In: 151, p. 547. doi: 10.1086/149455.
- Toft, S. et al. (Dec. 2007). "Hubble Space Telescope and Spitzer Imaging of Red and Blue Galaxies at $z \sim 2.5$: A Correlation between Size and Star Formation Activity from Compact Quiescent Galaxies to Extended Star-forming Galaxies". In: 671.1, pp. 285–302. doi: 10.1086/521810. arXiv: 0707.4484 [astro-ph].
- Toomre, Alar (Jan. 1977). "Mergers and Some Consequences". In: *Evolution of Galaxies and Stellar Populations*. Ed. by Beatrice M. Tinsley and D. Campbell Larson Richard B. Gehret, p. 401.
- Toomre, Alar and Juri Toomre (Dec. 1972). "Galactic Bridges and Tails". In: 178, pp. 623–666. doi: 10.1086/151823.
- Trujillo, I., Peter Erwin, A. Asensio Ramos, and Alister W. Graham (Apr. 2004). "Evidence for a New Elliptical-Galaxy Paradigm: Sérsic and Core Galaxies". In: 127.4, pp. 1917–1942. doi: 10.1086/382712. arXiv: astro-ph/0403659 [astro-ph].
- Trujillo, Ignacio, C. J. Conselice, Kevin Bundy, M. C. Cooper, P. Eisenhardt, and Richard S. Ellis (Nov. 2007). "Strong size evolution of the most massive galaxies since $z \sim 2$ ". In: 382.1, pp. 109–120. doi: 10.1111/j.1365-2966.2007.12388.x. arXiv: 0709.0621 [astro-ph].
- Valdes, Francisco, Ranjan Gupta, James A. Rose, Harinder P. Singh, and David J. Bell (June 2004). "The Indo-US Library of Coudé Feed Stellar Spectra". In: 152.2, pp. 251–259. doi: 10.1086/386343. arXiv: astro-ph/0402435 [astro-ph].
- van den Bergh, S. (June 1976). "A new classification system for galaxies." In: 206, pp. 883–887. doi: 10.1086/154452.
- van Dokkum, Pieter G. (Dec. 2005). "The Recent and Continuing Assembly of Field Elliptical Galaxies by Red Mergers". In: 130.6, pp. 2647–2665. doi: 10.1086/497593. arXiv: astro-ph/0506661 [astro-ph].
- van Dokkum, Pieter G. et al. (Apr. 2008). "Confirmation of the Remarkable Compactness of Massive Quiescent Galaxies at $z \sim 2.3$: Early-Type Galaxies Did not Form in a Simple Monolithic Collapse". In: 677.1, p. L5. doi: 10.1086/587874. arXiv: 0802.4094 [astro-ph].

- Vanderriest, C. (Dec. 1980). "A fiber-optics dissector for spectroscopy of nebulosities around quasars and similar objects". In: 92, pp. 858–862. doi: 10.1086/130764.
- Vazdekis, A., P. Sánchez-Blázquez, J. Falcón-Barroso, A. J. Cenarro, M. A. Beasley, N. Cardiel, J. Gorgas, and R. F. Peletier (June 2010). "Evolutionary stellar population synthesis with MILES - I. The base models and a new line index system". In: 404.4, pp. 1639–1671. doi: 10.1111/j.1365-2966.2010.16407.x. arXiv: 1004.4439 [astro-ph.CO].
- Vazdekis, A. et al. (May 2015). "Evolutionary stellar population synthesis with MILES - II. Scaled-solar and α -enhanced models". In: 449.2, pp. 1177–1214. doi: 10.1093/mnras/stv151. arXiv: 1504.08032 [astro-ph.GA].
- Vázquez-Mata, J. A. et al. (May 2022). "SDSS IV MaNGA: visual morphological and statistical characterization of the DR15 sample". In: 512.2, pp. 2222–2244. doi: 10.1093/mnras/stac635. arXiv: 2203.02565 [astro-ph.GA].
- Vika, Marina, Steven P. Bamford, Boris Häußler, and Alex L. Rojas (Nov. 2014a). "MegaMorph - multiwavelength measurement of galaxy structure: physically meaningful bulge-disc decomposition of galaxies near and far". In: 444.4, pp. 3603–3621. doi: 10.1093/mnras/stu1696. arXiv: 1408.4070 [astro-ph.GA].
- (Nov. 2014b). "MegaMorph - multiwavelength measurement of galaxy structure: physically meaningful bulge-disc decomposition of galaxies near and far". In: 444.4, pp. 3603–3621. doi: 10.1093/mnras/stu1696. arXiv: 1408.4070 [astro-ph.GA].
- Vika, Marina, Steven P. Bamford, Boris Häußler, Alex L. Rojas, Andrea Borch, and Robert C. Nichol (Oct. 2013). "MegaMorph - multiwavelength measurement of galaxy structure. Sérsic profile fits to galaxies near and far". In: 435.1, pp. 623–649. doi: 10.1093/mnras/stt1320. arXiv: 1307.4996 [astro-ph.CO].
- Vikram, Vinu, Yogesh Wadadekar, Ajit K. Kembhavi, and G. V. Vijayagovindan (Dec. 2010). "PYMORPH: automated galaxy structural parameter estimation using PYTHON". In: 409.4, pp. 1379–1392. doi: 10.1111/j.1365-2966.2010.17426.x. arXiv: 1007.4965 [astro-ph.IM].
- Vulcani, Benedetta et al. (Dec. 2014). "Understanding the Unique Assembly History of Central Group Galaxies". In: 797.1, 62, p. 62. doi: 10.1088/0004-637X/797/1/62. arXiv: 1410.7402 [astro-ph.GA].
- Weilbacher, Peter M. et al. (Sept. 2020). "The data processing pipeline for the MUSE instrument". In: 641, A28, A28. doi: 10.1051/0004-6361/202037855. arXiv: 2006.08638 [astro-ph.IM].
- White, S. D. M. (Nov. 1984). "Angular momentum growth in protogalaxies". In: 286, pp. 38–41. doi: 10.1086/162573.
- White, S. D. M. and M. J. Rees (May 1978). "Core condensation in heavy halos: a two-stage theory for galaxy formation and clustering." In: 183, pp. 341–358. doi: 10.1093/mnras/183.3.341.
- White, Simon D. M. and Carlos S. Frenk (Sept. 1991). "Galaxy Formation through Hierarchical Clustering". In: 379, p. 52. doi: 10.1086/170483.
- Whitmore, Bradley C. and Diane M. Gilmore (Jan. 1991). "On the Interpretation of the Morphology-Density Relation for Galaxies in Clusters". In: 367, p. 64. doi: 10.1086/169602.

- Wilkinson, David M., Claudia Maraston, Daniel Goddard, Daniel Thomas, and Taniya Parikh (Dec. 2017). “FIREFLY (Fitting ItERatively For Likelihood analYsis): a full spectral fitting code”. In: 472.4, pp. 4297–4326. doi: 10.1093/mnras/stx2215. arXiv: 1711.00865 [astro-ph.GA].
- Woo, Joanna, Dan Walters, Finn Archinuk, S. M. Faber, Sara L. Ellison, Hossen Teimoorinia, and Kartheik Iyer (June 2024). “Stellar populations with optical spectra: deep learning versus popular spectrum fitting codes”. In: 530.4, pp. 4260–4276. doi: 10.1093/mnras/stae1114. arXiv: 2401.12300 [astro-ph.GA].
- Worthey, G. (Jan. 1999). “The Age-Metallicity Degeneracy”. In: *Spectrophotometric Dating of Stars and Galaxies*. Ed. by Ivan Hubeny, Sally Heap, and Robert Cornett. Vol. 192. Astronomical Society of the Pacific Conference Series, p. 283.
- Yan, Renbin et al. (Dec. 2016). “SDSS-IV MaNGA IFS Galaxy Survey—Survey Design, Execution, and Initial Data Quality”. In: 152.6, 197, p. 197. doi: 10.3847/0004-6256/152/6/197. arXiv: 1607.08613 [astro-ph.GA].
- York, Donald G. et al. (Sept. 2000). “The Sloan Digital Sky Survey: Technical Summary”. In: 120.3, pp. 1579–1587. doi: 10.1086/301513. arXiv: astro-ph/0006396 [astro-ph].
- Zhang, Bing-Qing, Hong Wu, Wei Du, Pin-Song Zhao, Min He, and Feng-Jie Lei (Jan. 2024). “Low Surface Brightness Galaxies Selected by Different Model Fitting”. In: *Research in Astronomy and Astrophysics* 24.1, 015018, p. 015018. doi: 10.1088/1674-4527/ad0b86. arXiv: 2312.08179 [astro-ph.GA].
- Zibetti, Stefano, Anna R. Gallazzi, Michaela Hirschmann, Guido Consolandi, Jesús Falcón-Barroso, Glenn van de Ven, and Mariya Lyubenova (Jan. 2020). “Insights into formation scenarios of massive early-type galaxies from spatially resolved stellar population analysis in CALIFA”. In: 491.3, pp. 3562–3585. doi: 10.1093/mnras/stz3205. arXiv: 1906.02209 [astro-ph.GA].
- Zibetti, Stefano, Edoardo Rossi, and Anna R. Gallazzi (Feb. 2024). “On the maximum age resolution achievable through stellar population synthesis models”. In: 528.2, pp. 2790–2804. doi: 10.1093/mnras/stae178. arXiv: 2401.07335 [astro-ph.GA].

APPENDICES

SDSS PHOTOMETRY WITH BAGPIPES - STELLAR MASS DEPENDENCE OF E-FOLDING TIME τ

In Sect. 2.6.2, the MAH built from spectral fitting show a clear dependence on the component stellar mass. In the context of our photometric analysis, we again find that the more massive the component is, the quicker its assembly. The bulges and discs with the highest masses had assembled their stellar masses in a shorter timescale. The bulges also showed a higher fraction of rapid assembly compared to the discs, apart from the observed mass dependence.

In this section, we compare these global results from spectra to those we obtain from SED fitting of the corresponding SDSS photometry of the galaxies in the *ugriz* bands using BAGPIPES. In the setup for the SED fitting, we assume a parametric star-formation history that is exponentially declining (τ model), where τ is the e-folding time, which is the timescale needed for the star formation rate (SFR) to decline by a factor of e . This parameter essentially gives us information about star formation timescales in the galaxy bulges and discs - the shorter the e-folding time, the shorter is the star formation period. On the other hand, a longer e-folding time implies a more extended star formation period.

From the upper panel of Figure A.1, the median τ of galaxy bulges $< 10^{10} M_{\odot}$ show relatively high values between 6 and 8 Gyr, with no trend within the bins of this bulge mass range. These high e-folding times indicate slower star formation timescales over an extended period. After this, τ_{bulge} drops steeply with increasing stellar mass. This indicates that these higher mass bulges would have experienced a burst of star formation where a significant fraction of its stars formed over a short period, which becomes shorter with increasing bulge mass (dropping from ~ 6 Gyr to ~ 1 Gyr in the bins $> 10^{10} M_{\odot}$). The discs show a very similar trend with the disc stellar mass, in the low-mass regime of $< 10^{10} M_{\odot}$, where the e-folding times of both the bulges and discs appear to almost overlap with each other. At these lower masses defined earlier, the long and extended star formation dominates. At higher masses, the e-folding times of the disc again declines with increasing disc mass, but the trend is shallower compared

to the bulges and slowly drop by 1 - 2 Gyr. We note that the uncertainties on the median τ are quite large, spanning almost 8 Gyr in some cases, implying a large diversity in the star formation timescales, when we observe the dependence purely on the stellar mass. Nevertheless, the median trends agree well with our results from spectral analysis in Sect. 2.6.2.

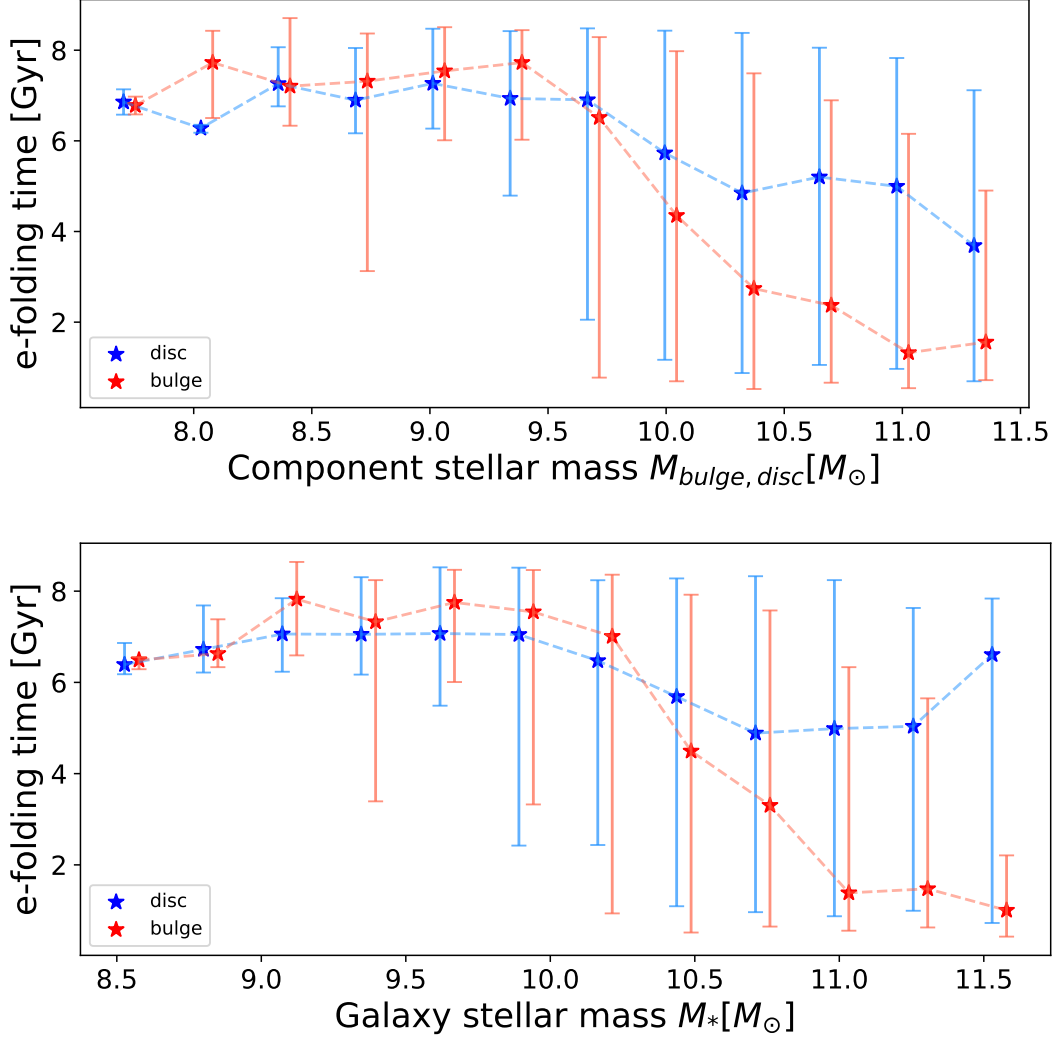


Figure A.1: Dependence of e-folding time as a function of stellar mass. Upper panel: Variation of e-folding times of bulges τ_{bulge} (red) and discs τ_{disc} (blue) as a function of their corresponding component stellar masses. The stars represent the median value in each mass bin, and the error bars show the 16th-84th percentile range in the spread of values in each bin. Lower panel: Similar to above but with the total galaxy stellar mass along the x-axis. In both panels, the τ_{bulge} was shifted by 0.05 dex for clarity in visualisation.

In the lower panel of Figure A.1, we observe the same general trend of the e-folding times as a function of the total galaxy stellar mass instead of the component mass, with the decline in τ beginning at $\sim 10^{10.5} M_{\odot}$. The decline in the discs is shallower (with the upturn at $\sim 11.5 M_{\odot}$ explained by low-number statistics of high mass discs in our sample). We associate the shallow drop in τ_{disc} with total mass to the significant diversity in star formation histories in discs. We assume an exponentially declining

SFH throughout for both bulges and discs to support an automated fitting process, but we acknowledge that some of the discs might need additional starburst models superimposed on the standard τ model.

BULGE SÉRSIC INDEX AS A FUNCTION OF GALAXY STELLAR MASS

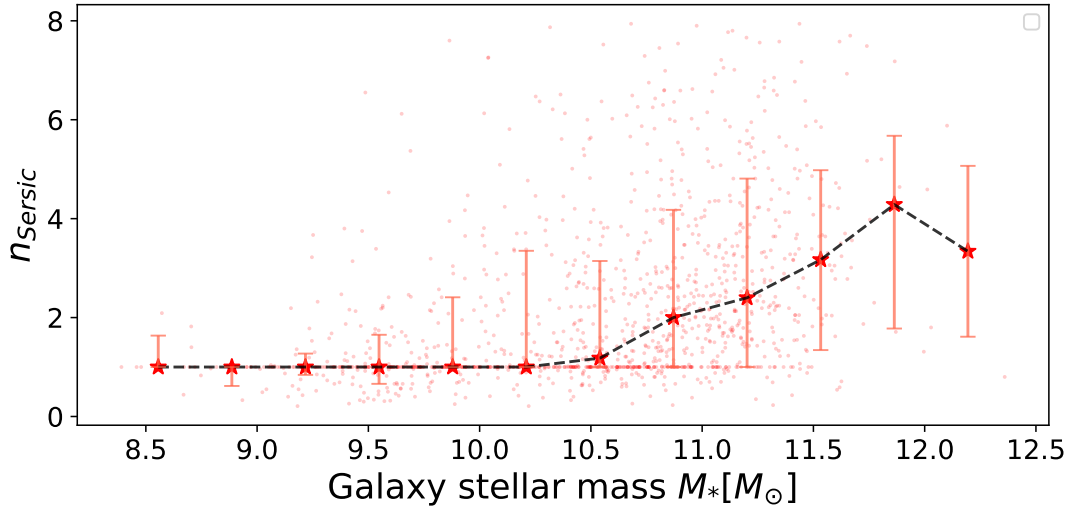


Figure B.1: Bulge Sérsic index as a function of the total galaxy stellar mass M_* . The red points show the individual galaxies, while the red stars show the binned median, with the error bars marking the 16th-84th percentile range. For statistically significant mass bins of $M_* > 10^{10} M_\odot$, the Sérsic index of the bulge increases with increasing galaxy mass, which arises from the bulge assembling from the discs. The timescale of assembly is expected to be shorter for the more massive galaxies, and longer for the less massive ones, which is consistent with our results on downsizing seen in low-redshift spiral galaxies.

STELLAR POPULATION PROPERTIES OF BULGES AND DISCS

In this section, we look at the dependence of the mass-weighted stellar populations on disc stellar mass in our spiral galaxy sample. In Figure C.1 the upper panel compares the mean stellar metallicities of the bulge with the discs, as in Sect. 2.7, this time colour-coded by the disc masses instead. The lower panel compares the mean logarithmic stellar ages of the bulges and discs, colour-coded by the disc masses.

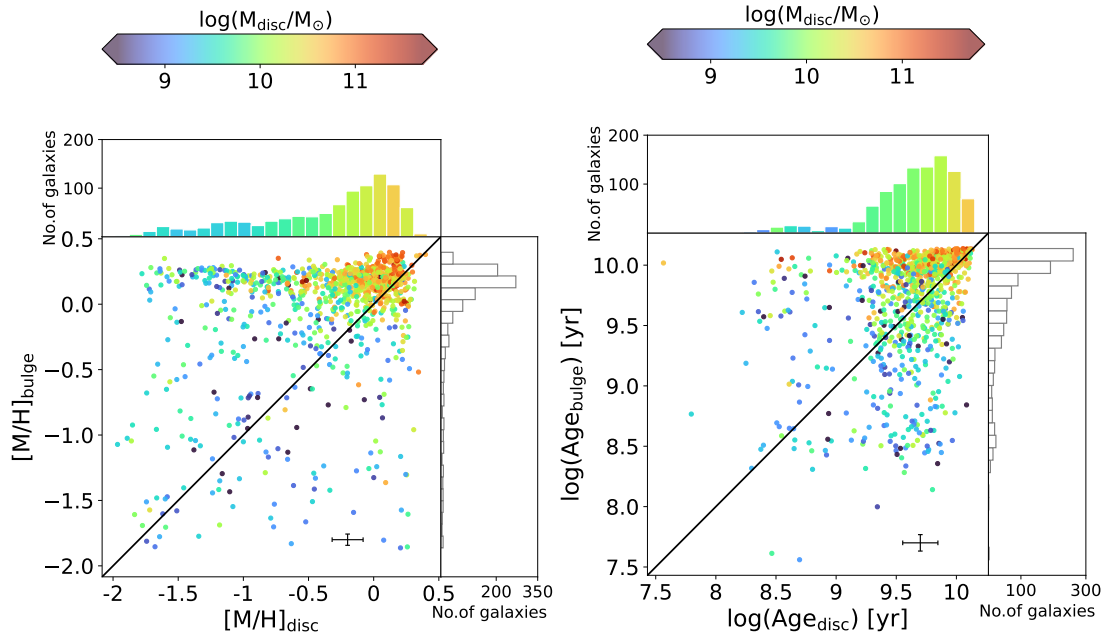


Figure C.1: *Stellar population properties of bulges and discs and their corresponding distributions. Upper panel: Comparison of mean mass-weighted stellar metallicities of the bulges and the discs (with their uncertainties), colour-coded by disc stellar masses. The distributions in bulge (disc) metallicities are shown in the right (upper) joint histograms. Each bin in the metallicity histogram of the bulges is colour-coded by the mean disc mass in that bin. Lower panel: Similar to the upper panel but for stellar ages. The black diagonal line marks the 1:1 correlation.*

From the upper panel, we find the same trends with respect to disc stellar mass as the bulge stellar mass in Sect. 2.7. The discs with the highest masses (red-orange points)

again are clustered above the 1:1 line, implying that the majority of the spiral galaxies where the bulges are more metal-rich than the discs have both bulges and discs of high metallicities. With decreasing disc masses (towards the green-blue points on the left of the plot), we find galaxies with discs that have low metallicities. This general trend is clearly visible on the upper-joint histogram - starting with the massive high-metallicity discs (orange bins) on the right, steadily decreasing in both stellar mass and metallicity (blue bins) towards the left.

The lower panel shows a similar trend for stellar ages, wherein the most massive discs are also old (red-orange points). The histogram above shows a smooth trend from old and massive discs (orange bins) to young low-mass discs (blue bins).

HALF-MASS FORMATION TIMESCALES OF BULGES AND DISCS

From Sect. 2.6.1.2, we define the half-mass formation timescale ($\tau_{1/2}$), as the difference between the time when stellar mass assembly (star formation) first occurred in each component, and the time when 50% of its current stellar mass had been assembled. The time of first star formation was taken to be the lookback time with the earliest non-zero weight measured by pPXF during the full-spectrum fitting. The results and inferences from Figure D.1 shown here are discussed in Sect. 2.6.1.2.

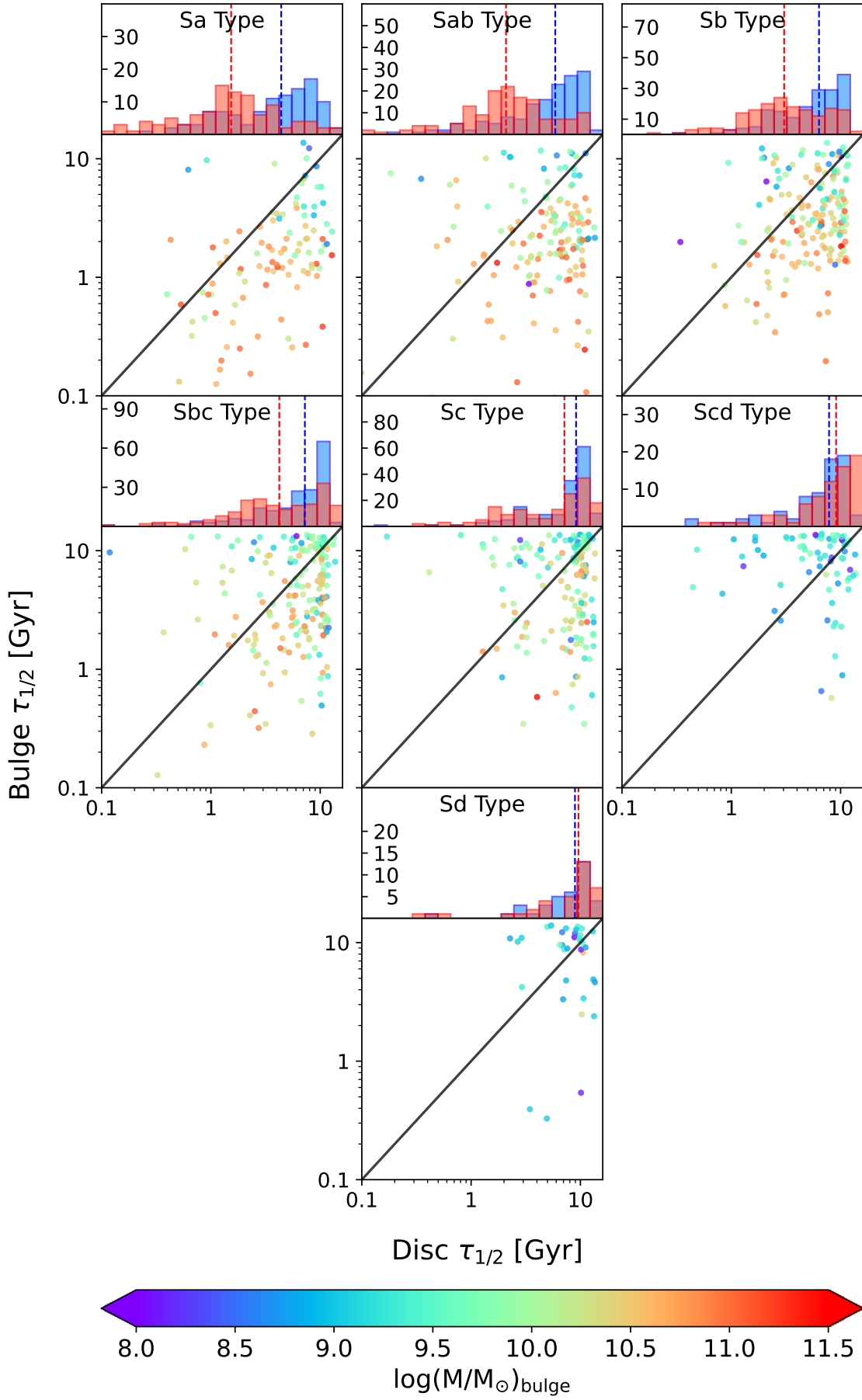


Figure D.1: Half-mass formation timescales of the bulges and discs, colour-coded by bulge mass. The upper panels show the histogram of these formation timescales for the bulge and disc in red and blue respectively, with their median times in dashed lines.

RECONCILING STELLAR HISTORIES OF ELLIPTICALS IN BUDDI-MaNGA AND MUSE

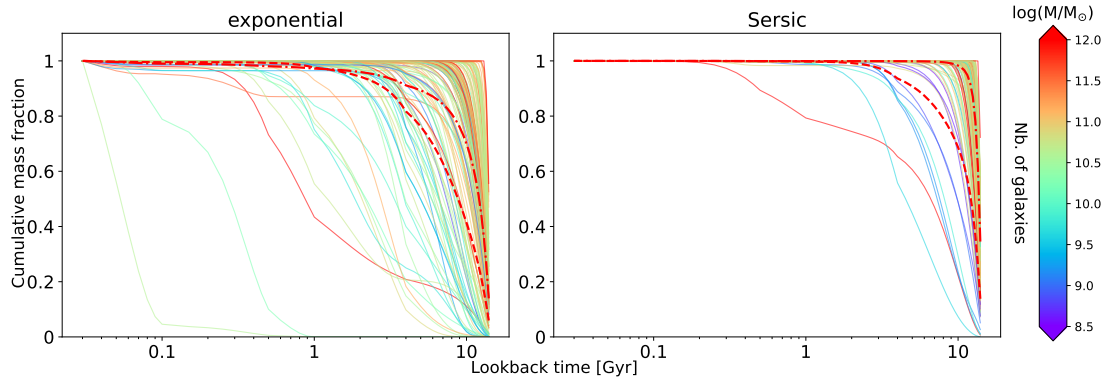


Figure E.1: Mass-assembly histories of two components (Sérsic+exponential) in elliptical galaxies in the BUDDI-MaNGA DR17 sample. The “exponential” component shows more delayed assembly histories possibly indicating accreted stellar mass in the later stages of evolution. In the Sérsic component, except for a few objects, the MAHs are clustered on the far right of the plot, where the entire stellar mass had been assembled in an extremely short timescale at the very initial stages of their formation.

UNIVERSIDAD DIEGO PORTALES

TRACING THE FORMATION HISTORIES OF
SPIRAL AND ELLIPTICAL GALAXIES WITH
INTEGRAL FIELD SPECTROSCOPY

SANTIAGO, CHILE
DECEMBER 2024